Facoltà di Ingegneria dell'Informazione, Informatica e Statistica

Dipartimento di Ingegneria dell'Informazione, Elettronica e Telecomunicazioni

Thesis for the Ph.D. degree in Remote Sensing

XXVI cycle

Active and Passive Multi-Sensor Radar Imaging Techniques Exploiting Spatial Diversity

Fabrizio Santi

Supervisor   **Prof. Debora Pastina**

INDEX

1. INTRODUCTION

1.1. BI/MULTI-STATIC RADAR

Although the overwhelming majority of radar systems have been developed as monostatic entities, the earliest radar were bistatic, i.e. in a configuration operating with separated transmitting and receiving antennas [1]. With the advent of pulsed operation and the duplexer in the late 1930s, the interest in bistatic radar dropped quickly and the monostatic radar, with its single-site operational advantage, become the configuration of choice and virtually all bistatic radar work ended after World War II [2]. However, the limits of monostatic radar are now beginning to be reached, and over the last years bistatic radar have been the focus of increased research activity [3].

One of the main issue relating to monostatic system is that the achievable information is limited by a single prospective. It is our common experience that observing an object, or a situation, by different points of view allows us to reach a greater information about that phenomenon. Extending the concept in the field of radar, the single prospective limitations can be addressed by using a multiplicity of transmitter and receivers leading directly to the concept of multi-sensor radar system. The spatial diversity offered by geographically distributing sensors allows for a much richer information set to be garnered from which both the detection and classification of targets can be improved [4]. Moreover, a monostatic radar represents a single point of failure. By having separated and multiple transmitters and receivers, the total system is much less vulnerable to out of services, since, if properly designed, the single sensor out of service does not necessarily render the system inoperative. Separation also has effect on the effectiveness of Electronic Counter Measures (ECM) since the transmitters and receivers are not co-located and therefore a receiver may be outside the main-lobe of the jammer or even outside Line Of Sight (LOS).

The concept of multistatic radar is not new. Since in 1960 is operating the Navspasur (NAVal SPace SURveillance), a US Navy multistatic continuous wave radar that detects orbiting objects as they pass through an electronic "fence" over the continental United States; three transmitting stations and six receiving stations are interspersed along a great circle from Fort Stewart (Georgia) to San Diego (California) [5]. The locations of the transmitting and receiving stations is shown in Figure 1-1. In 1978-1980 a multistatic measurement system was developed by the Lincoln Laboratory of Massachusetts of Technology to collect bistatic signature data and perform high-accuracy coherent tracking of re-entry targets [7]. Since in a multistatic scheme a receiver does not emit electromagnetic energy it is harder to locate than active radars, and therefore their potentiality in the military applications gained great attention from the late 1970s, [8]. Very soon, the concept was developed also in non-military applications, since the multistatic radar enables triangulation and allows a higher detection probabilities due to multiple observations [9]. Further information about the historical context of multistatic radar can be found in [10]. The recent technology advances, especially in digital transmission, better processing power, more reliable communications and precision navigation by Global Navigation Satellite System (GNSS) have led to a reassessment of multistatic radar, that now days can be considered an emerging technology [4].
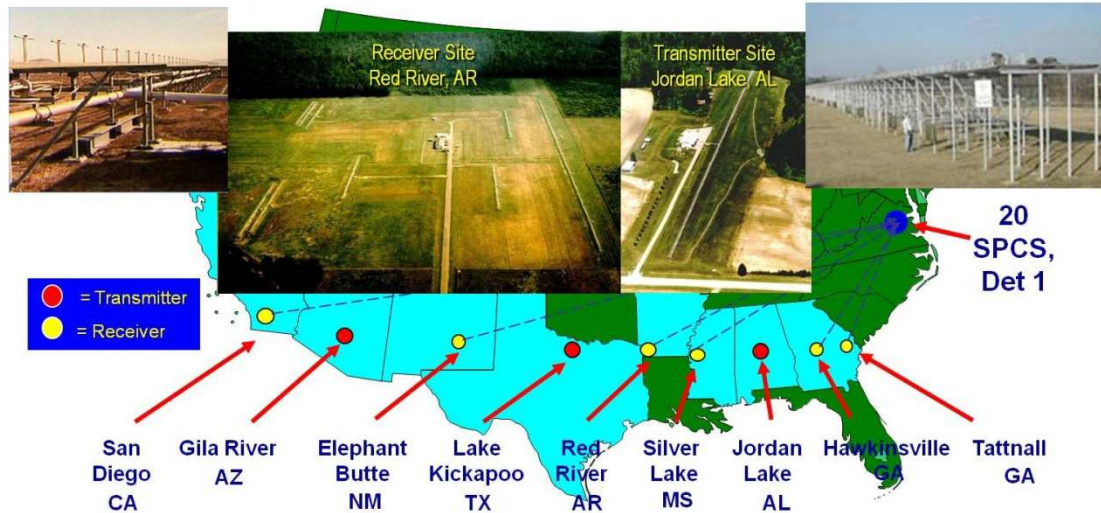
Figure 1-1. Navspasur sensors sites, [6].

1.2. MULTISTATIC AND MIMO RADAR

It should be noticed that different multi-sensor schemes can be developed and differing terms can be found in the literature, such as multistatic radar, multisite radar, radar network, distributed radar and MIMO (Multi-Input-Multi-Output) radar. So far we used the terms "multistatic" and "multi-sensor as "catch all" to embrace all forms possible. In this work a multi-sensor scheme is achieved as compositions of N bistatic transmitter-receiver couples. In some definitions a transmitter-receiver configuration is assumed to be bistatic if the distance between the antennas is "comparable" [11] or "a significant fraction" [12] of either the target-receiver or the target-transmitter distance. The only assumption when we refer to multi-sensor configurations is that the several transmit and receive antennas are on different platforms. Hereinafter we consider two possible scenarios, that we refer as Multistatic and MIMO. In the multistatic case, only one device of the network is transmitting and the other just receive, while in the MIMO case all the platforms carries an active radar and receives echoes from all the transmissions. The two possible situations are sketched in Figure 1-2: in Figure 1-2.a, only sensor 2 transmits while 1 and 3 just receive (multistatic case), while in Figure 1-2.b all the sensors transmit and receive the radar waveforms (MIMO). We point out that in literature, sometimes the two schemes are referred as semi-active and fully active [13].

1.2.1. MIMO RADAR

The concept of MIMO systems has been the focus of intense research activity in the field of the wireless communications, since its capability to dramatically improve the performance of communication systems over single antenna systems [14]. The concept of MIMO has been recently applied to the field of radar [15]. We remark that in literature the term MIMO radar can refer to a system using waveform diversity allowed by transmit and receive antenna arrays containing element that are collocated [16] or to a system exploiting the diversity offered by widely separated transmitting and receiving antennas [17].

The key aspect of a MIMO radar with respect to a multistatic configuration is the use of orthogonal waveforms [18]. They should have good auto-correlation and cross-correlation properties, as well as low Doppler loss. Several studies can be found in literature regarding waveform diversity in MIMO radar, e.g. [19], [20], [21], [22], [23], [24], [25], [26] and [27].

MIMO radar is nowadays a new, fast changing and controversial subject [28]. Although several problems have still to be resolved [29], MIMO radar represent a promising emerging technology.

1.2.2. MULTISTATIC RADAR

For the multistatic case a further categorization is applicable: active systems and passive systems. In this subsection we discuss about the latter configuration.

In the active configuration, the bi/multi-static radar operates with its own dedicated transmitter, which are specially designed for bistatic operation, or with transmitters of opportunity, which are designed for other purposes but found suitable for bistatic operation. When the transmitter of opportunity is from a monostatic radar the bistatic radar is often called a *hitchhiker*.

In the passive configuration, the transmitter of opportunity is from a non-radar transmission, such as broadcast, communications or radionavigation signal, and in literature the bistatic radar has been called many things including *passive radar, passive coherent location, parasitic radar* and *piggy-back radar* [30]. Bistatic radar using transmitters of opportunity have been a topic of increasing interest over the last years [31], since they have some significant attractions, in addition to those common to all bistatic radars. As well as being completely passive and hence potentially undetectable, they can allow the use of parts of the RF spectrum (VHF and UHF) that are not usually available for radar operation, and which may offer a counterstealth advantage, since stealth treatments designed for microwave radar frequencies may be less effective at VHF and UHF. Broadcast transmissions at these frequencies can have substantial transmit powers and the transmitters are usually sited to give excellent coverage.
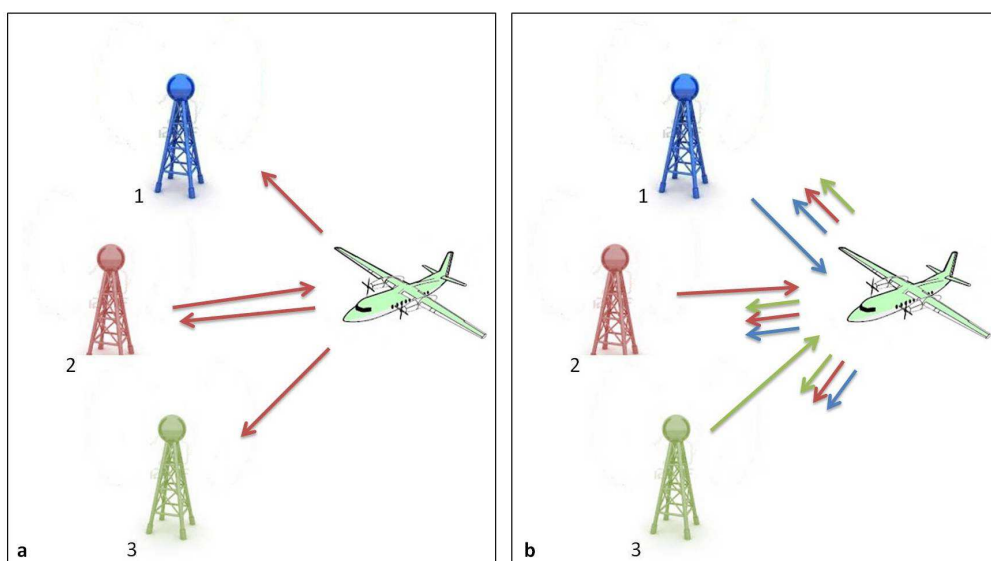

Figure 1-2. Multi-sensor configurations – a) Multi-static, b) Multi-Input-Multi-Output (MIMO).

1.3. MULTI-SENSOR RADAR IMAGING

1.3.1. BI/MULTI-STATIC SAR

Conventional monostatic Synthetic Aperture Radar (SAR) systems using a single-antenna high-power transmitter and a highly sensitive receiver onboard the same platform, represents today a mature remote sensing and surveillance system, and it is utilized routinely in a wide range of commercial and scientific applications. Many SAR systems are in operation, from both airborne and spaceborne platforms, to provide high resolution radar images.

Recently, the bistatic, as well multistatic and MIMO concepts, have been applied to the field of SAR, since the variety of potential gains in the scene information. Bistatic geometries give extra information regard the targets, since their radar cross section (RCS) is essentially different from monostatic case [32], [33]; different bistatic geometries result in target RCS variation, allowing a better Automatic Target Classification (ATC) procedure [34], [35]. The multi-perspective observation can improve the overall resolution when the scattered measurements are fused [36], it can provide a better ability to distinguish targets from clutter [37]; also, electronic countermeasure devised for monostatic SAR are less effective against distributed systems [38].

The research about bi/multi-static SAR have received increased attention over the last years. Several new SAR missions have been suggested, where the spatial diversity offered by the multi-sensor configurations increases capability, reliability and flexibility [13]. Potential application areas of multi-static and MIMO SAR systems include, but are not limited to, SAR interferometry [39], [40], wide-swath SAR imaging [41], resolution enhancement [42], interference suppression [43], ground moving target indication [44], spaceborne tomography [45] and multistatic imaging [46], [47].

Examples of spaceborne multistatic configurations are the interferometric cartwheel [48] and BISSAT [49]. The former is composed by three passive identical microsatellites set in a particular geometry and flying behind or ahead of an active SAR satellite illuminating a ground swath; the reflected signals are received by the microsatellites with specific viewing configurations; the obtained data are mainly used for the computation of a Digital Elevation Model (DEM). The latter, founded by the Italian Space Agency, consists in a passive SAR flying on board a small satellite, which observes the area illuminated by an active SAR, such a COSMO/SkyMed satellite.

An example of spaceborne MIMO configuration is the Techsat 21 (Technology Satellite of the twenty-first century) [50]. The topology of the system (Figure 1-3) involves a cluster of satellites in a single orbital plane. Each satellites transmits its own orthogonal signal at X-band and is receiving all reflected signals. The intended use for Techsat 21 includes RF multistatic imaging, GMTI, anti-jamming operation and geolocation. Another example is the German TanDEM-X (TerraSAR-X add-on for Digital Elevation Measurement) mission, lunched in June 2010 and aiming at realizing a spaceborne bistatic SAR interferometer based on two low-Earth-orbiting satellites flying in close formation [51] (Figure 1-4).

Regarding bistatic airborne SAR, experiments have been conducted in the United States and, more recently, also in Europe. A pioneering experiment took look in Michigan in 1983, involving two Convair CV-580 aircraft flying at ~330 Km/h and using several configurations with vertical or

horizontal separation between the platforms [53]. More recently, an experiment has been conducted by QinetiQ Malvern under the UK MoD Corporate Research Program in September 2002. It focuses on a fully airborne, synchronized BSAR demonstration using QinetiQ's enhanced surveillance radar and the Thales/QinetiQ airborne data acquisition system [54]. Other examples are the FGAN BSAR experiment (November 2003), using two SAR sensors PAMIR and AER-II [55] and the ONER-DLR Bistatic Airborne SAR Campaign (October 2002-February 2003) [56].
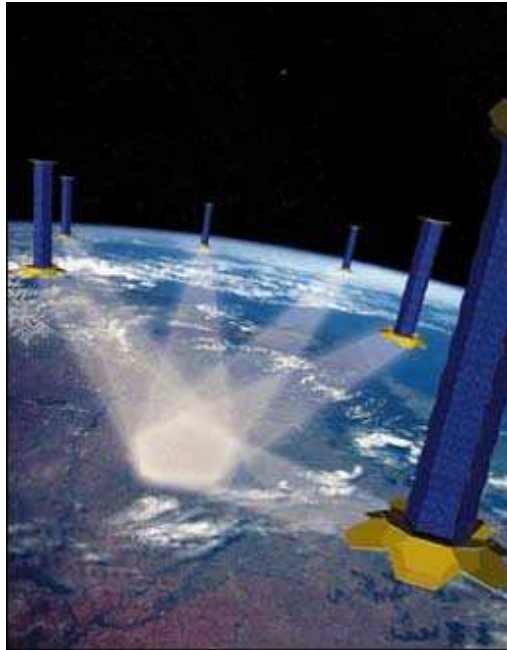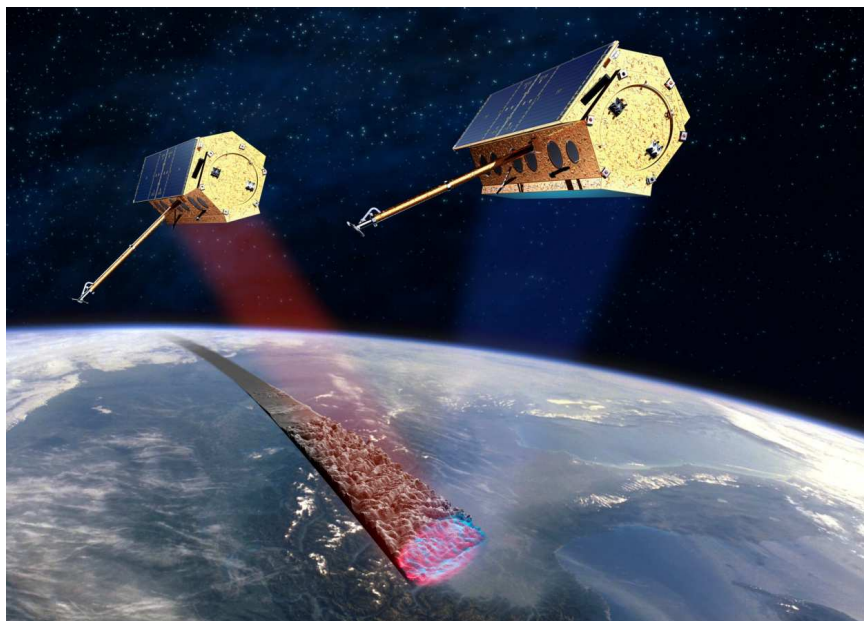

Figure 1-3. TechSat 21 topology.

Figure 1-4. TanDEM-X in formation flight, [52].

1.3.2. BI/MULTI-STATIC ISAR

In 1980, the Inverse SAR (ISAR) concept was proposed [57], [58]. Conversely to SAR, where the high resolution cross range profile is achieved exploiting the motion of the platform with respect to a stationary scene, in ISAR is the target's relative movement that produces the Doppler gradient making the cross-range resolution possible (this concept was exploited during the Sixties in the radar astronomy of the moon and planets, exploiting their rotation to produce the image of their surface [59]). Nowadays ISAR is a well established technique [60] and it is largely used in maritime surveillance for the classification of ships and other objects [61].

In the past, the bistatic ISAR case was considered to obtain separated images of the same target taken with different aspect angles in order to improve recognition capability [62], [63]. Also, multiple sensors was considered to improve ISAR interferometric capability [64], [65], [66].

1.3.3. PASSIVE RADAR IMAGING

The passive radar imaging technology based on external illuminators is a popular topic in recent years. Several contribution can be found in the field of SAR using different opportunity transmitters, as for example telecommunication geostationary satellite [67], TV broadcasting satellite [68] or GNSS satellite [69], [70], [71].

Regarding Inverse SAR (ISAR) few contributions can be found in the literature exploiting different opportunity transmitters. Terrestrial transmitters, radio FM and DVB-T, are exploited in [72] and [73] respectively, while GPS and geostationary telecommunications satellites are considered in [74] and [75], [76].

1.3.4. CHALLENGES IN MULTI-SENSOR RADAR IMAGING

Despite the number of potential using multiple transmitter-receivers couples, several technical issues have to be faced.

One of the main problem is the phase and time synchronization [13]. To maintain time and frequency synchronization in a multi-sensor configuration where no direct synchronization is practical, stable local oscillators are often used. Oscillator errors deserve special attention in distributed SAR systems since there is no cancellation of low-frequency phase errors as in a monostatic SAR, where the same oscillator signal is used for modulation and demodulation [77]. Possible solution for time synchronization are discussed in [78].

Other practical problems regard the flight coordination. Especially in the case of spaceborne configurations, the collision avoidance may be a major design driver. Interferometric applications require a very accurate knowledge of the position of the platforms, at the millimeter level, that could be achieved using GNSS measurements [79].

As in MIMO radar, in a MIMO SAR (as well as MIMO ISAR), each antenna should transmit a unique waveform, orthogonal to the waveforms transmitted by other antennas. In addition, the waveforms used in SAR should have a wide bandwidth so that high resolution can be obtained, and since usually the SAR are placed inside airplanes or satellites, a high average transmit power is required for the

transmitted waveforms [80]. Most of the MIMO radar waveforms are not suitable for MIMO SAR imaging and difficult to implement in the real world [29]. A practical solution is the use of linearly modulated (chirped) waveforms.

The processing of bi/multi-static data requires robust and efficient algorithms [13]. Several processing techniques have been proposed. The possibility to apply a specific processing algorithm is strictly dependent on the bistatic geometry and the relative motions between the platforms [81].

1.4. WORK OVERVIEW

The work here presented reports several innovative radar imaging techniques exploiting the spatial diversity offered by multi-sensor systems in order to improve the performance with respect to the conventional, single channel cases.

Chapter 2 and 3 are dedicated to the study of active multi-sensor ISAR technique. In ISAR, the imaging capability are strictly related to the target's intrinsic motion characteristics. This draws some lines at the imaging capability for two main reasons:

1) There is no way to *a priori* assign the desired value of the cross range resolution; moreover, depending on particular conditions, it could be very poor.
2) Since the target motion is generally unknown, the information necessary for focusing must be estimated directly from the received signal.

In [82] the Distributed ISAR (D-ISAR) technique has been proposed, consisting in the exploitation of the signal received by multiple surveys in order to improve the achievable cross-range resolution: the spatial diversity offered by the multiple view angles allows to achieve a much wider observation angle than for a single aperture, resulting in an ISAR with higher resolution. The work in [82] considered a multi-aspect formation and a dominant yaw motion. It has been extended in [83] for a multi-grazing formation exploiting the horizontal motion of the target and in [84] for targets undergoing 3D motion (i.e., simultaneously rolling, pitching and yawing targets).

Chapter 2 focuses on the D-ISAR technique making use of stepped-frequency waveforms, which have the advantage of reducing the instantaneous bandwidth and the sampling rate requirements. The proposed technique is validated by a set of real data we acquired in the anechoic chamber at the SELEX ES (ex SELEX Galileo) base in Caselle (Turin, Italy) in April 2011.

The multiple view angle observation are exploited in chapter 3 in order to improve the target rotation motion estimation performance. The key point of the proposed estimation techniques is that different view angle results in different Image Projection Plane (IPP) and as a consequence the Doppler position of a scatterer as viewed by a sensor is different by the other sensor. Properly exploiting this effect, the estimation accuracy of the estimation can be improved. Two cases will be presented for two kind of sensor displacement: in the first one, a multi-aspect formation is considered and it is studied in the case of a dominant vertical motion; in the second a joint multi-aspect/multi-grazing formation of sensor is studied, and target is considered undergoing a 3D motion; the joint multi-aspect/multi-grazing case not only allows an improvement in the accuracy of the target rotation motion estimation, but also it is able to perform the separate estimation of all the radial, horizontal and vertical components, that is useful for the selection of proper imaging interval

to feed ATR procedures. Both model-based and model-free criteria are considered and the analytical derivation of the Maximum Likelihood estimation scheme is reported along with the derivation of the Cramer Rao lower Bounds.

A similar concept to the D-ISAR has been proposed in [85] for improving range resolution by exploiting multiple SAR surveys of the same area, and it is extended for a MIMO SAR constellation in [86]. In chapter 4 we propose a combination of the MIMO-ISAR and MIMO-SAR concepts, defining a 2D-MIMO SAR/ISAR technique exploiting a reconfigurable formation of sensors. We will show the capability of the proposed technique to improve both the cross-range and the slant range resolutions of rotating targets, by properly processing the data acquired by properly located sensors. Proper cross-track and along-track displacements of the sensors allows to achieve a 2D resolution cell improvement that, exploiting all the monostatic and bistatic acquisitions, could be considerably greater than the number of the real sensors.

In the multi-sensor ISAR techniques considered until now cooperative transmitters have been exploited; moreover, we focused on the rotational motion of the target. In chapter 5 a multistatic ISAR technique is proposed exploiting a radar transmitter of opportunity. Specifically, we define and asses an ISAR-while-scan mode for coastal surveillance based on the exploitation of the data acquired by multiple properly located passive devices (receivers only) from the transmissions of a coastal surveillance radar system for the formation of ISAR images of ship targets of interest using their translational motion as source for the Doppler gradient for the image formation. An ad-hoc processing technique is described along with simulated results. As will be clearer in the following, differently from the D-ISAR technique where the multiple observations allow to increase the overall Doppler bandwidth (and therefore the cross-range resolution), here the multiple observations allows to improve the azimuth sampling frequency of the system, allowing to fulfill the Nyquist criteria and making the azimuth signal compression possible.

A fully passive technique is presented in chapter 6, where the use of GNSS transmitters of opportunity is considered for the formation of SAR images. The large number of satellites in a GNSS constellation offers a rather unique system diversity; signal reflections from multiple satellites can be acquired from a single receiver (this configuration is slightly different from the one depicted in Figure 1-2.a, where a single transmitters and multiple receivers were considered; however we can refer this configuration again as multistatic). The proper combination of the signal can improve the observed area information and here we consider the case of a non-coherent combination. A multistatic PSF for the system is defined and analyzed both against simulated and real data. Challenges of the proposed combination scheme are discussed and the first preliminary results obtained from real radar images are shown.

2. MULTI-ANGLE DISTRIBUTED ISAR FOR ENHANCED CROSS RANGE RESOLUTION OF MANMADE ROTATING TARGETS

As well known the Inverse Synthetic Aperture Radar (ISAR) technique exploits the rotational motion of a target with respect to its centre, as observed by a nearly stationary sensor platform, to provide high resolution images of the target itself, [58], [60]. This is the case of airborne or spaceborne systems (hovering helicopters/UAV or geostationary satellites) imaging ship targets interested by yaw, pitch and roll rotation motions induced by the sea.

Since the achievable cross range resolution depends on the intrinsic motion characteristics of the target (and specifically on its overall change of aspect angle $\Delta\theta$), there is no way to a-priori assign the desired value of cross range resolution, [60]. Moreover, depending on the particular conditions, the achievable resolution can be very poor. With reference to the case of ship targets imaging, this condition can occur in presence of a low sea state inducing very limited rotations: in this case the limited rotation motion can result in a very low cross range resolution. This is made even worse by the typical use of the short CPI (Coherent Processing Interval) that is required by the constraint of keeping fixed the ship rotation axis. These circumstances can have particularly negative implications as ISAR images are often used to feed NCTR (Non Cooperative Target Recognition) procedures. To counteract this effect and to increase the cross range resolution of ISAR images (especially in the case of very small changes in the target aspect angle) a possible strategy is represented by the exploitation of the data acquired by multiple radar sensors carried by multiple air platforms, [82]. If the sensors are appropriately spaced, each scatterer can be globally observed from a much wider observation angle than for a single aperture and therefore an ISAR image with a higher resolution can be obtained.

This new multi-sensor ISAR technique can be referred as Distributed ISAR (D-ISAR) and two different reference scenarios are possible for the sensors belonging to a formation of S platforms: in the first scenario (addressed as multistatic distributed ISAR) only one platform carries an active radar system and the other (S-1) carry receiving only sensors, while in the second one (addressed as MIMO, Multiple Input Multiple Output, distributed ISAR) all the S air platforms carry an active radar that autonomously transmits and receives the radar waveforms. In this latter case the active sensors are considered additionally able to separately receive also the waveforms transmitted from the other transmitters. It has to be noticed that echoes from all the transmitters (one in the multistatic and S in the MIMO case) will be received by each receiving device in the formation. This requires the use of appropriate transmitted waveforms to allow the separation of the echoes. A pictorial view of these two reference scenarios is presented in Figure 2-1 for the sake of clarity. Figure 2-1a sketches the multistatic distributed ISAR case where the flying formation is composed of an helicopter carrying the transmit/receive hardware and a few lightweight UAV used to carry the receive-only devices. Figure 2-1b presents the MIMO distributed ISAR case with several hovering helicopters carrying an active radar system each.
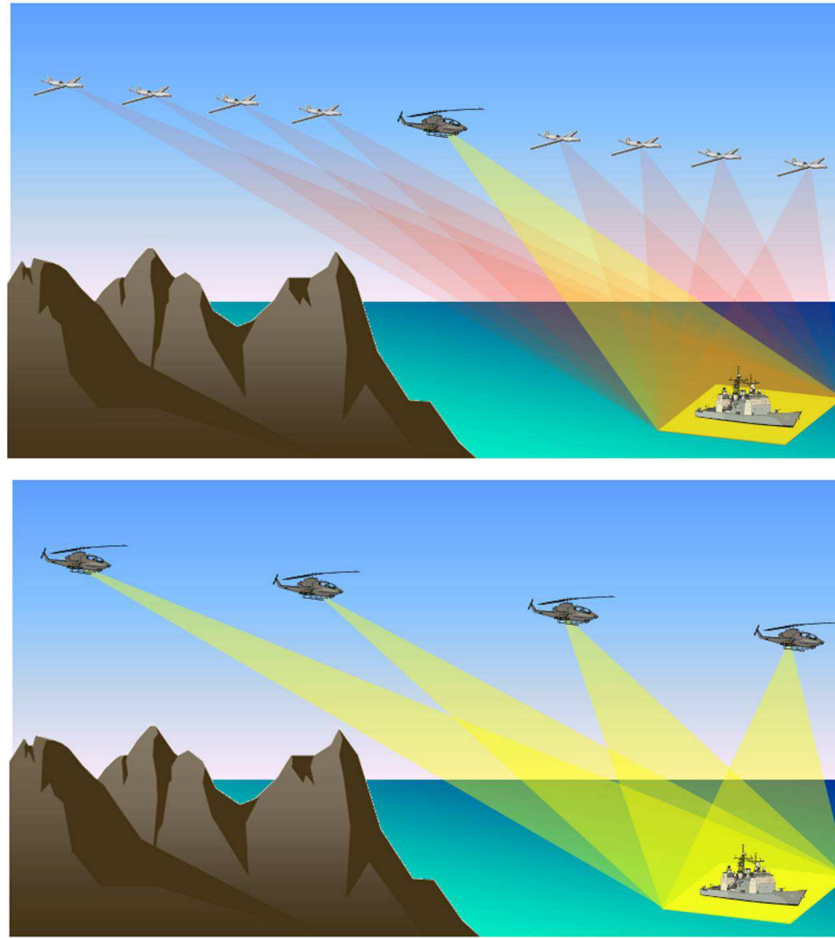
Figure 2-1 - Distributed ISAR scenarios in the (a) multistatic case and in the (b) MIMO case

2.1. DISTRIBUTED ISAR CONCEPT

The D-ISAR concept is summarized in Figure 2-2 for the case of two platforms (A and B) and a target rotating with constant velocity ω around its vertical axis and initial azimuth angle θ^0 and observed for an observation time T. A multi-aspect formation is here considered, as in [82], while the multi-grazing case is studied in [83].

The time-varying observation angle of the multistatic case is sketched in Figure 2-2A, for the case where the first sensor is a monostatic (transmit and receive radar) while the second sensor is a receiving-only sensor, positioned so to provide the appropriate change in the view angle (namely $\alpha_{n-1} - \alpha_n$). With the two sensors, the maximum increase achievable in observation angle, and therefore in resolution, is of a factor of 2, which is obtained by setting $\alpha_{n-1} - \alpha_n = \omega T = \Delta\theta$.

In the MIMO case (Figure 2-2B) platform A is supposed to carry an active radar system transmitting and receiving an up-chirp while platform B is equipped with a radar system transmitting a down-chirp with two receiving channels: the first one matched to its own transmission and the second one matched to the transmission from platform A. The angular separation between the two transmitting sensors 1 (from platform A) and 3 (from platform B) is $\alpha_1 - \alpha_3 = \alpha_{AB}$. We recall that a bistatic acquisition for limited values of the bistatic angle corresponds to an equivalent monostatic

10

configuration with a fictitious sensor at azimuth angle equal to the mean angle between the real transmit and receive platforms; therefore, the bistatic acquisition from platform B provides a fictitious sensor 2 for which $\alpha_1 - \alpha_2 = \frac{\alpha_{AB}}{2}$ applies.
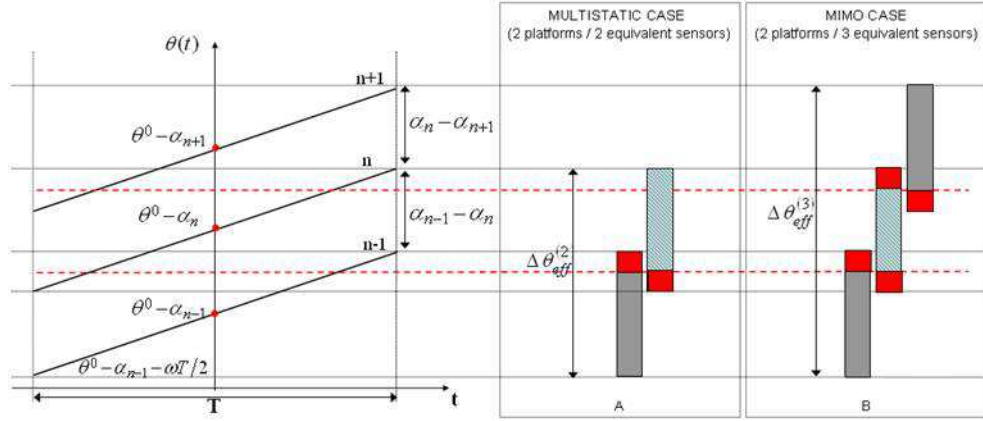

Figure 2-2. Multi-angle D-ISAR concept.

The extension of the dual platform case to a generic number N of equivalent sensors (N=S in the multistatic case and N>S) is straightforward, and leads to a global change of the view angle for the kth scatterer equal to:

$$\Delta\theta_{eff}^N = \theta_k^N\left(\frac{T}{2}\right) - \theta_k^1\left(\frac{T}{2}\right) = \left[\theta_k^0 - \alpha_N + \frac{\omega T}{2}\right] - \left[\theta_k^0 - \alpha_1 - \frac{\omega T}{2}\right] = \omega T + \alpha_1 - \alpha_N \tag{1}$$

In order to avoid gaps in the overall view angle, it is required that $\theta_k^n\left(-\frac{T}{2}\right) \leq \theta_k^{n-1}\left(\frac{T}{2}\right)$, namely: $\alpha_{n-1} - \alpha_n \leq \omega T$ for every value of n = 1,…,N. If neither gaps or overlapping between the sub-apertures, the upper bound for both global observation angle and achievable cross range resolution are equal to:

$$\Delta\theta_{eff}^N \leq \Delta\theta + (N-1)\omega T = \Delta\theta + (N-1)\Delta\theta = N\Delta\theta \tag{2}$$

$$\Delta_{cr} = \frac{\lambda}{2\Delta\theta_{eff}^N} \geq \frac{\lambda}{2N\Delta\theta} \tag{3}$$

To quantify the improvement in cross range resolution in practical situation, the γ_{cr} parameter is defined:

$$\gamma_{cr} = \frac{\Delta_{cr}}{\Delta_{cr}^N} = \frac{\Delta\theta_{eff}^N}{\Delta\theta} \leq N \tag{4}$$

2.2. SYNTHETIC BANDWIDTH D-ISAR

In the past, D-ISAR techniques have been considered using linearly modulated (chirped) waveforms. However the use of an instantaneous wideband waveform entails cost and complexity in the receiver, mainly related to the high requested sampling rate. Here we propose the use of the D-ISAR

system based on stepped-frequency waveforms, which have the advantage of reducing the instantaneous bandwidth and the sampling rate requirements. The changes induced in the D-ISAR technique by the use of synthetic bandwidth waveforms are also analyzed and a suitable focusing technique is proposed and tested against simulated target in both multistatic and MIMO cases. The proposed concept and processing scheme are also validated by using a set of real data acquired in anechoic chamber for the multistatic case.

As usual in ISAR literature, an arbitrary reference point in the target, called target fulcrum, is selected, and the target motion is decomposed into a translation of the fulcrum (which is assumed to be already compensated for) and a rotation of the target body around this point (rigid body hypothesis). The interest is in targets with a dominant rotation around the vertical axis (resulting in a plane image [60]), therefore pitch and roll are considered negligible with respect to the yaw component of the motion. The origin of the coordinate reference system is set in the target fulcrum and the target is assumed to rotate with a rate ω around the Z axis.

2.2.1. TRANSMITTED WAVEFORMS

MULTISTATIC CASE

The active sensor transmits a stepped-frequency waveform consisting in a series of K short narrowband (ideally monotone) pulses, being the carrier frequency increased pulse to pulse by a fixed frequency step Δf. We call T_2 the temporal interval between two consecutive pulses, so the PRT of the system is KT_2, and the set of K pulses is called burst (see Figure 2-3). Therefore the n-th baseband transmitted burst is expressed as:

$$s_n(t) = \sum_{i=1}^{K} rect_{T_p}\left(t - \frac{T_p}{2} - (i-1)T_2 - nKT_2\right) \cdot e^{j2\pi f_i t} \tag{5}$$

where T_p is the single pulse duration; n is an index referring to the slow-time axis, while i is an index referring to the fast-time axis.
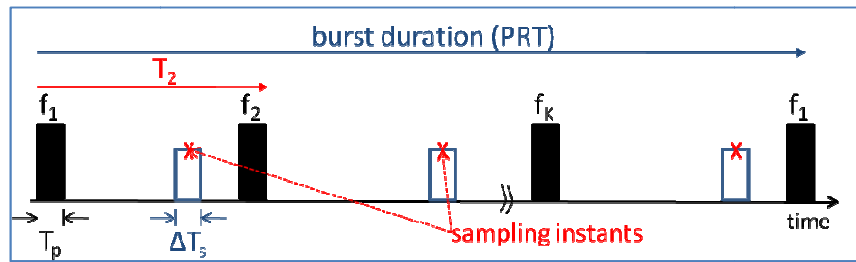

Figure 2-3. Fast time axis for the stepped-frequency waveforms.

Transmitting N bursts we can obtain N slant range profiles taking a complex sample in the center of the receiving window ΔT_s for each pulse in the burst (see Figure 2-3) and operating N inverse Fourier transforms, one for each burst. The obtained range resolution is:

$$\Delta r = \frac{c}{2K\Delta f} \tag{6}$$

being KΔf just the overall spanned bandwidth. Generally the following constraints hold for the frequency step Δf and the pulse duration T_p, being ΔR the slant range swath:

$$\Delta f \leq \frac{c}{2\Delta R} \ \& \ T_p \geq \frac{2\Delta R}{c} \tag{7}$$

In the general case, the baseband frequencies transmitted by the h-th active sensor can be collected in the vector

$$\mathbf{f^h} = [f_1^h, f_2^h, \ldots, f_K^h] \tag{8}$$

such that $f_i^h = f_1^h + (i-1)\Delta f, i = 1,2,\ldots,K$. Therefore, in the case of a single active sensor, the data received by each sensor in the formation are organized in a K×N matrix, each column collecting the complex samples relative to a specific burst.

MIMO CASE

For the MIMO D-ISAR to work, a set of stepped-frequency orthogonal waveforms must be defined, along with the pre-processing needed to correctly separate the receiving channels.

Referring to stepped frequency waveforms the i-th transmitted pulse is a rectangular no-modulated signal, so its frequency baseband response is a *sinc* function centered in f_i and having the first null in $f_i + \frac{1}{T_p}$: on this basis two pulses transmitted on two frequencies f_1 and f_2 such that $f_2 - f_1 = {}^C\!/_{T_p}$ with C integer number can be easily separated. Therefore we consider the platforms transmitting stepped frequency waveforms with interleaved frequency axes such that $f_i^h - f_i^l = (h-l)/T_p$ being f_i^h and f_i^l the i-th frequency transmitted by platform h and platform l respectively. If S is the number of the active sensors, we set T_p and Δf as:

$$T_p = S\frac{2\Delta R}{c} \ \& \ \Delta f = \frac{S}{T_p} \tag{9}$$

In the following we will consider the case of S=2; the cases S>2 can be easily generalized. The two active sensors transmit the n-th burst on two frequencies vectors $\mathbf{f^1}$ and $\mathbf{f^2}$ separated by the quantity Δf/2 (see Figure 2-4); the corresponding baseband responses are sketched in Figure 2-5.

Two samples are collected in each ΔTs with a sampling frequency Fs equal to Δf (see Figure 2-6). Therefore, in the MIMO case, the data received by each sensor in the formation are organized in a 2K×N matrix (SK×N in the more general case).
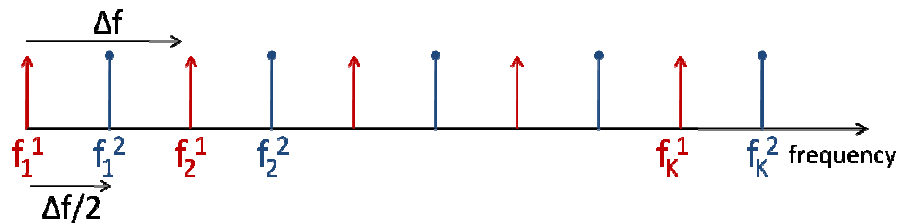
Figure 2-4. Frequency vectors for the case S = 2.
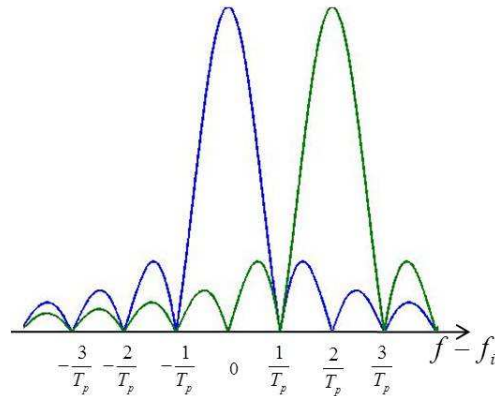
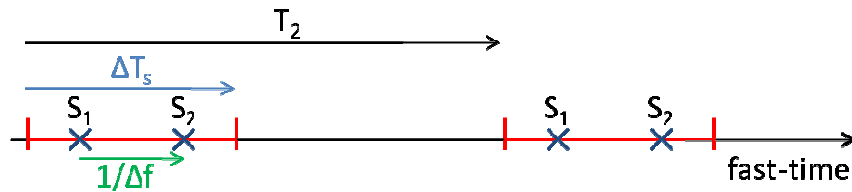Figure 2-5. Baseband responses for the case S = 2.

Figure 2-6. Sampling for the case S = 2.

2.3. FOCUSING TECHNIQUE

The block diagram of the proposed focusing technique is shown in Figure 2-7 for the case of N_{eq} equivalent sensors (when S = 2, N_{eq} = 2 in the multistatic case and N_{eq} = 3 in the MIMO case).
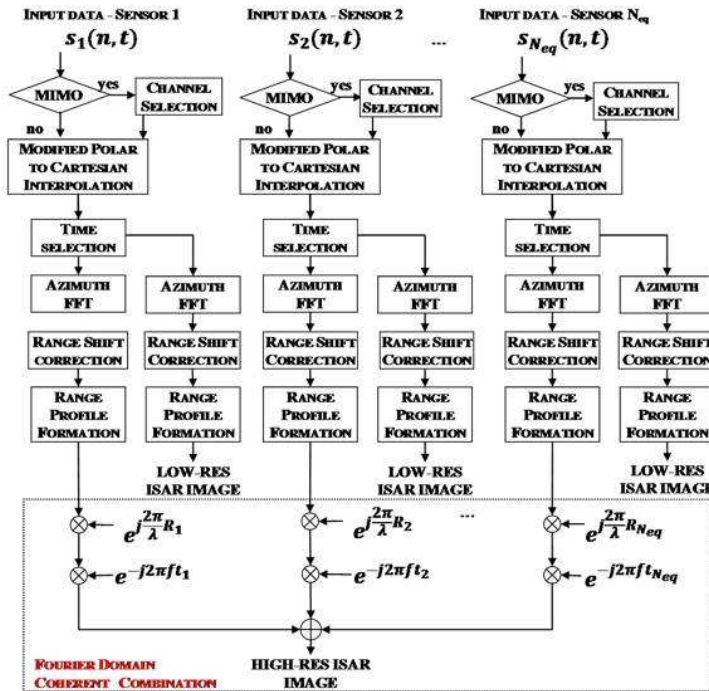

Figure 2-7. Synthetic bandwidth D-ISAR focusing technique.

The first step is channel selection, needed in the MIMO case and here explained under the hypothesis of waveforms completely overlapped in time domain. Specifically, referring to the case of S=2 and N_{eq}=3, for each transmitted burst each equivalent sensor has in input a 2K×1 **x** vector containing the samples taken at time instants S_1 and S_2 (Figure 2-6). These samples result from the coherent superposition of the echoes from the two transmitted waveforms. We aim at obtaining two K×1 vectors **x$_1$** and **x$_2$** equivalent to the vectors obtained if the receiver would sample distinctly the two signals taking only a sample in the center of each ΔT_s, i.e. in $S_0 = (S_1 + S_2)/2$. To this purpose, two operations are performed:

1. The orthogonality between the transmitted waveforms is used to separate the two contributions. The elements [2i-1,2i] of **x** contain the contributions of the pulses transmitted on f_i^1 and f_i^2, with i = 1,2,...,K. K scalar products are performed to select the opportune coefficient:

$$x_h'[i] = \frac{1}{2} \sum_{n=2i-1}^{2i} x[n] \cdot e^{-j2\pi f_i^h S_n} \tag{10}$$

where h = 1,2 and i=1,2,...,K and the instants are given by $S_n = S_0 + (-1)^n/(2\,\Delta f)$.

2. The reconstruction of the two vectors **x$_h$** is obtained by means of:

$$x_h[i] = x_h'[i] \cdot e^{j2\pi f_i^h \frac{(S_1+S_2)}{2}} \tag{11}$$

These operations must be performed for all the N transmitted bursts. Therefore, starting from a 2K×N data matrix, after the separation, two K×N matrices are obtained.

At this point a comment on the phase error (and Doppler shift) induced by the target motion during a single PRT is in order. As known in the case of synthetic bandwidth this Doppler shift can be not negligible, differently from the instantaneous bandwidth case (i.e. chirped waveforms). The change in the radar-target range due to the motion of the target during the burst duration can cause the shift and the blurring of the range Point Spread Function (PSF), [60]; to counteract this effect a motion compensation stage should be performed. To this purpose in the past several methods have been proposed (e.g. [87]). However we recall that in this paper we focus on targets with negligible translation and exploit the rotation motion. Under this hypothesis, the PRF of the system has a lower bound imposed by the Doppler bandwidth B_d:

$$PRF = \frac{1}{KT_2} \geq B_d = 2D\frac{\omega}{\lambda} \tag{12}$$

where D is the maximum target's cross-range extent (diameter of the target area assumed circular), ω is the angular speed and λ is the transmitted wavelength. Considering a target scatterer at cross-range position $x_{cr} = D/2$ (worst case) with respect to the rotation centre the change in the slant range distance from the generic antenna and the considered scatterer between the first and the last pulse of the burst is always upper bounded by $\lambda/4$ when the constraint in (12) is satisfied and therefore can be neglected. The shift of the peak of the range PSF (Point Spread Function) can be shown, [60], equal to:

$$\frac{v_r f_c T_2}{\Delta f} = \frac{D\omega}{\lambda} \cdot \frac{\Delta r}{PRF} \leq \frac{\Delta r}{2} \tag{13}$$

where v_r is the scatterer radial velocity (evaluated in the worst case for a scatterer at $x_{cr} = D/2$), Δr is the slant range resolution and the upper bound applies again when the constraint in (12) is satisfied. We can observe that the shift is spatially variant (it changes with changing x_{cr}) and its maximum value is contained in a fraction of the range resolution cell: therefore it does not affect the quality of the cross-range PSF; moreover, despite being very limited, it can also be easily compensated as explained in the following. Since the blurring of the range PSF appears for radial velocities considerably higher than the values causing the shift, [60], this point is not a concern in the case under study. Obviously in the case of not negligible translation a proper mocomp stage should be applied before going in the following processing steps.

Considering the transmission of the synthetic bandwidth waveforms and the target rotation, the raw data are defined in the wavenumber domain (range-frequency, azimuth-frequency), where the Polar Format Algorithm (PFA) operates. The approach here proposed to focus the distributed image is a Decentralized Technique for multi-angle ISAR focusing, based on a modified version of the PFA, as in [82]. This decentralized approach first focuses N low resolution ISAR images and then combines them coherently to achieve the high resolution image. After channel selection, if needed, for each branch in the scheme (Figure 2-7) the processing is organized in the following steps:

1. Modified Polar to Cartesian interpolation which removes the range and Doppler migration from single sensor data, sets the same Image Projection Plane (IPP) for the N_{eq} sensors and scales the axes as all the acquisitions were monostatic (see Figure 2-8).
2. Time Selection which is needed when the observations from the different sensors are partially overlapped in angle.
3. Azimuth Fourier transform which allows to go in cross-range domain.
4. Range shift correction which is performed by multiplying the data by a phase ramp in range frequency dimension with slope dependent on the cross-range position.
5. Range Fourier transform which transforms the data in the range & cross-range domain.
6. Phase alignment which compensates the different phase terms due to the different slant-range distances of the N equivalent sensors to the scene centre.
7. Coherent combination which consists of two operations. The first aligns the time selected acquisitions, as the corresponding data were acquired by a single monostatic sensor. The processed images are then summed to obtain the distributed ISAR image with improved cross-range resolution.

Note that in order to obtain the low resolution single-sensor ISAR images as intermediate outputs, after step 1 we can skip step 2 and perform steps 3-4-5.
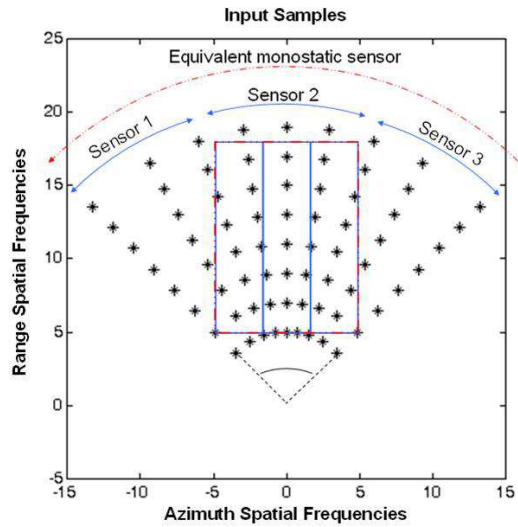
Figure 2-8. Polar to Cartesian grid for N = 3.

2.4. SIMULATED PERFORMANCE ANALYSIS

In this section we show the resulting images for a simulated ship target interested by a constant rotational yaw motion of angular speed ω = 0.4 [deg/sec] and a horizontal formation of platforms; the angular spacing between the platforms is such that no overlapping or gap is present in the equivalent overall view angle. The maximum target extent D is 120m and we choose a PRF value of 80Hz, therefore fulfilling (12). In order to have a slant range resolution of 0.5m the needed overall bandwidth is 300 MHz; since we set the slant range swath ΔR equal to 150m, that is slightly greater than D, the Δf is about 1MHz and then the number of sub-samples K is about 300. Therefore the sub-pulse repetition frequency is $PRF \cdot K \approx 24kHz$.

Figure 2-9 shows the obtained images for the following cases: a) single monostatic channel (conventional ISAR) with Δr_{cr}=1.5m; b) multistatic (S=2) with Δ_{cr}=0.75m; c) multistatic (S=3) with Δ_{cr}=0.5m; d) MIMO (S=2) with Δr_{cr}=0.5m.

The range and cross-range cuts are shown in Figure 2-10 for the target scatter in (30m,7m).

The quality enhancement moving from conventional to D-ISAR is evident: specifically when S=2 a cross-range resolution improvement equal to 2 and 3 are achieved respectively in the multistatic and MIMO cases. From the range cuts we observe that, as predicted by the theory, the range PSF is exactly obtained in all the considered cases; moreover the result obtained in the MIMO case highlight the effectiveness of the proposed set of waveforms. The cross-range cuts underline the cross-range enhancement and confirm that the cross-range PSF is not degraded by the use of the synthetic bandwidth waveforms.
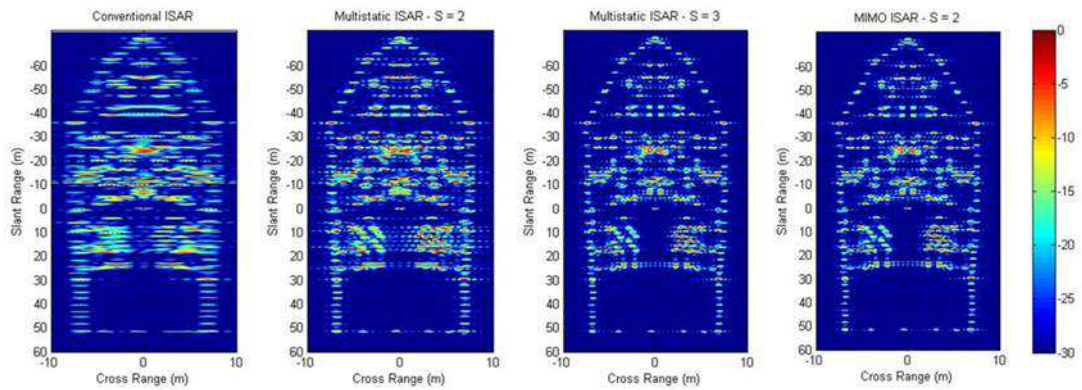
Figure 2-9. D-ISAR images of a simulated ship target – a) Conventional ISAR, b) Multistatic D-ISAR S = 2, c) Multistatic D-ISAR S = 3, d) MIMO D-ISAR S = 2.
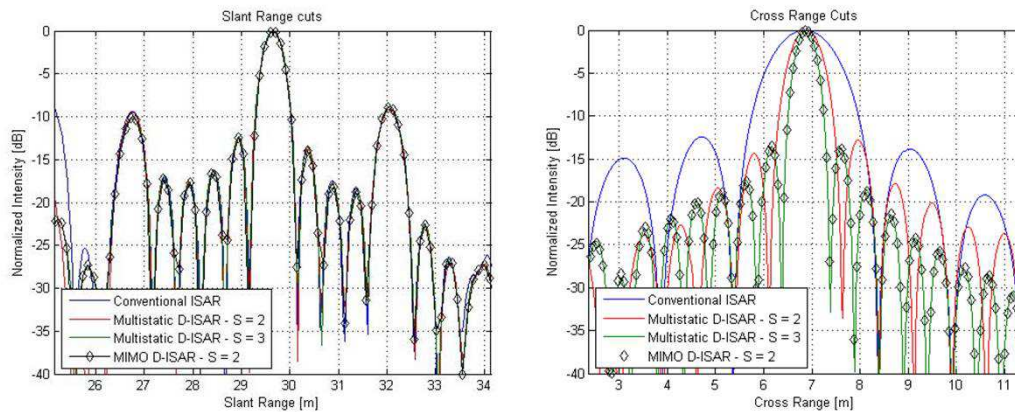
Figure 2-10. Range and cross range cuts.

2.5. APPLICATION TO LIVE D-ISAR DATA

In order to validate the multi-angle D-ISAR concept an experimental campaign has been carried on in April 2011. D-ISAR data have been acquired against targets on a rotating turntable in an anechoic chamber at the SELEX Galileo base in Caselle (Turin, Italy). A photo of the anechoic chamber is shown in Figure 2-11a.

The measurements are based on the use of a Compact Range system which generates a planar wave front in the test zone. The Compact Range System includes the parabolic reflector, the system of feeds and the positioner of the target under test. The reflector is an offset parabolic reflector P/N 5755 made by Scientific Atlanta (Figure 2-11b). The reflector is illuminated by a spherical wave front from a transmitting feed located into its focus; the signal from the target is focalized by the reflector into its focus where the receiving feed is located. A second receiving feed has been added 60 cm apart from the first one, thus giving the second bistatic channel with bistatic angle equal to 4.3°. The measurements instrumentation is based on a HP 8510C Network Analyzer (Figure 2-11c). The system transmits a stepped frequency waveform in the Ku-band (16.5GHz) with an equivalent overall bandwidth of 3GHz and Δf=3.75MHz. The turntable rotation yields an angular separation burst to burst of about 0.1°.
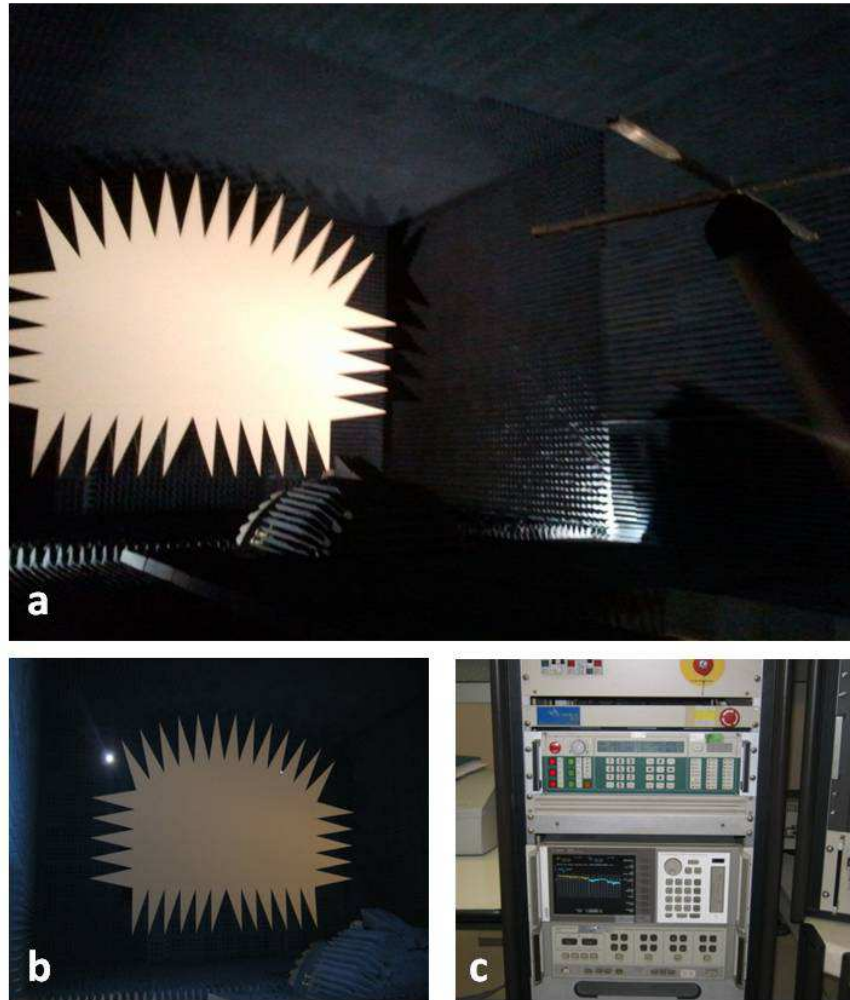
Figure 2-11. Anechoic chamber at the SELEX Galileo base in Caselle a) Anechoic chamber, b) Parabolic reflector, c) HP 8510C Network Analyzer. *By courtesy of Selex Galileo.*

The overall experimental setup is thus equivalent to the D-ISAR multistatic case with S=2, with the bistatic angle β equal to 4.3°. The equivalent geometry acquisition is sketched in Figure 2-12. The antennas are in the (z=0) plane (multi-aspect D-ISAR). In order to obtain a distributed image in the Image Projection Plane (IPP) with the distributed LOS aligned to the direction θ_0, we need to consider the sensor A with the LOS $\alpha_1 = \theta_0 - \frac{\beta}{4}$ and sensor B with the Line-of-Sight $\alpha_2 = \theta_0 + \frac{3\beta}{4}$. The distributed acquisition is then formed by sensor A, accounting for its monostatic acquisition, and equivalent sensor C, accounting for the bistatic acquisition due to sensor B that receives transmission from sensor A. Therefore, following the same approach in [82], when an observation angle equal to β/2 is available separately at each receiving channel, aiming at achieving the maximum resolution improvement, the maximum cross range resolution achievable in the D-ISAR image is equal to $\Delta_{cr}=\lambda/(2\beta)$: for f_c=16.5GHz we have max $\Delta_{cr}\approx$12cm.

Figure 2-12. Equivalent acquisition geometry.

The first analyzed target is a grid of metallic cylinders, acting like point scatterers; the framework with point scatterers, the metallic cylinders and grid structure are shown in Figure 2-13.

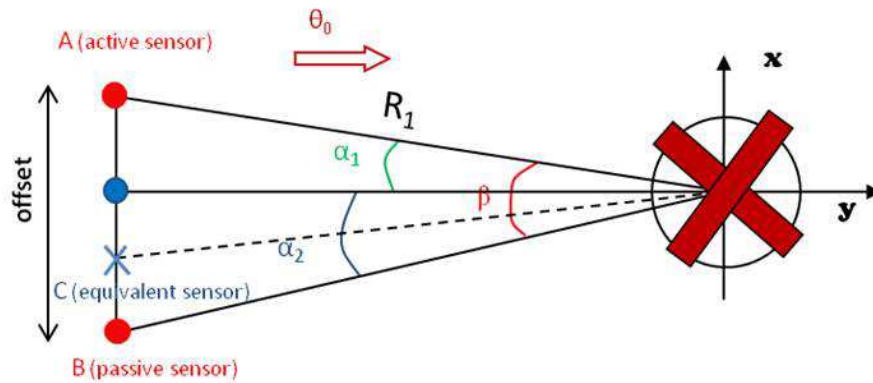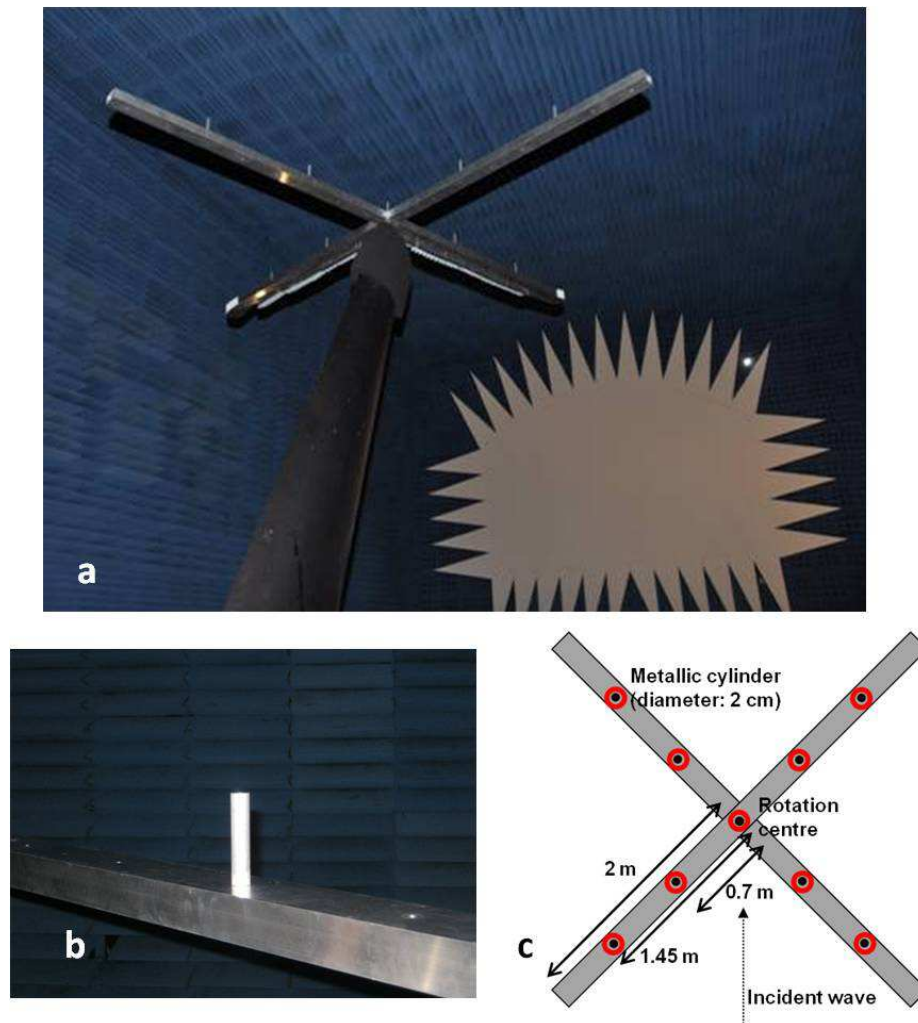Figure 2-13. Grid of metallic cylinders- a) framework, b) metallic cylinder, c) target structure.

To have a square resolution cell in the final image we consider only a portion of the available bandwidth (1.24GHz). Figure 2-14 shows the obtained images for conventional ISAR with Δ_{cr}=0.24m and multistatic (S=2) D-ISAR case with Δ_{cr}=0.12m, with the comparison of the cross range cuts. We can appreciate the improved in the cross range resolution that is equal to 2 as we expected (this can be easily verified looking at the null position of the D-ISAR cross range cut compared with the conventional ISAR case).
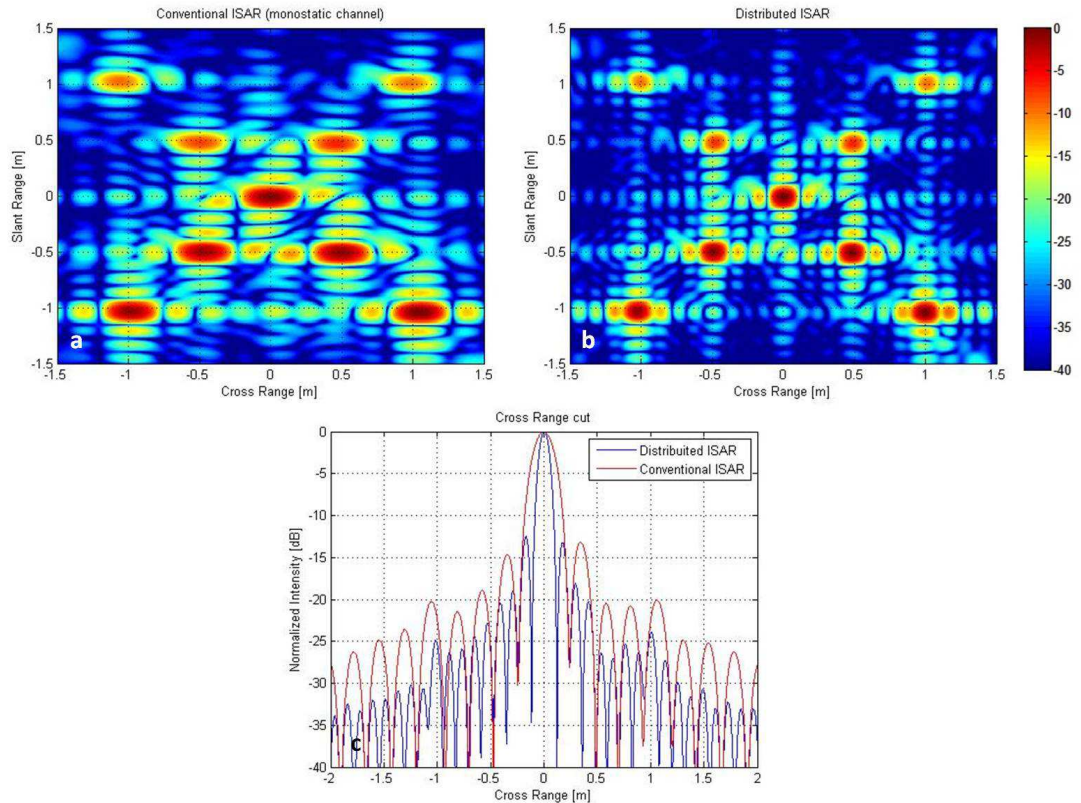
Figure 2-14. Grid of metallic cylinders D-ISAR images – a) Conventional ISAR, b) D-ISAR, c) Cross range cuts comparison for the target fulcrum.

After the analysis of performance achievable against simple targets such as isolated scatterers or grid of scatterers, a complex target has been considered; in particular the target is an aircraft model of an ATR 42, of dimensions of about 2×1.5 m², shown in Figure 2-15.

In this case the overall achievable bandwidth is exploited, hence the slant range resolution is 5 cm.

Figure 2-16 shows the comparison between the D-ISAR image achieved when an aperture equal to β/2 is selected from both the channel (Figure 2-16a) and the conventional ISAR image achieved when a view angle equal to β is selected (Figure 2-16b). As we can observe the two images are quite similar, and this is confirmed comparing the cross range cuts of the isolated scatterer in ~(0,1.2) m. This confirms that the D-ISAR technique allows us to reduce the acquisition time (and therefore the global view angle) achieving the same resolution capability.
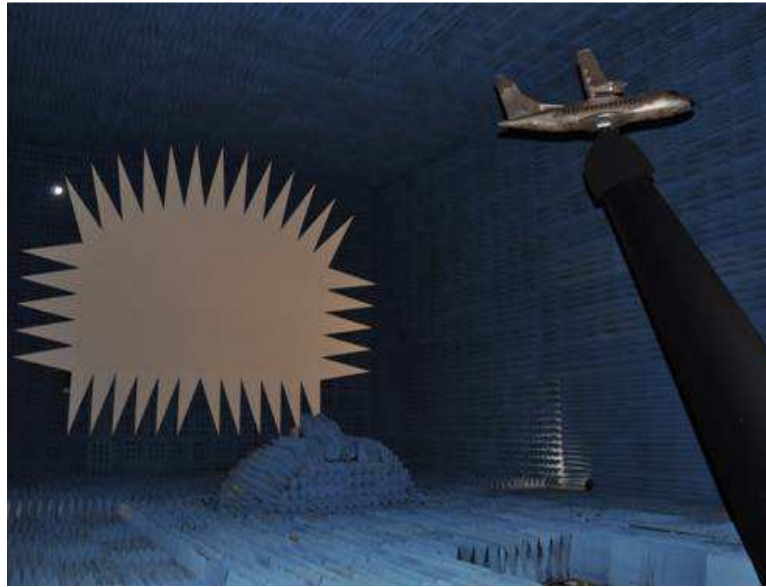
Figure 2-15. ATR 42 model – scale 1:20.
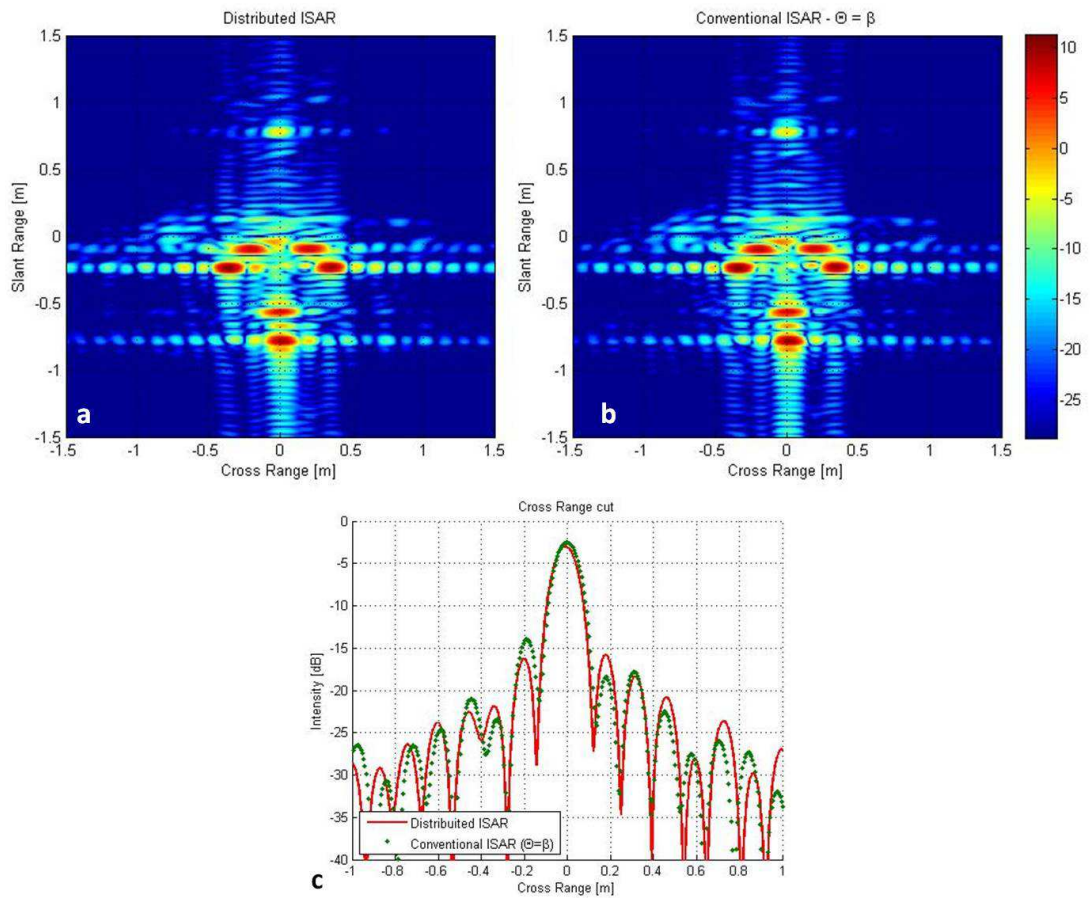
Figure 2-16. ATR42 model D-ISAR images – a) D-ISAR for Δθ single sensor equal to β/2 , b) Conventional ISAR for Δθ single sensor equal to β, c) Cross range cuts comparison.

2.6. CONCLUSIONS

The multi-angle distributed ISAR technique making use of stepped frequency waveforms has been proposed and analysed. Suitable orthogonal synthetic waveforms have been proposed for the MIMO case and the required focusing technique has been shown. The target rotation effect during the burst time has been analyzed and a range shift correction step has been proposed. The results obtained by processing simulated data confirmed that the proposed technique is able to provide an increase of the cross-range resolution up to the number of equivalent sensors in the formation; for the two platforms configuration, the multistatic configuration provided a cross-range resolution improvement factor $\gamma_{cr}=2$ while with the MIMO D-ISAR $\gamma_{cr}=3$ has been obtained. The results obtained by processing live D-ISAR data making use of stepped-frequency waveforms have also been shown. The complete agreement between the results obtained against simulated and real data indicates that the performance prediction derived via the theoretical analysis is representative of the performance achievable in practical applications.

3. TARGET ROTATION MOTION ESTIMATION EXPLOITING DISTRIBUTED ISAR DATA

Generally speaking, the ISAR image is the range-Doppler (RD) plane projection of a 3-D target [58]. In the range dimension the resolution of the image is directly related to the transmitted bandwidth (and therefore can be a priori set). On the contrary, in the Doppler domain it depends on the unknown target's relative motion [60].

The target motion can be divided into rotational and translational motion. Usually only the rotational motion contributes to imaging, giving rise to the Doppler gradient that makes the cross range resolution possible; in contrast, the translation motion produces unwanted phase error terms that yield distortions in the final image, and therefore it must be accurately compensated in order to obtain a well focused image. The compensation of the phase error terms due to the translational motion is called ISAR autofocus and several techniques can be found in literature (see e.g. [88], [89], [90]). However, in this contest we assume already compensated any relative translational motion of the target and focus on the rotation motion.

Most of the characteristics of the resulting image depends on the target rotational motion, which is typically is described by a vector ω_{XYZ}, whose components refer to roll, pitch and yaw, [91], [92].First of all, the amount of the target rotation, and specifically its overall change of aspect angle, entails the cross range resolution of the image. Moreover, the target is imaged on the Image Projection Plane (IPP), namely on the plane normal to the effective rotation rate vector ω_{eff}, which is a projection of ω_{XYZ} on the plane normal to the Line Of Sight (LOS). Therefore the orientation of the IPP depends on the target motion: in particular, top-view images arise when ω_{eff} has only a vertical component, while side-views when ω_{eff} has only a horizontal component.

Since the image quality depends on the intrinsic target motion, ISAR processing could be a complicated issue. Specifically, if the target is interested by a slow rotational motion (e.g. a ship observed in low sea state condition), its overall change of the view angle will be limited and as a consequence the achievable cross-range resolution will be very poor. This is made even worse by the constraint to keep limited the coherent processing interval (CPI): the orientation of ω_{eff} changes with time and high quality images can be obtained when the rotation axis is almost fixed during the CPI. Moreover, automatic target recognition (ATR) systems could require a specific orientation of the IPP in order to achieve top-view or side view images (the most useful for classification/identification, [93]).

Since the target motion is usually unknown, it has to be estimated directly to the received signal in order to correctly scale and focus the target image. Plus, in order to achieve the images on a desired IPP, the knowledge of the horizontal and vertical components of the rotation motion is required.

In the previous chapter we shown that the exploitation of multiple radar sensor observing the rotating target from multiple view angles (Distributed ISAR technique) is able to provide an increase of the cross-range resolution up to the number of sensors in the multistatic case (one sensor one sensor of the formation transmits and the remaining just receive) or even higher in the MIMO case (each platform carries an active radar and receives echoes from all the transmissions). In the analysis that has been carried on an exact knowledge of the rotational motion has been considered. In the D-

ISAR the accurate knowledge of the rotational motion is an essential information to correctly combine the signals received from the several sensor; an analysis of the degradation of the technique performance when errors on the knowledge of the rotational motion are considered is presented in [82]. Moreover, [84] addresses the focusing technique for the case of a motion composed not only by the yaw but also by pitch and roll.

The exploitation of angular diversity is here considered with the aim of target rotation motion estimation: we propose the performing of the target rotation motion estimation by means of the use of multiple radar sensor (Multi-Sensor (MS) techniques), i.e. using platform formation geometries similar to the ones considered in the D-ISAR techniques. We analyze the case of a single active radar and two additional receivers and consider two kind of sensors displacement: in the former, we consider a multi-aspect formation, i.e. the additional receivers observe the target with the same grazing angle of the transmitter but with different aspect angle, while in the latter a joint multi-aspect multi-grazing formation has been considered, i.e. the three sensors have different grazing and aspect angles.

In both the scenario Maximum Likelihood (ML) estimators have been analyzed and their theoretical performance have been evaluated by means of the Cramer Rao Bound (CRB). Since the ML is highly dependent on the target model, other model-free estimation schemes are here considered, based on the maximization of the contrast and on the minimization of the entropy. The performance analysis for simulated scenario is presented and the impact of non-idealities is analyzed. The theoretical results for the multi-aspect case are also validated by applying the proposed MS techniques to D-ISAR data acquired in anechoic chamber.

In ISAR literature we can find several target rotation motion estimation techniques concerning Single-Sensor (SS) ISAR data (as examples [94], [95], [96]). In other works, rotation motion estimation has been addressed using planar geometries: in [64], [65] and [66] the double angular diversity is exploited in order to find the position of the scatterers resolving the ambiguity in the Range-Doppler plane arising when scatterers having different position are projected onto the same 2D cell exploiting interferometric approaches (InISAR); in [97] the use of multiple receivers is considered in order to achieve a sequence of ISAR movies enabling to estimate the rate of change of the Doppler frequency and then the target motion and the 3D shape of the observed object. However, these techniques considered small values of the distance among the several receivers (about 1m), whereas in this work we exploit the angular diversity in a multi-platform system, i.e. with considerably greater distances between the receiving channels.

3.1. TARGET AND SIGNAL MODEL

We consider a moving target, such a ship, modeled as a rigid body in the far field with K dominant scatterers, with complex reflectivity constant during the time aperture T. Its motion is decomposed as the translation of a reference point (assumed negligible or already compensated) and the rotation of the body around that point.

The considered MS formation is composed by three platforms: platform C is equipped with an active senor, while A and B carry receiving only devices. In the XYZ reference system centered in the target fulcrum the Γ-th sensor (Γ = A, B, C) is located in $[R_0 \tan(\zeta_\Gamma) \quad -R_0 \quad R_0 \tan(\psi_\Gamma)]^T$, being R_0 the distance between the sensor C and the target fulcrum, ζ_Γ and ψ_Γ the aspect and grazing angle

concerning the sensor Γ, see Figure 3-1; without loss of generality we consider $\zeta_C = \psi_C = 0°$. The k-th scatterer is located in $[x_k^0 \quad y_k^0 \quad z_k^0]^T$ at aperture centre t_0 and its rotation is described by the rotation vector $\boldsymbol{\omega}_{XYZ} = [\omega_X \quad \omega_Y \quad \omega_Z]^T = M_\theta \cdot [\omega_{roll} \quad \omega_{pitch} \quad \omega_{yaw}]^T$, whose components represents the rotation rate around the X, Y and Z axes respectively; M_θ is the rotation matrix accounting for the initial heading angle of the target.

For each platform belonging to the formation we can introduce the (O,H,R,V) reference system representing the point of view of the corresponding radar, [96]. The R-axis ($\hat{r}$ unit vector) is the LOS direction, the H-axis is given by the unit vector $\widehat{h}$ normal to $\hat{r}$ and belonging the (X,Y) plane and the V-axis is given by the unit vector $\widehat{v}$ normal to the (R,H) plane. The three HRV systems are highlighted in Figure 3-2 for the geometry in Figure 3-1.
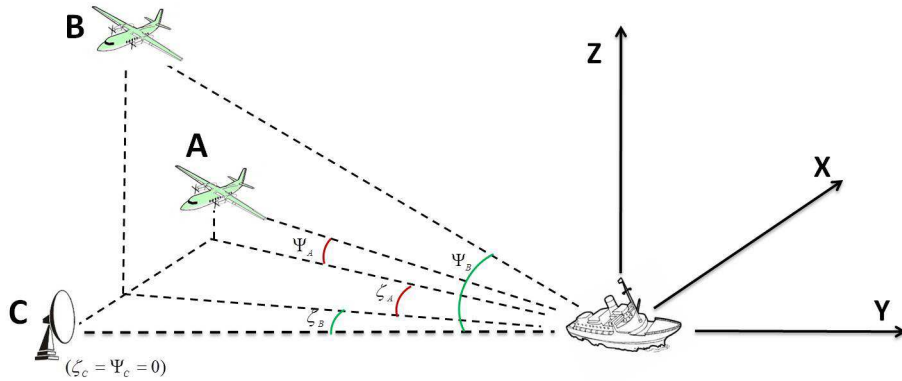
Figure 3-1. Multi-sensor ISAR geometry.
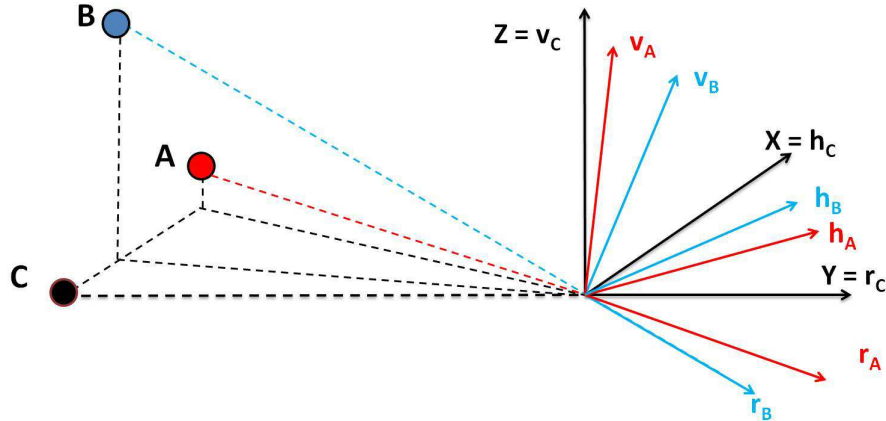
Figure 3-2. Radars point of view reference systems.

The change from reference (O,X,Y,Z) to (O, H$^\Gamma$,R$^\Gamma$,Z$^\Gamma$) for sensor Γ can be expressed by means of the matrixes M_ψ^Γ and M_ζ^Γ, which describe respectively an anticlockwise rotation of the reference system around the X axis with the grazing angle ψ_Γ and a clockwise rotation around the Z axis with the aspect angle ζ_Γ.

The rotation rate vector as viewed from the sensor Γ in the HRV system can be expressed as a function of its horizontal, radial and vertical components as:

$$\boldsymbol{\omega}^{\Gamma} = [\omega_{H}^{\Gamma} \quad \omega_{R}^{\Gamma} \quad \omega_{V}^{\Gamma} \;]^{T} = M_{\psi}^{\Gamma} M_{\zeta}^{\Gamma} \, \boldsymbol{\omega}_{XYZ}. \tag{1}$$

Moreover, in the same reference system, the scatterer coordinates at aperture centre t_0 and at a generic slow time instant t can be expressed respectively as:

$$\left[h_{k,\Gamma}^{0} \; r_{k,\Gamma}^{0} \; v_{k,\Gamma}^{0}\right]^{T} = M_{\psi}^{\Gamma} \, M_{\zeta}^{\Gamma} \, [x_{k}^{0} \quad y_{k}^{0} \quad z_{k}^{0}]^{T} \tag{2}$$

$$[h_{k,\Gamma}(t) \quad r_{k,\Gamma}(t) \quad v_{k,\Gamma}(t) \;]^{T} = M_{V}^{\Gamma} M_{R}^{\Gamma} M_{H}^{\Gamma} \left[h_{k,\Gamma}^{0} \quad r_{k,\Gamma}^{0} \quad v_{k,\Gamma}^{0}\right]^{T} \tag{3}$$

where M_{γ}^{Γ} is the matrix concerning a counter-clockwise rotation around the γ-axis (γ = H,R,V). The amount of the rotation is described by the angle $_{\gamma}^{\Gamma}(t)$ swept around the γ-axis, changing with time and depending on ω_{γ}^{Γ}.

The three $r_{k,\Gamma}^{0}$ are the slant range distances of the k-th scatterer measured by the Γ-th sensor, i.e. are known quantities. The horizontal and vertical components of the scatterer as viewed by the reference sensor could be obtained from the three $r_{k,\Gamma}^{0}$ coordinates resolving the linear system given by:

$$L\mathbf{w} = \mathbf{u} \tag{4}$$

where L is the matrix accounting for the system geometry given by:

$$L = \begin{bmatrix} S_{\zeta_A} C_{\psi_A} & S_{\psi_A} \\ S_{\zeta_B} C_{\psi_B} & S_{\psi_B} \end{bmatrix} \tag{5}$$

$\mathbf{w} = \left[h_{k,C}^{0} \quad v_{k,C}^{0}\right]^{T}$ and $\mathbf{u} = \left[r_{k,C}^{0} C_{\psi_A} C_{\zeta_A} - r_{k,A}^{0} \quad r_{k,C}^{0} C_{\psi_B} C_{\zeta_B} - r_{k,B}^{0}\right]^{T}$ is the is the 2×1 vector of known terms being $C_x = \cos(x)$ and $S_x = \sin(x)$. Hence, from (2) we could have the $h_{k,C}^{0}$ and $v_{k,C}^{0}$ coordinates for all the sensors. However, this is possible if and only if L is invertible, i.e. if and only if $|L| \neq 0$; this condition depends on the sensors displacement being $|L| = S_{\zeta_A} C_{\psi_A} S_{\psi_B} - S_{\zeta_B} C_{\psi_B} S_{\psi_A}$. We have to analyze the cases of multi-aspect and joint multi-aspect multi-grazing formation:

- ***multi-aspect case***: in this case we have $\psi_A = \psi_B = \psi_C = \psi$; in the analyzed cases we set $\psi = 0$, and therefore $|L| = 0$. If $\psi \neq 0$, $|L| \neq 0$ and in principle we could recover $h_{k,C}^{0}$ and $v_{k,C}^{0}$; however in practical application (4) is a perturbed linear system, since, as well as error in the knowledge of the sensors position, the precision whereby the slant range values are measured is limited by the transmitted bandwidth. To recover the scatterer position in presence of errors the linear system has to hold a good degree of stability, i.e. it has to be a well-conditioned problem. It is easy to prove that if the geometry of the observation has a low grazing angle (condition fulfilled for our case of long range surveillance), the inversion problem is highly ill-conditioned so that the perturbation will amplify greatly the errors in the solution. For this reason, in the multi-aspect case we consider as unknown parameters the horizontal and vertical positions of the scatterers.
- **joint multi-aspect multi-grazing case**: since the double angular diversity, L is nonsingular; moreover, (4) has a good degree of stability and also in presence of errors due to imprecision in sensors positions and the quantization of the slant range axes we are able to obtain all the HRV scatterers coordinates in (2). For this reason, in the joint multi-aspect multi-grazing case

we consider as known parameters the coordinates of the scatterers. We point out that the minimum number of needed channels to resolve the system is three; if more than three receivers are considered, we could always obtain the desired coordinates using (4), as long as we have both the aspect and grazing diversity. In such case the minimum square error solution of the system could be adopted.

The signal received by sensor Γ pertaining to the k-th scatterer is an echo of the transmission from sensor C. Neglecting the complex reflectivity of the scatterer and the constant phase term due to the distance between sensor Γ and the scatterer fulcrum, it can be expressed as a function of the component $r_{k,\Gamma}(t)$ in (3) and the wavelength λ as:

$$s_{k,\Gamma}(t) = \exp\left\{-j\frac{2\pi}{\lambda}\left[r_{k,C}(t) + r_{k,\Gamma}(t)\right]\right\} \tag{6}$$

In the hypothesis of uniform rotations ($\vartheta_\gamma^\Gamma(t) = \omega_\gamma^\Gamma t$), choosing C as the reference sensor in the formation ($\boldsymbol{\omega}^C = \boldsymbol{\omega}$) and expanding in Taylor series at second order the phase term, (6) can be approximated as:

$$s_{k,\Gamma}(t) \approx \exp\left\{-j\frac{2\pi}{\lambda}\left[\alpha_{k,\Gamma}(\boldsymbol{\omega})\cdot t + \beta_{k,\Gamma}(\boldsymbol{\omega})\cdot t^2\right]\right\} = \exp\{-j\phi_{k,\Gamma}(t)\} \tag{7}$$

The parameter $\alpha_{k,\Gamma}(\boldsymbol{\omega})$ is the scatterer Doppler frequency at time t_0, while $\beta_{k,\Gamma}(\boldsymbol{\omega})$ is the focus parameter:

$$
\begin{aligned}
\alpha_{k,\Gamma}(\boldsymbol{\omega}) &= \sum_{\gamma=H,R,V} \alpha_{k,\Gamma}^\gamma \\
\beta_{k,\Gamma}(\boldsymbol{\omega}) &= \sum_{\gamma=H,R,V}\sum_{\delta=H,R,V} \omega^\gamma \omega^\delta \beta_{k,\Gamma}^{\gamma\delta}
\end{aligned}
\tag{8}
$$

The parameters $\alpha_{k,\Gamma}^\gamma$ and $\beta_{k,\Gamma}^{\gamma\delta}$ in (8) are quantities depending on system geometry and scatterers position. They can be expressed as linear combination of the HRV scatterer position with respect to the reference sensor:

$$
\begin{aligned}
\alpha_{k,\Gamma}^H &= -v_{k,C}^0 - v_{k,\Gamma}^0 C_{\zeta_\Gamma} - h_{k,\Gamma}^0 S_{\psi_\Gamma} S_{\zeta_\Gamma} \\
\alpha_{k,\Gamma}^R &= h_{k,\Gamma}^0 S_{\psi_\Gamma} C_{\zeta_\Gamma} - v_{k,\Gamma}^0 S_{\zeta_\Gamma} \\
\alpha_{k,\Gamma}^V &= h_{k,C}^0 + h_{k,\Gamma}^0 C_{\psi_\Gamma} \\
\beta_{k,\Gamma}^{HH} &= \frac{r_{k,C}^0}{2} + \frac{r_{k,\Gamma}^0}{2}\left(C_{\zeta_\Gamma}^2 + S_{\zeta_\Gamma}^2 S_{\psi_\Gamma}^2\right) - \frac{v_{k,\Gamma}^0}{2} S_{\zeta_\Gamma}^2 S_{2\psi_\Gamma} \\
\beta_{k,\Gamma}^{RR} &= \frac{r_{k,\Gamma}^0}{2}\left(S_{\zeta_\Gamma}^2 + S_{\psi_\Gamma}^2 C_{\zeta_\Gamma}^2\right) - \frac{v_{k,\Gamma}^0}{2}\left(S_{2\psi_\Gamma} C_{\zeta_\Gamma}^2\right) \\
\beta_{k,\Gamma}^{VV} &= \frac{r_{k,C}^0}{2} + \frac{r_{k,\Gamma}^0}{2} C_{\psi_\Gamma}^2 + \frac{v_{k,\Gamma}^0}{2} S_{2\psi_\Gamma} \\
\beta_{k,\Gamma}^{HR} &= \beta_{k,\Gamma}^{RH} = \frac{r_{k,\Gamma}^0}{4} S_{2\zeta_\Gamma}\left(1 - S_{\psi_\Gamma}^2\right) + \frac{v_{k,\Gamma}^0}{4} S_{2\psi_\Gamma} S_{2\zeta_\Gamma} \\
\beta_{k,\Gamma}^{HV} &= \beta_{k,\Gamma}^{VH} = \frac{v_{k,\Gamma}^0}{2} S_{\zeta_\Gamma} C_{2\psi_\Gamma} - \frac{r_{k,\Gamma}^0}{4} S_{\zeta_\Gamma} S_{2\psi_\Gamma} \\
\beta_{k,\Gamma}^{RV} &= \beta_{k,\Gamma}^{VR} = \frac{r_{k,\Gamma}^0}{4} C_{\psi_\Gamma} S_{2\psi_\Gamma} - \frac{v_{k,\Gamma}^0}{2} C_{\zeta_\Gamma} C_{2\psi_\Gamma} - \frac{v_{k,C}^0}{2}
\end{aligned}
\tag{9}
$$

In the hypothesis of K dominant scatterers, in K different range cells, embedded in white Gaussian background, the signal received by the sensor Γ for the k-th cell in the m-th slow time instant (m = -M/2,...,M/2) is written as:

$$g_{k,\Gamma}(t_m) = A_{k,\Gamma} \cdot s_{k,\Gamma}(t_m) + \eta_{k,\Gamma}(t_m) \tag{10}$$

where $A_{k,\Gamma}$ is the unknown but deterministic complex reflectivity as viewed by sensor Γ and $\eta_{k,\Gamma}$ is the background contribution with power σ_n^2. Note that the assumption of a white Gaussian background can be acceptable since Doppler filtering can be applied to the selected target dominant scatterers thus discarding the contribution of clutter.

The joint probability density function of the collected data is therefore given by:

$$p_G(\mathbf{g}) = (\pi^{3KM} \sigma_n^{2 \cdot 3KM})^{-1} \exp\left\{-\frac{1}{\sigma_n^2}(\mathbf{g} - \mathbf{Sa})^\dagger(\mathbf{g} - \mathbf{Sa})\right\} \tag{11}$$

$\mathbf{g} = \begin{bmatrix} \mathbf{g}_1^T & \mathbf{g}_2^T & \dots & \mathbf{g}_K^T \end{bmatrix}^T$ is the $3KM \times 1$ data vector with $\mathbf{g}_k = \begin{bmatrix} \mathbf{g}_{k,A}^T & \mathbf{g}_{k,B}^T & \mathbf{g}_{k,C}^T \end{bmatrix}^T$ and $\mathbf{g}_{k,\Gamma} = \begin{bmatrix} g_{k,\Gamma}(t_{-M/2}) \dots g_{k,\Gamma}(t_{+M/2}) \end{bmatrix}^T$, $\mathbf{a} = \begin{bmatrix} \mathbf{a}_1 & \mathbf{a}_2 \dots \mathbf{a}_K \end{bmatrix}^T$ is the $3K \times 1$ complex amplitude vector with $\mathbf{a}_k = \begin{bmatrix} A_{k,A} & A_{k,B} & A_{k,C} \end{bmatrix}$ and $\mathbf{S}$ is the $3KM \times 3$ phase matrix, where the k-th $3M \times 3$ block is a diagonal block matrix and $\mathbf{s}_{k,\Gamma} = \begin{bmatrix} \exp\{j\varphi_{k,\Gamma}(t_{-M/2})\} \dots \exp\{j\varphi_{k,\Gamma}(t_{+M/2})\} \end{bmatrix}^T$ is the $M \times 1$ block; † is the hermitian operator.

3.2. MULTI-SENSOR ESTIMATION TECHNIQUES

In the phase term of (7) the two contributions depending on the target rotation rate vector are the scatterer Doppler frequency $\alpha_{k,\Gamma}(\boldsymbol{\omega})$ (linear with t) and the focus parameter $\beta_{k,\Gamma}(\boldsymbol{\omega})$ (quadratic with t). As well known, for a point scatterer the correct compensation of the $\beta_{k,\Gamma}(\boldsymbol{\omega})$ allows to achieve an azimuth Point Spread Function (PSF) with a resolution comparable with the theoretical limit and which position is related to the $\alpha_{k,\Gamma}(\boldsymbol{\omega})$. Most of the conventional motion estimation technique are based on the compensation of the quadratic term, e.g. [94], looking for the $\boldsymbol{\omega}$ value which maximizes some specific cost functions related to the quality of the achieved PSF. In our multi-platform case the view angles diversity results in different Doppler positions of the scatterer, since the different IPPs. Therefore we can exploit this diversity to improve the performance of the estimation process.

The main idea here is to perform an azimuth coherent compensation in two steps: Doppler based IPP alignment depending on functions of $\alpha_{k,\Gamma}(\boldsymbol{\omega})$ and dechirping based on $\beta_{k,\Gamma}(\boldsymbol{\omega})$ for the signal received by each sensor for each selected range cell. Signals from the different sensors are then properly processed and combined in order to carry on the optimization process resulting in the estimation of the rotation $\hat{\boldsymbol{\omega}}$ (Figure 3-3). The innovative contribution is to exploit not only the azimuth compression in order to obtain a well-focused PSF, but also looking for the $\boldsymbol{\omega}$ value resulting in the best IPPs alignment.

For both the considered geometries, the Maximum Likelihood estimation technique (MS-ML) will be presented and analyzed. As well known, this kind of estimation can be proven to reach the best accuracy (i.e. the Cramer Rao Lower Bound, CRB), but has the main drawback of being dependent on the target model. Therefore it is of great interest to investigate also different model-free criteria.

Specifically we consider MS model free estimation techniques based on the maximization of the peak power and of the contrast and on the minimization of the entropy.
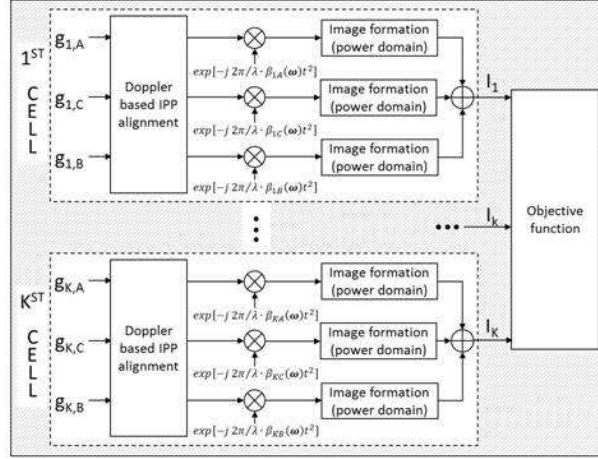

Figure 3-3. Multi-sensor motion estimation processing scheme.

3.3. MULTI-ASPECT FORMATION

The considered geometry is depicted in Figure 3-4 and we consider the target interested by a dominant yaw motion. It should be pointed out that the dominant yaw motion case applies to a large number of situations: in ISAR imaging, to turning ground targets, to air targets undergoing yaw maneuvers and to ship targets changing their route; in hybrid SAR/ISAR imaging, to the scatterers in the imaged scene after translation motion compensation of scene center.
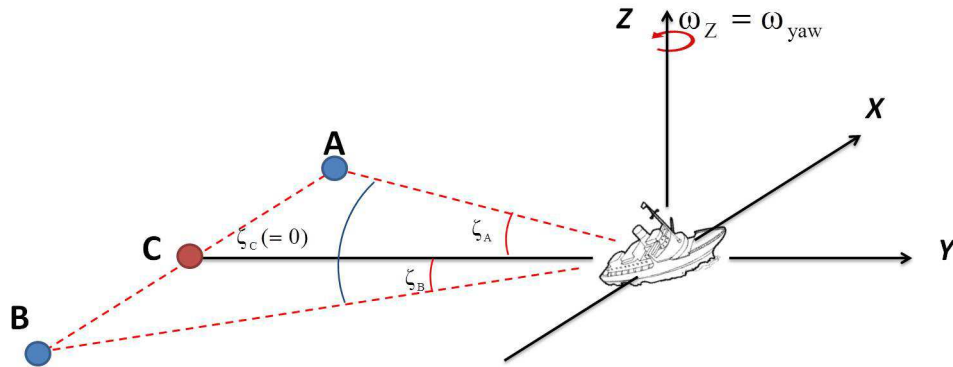
Figure 3-4. Multi-aspect ISAR geometry.

Under the hypothesis of negligible radial and horizontal component of the rotation rate vector, we can write the phase of the received signal in (7), neglecting the constant terms, as:

$$\phi_{k,\Gamma}(t) = -\frac{2\pi}{\lambda}\left\{\alpha_{k,\Gamma}^{V}\omega_V t + \beta_{k,\Gamma}^{VV}\omega_V^2 t^2\right\} \tag{12}$$

Considering negligible grazing angle, we can write:

$$\alpha_{k,\Gamma} = \omega_V\left\{h_{k,C}^0 + h_{k,C}^0\cos\zeta_\Gamma + r_{k,C}^0\sin\zeta_\Gamma\right\} \tag{13}$$

being C the reference sensor we can set $\zeta_C = 0°$ and therefore $\alpha_{k,C} = 2\omega_V h^0_{k,C}$, representing the scatterer Doppler frequency as viewed by the reference sensor. Because of the different view angle, the scatterer will be projected onto different Doppler cell in the three different IPP; the Doppler Shift of the k-th scatterer as viewed by the Γ sensor with respect to $\alpha_{k,C}$ can be written as:

$$\Delta f_{k,\Gamma} = \alpha_{k,c} - \alpha_{k,\Gamma} = \omega_V\{h^0_{k,C}(1 - \cos\zeta_\Gamma) - r^0_{k,C}\sin\zeta_\Gamma\} \tag{14}$$

We point out that both $\alpha_{k,C}$ and $\Delta f_{k,\Gamma}$ depend on, as well as the target rotation rate, the unknown horizontal position of the scatterer. However, while reference scatterer Doppler frequency has a strong dependence on the $h^0_{k,C}$, in the Doppler shifts this can be neglected: for all the cases of interest, $\cos\zeta_\Gamma \approx 1$, since the differences in the view angle among the several sensors have to be keep limited in order to observe the same scatterer reflectivity. Therefore we can approximate the Doppler shifts as:

$$\Delta f_{k,\Gamma} \approx -\omega_V r^0_{k,C}\sin\zeta_\Gamma \tag{15}$$

and therefore:

$$\alpha_{k,\Gamma} = \alpha_{k,C}(h^0_{k,C}) - \Delta f_{k,\Gamma}(\omega_V) \tag{16}$$

In (16) we have considered $\alpha_{k,C}$ depending only on $h^0_{k,C}$: even if the target rotation rate would be known, however we cannot know the scatterer Doppler cell before the azimuth compression. Since the scatterer slant range position is a measured quantity, the only unknown parameter in its expression is ω_V; the approximation in (15) means that the term $h^0_{k,C}(1 - \cos\zeta_\Gamma)$ does not entail a change of the Doppler cell for the scatterer.

The Focus Parameter is given by:

$$\beta_{k,\Gamma} = \beta^{VV}_{k,\Gamma}\omega^2_V = \frac{\omega^2_V}{2}\{r^0_{k,C}(1 + \cos\zeta_\Gamma) - h^0_{k,\Gamma}\sin\zeta_\Gamma\} \approx \omega^2_V r^0_{k,C} = \beta_k \tag{17}$$

where again the approximations $\cos\zeta_\Gamma \approx 1$ and $\sin\zeta_\Gamma \approx 0$ hold.

Considering (16) and (17), the phase term in (12) can be expressed as:

$$\phi_{k,\Gamma}(t) = -\frac{2\pi}{\lambda}\{[\alpha_{k,C} - \omega_V r^0_{k,C}\sin\zeta_\Gamma]t + \omega^2_V r^0_{k,C}t^2\} \tag{18}$$

3.3.1. ESTIMATION TECHNIQUES

Based on (11) and accounting for the phase model in (18), the MS-ML estimator can be proven (appendix A1) being equal to:

$$\hat{\omega}_{V_{ML}} = \arg\max_{\omega_V}\left\{\sum^K_{k=1}\arg\max_{\alpha_{k,C}}\left\{\sum_\Gamma\left|\mathbf{s}^\dagger_{k,\Gamma}\mathbf{g}_{k,\Gamma}\right|^2\right\}\right\} \tag{19}$$

The MS-ML estimate is the $\hat{\omega}_V$ value which maximizes the output of the scheme in Figure 3-5: for every ω_V value under test, the signal from the k-th range cell is first re-aligned to its Doppler frequency (as viewed in the reference IPP concerning the sensor C) and dechirped, then it is Fourier

transformed. For each cell the squared modulus of the re-aligned, dechirped and Fourier transformed signals from each sensor are averaged. The value of the rotation rate which maximizes the signal mean power is assumed as the estimated value $\widehat{\omega}_{V_{ML}}$.

The ML is a "local" cost function: it means that the $\widehat{\omega}_{ML}$ value is selected as that value providing the highest averaged (over the available range bins and sensors) peak power. Therefore in the multi-aspect formation case the ML technique corresponds to a peak power (PP) technique.

Different criteria can be based on a "global" view of the output signal. We apply three model free objective functions: contrast optimization for the amplitude (AC), for the intensity (IC) and entropy minimization (He). Their processing scheme are obtained by replacing the evaluation of the averaged peak power after the fusion of the data from different sensors and range bins has been carried on (see Figure 3-6).
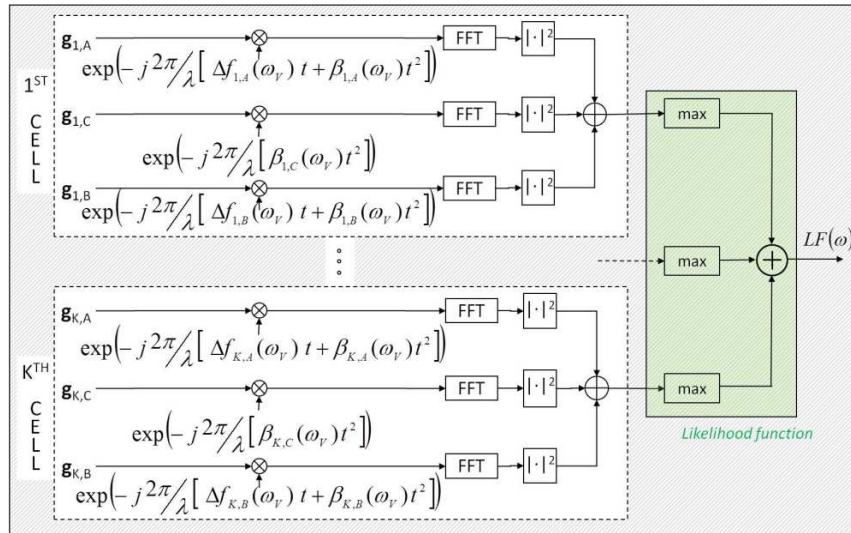

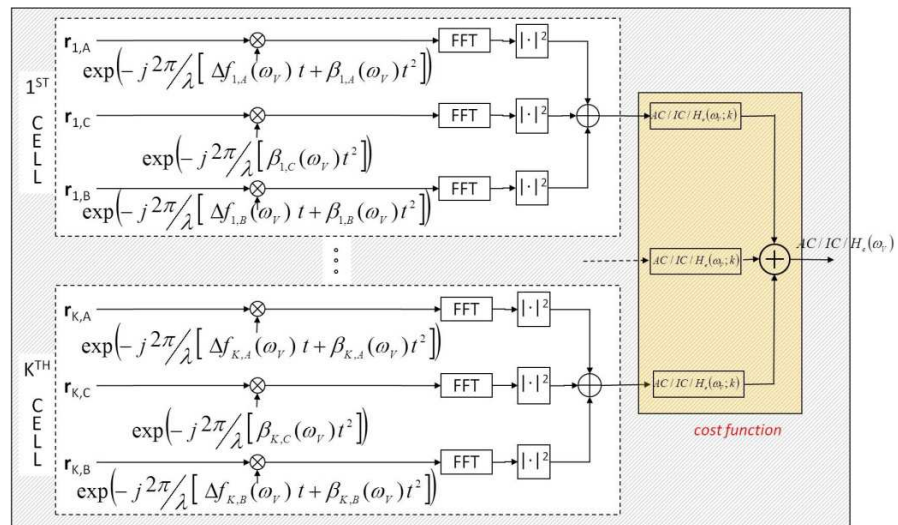Figure 3-5. Multi-aspect formation. Multi-sensor Maximum Likelihood processing scheme.

Figure 3-6. Multi-aspect formation. Multi-sensor model free processing scheme.

The $\widehat{\omega}_{V_{IC}}$ and $\widehat{\omega}_{V_{AC}}$ estimates are the ω_V value which maximize the contrast (evaluated on the amplitude and on the intensity respectively and averaged over the K range bin) of the re-aligned, dechirped and averaged intensity image I_k:

$$\widehat{\omega}_{V_{IC}} = \arg\max_{\omega_V}\left\{\sum_{k=1}^{K} IC_k\right\}$$

$$\widehat{\omega}_{V_{AC}} = \arg\max_{\omega_V}\left\{\sum_{k=1}^{K} AC_k\right\}$$

(20)

where $AC_k = std[VI_k]/E[VI_k]$ and $IC_k = std[I_k]/E[I_k]$.

The $\widehat{\omega}_{V_{He}}$ is the ω_V value which minimizes the mean entropy over the K range bin:

$$\widehat{\omega}_{V_{He}} = \arg\min_{\omega_V}\left\{\sum_{k=1}^{K} He_k\right\} = \arg\min_{\omega_V}\left\{-\sum_{k=1}^{K}\sum_{m=1}^{M} P_{km}\ln P_{km}\right\}$$

(21)

where $P_{km} = {I_{km}}\Big/{\sum_{m=1}^{M} I_{km}}$.

3.3.2. THEORETICAL ESTIMATION ACCURACY

Based on the phase model in (18), it can be shown (see Appendix B1) that the maximum achievable accuracy on the estimation error on ω_V, defined as $\delta\omega_V = \widehat{\omega}_V - \omega_V^0$ (being ω_V^0 the true value of the rotation rate), can be expressed as:

$$CRB \doteq \sigma_{\omega_V}^2 = \frac{1}{\chi + \mu - \xi}$$

(22)

where

$$\chi = \frac{2\pi^2 MT^2}{\lambda^2\sigma_n^2}\frac{4\omega^2 T^2}{45}\sum_{\Gamma}\sum_{k=1}^{K} r_{k,C}^2 M_{k,\Gamma}^2$$

(23)

$$\mu = \frac{2\pi^2 MT^2}{\lambda^2\sigma_n^2}\sum_{\Gamma}\sum_{k=1}^{K}\left\{\frac{r_{k,C}^2 M_{k,\Gamma}^2 \sin^2(\zeta_\Gamma)}{3}\right\}$$

(24)

$$\xi = \frac{2\pi^2 MT^2}{\lambda^2\sigma_n^2}\sum_{k=1}^{K} r_{k,C}^2 \frac{\left(\sum_\Gamma M_{k,\Gamma}^2 \sin\zeta_\Gamma\right)^2}{\sum_\Gamma M_{k,\Gamma}^2}$$

(25)

The quantity χ depends on the quadratic term in (18) and therefore it takes into account for the dechirping operation. If we would not express the scatterer Doppler frequency as a reference Doppler frequency plus a Doppler shift but we would express the phase of the received signal as:

$$\phi_{k,\Gamma}(t) = -\frac{2\pi}{\lambda}\left\{\alpha_{k,\Gamma}t + \omega_V^2 r_{k,C}^0 t^2\right\}$$

(26)

the corresponding ML estimator would be (see Appendix A1)

$$\hat{\omega}_{V_{SS^{av}}} = \arg\max_{\omega_V}\left\{\sum_\Gamma\sum_{k=1}^{K}\arg\max_{\alpha_{k,\Gamma}}\left|\mathbf{s}_{k,\Gamma}^\dagger\mathbf{g}_{k,\Gamma}\right|^2\right\} \tag{27}$$

and the corresponding CRB (see Appendix B1) would be:

$$CRB_{SS^{av}} = \frac{1}{\chi} \tag{28}$$

This estimator corresponds to perform the estimation separately for each channel compensating only the quadratic term, avoiding the re-alignment of the several IPP, i.e. the Doppler shift compensations to the IPP of the reference sensor, and then maximizing (minimizing) the averaged objective function (SS^{av}).

The quantities μ and ξ derive from the effect of the Doppler shift. Specifically μ is a gain in the estimation accuracy: in the distributed estimation we look for the ω value that not only provides the best cross range compression of the signals, but also the best IPPs alignment. We underline that, since $\zeta_C = 0°$, this term does not depend on the signal power received by the reference sensor. On the contrary ξ is a reduction of this gain depending on the difference between the signal power received by the sensors A and B: if one is much greater than the other, the Doppler re-alignment becomes less important than the dechirping. It is worth noticing that, in the hypothesis of a limited angular separation between the sensors (condition that should be fulfilled for the imaging purpose) it is reasonable to assume that $\left|A_{k,\Gamma}\right|^2 = |A_k|^2$, $\forall\Gamma\in[A, B, C]$: in such a case ξ is equal to zero.

We consider the three sensors in Figure 3-4 with $\zeta_B = -\zeta_A = 5°$, null grazing angle, λ = 3 cm, observing a ship target with an initial heading angle $\theta_0 = 45°$ interested by a yaw motion given by ω_V = 0.0541 rad/sec. In Figure 3-7 we show the comparison between the theoretical standard deviation of $\delta\omega_V$ as a function of the integrated signal to noise ratio SNR, defined as $SNR_{k,\Gamma} = M\left|A_{k,\Gamma}^2\right|/\sigma_n^2$ and hereinafter assumed the same for all the scatterers and sensors, for a bow scatterer of the ship with T = 0.56 s (corresponding to a cross range resolution Δr_{cr} = 50 cm); blue plot refers to the SS case, the green plot to the SS^{av} case, i.e. the MS case exploiting only the quadratic term (dechirping) and therefore with only the χ contribution, the red plot to MS case with only the μ contribution, i.e. exploiting only the linear term (Doppler re-alignment) and finally the black plot to the MS overall bound in (22). The quantity ξ is assumed to be zero. As it is apparent, the main contribution in the estimation accuracy improvement with respect to the SS case is due to the Doppler Shift re-alignment; moreover this term represents just the benefit of the distributed approach with respect to the estimation achieved averaging the single sensor dechirping-based objective functions ($\sigma_{\omega_V}^2 = 1/\chi$ case).

Figure 3-8 shows the theoretical standard deviation of the estimation error $\sigma_{\omega_V}^2$ normalized to ω_V^0 as a function of the slant range of the scatterer as viewed by the reference sensor for several SNR values, using the SS, SS$_{av}$ and MS techniques. The simulated scenario is the same one of Figure 3-7. Different colors represent different SNR values, while different symbols refer to different estimation approaches. As it is apparent, the normalized accuracy improves as r_C^0 increases; moreover, fixing r_C^0, the error decreases when SNR increases. It is also visible how the MS approach outperforms SS/SS$_{av}$

techniques, implying that, for a specific SNR, a given normalized accuracy can be achieved with targets of considerably smaller size moving from SS, SS_{av} to the MS case.
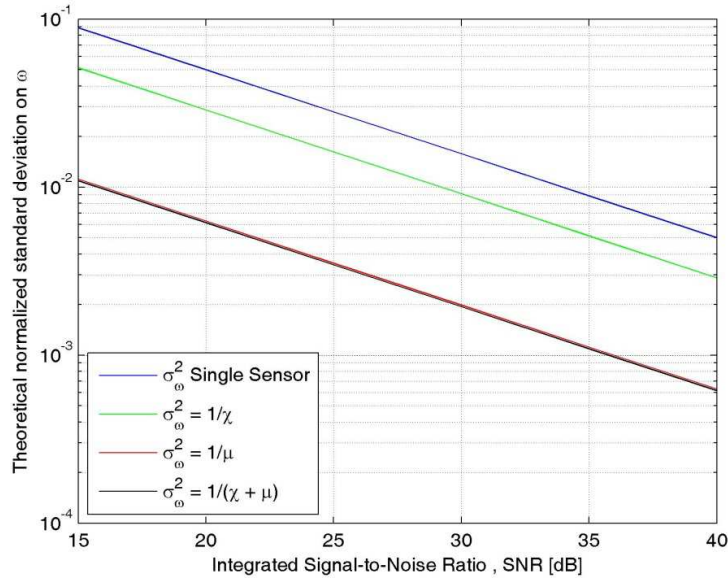

Figure 3-7. Theoretical standard deviation of the estimation error as a function of the SNR for a bow scatterer.
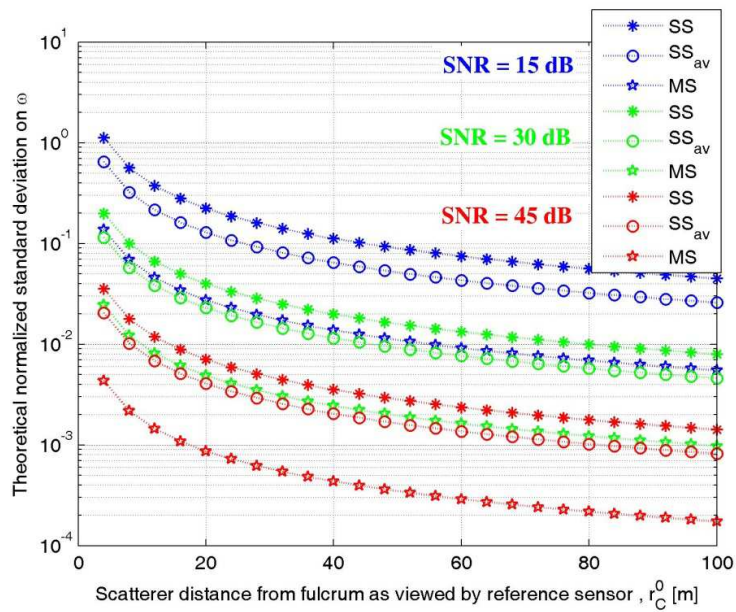
Figure 3-8. Theoretical normalized standard deviation of the estimation error as a function of the scatterer slant range.

3.3.3. SIMULATED PERFORMANCE ANALYSIS

To confirm the theoretical results presented in the previous section, a simulated analysis is here performed. We considered the case of a single range cell (K = 1) and analyzed two different situations: in the first one we considered a single scatterer per range cell, matching the MS-ML

target model, in the second one we considered the presence of several scatterers. This allowed us to test the MS-ML technique when the application doesn't match the analytical model for the target and to compare its performance with respect to the other model-free MS estimation techniques here investigated.

In the first case we considered the same study case as in Figure 3-7. We applied the proposed MS techniques and compared the performance to the case in which the averaged single sensors estimation is performed. Figure 3-9 shows the normalized standard deviation of the estimation error as a function of SNR for the single sensor averaged and distributed techniques (blue and red curves respectively). As it is apparent, all the MS techniques are very close to the theoretical results represented by the CRBs, except the maximization of the contrast on the amplitude AC. Moreover it could be shown that in this same condition all the considered techniques are almost unbiased.
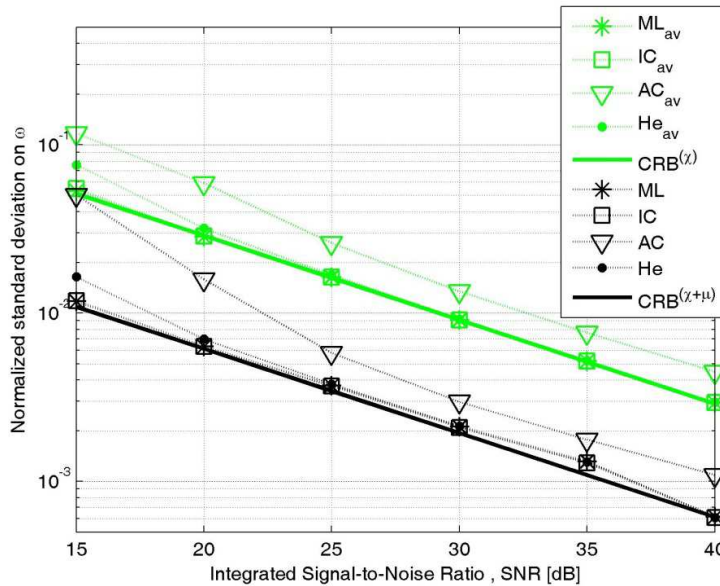

Figure 3-9. Simulated normalized standard deviation of the estimation error for a bow scatterer as a function of the SNR.

The case of several scatterers in the same range cell has been analyzed by considering two scatterers with amplitude A_1 and A_2 and phase difference $\Delta\phi$ uniformly distributed in $[0, 2\pi]$. The difference of the horizontal coordinates Δh between the two scatterers is uniformly distributed in $[0.5, 1.5]\cdot\Delta r_{cr}$, i.e. the main lobe of the second scatterer pulse response is comprised between the main lobe and the second right lobe of the first scatterer. The impact of the interference among the scatterers is studied in noise free conditions by evaluating the mean value and the standard deviation of the estimation error and the average cost function as obtained by averaging over 10000 realizations of the phase and cross-range difference among the scatterers.

Figure 3-10 shows the objective functions averaged over the trials for the case $A_1 = A_2$ as a function of the normalized estimation error (to compare the plots of all the objective functions in the same figure, instead of He we plot 1/He). We observe that the ML curve presents a bimodal behavior, having a minimum in correspondence of the true value of the rotation speed. This is due to the fact that the ML estimator has been formulated for the case of one single scatterer per range cell and we

applied it for a different target model. This demonstrates how strong is the model dependence in the MS-ML technique. The AC, IC, He cost functions don't depend on the target model: even if the presence of the second scatterer worsens the estimation, they maintain the maximum just in correspondence of the true value of the rotation speed.

In Table 3-1 are reported the mean and the standard deviation of the normalized error ($\bar{\eta}_{\omega_v}$ and $\bar{\sigma}_{\omega_v}$, respectively) for the simulations of two scatterers in a range cell with different ratios between amplitude values. It is apparent how the MS model-free techniques outperform the MS-ML and at the same time how the performance worsens as the amplitudes of the two scatterers become comparable.
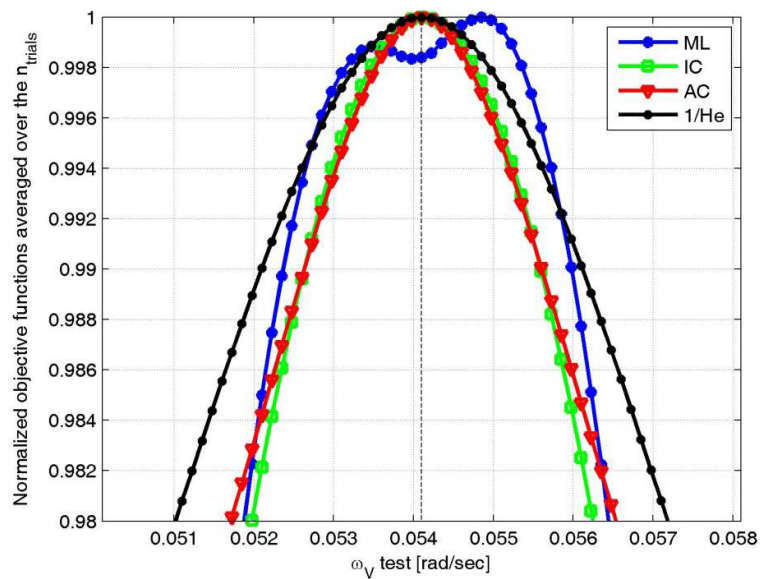

Figure 3-10. Multi-aspect formation. Normalized objective functions for the case of two scatterers in the same range bin with equal amplitude.

A_2/A_1	ML		IC		AC		He	
	$\bar{\eta}_{\omega_v}$	$\bar{\sigma}_{\omega_v}$	$\bar{\eta}_{\omega_v}$	$\bar{\sigma}_{\omega_v}$	$\bar{\eta}_{\omega_v}$	$\bar{\sigma}_{\omega_v}$	$\bar{\eta}_{\omega_v}$	$\bar{\sigma}_{\omega_v}$
0.1	0.0125	0.2798	-0.0025	0.2802	0.0015	0.2659	-0.0026	0.2719
0.5	0.0096	1.2758	0.0093	1.1418	0.0038	1.1100	0.0027	0.9814
1.0	-0.1024	2.2920	-0.0327	0.9342	-0.0779	1.9969	-0.0122	0.5180
1.5	-0.0336	1.5993	-0.0254	1.3620	0.0579	1.7244	-0.0156	1.1215

TABLE 3-1. MEAN AND STANDARD DEVIATION OF THE NORMALIZED ERROR OF THE ROTATION SPEEED ESTIMATION FOR THE SIMULATED DATA FOR THE CASE OF TWO SCATTERERS IN THE SAME RANGE BIN [%].

So far we have considered the case of a dominant vertical motion. Now we show how the performances of the MS techniques degrade in the case of a 3D motion, namely when yaw, pitch and roll are simultaneously non null.

Figure 3-11 shows the bias of the normalized estimation error on the vertical component of the rotation vector when the target is interested by a 3D motion, described by: $\boldsymbol{\omega} = [\omega_H \quad \omega_R \quad \omega_V] = [0.0491 \quad -0.0215 \quad 0.0228]$rad/sec. Figure 3-11a is for the case of a bow scatterer, while Figure 3-11b is for a mainmast scatterer. In both the cases we can observe the great bias of the estimation error, making the multi-aspect technique non applicable when the horizontal and radial component of the rotation motion are not negligible.
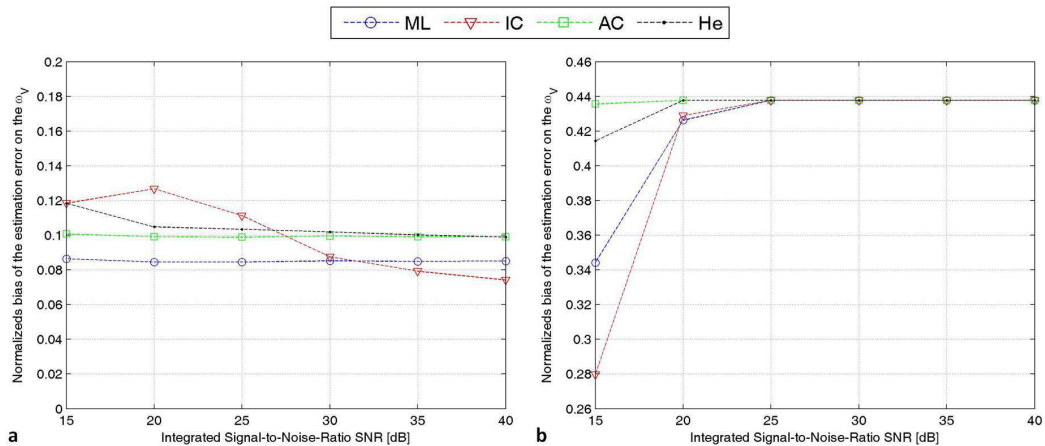

Figure 3-11. Bias of the normalized estimation error on the ω_V for a ship target undergoing a 3D motion – a) bow scatterer, b) mainmast scatterer.

3.4. JOINT MULTI-ASPECT – MULTI-GRAZING FORMATION

In the case of a joint multi-aspect multi-grazing displacement of the sensors, we investigated the particular case of an L shape formation: sensor A and C have the same grazing but different aspect and sensor B and C different grazing but same aspect (see Figure 3-12). We underline that it is a special case of sensors displacement and the quality of the results to follow hold for different formation as long we have both the aspect and grazing diversity. In regard to the target motion, we consider a yawing, pitching and rolling target, so that the all of target rotation vector components in (1) are simultaneously not null.

As discussed in section 3.1, for this kind of geometry the parameters in (9) can be assumed known, and it is the main difference with respect to the multi-aspect formation case; moreover, since now we are considering a three-dimensional motion, instead of a scalar value we have to estimate a vector.
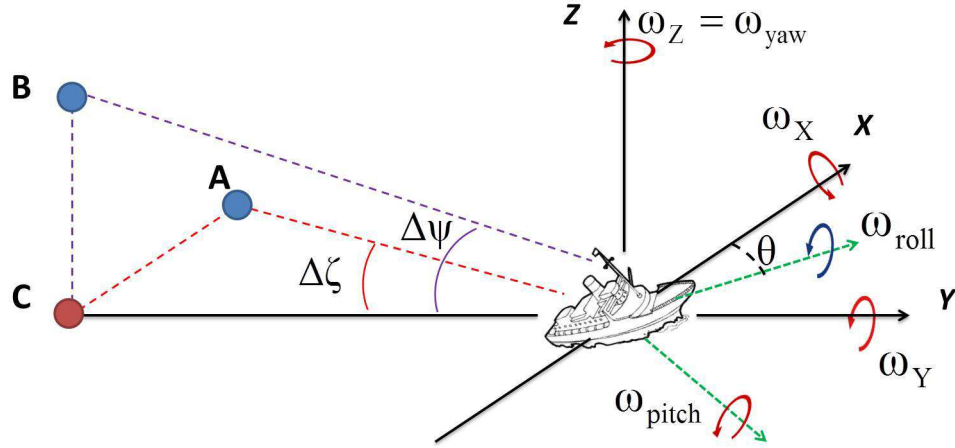
Figure 3-12. Multi-aspect/multi-grazing ISAR geometry (special case of the L shape formation).

3.4.1. ESTIMATION TECHNIQUES

Based on (11) and accounting for the phase model in (7) when, the MS-ML estimator can be proven (Appendix A2) equal to:

$$\hat{\boldsymbol{\omega}}_{ML} = \arg\max_{\boldsymbol{\omega}} \left\{ \sum_{\Gamma} \sum_{k=1}^{K} \left| \mathbf{s}_{k,\Gamma}^{\dagger} \mathbf{g}_{k,\Gamma} \right|^2 \right\} \tag{29}$$

Based on (29), the MS-ML estimate of **ω** is the $\hat{\boldsymbol{\omega}}$ value which maximizes the output of the scheme in Figure 3-13. For every **ω** under test the signal from the k-th range cell is first re-aligned to the zero Doppler frequency and dechirped, then a coherent integration is performed; for each cell the powers of the signals received from each sensor are averaged. The value of the rotation rate which maximizes the signal mean power is assumed as the estimated $\hat{\boldsymbol{\omega}}_{ML}$.

The processing schemes of the model free estimation techniques can be obtained exploiting the compensation of the Doppler shift $\Delta f_{k,\Gamma} = \alpha_{k,\Gamma} - \alpha_{k,C}$, as in the multi-aspect case, rather than the Doppler frequency $\alpha_{k,\Gamma}$, as in the MS-ML case. $\Delta f_{k,\Gamma}$ is the shift in the Doppler position of the k-th scatterer as viewed by the sensor Γ with respect to sensor C. The corresponding processing scheme is sketched in Figure 3-14.

Apart from the specific cost function, the main difference between this scheme and the MS-ML is represented by the FFT block; in the ML case we are looking for the **ω** value which maximizes the signal mean power at the zero Doppler frequency, namely we are looking at the power of the scatterer in a constrained Doppler filter. In contrast with the model-free cases we look for the **ω** value which maximizes the cost function evaluated over all the Doppler filters.

We analyze four model free objective functions: peak power (PP), contrast optimization for the amplitude (AC) and for the intensity (IC) and entropy minimization (He).

The $\hat{\boldsymbol{\omega}}_{PP}$ estimate is given by:

$$\hat{\boldsymbol{\omega}}_{\text{PP}} = \arg\max_{\boldsymbol{\omega}} \left\{ \sum_{k=1}^{K} \arg\max_{\alpha_{k,C}} \left\{ \sum_{\Gamma} |s_{k,\Gamma}^* g_{k,\Gamma}|^2 \right\} \right\} \qquad (30)$$

The PP is a local cost function: among all the tested $\boldsymbol{\omega}$ values, the chosen rotation rate vector is the one maximizing the output peak power.

The $\hat{\boldsymbol{\omega}}_{\text{IC}}$, $\hat{\boldsymbol{\omega}}_{\text{IC}}$ and $\hat{\boldsymbol{\omega}}_{\text{IC}}$ are the same in (20) and (21), respectively, where the scalar ω_γ is replaced by the vector $\boldsymbol{\omega}$.
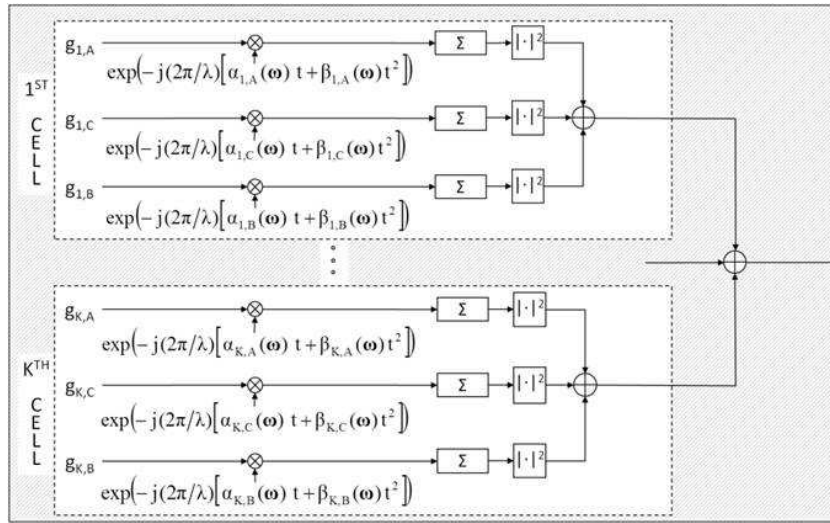

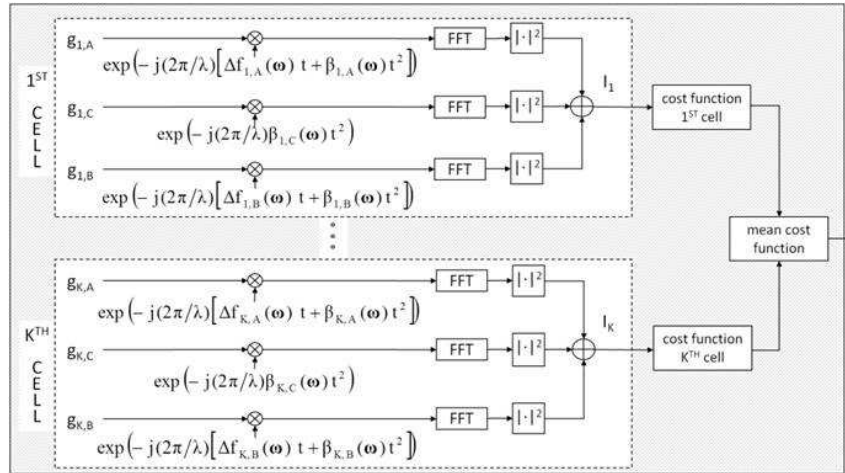Figure 3-13. Joint Multi-aspect-multi-grazing formation. Multi-sensor Maximum Likelihood processing scheme

Figure 3-14. Joint Multi-aspect-multi-grazing formation. Multi-sensor model free processing scheme.

3.4.2. THEORETICAL ESTIMATION ACCURACY

It could be shown (Appendix B2) that the second moment of the estimation error for the γ-th component of the rotation vector (defined as $\delta\omega_\gamma = \widehat{\omega_\gamma} - \omega_\gamma^0$, where $\widehat{\omega_\gamma}$ and ω_γ^0 are the estimated and true value of ω_γ) is given by:

$$\text{CRB}_{\omega_\gamma} \doteq \sigma^2_{\omega_\gamma} = \frac{z_{\delta,\delta} z_{\mu,\mu} - z^2_{\delta,\mu}}{\det\{Z\}} \quad , \quad \begin{cases} \gamma, \delta, \mu = H, R, V \\ \delta \neq \gamma \, ; \mu \neq \gamma \, ; \mu \neq \delta \end{cases} \tag{31}$$

being Z the 3×3 matrix which $z_{\gamma,\delta}$ element (γ - δ = H,R,V):

$$z_{\gamma,\delta} = \frac{2\pi^2 M T^2}{\lambda^2 \sigma^2_n} \left\{ \frac{1}{3} \sum_\Gamma \sum_{k=1}^{K} |A|^2_{k,\Gamma} \alpha^\gamma_{k,\Gamma} \alpha^\delta_{k,\Gamma} + \frac{T^2}{45} \sum_\Gamma \sum_{k=1}^{K} |A|^2_{k,\Gamma} \beta^{\gamma\,'}_{k,\Gamma} \beta^{\delta\,'}_{k,\Gamma} \right\} \tag{32}$$

where $\beta^{\gamma\,'}_{k,\Gamma} = \partial \beta_{k,\Gamma}(\boldsymbol{\omega}) / \partial \omega_\gamma$.

Figure 3-15 shows the theoretical normalized standard deviations of the estimation error on ω_H and ω_V (log-scale) as a function of the r and h coordinates as viewed by the sensor C for different v coordinate values. The integrated signal to noise ratio, defined as $\text{SNR}_{k,\Gamma} = M|A_{k,\Gamma}|^2 / \sigma^2_n$, is assumed to be independent on Γ and equal to 30 dB (i.e. $\text{SNR}_{k,\Gamma} = \text{SNR} = 30$ dB) and the CPI is equal to 0.55 s, resulting in a cross-range resolution of about 50 cm. The platform formation is the same in Figure 3-12 with $\Delta\zeta = \Delta\psi = 5°$, $\lambda = 3$ cm, observing a ship target with initial heading angle $\theta = 45°$ interested by a constant rotational motion given by $\boldsymbol{\omega} = [\omega_H, \omega_R, \omega_V] = [0.0491, -0.0215, 0.0228]$ rad/s and a dominant scatterer in the range bin is assumed.

Although the CRB values in Figure 3-15 depend on the considered study case, it could be proven that the qualitative trend of these figures remains unchanged for different cases. This allows us to make same general considerations on the suitability of a scatterer for the estimation of a specific component of the motion. For example Figure 3-15a shows that in order to estimate ω_H, a propitious scatterer lying on the (R,H) plane is the one with a h coordinate great enough, regardless of the r coordinate; the reverse situation could be shown for the radial component, since the figures of the σ_R/ω_R cases are very similar to the σ_H/ω_H ones but rotated of 90°; Figure 3-15d,e,f show that the most propitious scatterer to be selected for the ω_V estimation is the one with a small vertical coordinate, while in the case of v not null is better to select a scatterer with almost the same h and v coordinates.
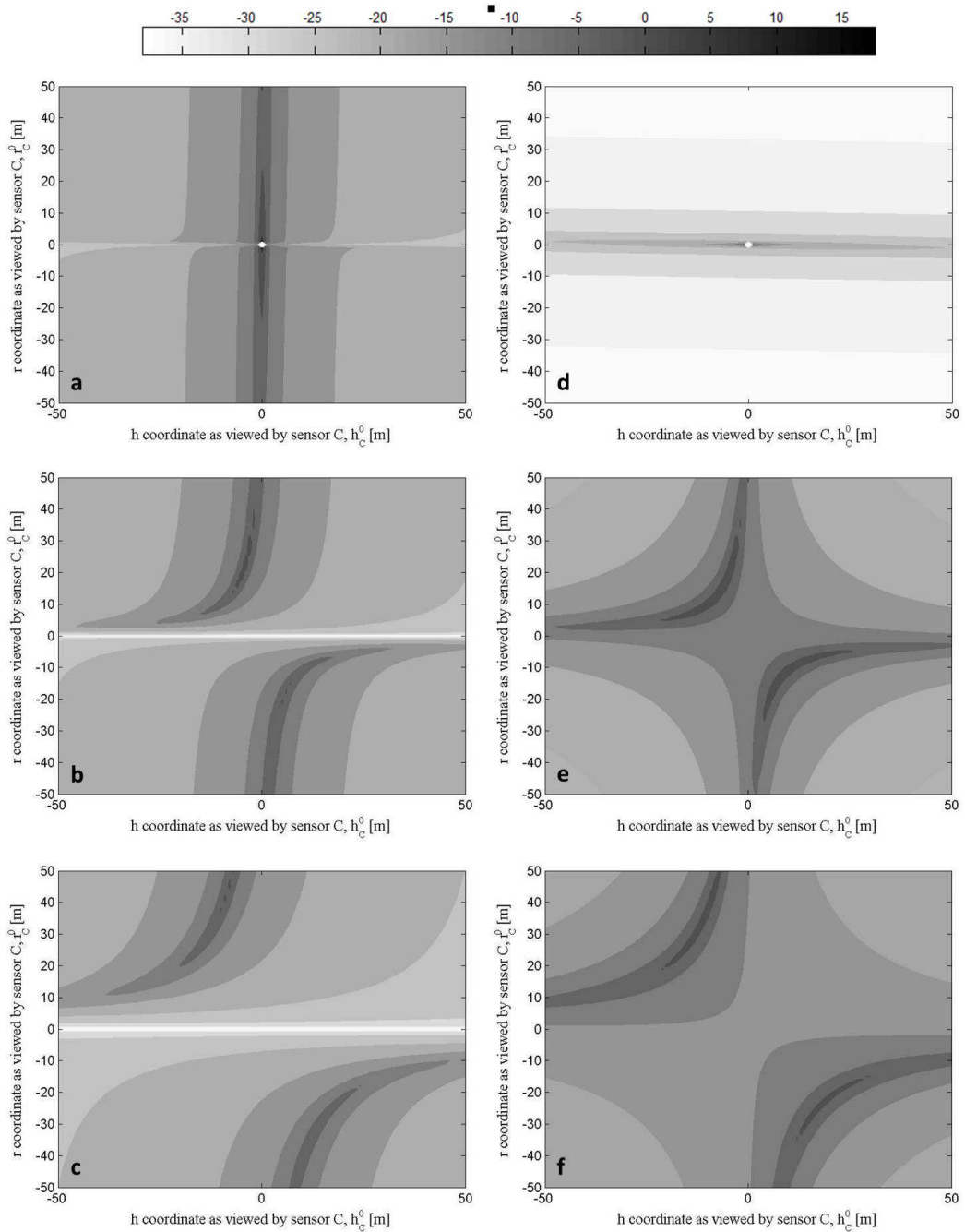
Figure 3-15. Theoretical normalized standard deviation of the estimation error (log-scale) as a function of the plane (R,H) as viewed by the sensor C for different v coordinates - a) σ_H/ω_H, v=0 m ; b) σ_H/ω_H, v=15 m ; c) σ_H/ω_H, v=30 m ; d) σ_V/ω_V, v=0 m ; e) σ_V/ω_V, v=15 m ; f) σ_V/ω_V, v=30 m.

3.4.3. SIMULATED PERFORMANCE ANALYSIS

The performance of the MS techniques are analyzed against simulated data for the same parameters in Figure 3-15. Figure 3-16 shows the normalized standard deviation (STD) of the estimation error on ω_γ for a bow scatterer with aperture time $T_{low-res} \approx 0.18$ s and $T_{high-res} \approx 0.55$ s. The proposed MS

techniques are able to estimate separately the components of **ω** and it could be shown to be almost unbiased. It is also apparent that the estimation accuracy improves with finer cross-range resolution (i.e. longer CPI). Moreover MS-ML shows the best accuracy, reaching the theoretical CRB, with respect to the other MS techniques.

Figure 3-17 shows the normalized STD of the estimation error for a main mast scatterer in the case of sinusoidal yaw (amplitude $A_y=1°$, frequency $f_y = 0.2083$ Hz), pitch ($A_p = 1°$, $f_p = 0.178$ Hz) and roll ($A_r = 5°$, $f_r = 0.091$ Hz), being ω_{yaw}, ω_{pitch} and ω_{roll} defined as their first derivative at $t = t_0$ and leading to the same **ω** as in the constant rotational motion case. T is set to 0.55 s. As it is apparent, keeping reasonably limited the CPI, the MS estimation techniques with non-uniform rotational motion have nearly the same performance as in the constant rotational motion case.

Figure 3-18 shows the results obtained in the case of the estimation performed using together the bow and the main mast scatterers, in the case of constant rotational motion and T ≈ 0.55 s. From the comparison with the curves in Figure 3-16 and Figure 3-17 referring to the same case of motion and aperture time, some considerations can be done. In the K = 2 case (bow and mast jointly), the accuracy of the model-free techniques improves with respect to the accuracy in the K = 1 cases (bow and mast separately) being however very close to the performance provided by the best K = 1 case. On the contrary, ML estimator provided a great gain in the estimation accuracy moving from K = 1 to K = 2. This different behavior can be explained by recalling that the ML technique has a strong sensitivity to the Doppler alignment, namely to the compensation of the linear part of the phase. Moreover it could be proven that an estimation based on the Doppler alignment only is not possible when K = 1 (ill-conditioned problem), whereas it becomes possible when K > 1. This explains why moving from K = 1 to K = 2 the ML technique greatly outperforms the other MS techniques.

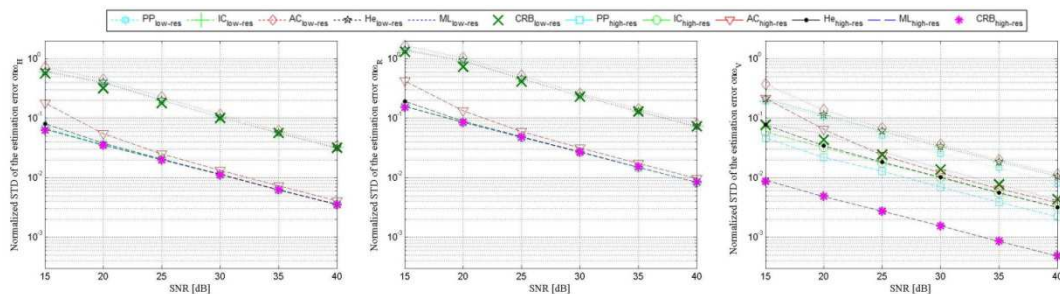Figure 3-16. Normalized STD of the estimation error on ω_H, ω_R and ω_V for a bow scatterer with constant rotational motion.
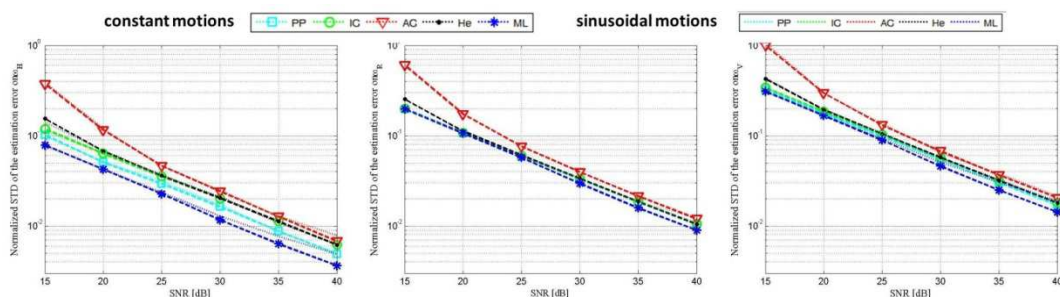
Figure 3-17. Normalized STD of the estimation error on ω_H, ω_R and ω_V for a main mast scatterer: constant vs sinusoidal rotational motion.
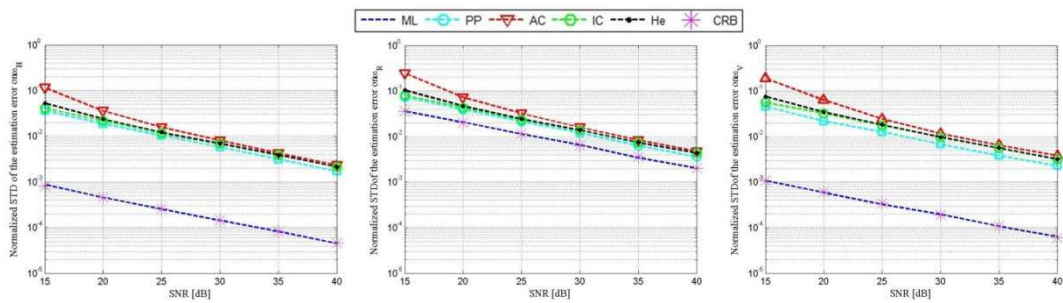
Figure 3-18. Normalized STD of the estimation error on ω_H, ω_R and ω_V using both bow and main mast scatterers with constant rotational motion.

Figure 3-19 shows the normalized STD of the estimation error on ω_v when the ideal compensation of the linear phase terms is performed (already realigned IPPs) and only the focus parameter (curves labeled with subscript β) contributes to the estimation, in comparison with the output of the MS techniques previously described. We analyzed the bow scatterer case with T ≈ 0.18 s. It is apparent the improvement in the estimation performance due to the exploitation of both the Doppler frequency realignment and dechirping, for the special case of limited aperture time.
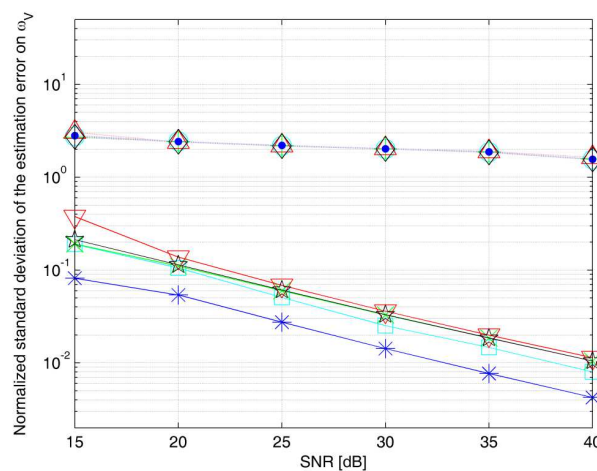

Figure 3-19. Normalized STD of the estimation error on ω_v for a bow scatterer: dechirping vs Doppler realignment + dechirping based techniques.

So far we have assumed the exact knowledge of the slant range positions of the scatterers. In practical situations, the precision whereby the slant range values are measured is limited by the transmitted bandwidth. Here, we analyze by simulation the performance of the MS techniques when an error on the knowledge of the r coordinates is taken into account. Specifically we assume the measures of the three slant range coordinates affected by independent errors with uniform distribution between [-Δr/2 ; Δr/2], being Δr the slant range resolution.

Figure 3-20 shows the performance of the estimation of ω_v as a function of the slant range resolution in noise free-condition for the bow scatterer. As it is apparent the quantization error on the slant range coordinates entails a lower bound on the achievable accuracy, increasing with the

reduction of the transmitted bandwidth. Moreover, we observe that the worst case is provided by the ML estimator, due to its strong dependence on the target model.
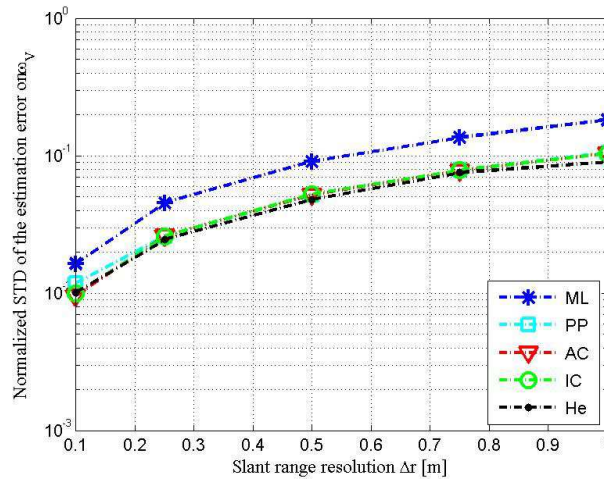

Figure 3-20. Normalized STD of the estimation error on ω_v for a bow scatterer in noise-free condition vs radar range resolution.

3.5. APPLICATION TO LIVE MULTI-SENSOR ISAR DATA

In order to validate the performance analysis previously obtained, we applied the MS estimation schemes to the live D-ISAR data presented in Section 2.5. We recall that the system transmits a series of narrowband pulses in the X-band (λ = 3 cm) and in the Ku-band (λ = 1.82 cm), being the carrier frequency increased by a fixed frequency step equal to 3.75 MHz to form a burst (stepped-frequency waveform). The overall spanned bandwidth is 3 GHz and the turntable yields an angular step $\Delta\theta_0 = 0.07°$ burst to burst (the turntable is fixed during the single burst transmission).

The equivalent geometry of the acquisition (depicted in Figure 2-12) corresponds to an active radar and one additional receiver located at same grazing angle. Hence we are analyzing the multi-aspect formation in Figure 3-4 whit bistatic aspect angle $\Delta\zeta$ = 4.3° and a target characterized by a constant yaw motion.

We point out that the objective of the estimation process is the angular step $\Delta\theta_0$ (the corresponding ω_v is simply given by $\Delta\theta_0$ divided by the burst duration, that for these data is not defined). After the range compression and the range cell selection, the estimation techniques are performed by means of the following steps for each $\Delta\theta$ under test: signals from both channels are dechirped and the signal from the bistatic channel is re-aligned to the Doppler frequency pertaining to the monostatic channel; the FFT on the angular domain is performed and the squared modulus are extracted obtaining two vectors V_A and V_B; V_A and V_B are averaged element by element to obtain the image I; finally the different objective functions are evaluated.

The first analyzed dataset is the grid of metallic cylinders acting like point scatters shown in Figure 2-13; here we analyzed the dataset acquired for the X-band transmission. We selected an overall view angle of about 2.86°, resulting in a cross range resolution of 30 cm for the single (mono-/bi-static) ISAR image. To avoid range cell migration effects we decided for a slant range resolution equal

to 15 cm. In order to have one scatterer in the range cell to be selected for the estimation, we properly chose the central view angle. Figure 3-21 shows the normalized objective functions vs the normalized estimation error, defined as $(\Delta\theta_{test}-\Delta\theta_0)/\Delta\theta_0$, being $\Delta\theta_{test}$ the vector of tested $\Delta\theta$. Figure 3-21a,b refer to the objective functions for the SS (monostatic channel) and SS_{av} estimation techniques respectively. Figure 3-21c shows the MS objective functions applied to the distributed data. As it is apparent, when the distributed approach is considered, the objective functions become narrow around the true value. In Table II we report the normalized estimation error on $\Delta\theta$ obtained for the ML, AC, IC and H_e techniques with the SS (monostatic channel), SS_{av} and MS approaches. It is apparent how the overall angular aperture is too small to make the quadratic term compensation significant for the estimation problem and how in this case the Doppler shift realignment helps in improving the estimation performance.
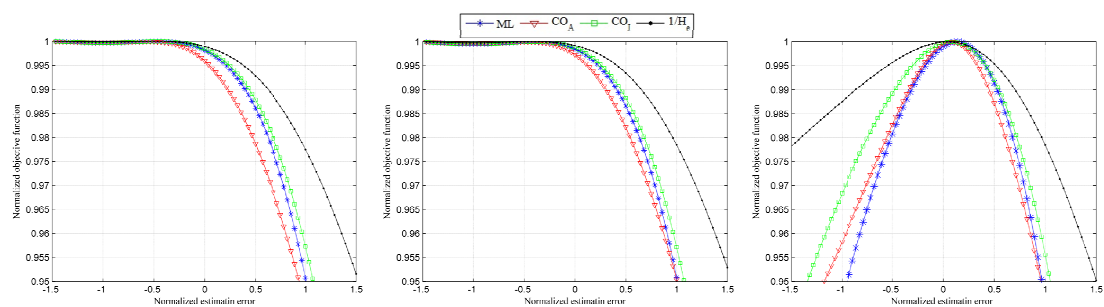

Figure 3-21. Normalized cost functions vs the normalized estimation error for the a) SS, b) SS_{av} and c) MS techniques applied to a grid of metallic cylinders.

	SS	SS_{av}	MS ($\Delta\zeta$ = 4.3°)
ML	-46.8	-39.6	15.0
AC	-58.2	-49.3	7.9
IC	-46.1	-38.6	8.2
He	-48.9	-40.7	4.3

TABLE 3-2. NORMALIZED ESTIMATION ERROR FOR THE GRID OF METALLIC CYLINDERS [%].

The case of a complex target is here considered analyzing the aircraft model in Figure 2-15 acquired in the Ku-band. To have a cross range resolution of 30 cm, we selected an overall view angle of about 1.74° from the monostatic and the bistatic channels, being the bistatic aspect angle equal to 4.3°, as in the previous analysis. Moreover, in order to evaluate the impact of a wider bistatic angle on the estimation performance, the monostatic and bistatic data can be processed around two different central view angles, thus emulating an higher separation between the receiving antennas; following this approach, in the subsequent analysis a second bistatic aspect angle value of 8.3° will be considered. For the estimation process we selected the range cell containing the scatter corresponding to the nose of the aircraft (about in (-0.8 m, 0 m) in Figure 2-16b); the slant range resolution is again 15 cm. Table III shows the normalized estimation error on $\Delta\theta$ for the ML, AC, IC and H_e techniques for the SS, SS_{av} and MS estimation techniques.

Again it can be seen the ineffectiveness of the SS and SS_{av} techniques due to the small overall angular aperture: with the Doppler shift realignment based technique better results are obtained. Moreover Figure 3-22 shows the MS objective functions vs the normalized estimation error for different values of the bistatic aspect angle: 4.3° (Figure 3-22a) and 8.3° (Figure 3-22b). Same colors refer to the same objective cost function; moving from the lower to the higher value of the bistatic angle we observe how the curves become narrower around the null estimation error, proving the ameliorative effect of the increased bistatic angle on the MS estimation process.
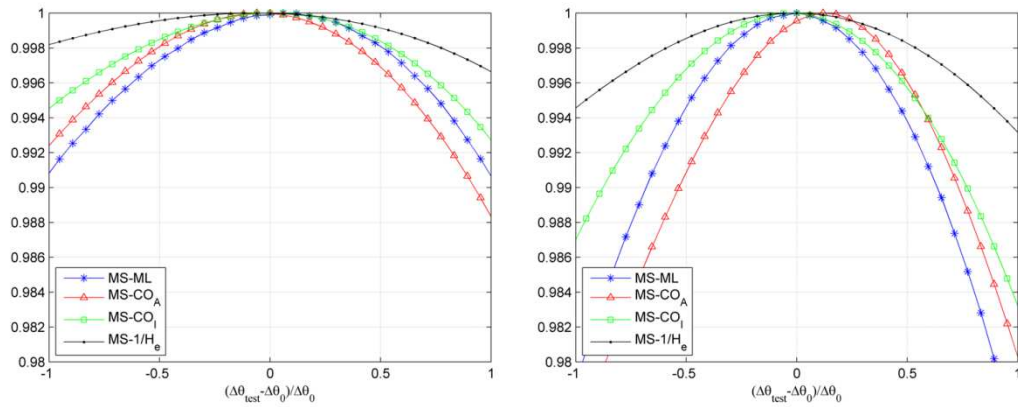

Figure 3-22. Normalized cost functions vs the normalized estimation error for the MS estimation techniques applied to the aircraft model – a) β = 4.3°, b) β = 8.3°.

	SS	SS_{av}	MS (Δζ = 4.3°)
ML	116.00	32.14	7.74
AC	128.00	82.13	-4.16
IC	123.80	53.56	1.19
He	127.40	61.30	-6.55

TABLE 3-3. NORMALIZED ESTIMATION ERROR FOR THE AIRCRAFT MODEL [%].

3.6. CONCLUSIONS

In this chapter we proposed and analyzed rotation motion estimation techniques exploiting the data acquired by formation of sensors with angular diversity in aspect and in both aspect and grazing. Both model-based and model-free criteria have been considered and the corresponding CRBs have been derived.

The study of the multi-aspect case underline how the exploitation of the angular diversity in the estimation process to greatly improve the accuracy of the estimation of the rotation motion component normal to the sensor baseline with respect to the single sensor case exploiting the angular diversity. Specifically, the simulated performance analysis proved the improvement in the estimation accuracy rising from the distributed approach exploiting a Doppler re-alignment, i.e. a

IPPs re-alignment, with respect to the conventional estimation techniques based only on the quality of the cross range compression of the single ISAR image. The application of the technique against live multi-sensor ISAR data confirmed the results achieved against simulated data and showed the ameliorative effect of the Doppler shift re-alignment in the estimation process in the case of a small angular aperture; moreover, the analysis showed how increasing the bistatic angle leads to a further performance improvement.

Increasing the angular diversity in the formation considering the case of joint grazing/aspect diversity allows the sensitivity to all the component of the rotation rate vector. The accurate estimation of the horizontal, radial and vertical component of the rotational motion allows to select proper imaging intervals to achieved high quality scaled images. The case of non-idealities due to the quantization of the measured range has been analyzed, showing the degradation of the performance when a poor slant range resolution is provided. We point out that this degradation could be reduced using additional receivers, allowing a more accurate location of the scatterers.

APPENDIX

A. ANALYTICAL DERIVATION OF THE MAXIMUM LIKELIHOOD ESTIMATORS

For the joint statistic in (11), the log-likelihood function is given by:

$$\ln[p_G(\boldsymbol{g})] = -3KM(\ln \pi + \ln \sigma_n^2) - \frac{1}{\sigma_n^2}(\boldsymbol{g} - \boldsymbol{Sa})^{\mathrm{H}}(\boldsymbol{g} - \boldsymbol{Sa}) \tag{A1}$$

being H the hermitian operator.

1. Multi-aspect formation

Considering the expression of the phase of the signal in (18), the unknown quantities in (A1) are $\sigma_n^2, \mathbf{a}, f_{d_k}^0 (k = 1, \dots, K)$ and $\omega_V = \omega$: the ML estimate of the rotation rate ω can be obtained as:

$$\hat{\omega}_{\mathrm{ML}} = \arg \max_{\omega} \left\{ \arg \max_{\sigma_n^2, \mathbf{a}, f_{d_k}^0} \{\ln[\mathrm{p_G}(\mathbf{g})]\} \right\} \tag{A2}$$

The maximization with respect to σ_n^2 carries to:

$$\sigma_n^2 = \frac{(\mathbf{g} - \mathbf{Sa})^{\mathrm{H}}(\mathbf{g} - \mathbf{Sa})}{3\mathrm{KM}} \tag{A3}$$

Substituting (A3) into (A2) and carrying the maximization with respect to **a** we have:

$$\mathbf{a} = (\mathbf{S}^{\mathrm{H}}\mathbf{S})^{-1}\mathbf{g}^{\mathrm{H}}\mathbf{S} \tag{A4}$$

Therefore we obtain:

$$\hat{\omega}_{\mathrm{ML}} = \arg \min_{\omega} \left\{ \arg \min_{f_{d_k}^0} \{|(\mathbf{I} - \mathbf{S}(\mathbf{S}^{\mathrm{H}}\mathbf{S})^{-1}\mathbf{S}^{\mathrm{H}})\mathbf{g}|^2\} \right\} \tag{A5}$$

Based on (A5), the ML estimate is the value which minimizes the power of the projection of the received signal into the subspace orthogonal to the useful signal: this corresponds to maximizing the power of the projection of the received signal into the useful signal subspace.

Setting $LL^H = (S^H S)^{-1}$, we can write:

$$|(\mathbf{I} - \mathbf{S}(\mathbf{S}^H \mathbf{S})^{-1}\mathbf{S}^H)\mathbf{g}|^2 = (\mathbf{g} - \mathbf{S}\mathbf{L}\mathbf{L}^H\mathbf{S}^H\mathbf{g})^H(\mathbf{g} - \mathbf{S}\mathbf{L}\mathbf{L}^H\mathbf{g}) = \mathbf{g}^H\mathbf{g} - \mathbf{g}^H\mathbf{S}(\mathbf{S}^H\mathbf{S})^{-1}\mathbf{g} \tag{A6}$$

Hence, (A5) yields to (19).

Considering the expression of the phase of the signal in (26), the unknown quantities in (A1) are $\sigma_n^2, \mathbf{a}, \alpha_{k,\Gamma}(k = 1, \dots, K; \Gamma = A, B, C)$ and $\omega_V = \omega$: the ML estimate of the rotation rate ω can be obtained as:

$$\hat{\omega}_{ML} = \arg\max_{\omega}\left\{\arg\max_{\sigma_n^2, \mathbf{a}, \alpha_{k,\Gamma}}\{\ln[p_G(\mathbf{g})]\}\right\} \tag{A7}$$

Performing the maximizations with respect to $\sigma_n^2, \mathbf{a}, \alpha_{k,\Gamma}$ as above we find (27).

2. *Multi-aspect/multi-grazing formation*

For the joint multi-aspect multi-grazing formation, the scatterer Doppler frequency as viewed by the sensor **Γ** is a parameter depending only on **ω**. Therefore, the unknown quantities in (A1) are $\sigma_n^2, \mathbf{a}, \boldsymbol{\omega} = [\omega_H \quad \omega_R \quad \omega_V]$: the ML estimate of the rotation rate vector **ω** can be obtained as:

$$\hat{\boldsymbol{\omega}}_{ML} = \arg\max_{\omega_H, \omega_R, \omega_V}\{\arg\max_{\sigma_n^2, \mathbf{a}}\{\ln[p_G(\mathbf{g})]\}\} \tag{A8}$$

Performing the maximizations with respect to σ_n^2 and **a** we find:

$$\hat{\boldsymbol{\omega}}_{ML} = \arg\min_{\boldsymbol{\omega}}\{|(\mathbf{I} - \mathbf{S}(\mathbf{S}^H\mathbf{S})^{-1}\mathbf{S}^H)\mathbf{g}|^2\} \tag{A9}$$

Considering (A6), we obtain (29).

B. ANALYTICAL DERIVATION OF THE CRAMER RAO LOWER BOUNDS

The CRB can be evaluated via the Fisher information matrix F, defined as:

$$\mathbf{F} = [f_{i,j}] \Rightarrow f_{i,j} = E\left\{\frac{\partial \ln p_Y(y)}{\partial \theta_i}\frac{\partial \ln p_Y(y)}{\partial \theta_j}\right\} \tag{A10}$$

being $E\{\cdot\}$ the mean operator and (θ_i, θ_j) any pair of unknown parameters.

1. *Multi-aspect formation*

In (A1), accounting the phase model in (18), there are 7K+2 unknown parameters: the noise power σ_n^2, the 3K modulus $A_{k,\Gamma}$ and the 3K phase $\phi_{k,\Gamma}$ of the K scatterers, the K scatterers Doppler frequencies $f_{d_k}^0$ and the rotation rate ω. Therefore $[F] = [7K + 2] \times [7K + 2]$ and it is given by:

$$\mathbf{F} = \begin{bmatrix} F_{1,1} & \cdots & F_{1,5} \\ \vdots & \ddots & \vdots \\ F_{5,1} & \cdots & F_{5,5} \end{bmatrix} \tag{A11}$$

being:

$$F_{1,1} = E\left\{\left|\frac{\partial(\cdot)}{\partial\omega}\right|^2\right\} \Rightarrow [F_{1,1}] = [1 \times 1]$$

$$F_{2,2} = E\left\{\left|\frac{\partial(\cdot)}{\partial\varphi_{k,\Gamma}}\right|^2\right\} \xrightarrow[\substack{k=1,\dots,K \\ \Gamma=A,B,C}]{} [F_{2,2}] = [3K \times 3K]$$

$$F_{3,3} = E\left\{\left|\frac{\partial(\cdot)}{\partial f_{d_k}^0}\right|^2\right\} \xrightarrow[k=1,\dots,K]{} [F_{3,3}] = [K \times K]$$

$$F_{4,4} = E\left\{\left|\frac{\partial(\cdot)}{\partial A_{k,\Gamma}}\right|^2\right\} \xrightarrow[\substack{k=1,\dots,K \\ \Gamma=A,B,C}]{} [F_{4,4}] = [3K \times 3K]$$

$$F_{5,5} = E\left\{\left|\frac{\partial(\cdot)}{\partial\sigma_n^2}\right|^2\right\} \Rightarrow [F_{1,1}] = [1 \times 1]$$

$$F_{1,2} = F_{2,1}^T = E\left\{\frac{\partial(\cdot)}{\partial\omega}\frac{\partial(\cdot)}{\partial\varphi_{k,\Gamma}}\right\} \xrightarrow[\substack{k=1,\dots,K \\ \Gamma=A,B,C}]{} [F_{1,2}] = [1 \times 3K]$$

$$F_{1,3} = F_{3,1}^T = E\left\{\frac{\partial(\cdot)}{\partial\omega}\frac{\partial(\cdot)}{\partial f_{d_k}^0}\right\} \xrightarrow[k=1,\dots,K]{} [F_{1,3}] = [1 \times K]$$

$$F_{1,4} = F_{4,1}^T = E\left\{\frac{\partial(\cdot)}{\partial\omega}\frac{\partial(\cdot)}{\partial A_{k,\Gamma}}\right\} \xrightarrow[k=1,\dots,K]{} [F_{1,4}] = [1 \times 3K] \tag{A12}$$

$$F_{1,5} = F_{5,1}^T = E\left\{\frac{\partial(\cdot)}{\partial\omega}\frac{\partial(\cdot)}{\partial\sigma_n^2}\right\} \Rightarrow [F_{1,5}] = 1$$

$$F_{2,3} = F_{3,2}^T = E\left\{\frac{\partial(\cdot)}{\partial\varphi_{k,\Gamma}}\frac{\partial(\cdot)}{\partial f_{d_u}^0}\right\} \xrightarrow[\substack{k,u=1,\dots,K \\ \Gamma=A,B,C}]{} [F_{2,3}] = [3K \times K]$$

$$F_{2,4} = F_{4,2}^T = E\left\{\frac{\partial(\cdot)}{\partial\varphi_{k,\Gamma}}\frac{\partial(\cdot)}{\partial A_{u,\Delta}}\right\} \xrightarrow[\substack{k,u=1,\dots,K \\ \Gamma,\Delta=A,B,C}]{} [F_{2,4}] = [3K \times 3K]$$

$$F_{2,5} = F_{5,2}^T = E\left\{\frac{\partial(\cdot)}{\partial\varphi_{k,\Gamma}}\frac{\partial(\cdot)}{\partial\sigma_n^2}\right\} \xrightarrow[\substack{k=1,\dots,K \\ \Gamma=A,B,C}]{} [F_{2,5}] = [3K \times 1]$$

$$F_{3,4} = F_{4,3}^T = E\left\{\frac{\partial(\cdot)}{\partial f_{d_k}^0}\frac{\partial(\cdot)}{\partial A_{u,\Delta}}\right\} \xrightarrow[\substack{k,u=1,\dots,K \\ \Delta=A,B,C}]{} [F_{3,4}] = [K \times 3K]$$

$$F_{3,5} = F_{5,3}^T = E\left\{\frac{\partial(\cdot)}{\partial f_{d_k}^0}\frac{\partial(\cdot)}{\partial\sigma_n^2}\right\} \xrightarrow[\substack{k=1,\dots,K \\ \Gamma=A,B,C}]{} [F_{3,5}] = [K \times 1]$$

$$F_{4,5} = F_{5,4}^T = E\left\{\frac{\partial(\cdot)}{\partial A_{k,\Gamma}}\frac{\partial(\cdot)}{\partial\sigma_n^2}\right\} \xrightarrow[\substack{k=1,\dots,K \\ \Gamma=A,B,C}]{} [F_{4,5}] = [3K \times 1]$$

The derivates of (A1) needed to evaluate F are:

$$\frac{\partial(\cdot)}{\partial\sigma_n^2} = -\frac{3KM}{\sigma_n^2} + \frac{1}{\sigma_n^4}\sum_\Gamma\sum_{k=1}^{K}\sum_{m=-\frac{M}{2}}^{\frac{M}{2}}\left\{\left|g_{k,\Gamma}(t_m) - A_{k,\Gamma}e^{-j[\varphi_{k,\Gamma}+\phi_{k,\Gamma}(t_m)]}\right|^2\right\}$$

$$\frac{\partial(\cdot)}{\partial A_{k,\Gamma}} = \frac{2}{\sigma_n^2}\sum_{m=-\frac{M}{2}}^{\frac{M}{2}}\left\{\mathrm{Re}\left\{g_{k,\Gamma}(t_m)e^{-j[\varphi_{k,\Gamma}+\phi_{k,\Gamma}(t_m)]} - A_{k,\Gamma}\right\}\right\}$$

$$\frac{\partial(\cdot)}{\partial\varphi_{k,\Gamma}} = \frac{2}{\sigma_n^2}\sum_{m=-\frac{M}{2}}^{\frac{M}{2}}\left\{A_{k,\Gamma}\mathrm{Im}\left\{g_{k,\Gamma}(t_m)e^{-j[\varphi_{k,\Gamma}+\phi_{k,\Gamma}(t_m)]}\right\}\right\} \tag{A13}$$

$$\frac{\partial(\cdot)}{\partial f_{d_k}^0} = -\frac{4\pi}{\lambda\sigma_n^2}\sum_\Gamma\sum_{m=-\frac{M}{2}}^{\frac{M}{2}}\left\{A_{k,\Gamma}\mathrm{Im}\left\{g_{k,\Gamma}(t_m)e^{-j[\varphi_{k,\Gamma}+\phi_{k,\Gamma}(t_m)]}\right\}t_m\right\}$$

$$\frac{\partial(\cdot)}{\partial\omega} = -\frac{4\pi}{\lambda\sigma_n^2}\sum_\Gamma\sum_{k=1}^{K}\sum_{m=-\frac{M}{2}}^{\frac{M}{2}}\left\{A_{k,\Gamma}\mathrm{Im}\left\{g_{k,\Gamma}(t_m)e^{-j[\varphi_{k,\Gamma}+\phi_{k,\Gamma}(t_m)]}\right\}(\sin(\zeta_\Gamma)\,t_m + 2\omega t_m^2)\right\}$$

Being $\mathrm{Re}\{\cdot\}$ and $\mathrm{Im}\{\cdot\}$ the real and imaginary part operators and $\phi_{k,\Gamma}(t_m)$ defined as in (18).

The mean values in (A12) are (k, u = 1,...,K; Γ, Δ = A,B,C):

$$E\left\{\frac{\partial(\cdot)}{\partial\sigma_n^2}\frac{\partial(\cdot)}{\partial\theta}\right\} = \begin{cases}\dfrac{3KM}{\sigma_n^4} & , \ \theta = \sigma_n^2 \\[2mm] 0 & , \ \theta \neq \sigma_n^2\end{cases}$$

$$E\left\{\frac{\partial(\cdot)}{\partial A_{k,\Gamma}}\frac{\partial(\cdot)}{\partial A_{u,\Delta}}\right\} = \begin{cases}\dfrac{2M}{\sigma_n^2} & , \ (k,\Gamma) = (u,\Delta) \\[2mm] 0 & , \ (k,\Gamma) \neq (u,\Delta)\end{cases}$$

$$E\left\{\frac{\partial\,\partial(\cdot)}{\partial\varphi_{k,\Gamma}}\frac{\partial(\cdot)}{\partial\varphi_{u,\Delta}}\right\} = \begin{cases}\dfrac{2M}{\sigma_n^2}A_{k,\Gamma}^2 & , \ (k,\Gamma) = (u,\Delta) \\[2mm] 0 & , \ (k,\Gamma) \neq (u,\Delta)\end{cases}$$

$$E\left\{\frac{\partial(\cdot)}{\partial f_{d_k}^0}\frac{\partial(\cdot)}{\partial f_{d_u}^0}\right\} = \begin{cases}\dfrac{2\pi^2 MT^2}{3\lambda^2\sigma_n^2}\sum_\Gamma A_{k,\Gamma}^2 & , \ k = u \\[2mm] 0 & , \ k \neq u\end{cases} \tag{A14}$$

$$E\left\{\frac{\partial(\cdot)}{\partial\varphi_{k,\Gamma}}\frac{\partial(\cdot)}{\partial A_{u,\Delta}}\right\} = 0$$

$$E\left\{\frac{\partial(\cdot)}{\partial\varphi_{k,\Gamma}}\frac{\partial(\cdot)}{\partial f_{d_u}^0}\right\} = 0$$

$$E\left\{\frac{\partial(\cdot)}{\partial\omega}\frac{\partial(\cdot)}{\partial A_{k,\Gamma}}\right\} = 0$$

$$E\left\{\frac{\partial(\cdot)}{\partial\omega}\frac{\partial(\cdot)}{\partial\varphi_{k,\Gamma}}\right\} = -\frac{2\pi MT^2}{3\lambda\sigma^2}\,\omega r_{k,C}A_{k,\Gamma}^2$$

$$E\left\{\frac{\partial(\cdot)}{\partial\omega}\frac{\partial(\cdot)}{\partial f_{d_k}^0}\right\} = \frac{2\pi^2 MT^2}{3\lambda^2\sigma^2}\,r_{k,C}\sum_\Gamma A_{k,\Gamma}^2\sin(\zeta_\Gamma)$$

$$E\left\{\left|\frac{\partial(\cdot)}{\partial\omega}\right|^2\right\} = \frac{2\pi^2 MT^2}{\lambda^2\sigma^2}\sum_\Gamma\sum_{k=1}^{K}\left(\frac{r_{k,C}^2 A_{k,\Gamma}^2\sin^2(\zeta_\Gamma)}{3}+\frac{r_{k,C}^2 A_{k,\Gamma}^2\omega^2 T^2}{5}\right)$$

We can rearrange F as:

$$F = \begin{bmatrix} F_{AA} & F_{BA} \\ F_{AB} & F_{BB} \end{bmatrix} \tag{A15}$$

being

$$F_{AA} = \begin{bmatrix} F_{11} & F_{12} & F_{1,3} \\ F_{21} & F_{22} & F_{23} \\ F_{31} & F_{32} & F_{33} \end{bmatrix},\quad F_{BA} = \begin{bmatrix} F_{14} & F_{15} \\ F_{24} & F_{25} \\ F_{34} & F_{35} \end{bmatrix} = F_{AB}^T,\quad F_{BB} = \begin{bmatrix} F_{44} & F_{45} \\ F_{54} & F_{55} \end{bmatrix} \tag{A16}$$

The inverse of F can be easily evaluated by means of the Frobenius relations for partitioned matrices:

$$F = \begin{bmatrix} F_{AA} & F_{AB} \\ F_{BA} & F_{BB} \end{bmatrix},\; F^{-1} = \begin{bmatrix} P_{AA} & P_{AB} \\ P_{BA} & P_{BB} \end{bmatrix} \tag{A17}$$

being

$$\begin{aligned} P_{AA} &= (F_{AA} - F_{AB}F_{BB}^{-1}F_{BA})^{-1} \\ P_{BA} &= -F_{BB}^{-1}F_{BA}P_{AA} = P_{AB}^T \\ P_{BB} &- P_{AA}^{-1}P_{BA}P_{AB} = F_{BB}^{-1} \end{aligned} \tag{A18}$$

Since $F_{BA} = F_{BA}^H = \underline{0}$ we have $P_{BA} = P_{AB}^H = \underline{0}$, $P_{BB} = F_{BB}^{-1}$ and $P_{AA} = F_{AA}^{-1}$. To evaluate the CRB we need to evaluate only P_{AA}, therefore we need only to invert the block F_{AA}. We subdivide F_{AA} in this four blocks ($F_{23} = F_{32}^T = \underline{0}$):

$$F_{AA} = \begin{bmatrix} [F_{11}] & [F_{12}, F_{13}] \\ \begin{bmatrix} F_{21} \\ F_{31} \end{bmatrix} & \begin{bmatrix} F_{22} & \underline{0} \\ \underline{0} & F_{33} \end{bmatrix} \end{bmatrix} \tag{A19}$$

From the Frobenius relations, and considering that F_{AA} is a scalar, we can write:

$$\sigma_\omega^2 = F_{AA}^{-1} = \frac{1}{F_{11} - [F_{12}\quad F_{13}]\begin{bmatrix} F_{22} & 0 \\ 0 & F_{33} \end{bmatrix}^{-1}\begin{bmatrix} F_{21} \\ F_{23} \end{bmatrix}} \tag{A20}$$

Carrying out the calculus we find the CRB in (22).

Accounting the phase the phase model in (26), i.e. considering the whole Doppler frequency as an unknown parameters, we can use the same process to derive the CRB. In this case we have $[F] = [9K + 2] \times [9K + 2]$. The structure of F is given again by (A11) but $[F_{13}] = [1 \times 3K]$, $[F_{23}] =$

[$3K \times 3K$], [F_{33}] = [$3K \times 3K$], [F_{43}] = [$3K \times 3K$] and [F_{35}] = [$1 \times 3K$], since there are 3K (instead ok K) unknown Doppler frequencies.

The derivates of (A1) with respect to $\sigma_n^2, A_{k,\Gamma}$ and $\varphi_{k,\Gamma}$ are as in (A13) (since they do not depend on the expression of $\phi_{k,\Gamma}(t_m)$) and we have to calculate again the derivates with respect to the Doppler frequencies and the rotation rate:

$$\frac{\partial(\cdot)}{\partial\omega} = -\frac{8\pi}{\lambda\sigma_n^2}\sum_{\Gamma}\sum_{k=1}^{K}\sum_{m=-\frac{M}{2}}^{\frac{M}{2}}\{A_{k,\Gamma}\text{Im}\{g_{k,\Gamma}(t_m)e^{-j[\varphi_{k,\Gamma}+\phi_{k,\Gamma}(t_m)]}\}(\omega t_m^2)\}$$

$$\frac{\partial(\cdot)}{\partial f_{d_{k,\Gamma}}} = -\frac{4\pi}{\lambda\sigma_n^2}\sum_{m=-\frac{M}{2}}^{\frac{M}{2}}\{A_{k,\Gamma}\text{Im}\{g_{k,\Gamma}(t_m)e^{-j[\varphi_{k,\Gamma}+\phi_{k,\Gamma}(t_m)]}\}t_m\}$$

(A21)

All the expressions (A13) that do not depend on the expression of $\phi_{k,\Gamma}(t_m)$ held also in this case. The main difference is in the elements $E\left\{\frac{\partial(\cdot)}{\partial\omega}\frac{\partial(\cdot)}{\partial f_{d_k}^0}\right\}$, being here equal to zero, therefore $F_{13} = F_{31}^T = \underline{0}$.

Therefore, to calculate the bound we need to invert only the block of F given by: $\begin{bmatrix} F_{11} & F_{21} \\ F_{21}^T & F_{22} \end{bmatrix}$. Using the Frobenius relations we find (28).

2. *Multi-aspect/multi-grazing formation*

The unknown quantities in (A1) are: the noise power σ_n^2, the 3K modulus $A_{k,\Gamma}$ and the 3K phase $\phi_{k,\Gamma}$ of the K scatterers, the horizontal, vertical and radial components of the rotation rate vector $\boldsymbol{\omega}$. Therefore [F] = [6K + 4] × [6K + 4] and it is given by:

$$F = \begin{bmatrix} F_{1,1} & \cdots & F_{1,4} \\ \vdots & \ddots & \vdots \\ F_{4,1} & \cdots & F_{4,4} \end{bmatrix}$$

(A22)

being

$$F_{1,1} = E\left\{\frac{\partial(\cdot)}{\partial\omega_\gamma}\frac{\partial(\cdot)}{\partial\omega_\delta}\right\}\xRightarrow[\substack{\gamma=H,R,V\\\delta=H,R,V}]{}[F_{1,1}] = [3\times 3]$$

$$F_{2,2} = E\left\{\left|\frac{\partial(\cdot)}{\partial\varphi_{k,\Gamma}}\right|^2\right\}\xRightarrow[\substack{k=1,\ldots,K\\\Gamma=A,B,C}]{}[F_{2,2}] = [3K\times 3K]$$

$$F_{3,3} = E\left\{\left|\frac{\partial(\cdot)}{\partial A_{k,\Gamma}}\right|^2\right\}\xRightarrow[\substack{k=1,\ldots,K\\\Gamma=A,B,C}]{}[F_{3,3}] = [3K\times 3K]$$

$$F_{4,4} = E\left\{\left|\frac{\partial(\cdot)}{\partial\sigma_n^2}\right|^2\right\}\Rightarrow[F_{1,1}] = [1\times 3K]$$

$$F_{1,2} = F_{2,1}^T = E\left\{\frac{\partial(\cdot)}{\partial\omega_\gamma}\frac{\partial(\cdot)}{\partial\varphi_{k,\Gamma}}\right\}\xRightarrow[\substack{\gamma=H,R,V\\k=1,\ldots,K\\\Gamma=A,B,C}]{}[F_{1,2}] = [3\times 3K]$$

$$F_{1,3} = F_{3,1}^T = E\left\{\frac{\partial(\cdot)}{\partial\omega_\gamma}\frac{\partial(\cdot)}{\partial A_{k,\Gamma}}\right\}\xRightarrow[\substack{\gamma=H,R,V\\k=1,\ldots,K\\\Gamma=A,B,C}]{}[F_{1,3}] = [3\times 3K]$$

$$F_{1,4} = F_{4,1}^T = E\left\{\frac{\partial(\cdot)}{\partial\omega_\gamma}\frac{\partial(\cdot)}{\partial\sigma_n^2}\right\}\xRightarrow[\gamma=H,R,V]{}[F_{1,4}] = [3\times 1]$$

$$F_{2,3} = F_{3,2}^T = E\left\{\frac{\partial(\cdot)}{\partial\varphi_{k,\Gamma}}\frac{\partial(\cdot)}{\partial A_{u,\Delta}}\right\}\xRightarrow[\substack{k,u=1,\ldots,K\\\Gamma,\Delta=A,B,C}]{}[F_{2,3}] = [3K\times 3K]$$

$$F_{2,4} = F_{4,2}^T = E\left\{\frac{\partial(\cdot)}{\partial\varphi_{k,\Gamma}}\frac{\partial(\cdot)}{\partial\sigma_n^2}\right\}\xRightarrow[\substack{k=1,\ldots,K\\\Gamma=A,B,C}]{}[F_{2,4}] = [3K\times 1]$$

$$F_{3,4} = F_{4,3}^T = E\left\{\frac{\partial(\cdot)}{\partial A_{k,\Gamma}}\frac{\partial(\cdot)}{\partial\sigma_n^2}\right\}\xRightarrow[\substack{k=1,\ldots,K\\\Gamma=A,B,C}]{}[F_{3,4}] = [3K\times 1]$$

(A23)

The derivates of (A1) with respect to σ_n^2, $A_{k,\Gamma}$, and $\varphi_{k,\Gamma}$ are as in (A13), while the derivates with respect to the γ-th component of the rotation vector is:

$$\frac{\partial(\cdot)}{\partial\omega_\gamma} = -\frac{4\pi}{\lambda}\frac{1}{\sigma^2}\sum_\Gamma\sum_{k=1}^K\sum_{m=-M/2}^{M/2}M_{k,\Gamma}\left(\alpha_{k,\Gamma}^\gamma t_m + \beta_{k,\Gamma}^{\gamma\,\prime}t_m^2\right)\text{Im}\left\{g_{k,\Gamma}(t_m)e^{-j\left(\varphi_{k,\Gamma}+\phi_{k,\Gamma}(t_m)\right)}\right\},$$

$$\gamma = H, R, V$$

(A24)

being $\beta_{k,\Gamma}^{\gamma\,\prime} = \frac{\partial\beta_{k,\Gamma}}{\partial\omega_\gamma}$, i.e.:

$$\beta_{k,\Gamma}^{H\,\prime} = \frac{\partial\beta_{k,\Gamma}}{\partial\omega_H} = 2\omega_H\beta_{k,\Gamma}^{HH} + \omega_R\beta_{k,\Gamma}^{HR} + \omega_V\beta_{k,\Gamma}^{HV}$$

$$\beta_{k,\Gamma}^{R\,\prime} = \frac{\partial\beta_{k,\Gamma}}{\partial\omega_R} = 2\omega_R\beta_{k,\Gamma}^{RR} + \omega_H\beta_{k,\Gamma}^{RH} + \omega_V\beta_{k,\Gamma}^{RV}$$

$$\beta_{k,\Gamma}^{V\,\prime} = \frac{\partial\beta_{k,\Gamma}}{\partial\omega_V} = 2\omega_V\beta_{k,\Gamma}^{VV} + \omega_H\beta_{k,\Gamma}^{VH} + \omega_R\beta_{k,\Gamma}^{VR}$$

(A25)

The several mean values in (A23) are (k, u = 1,…,K; Γ, Δ = A,B,C):

$$E\left\{\frac{\partial(\cdot)}{\partial\sigma_n^2}\frac{\partial(\cdot)}{\partial\theta}\right\} = \begin{cases} \dfrac{3KM}{\sigma_n^4} & , \ \theta = \sigma_n^2 \\ 0 & , \ \theta \neq \sigma_n^2 \end{cases}$$

$$E\left\{\frac{\partial(\cdot)}{\partial A_{k,\Gamma}}\frac{\partial(\cdot)}{\partial A_{u,\Delta}}\right\} = \begin{cases} \dfrac{2M}{\sigma_n^2} & , (k,\Gamma) = (u,\Delta) \\ 0 & , (k,\Gamma) \neq (l,\Delta) \end{cases} \begin{cases} k = 1,\dots,K \\ \Gamma = A,B,C \end{cases}$$

$$E\left\{\frac{\partial(\cdot)}{\partial\varphi_{k,\Gamma}}\frac{\partial(\cdot)}{\partial\varphi_{u,\Delta}}\right\} = \begin{cases} \dfrac{2M}{\sigma_n^2}M_{k,\Gamma}^2 & , (k,\Gamma) = (u,\Delta) \\ 0 & , (k,\Gamma) \neq (u,\Delta) \end{cases} \begin{cases} k,u = 1,\dots,K \\ \Gamma,\Delta = A,B,C \end{cases}$$

$$E\left\{\frac{\partial(\cdot)}{\partial\varphi_{k,\Gamma}}\frac{\partial(\cdot)}{\partial A_{u,\Delta}}\right\} = 0 \quad , \begin{cases} k,u = 1,\dots,K \\ \Gamma,\Delta = A,B,C \end{cases} \tag{A26}$$

$$E\left\{\frac{\partial(\cdot)}{\partial A_{k,\Gamma}}\frac{\partial(\cdot)}{\partial\omega_\gamma}\right\} = 0 \quad , \begin{cases} k = 1,\dots,K \\ \Gamma = A,B,C \\ \gamma = H,R,V \end{cases}$$

$$\left\{\frac{\partial(\cdot)}{\partial\varphi_{k,\Gamma}}\frac{\partial(\cdot)}{\partial\omega_\gamma}\right\} = -\frac{\pi}{\lambda\sigma_n^2}\frac{MT^2}{3}{\beta_{k,\Gamma}^\gamma}' \quad , \begin{cases} k = 1,\dots,K \\ \Gamma = A,B,C \\ \gamma = H,R,V \end{cases}$$

$$\left\{\frac{\partial(\cdot)}{\partial\omega_\gamma}\frac{\partial(\cdot)}{\partial\omega_\delta}\right\} = \frac{2\pi^2MT^2}{\lambda^2\sigma_n^2}\sum_\Gamma\sum_{k=1}^K\left(\frac{\alpha_{k,\Gamma}^\gamma\alpha_{k,\Gamma}^\delta}{3} + \frac{{\beta_{k,\Gamma}^\gamma}'{\beta_{k,\Gamma}^\delta}'}{20}T^2\right); \gamma,\delta = H,R,V$$

The bounds relative of the three components of the rotation rate vector are the first three elements of the diagonal of the inverse of F. We can rearrange F as in (A15) setting:

$$F_{AA} = \begin{bmatrix} F_{11} & F_{21} \\ F_{12} & F_{22} \end{bmatrix} , \ F_{BA} = \begin{bmatrix} F_{13} & F_{14} \\ F_{23} & F_{24} \end{bmatrix} = F_{AB}^T , \ F_{BB} = \begin{bmatrix} F_{33} & F_{34} \\ F_{43} & F_{44} \end{bmatrix} \tag{A27}$$

As in the multi-aspect case, we have $F_{BA} = \underline{0}$, and the bounds can be evaluated inverting only the matrix F_{AA}. Using again the Frobenius relations we obtain:

$$Z = (F_{11} - F_{12}F_{22}^{-1}F_{12}^T)^{-1} \tag{A28}$$

Z is a symmetric $[3 \times 3]$ matrix whose generic element is given by (32). Performing the inversion and taking the elements of the diagonal we find the bounds in (31).

4. MIMO SAR/ISAR IMAGING OF ROTATING TARGETS WITH RECONFIGURABLE FORMATION OF PLATFORMS

In recent years the radar community has devoted considerable attention to the study of networks of low-mass and low-cost jointly operating sensors. This is due to the well known advantages of a constellation, namely the robustness to out of services and the reconfiguration capability of the overall system, thus enabling many different applications, [13]. Moreover, despite the poor performance of each sensor in the network and the synchronization issues, [77], [78], [98], the possibility of achieving comparable or even better performance with respect to conventional single sensor (SS) systems has been widely addressed.

When imaging man-made targets (such as ships) the resolution of achievable radar images is a key point. As well known, the range resolution of a Synthetic Aperture Radar (SAR) image depends on the transmitted bandwidth, which can be limited if a low cost and low-mass sensor is considered or more in general is limited by regulation constraints: a wider bandwidth imposes both stronger requirements on the hardware of the transmit and receive chain, and the requirement of a higher downlink capacity to ground; moreover, the international rules assign to radar applications only a limited fraction of bandwidth (e.g. the International Telecommunication Union reserves only about 300 MHz at X-band). In order to build a cheaper and lighter single sensor, one might reduce the system bandwidth at the expense of a reduced range resolution.

In chapter 2 we shown how the exploitation of multiple radar sensor properly spaced allows us to configure a Distributed ISAR (D-ISAR) system where a wider observation angle than in the single sensor case is emulated, resulting in an enhanced cross range resolution. A similar concept can be considered for the range dimension.

In the past the exploitation of proper angular diversity in a multiple radar system has been proofed allowing to improve the range resolution, [85] (see also [99], [100]). The joint processing of the multiple-surveys acquired signals could result in an overall synthetic bandwidth greater than the transmitted one: an improvement of range resolution up to the number of surveys could be achieved selecting proper acquisition geometries. The concept has been generalized in [86] for a Multi-Input-Multi-Output (MIMO) SAR system able to exploit both monostatic and bistatic acquisitions to allow a maximum theoretical improvement factor greater than the number of operating systems, [101].

In this chapter we consider a generalization of the MIMO SAR [86] (that we recall in 4.1) and MIMO ISAR [82] (discussed in section 2.1) concepts: a 2D-MIMO SAR/ISAR system is proposed based on a formation of platforms which can be configured with proper cross-track and along-track displacements. A maximum theoretical 2D resolution cell improvement factor can be achieved significantly greater than the number of flying platforms, by jointly exploiting both the monostatic and the bistatic acquisitions.

The 2D-MIMO SAR/ISAR system concept mainly addresses those applications where the resolution requirements change with the specific operational conditions: in such a case the use of a reconfigurable system could allow in almost all conditions the achievement of radar images of man-made targets with the required quality for classification or identification purposes. A typical case is

maritime surveillance where, depending on the target aspect angle (angle between the radar Line Of Sight - LOS and the ship centerline) and on the sea state, conventional single-channel techniques can result in ship images with poor quality. The flexible use of a constellation of platforms could be therefore of great importance for both non-cooperative target classification/identification and vessel traffic management, allowing complete real-time control, surveillance and monitoring in wide sea areas.

4.1. DISTRIBUTED SAR CONCEPT

The MIMO SAR concept is based on the consideration that SAR surveys of the same area with different off-nadir angles contain different parts of the ground reflectivity spectrum: different observations from different incidence angles observe different spectral shifts in the down-converted signals. This effect is known as the "wavenumber shift" in SAR interferometry [102]. The basic principle of range resolution improvement is to coherently combine the different parts of the measured spectra, in order to increase the total range bandwidth.

4.1.1. WAVENUMBER SHIFT DERIVATION BASED ON EQUIVALENT CROSS-TRACK APERTURES

When dealing with SAR systems, one is familiar with the equivalence between the platform formation motion in the along-track direction (synthetic aperture) and the frequency bandwidth of the corresponding chirp signal in the slow-time domain [60]. Applying the dual form of this equivalence to the range dimension we can consider the frequency bandwidth of the transmitted signal in the fast-time domain as equivalent to an aperture in the cross-track direction. The range resolution cell obtained after the signal compression can be treated as the illuminated region corresponding to an equivalent aperture of length L' having a beamwidth $\Delta\theta^{eq}$, as sketched in Figure 4-1.
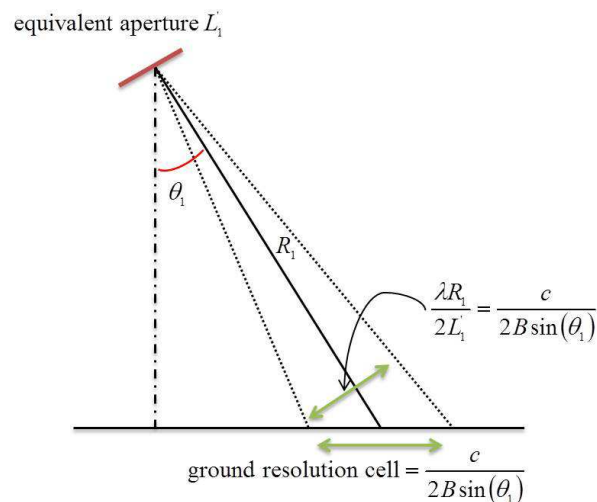

Figure 4-1. Range resolution and equivalent aperture.

The expression of the equivalent beamwidth $\Delta\theta_1^{eq}$ as a function of the off-nadir angle θ_1 and of the bandwidth of transmitted signal B can be obtained considering that the projection of the equivalent beam in the ground range direction has to be equal to the achievable ground range resolution:

$$\text{ground range resolution cell} = \frac{\lambda}{2\Delta\theta_1^{eq}\cos(\theta_1)} = \frac{c}{2B\sin(\theta_1)} \tag{1}$$

and therefore:

$$\Delta\theta_1^{eq} = \frac{\lambda B tg(\theta_1)}{c} \tag{2}$$

being λ the wavelength and c the speed of light.

Considering several SAR sensors observing the same area on the ground with different off-nadir angles we are able to increase the corresponding equivalent aperture, and therefore $\Delta\theta_1^{eq}$. As in the D-ISAR technique some constraints hold for the aspect angles of the sensors in order to avoid gaps in adjacent apertures (see section 2.1 eq. (1)), in the MIMO SAR technique a constraint has to be posed for the selection of the off-nadir angles.

As sketched in Figure 4-2 let us consider a second survey of the same area with an off-nadir angle θ_2, transmitting signal with the same bandwidth. Indicating the middle off-nadir angle as $\theta_0 = \frac{\theta_1 + \theta_2}{2}$ and the difference between the two angles $\Delta\theta = \theta_1 - \theta_2$, the expression in (2) can be re-written as:

$$\Delta\theta_1^{eq} = \frac{\lambda B}{c} tg\left(\theta_0 + \frac{\Delta\theta}{2}\right) \approx \frac{\lambda B}{c}\left(tg(\theta_0) + \frac{\Delta\theta}{2\cos^2(\theta_0)}\right) \tag{3}$$

Analogously, for the second sensor:

$$\Delta\theta_2^{eq} = \frac{\lambda B}{c} tg\left(\theta_0 - \frac{\Delta\theta}{2}\right) \approx \frac{\lambda B}{c}\left(tg(\theta_0) - \frac{\Delta\theta}{2\cos^2(\theta_0)}\right) \tag{4}$$
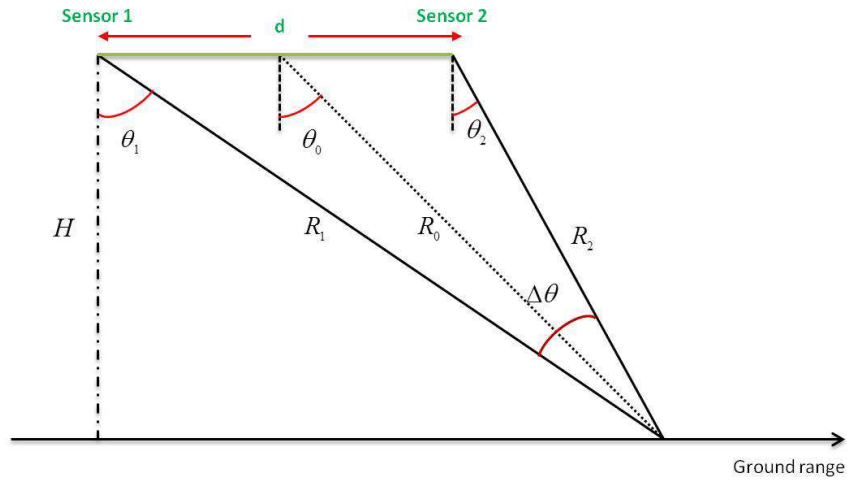

Figure 4-2. Multiple SAR surveys acquisition geometry.

The two equivalent apertures result contiguous if:

$$\Delta\theta = \frac{\Delta\theta_1^{eq}}{2} + \frac{\Delta\theta_1^{eq}}{2} = \frac{\lambda B}{c} tg(\theta_0) \tag{5}$$

A different approach to derive (5) has been proposed in [85].

Let $s_1^{RF}(t_1)$ and $s_2^{RF}(t_2)$ be the two received signal at radio-frequency:

$$\begin{cases} s_1^{RF}(t_1) = g\left(t_1 - \frac{2R_1}{c}\right) \cdot \exp\left\{j2\pi f_c\left(t_1 - \frac{2R_1}{c}\right)\right\} \\ s_2^{RF}(t_2) = g\left(t_2 - \frac{2R_1}{c}\right) \cdot \exp\left\{j2\pi f_c\left(t_2 - \frac{2R_2}{c}\right)\right\} \end{cases} \tag{6}$$

being t_1 and t_2 the fast-time domains, $g(\cdot)$ the transmitted waveform and f_c the carrier frequency..

As derived in [85], the transformations between the two fast-time domains and the ground range are the following:

$$\begin{cases} t_1 = \frac{2R_1}{c} + \frac{2u}{c}\sin(\theta_1) \\ t_2 = \frac{2R_2}{c} + \frac{2u}{c}\sin(\theta_2) \end{cases} \tag{7}$$

Being u the ground range coordinate centered in the middle of the observed scene. Therefore we can re-write (6) in terms of ground range as:

$$\begin{cases} s_1^{RF}(u) = g\left(\frac{2u\sin(\theta_1)}{c}\right) \cdot \exp\left\{j2\pi f_p\frac{2u\sin(\theta_1)}{c}\right\} \\ s_2^{RF}(u) = g\left(\frac{2u\sin(\theta_2)}{c}\right) \cdot \exp\left\{j2\pi f_p\frac{2u\sin(\theta_2)}{c}\right\} \end{cases} \tag{8}$$

The two signals are demodulated by a multiplication for a reference function depending on θ_0:

$$s_{DEMOD}(u) = \exp\left\{-j2\pi f_c\frac{2u\sin(\theta_1)}{c}\right\} \tag{9}$$

The resulting down-converted signals can be expressed as:

$$\begin{cases} s_1(u) = g\left(\frac{2u\sin(\theta_1)}{c}\right) \cdot \exp\left\{j2\pi f_p\frac{2u\sin(\theta_0)}{c}\left(\frac{\sin(\theta_1)}{\sin(\theta_0)} - 1\right)\right\} \\ s_2(u) = g\left(\frac{2u\sin(\theta_2)}{c}\right) \cdot \exp\left\{j2\pi f_p\frac{2u\sin(\theta_0)}{c}\left(\frac{\sin(\theta_2)}{\sin(\theta_0)} - 1\right)\right\} \end{cases} \tag{10}$$

Since in practical applications the difference between the two off nadir angles will be very limited, we can assume the two scaling factor of the transmitted waveform $g(\cdot)$ equal to the scaling experienced at θ_0, i.e. $g\left(\frac{2u\sin(\theta_1)}{c}\right) \approx g\left(\frac{2u\sin(\theta_2)}{c}\right) \approx g\left(\frac{2u\sin(\theta_0)}{c}\right)$.

Indicating with $G(\cdot)$ the Fourier transform of $g(\cdot)$, the spectra of $s_1(u)$ and $s_2(u)$ are given by:

$$\begin{cases} S_1(f) = G\left(f - f_c\left(\dfrac{\sin(\theta_1)}{\sin(\theta_0)} - 1\right)\right) \\[3mm] S_2(f) = G\left(f - f_c\left(\dfrac{\sin(\theta_2)}{\sin(\theta_0)} - 1\right)\right) \end{cases} \qquad (11)$$

Where f is the transformed variable of $\frac{2u\sin(\theta_0)}{c}$, thus having dimension [Hz] and corresponding to a temporal frequency. In this domain, signals in (11) have a relative shift equal to:

$$\Delta f = f_c\left\{\left(\frac{\sin(\theta_1)}{\sin(\theta_0)} - 1\right) - \left(\frac{\sin(\theta_2)}{\sin(\theta_0)} - 1\right)\right\} = f_p\left\{\frac{\sin(\theta_1) - \sin(\theta_2)}{\sin(\theta_0)}\right\} \cong f_c\frac{\Delta\theta}{tg(\theta_0)} \qquad (12)$$

4.1.2. MIMO SAR CONCEPT

The concept presented in the previous section can be extended for constellation composed by active sensors transmitting a set of orthogonal waveforms, that we referred as MIMO SAR system. In particular, the sensors are assumed able to separate the echoes from their own transmissions from the echoes of other sensors transmissions.

Let us consider the geometry depicted in Figure 4-3. The two real platforms A and B carry active radar systems transmitting almost orthogonal waveforms and have a cross-track displacement such that they observe the target with off-nadir angles θ_A and θ_B, respectively. The equivalent apertures L_A and L_B obtained by sensors A and B, working as usual monostatic systems. The equivalent aperture L_C is obtained when sensor A transmits and sensor B receives, namely exploiting a bistatic acquisition. As already discussed in section 2.1, the bistatic acquisition is equivalent to a monostatic one located on the bisector between the transmitter and receiver path, leading to the virtual sensor C with off-nadir angle $\theta_C = (\theta_A + \theta_B)/2$. By properly selection both the two off-nadir angles and the equivalent aperture lengths, it is possible to define a geometry in which the bistatic equivalent aperture L_C exactly fills the gap between the aperture L_A and L_B, thus ensuring the continuity in the overall aperture.
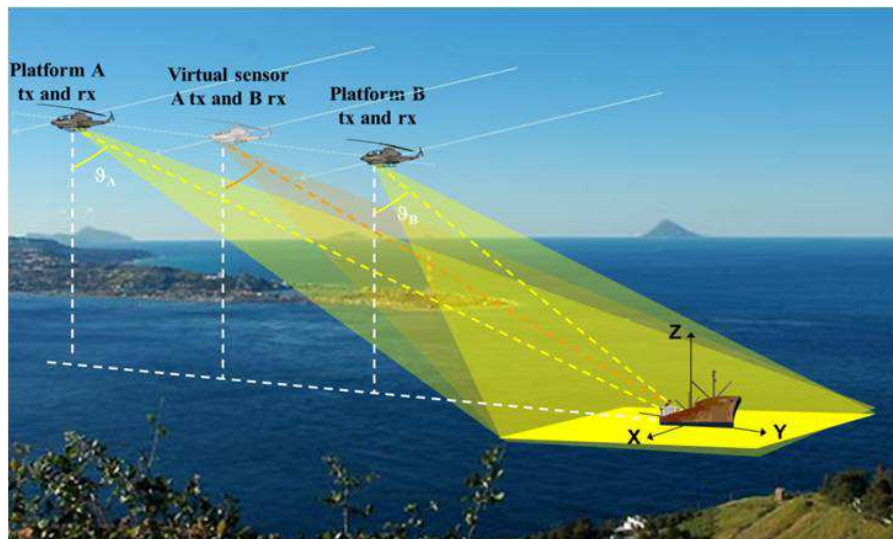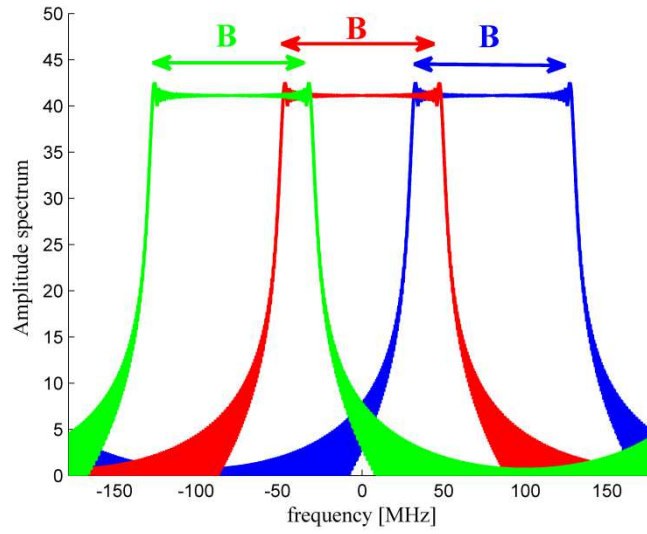

Figure 4-3. MIMO SAR acquisition geometry.

Figure 4-4. MIMO SAR overall received bandwidth.

From a spectral point of view, the three off-nadir angles result in the spectral shifts Δf_Γ (Γ=A,B,C) (12) in the down converted signals, where $\Delta\theta$ is replaced by $\Delta\theta_\Gamma$, i.e. the difference between the off-nadir angle pertaining the Γth sensor and the reference off-nadir, equal to θ_C.

Let us consider sensors A and B transmitting orthogonal waveforms with bandwidth 100 MHz and θ_A and θ_B angles such that Δf_A = - Δf_B = 80 MHz. The spectra of the downconverted signal after range compression are shown in Figure 4-4 using two real sensors: as we can observe, an overall synthetic bandwidth equal to 260 MHz can be achieved, resulting in an improvement in the range resolution.

The maximum spectral shift that ensures contiguity between the three spectra is equal to the transmitted bandwidth (substituting the bandwidth B in (12) the equivalence between (5) and (12) can be easily verified).

It is worth noticing that since the use of a MIMO constellation an improvement factor in range resolution greater than the number of real platforms can be achieved. Referring to the previous example, using two real sensors the maximum range resolution improvement is equal to 3 when Δf_A = - Δf_B = transmitted bandwidth B = 100 MHz. This is obtained by using both the monostatic and bistatic acquisitions, giving rise to a number of equivalent sensor N generally greater than the number of real sensors S. The optimization of the positions of a set of MIMO sensors to provide maximum angular coverage without gaps has been obtained in [101].

In Figure 4-5 black and white squares respectively represent the real and the fictitious cross-track angular apertures used in the distributed configuration, where the term "real aperture" indicates the equivalent cross-track aperture for the sensor operating in monostatic configuration, whereas "virtual aperture" corresponds to bistatic acquisitions. It could be shown, [101], that in the limit $S \to \infty$, the value $N \to S^2$, so that the MIMO improvement tends to be quadratically related to the number of real platforms.
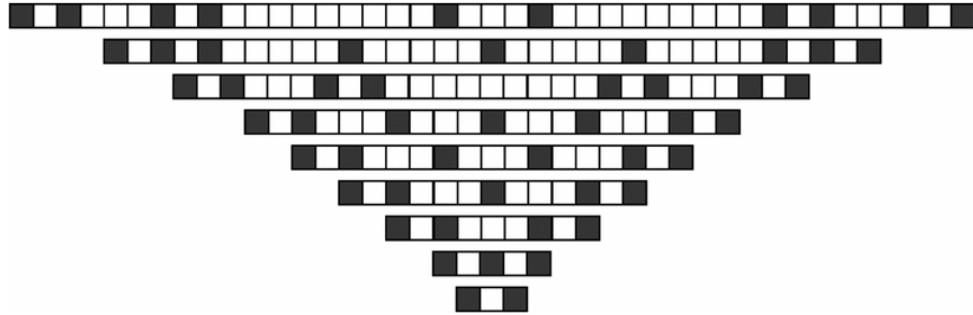
Figure 4-5. Map of real and virtual apertures (angle of view) in the MIMO distributed SAR.

4.2. 2D-MIMO SAR/ISAR CONCEPT

The operative scenario here considered accounts for the presence of a formation of S air - or space - platforms. Each one is equipped with an active radar system, able to receive and separate echoes from the different transmissions through the use of almost orthogonal waveforms. Sensor antennas are appropriately steered toward the moving target to be imaged. The considered geometry is sketched in Figure 4-6 for the case of S = 4.
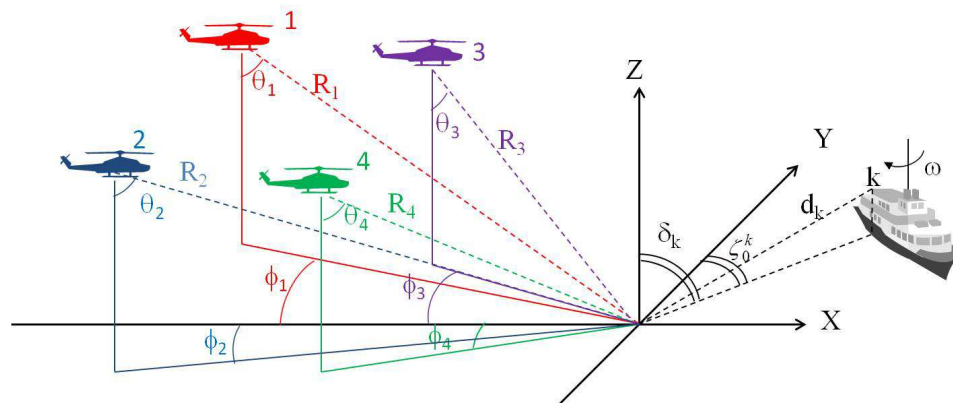
Figure 4-6. 2D-MIMO SAR/ISAR scenario.

Generally the position of each platform is defined according to a couple of angles, namely an aspect angle ϕ_i and an off-nadir angle θ_i for i=1,...,S defined in the XYZ reference system. If we consider the h-th transmitting platform and l-th receiving platform (h,l = 1,...,S) we can define the n-th equivalent sensor position: it is a real position in the case of a monostatic acquisition, i.e. couple (h,h), and a fictitious position for a bistatic couple (h,l) with h ≠ l. Therefore we consider a formation of equivalent sensors characterized by different off-nadir angles $\vartheta_n = \vartheta_{hl} = (\theta_h + \theta_l)/2$ and azimuth angles $\varphi_n = \varphi_{hl} = (\phi_h + \phi_l)/2$ with n = 1,…, N (N = 9 when S = 4, as depicted in Figure 4-5).

Signals received by all the equivalent sensors (therefore both monostatic and bistatic acquisitions) can be properly processed in order to produce an output image with better slant and cross range resolution. This improved image is equivalent to the output image one would achieve if processing the signal received by fictitious monostatic sensor with reference aspect and off-nadir angle equal to ϕ_0 and θ_0 respectively, acquiring for a longer time and transmitting a wider bandwidth with respect to the real sensors in the formation.

As explained in section 4.1, the demodulation of the signals received from each sensor with respect to the common reference results in a relative spectral shift between the different equivalent sensors. Accounting for the scenario in Figure 4-6, the spectral shift (12) of the n-th equivalent sensor can be written as:

$$\Delta f_n \cong f_c \frac{(\theta_n - \theta_0)}{tg(\theta_0)} \tag{13}$$

It is worth noticing that the spectral shift in (13) is defined with respect to the target fulcrum (O in Figure 4-6); this shift can slightly vary with changing the position inside the imaged scene as a consequence of variation of the local incidence angle. This characteristic has to be properly taken into account in the derivation of the 2D-MIMO focusing technique.

The target is modeled as a rigid body consisting in a set of K scatterers. Here we assume the translational motion negligible or already compensated [60] and focus on the rotation motion. Moreover we assume the coherent processing interval T suitable for image formation already selected and limited to some specific value [96], [103]. In first approximation the target is supposed to undergo a 1D rotational motion around the axis Z with a rotation rate equal to ω. This induces for each scatterer in the target and for each equivalent sensor in the formation a linear angular shift in the time aperture, [82], equal to:

$$\zeta_n^k(t) = \zeta_0^k - \varphi_n + \omega(t - t_0) \tag{14}$$

where ζ_0^k is the aspect of the k-th scatterer as observed from the reference aspect ϕ_0.

Based on (13) and (14), the data corresponding to the different sensors are displaced in the polar plane (range frequency & view angle) as shown in Figure 4-7 for the same scenario of Figure 4-6. From Figure 4-7 it is possible to identify N = 9 different acquisitions (the striped ones monostatic while the gray ones bistatic) partially overlapped both in the range frequency and in the view angle domain.
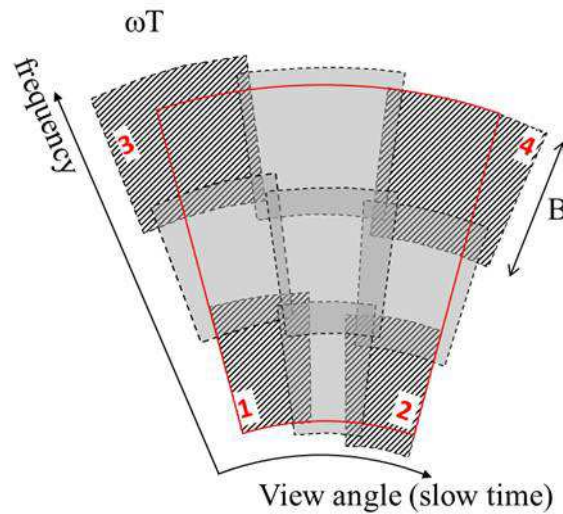

Figure 4-7. 2D-MIMO SAR/ISAR data grids.

Looking at Figure 4-7, since $(\phi_1, \phi_3) \leq \phi_0 \leq (\phi_2, \phi_4)$ and $(\theta_1, \theta_2) \leq \theta_0 \leq (\theta_3, \theta_4)$, it is evident that by coherently processing the data portion identified by the red box it is possible to obtain a range and a cross-range resolution improvement factor γ_r and γ_{cr} equal to:

$$\gamma_r = 1 + \frac{f_c}{B} [\min(\theta_0 - \theta_1, \theta_0 - \theta_2) - \max(\theta_0 - \theta_3, \theta_0 - \theta_4)] \Big/ tg(\theta_0) \tag{15}$$

$$\gamma_{cr} = 1 + [\min(\phi_0 - \phi_1, \phi_0 - \phi_3) - \max(\phi_0 - \phi_2, \phi_0 - \theta_4)] \Big/ \omega T \tag{16}$$

where B is the bandwidth of the transmitted waveform.

When the platforms are symmetrically displaced ($\phi_1 = \phi_3$, $\phi_2 = \phi_4$, $\theta_1 = \theta_2$, $\theta_3 = \theta_4$ and $R_i = R$ for i = 1,...,S) and maximally spaced still assuring a continuous coverage in range frequency and observation angle (i.e. no gaps or overlaps in the polar domain), $\gamma_r = \gamma_{cr} = 3$ for the case S = 4 and a global improvement factor equal to $\gamma = \gamma_r \cdot \gamma_{cr} = 9$ is obtained for the 2D cell area.

4.3. 2D-MIMO SAR/ISAR FOCUSING TECHNIQUE

To focus an image with improved range and cross-range resolutions a 2D processing technique is required to properly combine radar signals acquired from the multiple sensors and to correct the migration through range and Doppler resolution cells. The proposed approach is a decentralized technique for multi-angle SAR/ISAR focusing, based on a modified version of the Polar Format Algorithm (PFA). This decentralized approach first focuses N low resolution ISAR images (intermediate output) and then combines them coherently to achieve the high resolution image (final output). The scheme is sketched in Figure 4-8.

For each branch in the scheme (i.e. for each equivalent sensor, N = 9 branches for the case in Figure 4-6) the processing is organized in the following steps:

1) Fast-time compression.
2) Modified Polar to Cartesian interpolation which removes the range and Doppler migration from single sensor data, co-registers the N low-resolution focused images and scales the axes as all the acquisitions were monostatic.
3) Range profile formation.
4) Slow-time Fourier transform.

At this point the low resolution single-sensor ISAR images LR_n for n=1,..., N are obtained as intermediate output. The following steps refer specifically to the processing of the multi-sensor data:

5) Azimuth distributed processing (here named MIMO-ISAR, following the nomenclature in [82]), which provides M high cross range resolution images. Each one is achieved by means of the appropriate combination of a subset of the N low resolution images.
6) Range distributed processing (here named MIMO-SAR, following the nomenclature in [86]), which properly combines the M high cross-range resolution images to yield the final high resolution image.
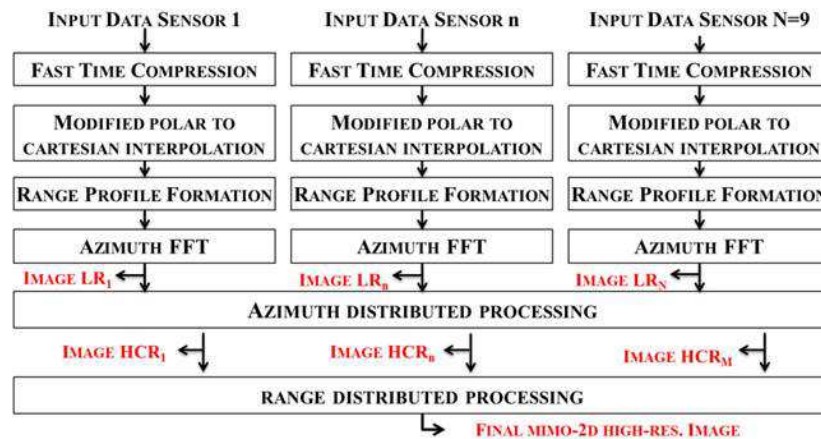
Figure 4-8. 2D-MIMO SAR/ISAR processing scheme.

The MIMO ISAR processing is detailed in Figure 4-9. If the total frequency extent is divided in M intervals, then the goal of azimuth processing is to obtain M high cross-range resolution images HCR_m for m=1,...,M, by separately processing a group of images LR_n, which are selected in the "Low resolution image and data selection" step. In the case N = 9 each subset is always formed by 3 images (a, b and c); they correspond to raw data filling an angular portion of the polar support in Figure 4-7 pertaining to a specific frequency interval, whose central value is relative to a specific off-nadir angle. For the symmetric geometry of acquisition previously described, azimuth distributed processing can be applied separately to 3 subsets of 3 low-resolution images pertaining to the same off-nadir angle (θ_0 or θ_1 or θ_3) and therefore M = 3 high cross-range resolution images are achieved. After compensating the constant phase term depending on the distance between the sensor and the target fulcrum, signals are time shifted in order to synthesize an overall CPI equal to $\gamma_{cr} \cdot T$. Local variations of the off-nadir angle, inside the imaged scene and with the considered sensor, can cause abrupt slow time phase changes; therefore an azimuth phase junction step is applied to each cross-range cell. To this purpose for each cross-range cell the corresponding sub-image is obtained by selecting a proper strip centered on the cross-range under consideration. For each range bin the phase compensation term of sensor a (c) with respect to reference b is extracted from the scalar product between sub-image a (c) and b. After phase compensation only the cross-range cell under test is retained. The azimuth phase junction procedure is repeated for all cross-range cells, then time selection is applied and finally the images are coherently combined. It is worth noticing that time selection is needed when the observations from the different sensors are partially overlapped: this turns out in a γ_{cr} value lower than the maximum bound (3 in our case). However a partial overlap is needed in order to apply the phase junction step: particularly higher overlaps would guarantee the extraction of more reliable values of the phase compensation term thus allowing the achievement of a pulse response of the overall imaging system with the desired characteristics (peak position, mainlobe resolution and side lobe level). Therefore there is an implicit trade-off between resolution gain and quality of the final image. From our experience 10-20% overlap would suffice, thus allowing γcr=2.8-2.6. We point out that the application of time selection requires the knowledge of the target rotation motion. This motion can be very accurately estimated by applying the techniques exploiting multi-sensor data described in chapter 3.
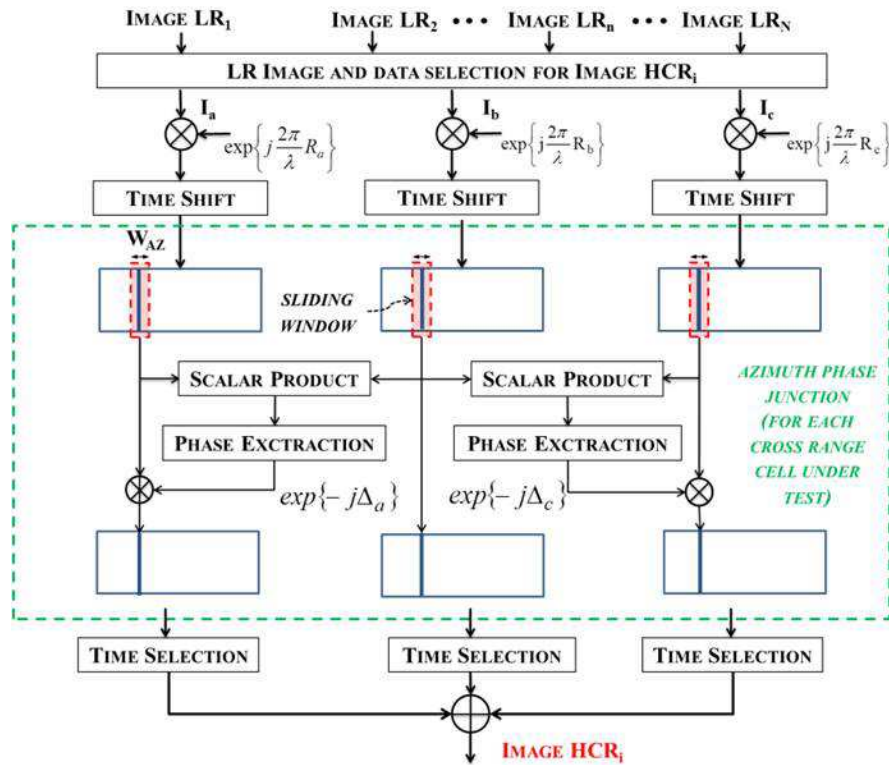
Figure 4-9. MIMO-ISAR distributed processing scheme.

The M high cross-range resolution images from the MIMO ISAR distributed processing feed the subsequent MIMO SAR distributed processing sketched in Figure 4-10. The chain is composed by the cascade of three main steps: a range phase junction stage, a frequency selection stage and coherent combination stage. The MIMO SAR processing performs similarly to MIMO ISAR but works in range direction: almost the same considerations apply. At the output of the range distributed processing the final high range and cross-range resolution image is obtained.

It is worth noticing that the MIMO ISAR or the MIMO SAR processing could be bypassed, exploiting only the images pertaining to equivalent sensors with the same aspect or grazing angle respectively and achieving images with single dimension resolution improvement.
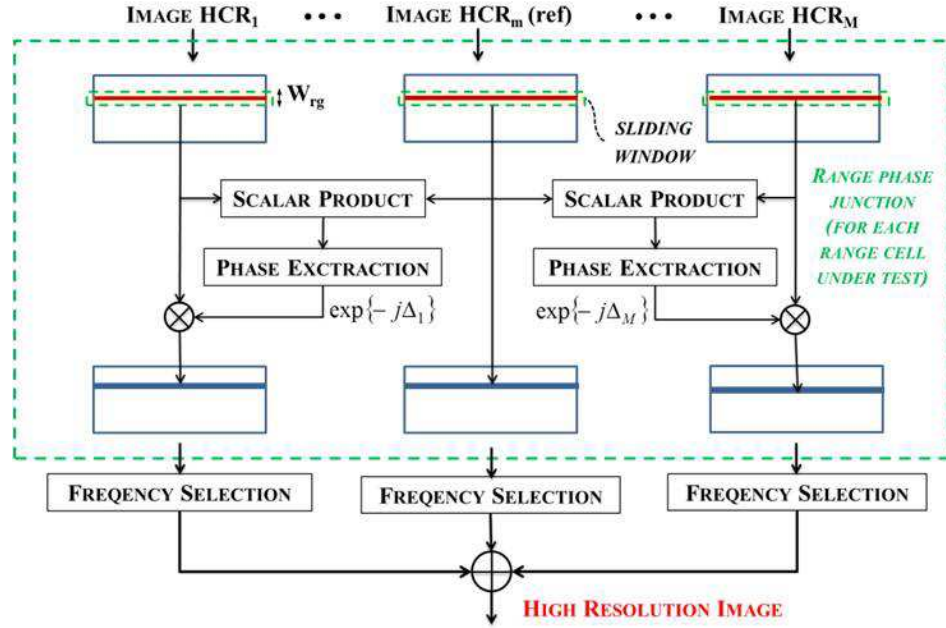
Figure 4-10. MIMO-SAR distributed processing scheme.

4.4. SIMULATED PERFORMANE ANALYSIS

To test the proposed technique we simulated the case of S = 4 X-band (f_c=10 GHz) space-borne (R_0=850 km and θ_0=60°) radar systems working in the symmetric formation case and observing the moving target. In a first case study the target is supposed to rotate around the Z axis with constant rotation rate ω (0.4°/sec). In a second case we considered a target undergoing 3D motion comprising also sinusoidal yaw, pitch and roll with amplitude and frequency equal to A_{yaw}=0.1°, f_{yaw}=0.2 Hz, A_{pitch}=0.1°, f_{pitch}=0.18 Hz, A_{roll}=0.5° and f_{roll}=0.09 Hz respectively. The 3D rotation can be also represented by the rotation vector $\boldsymbol{\omega}=[\omega_h\ \omega_r\ \omega_v]$ described in the *hrv* reference system, [96], representing the point of view of the fictitious monostatic equivalent radar at reference angles ϕ_0 and θ_0, where *r* is the LOS, *h* belongs to the XY plane and is orthogonal to *r*, while *v* is orthogonal to *r* and *h*. So the first case results in $\omega_v{\neq}0$ and ω_h=0 while for the second we have $\omega_v{\neq}0$ and $\omega_h{\neq}0$. Results shown in this paper were obtained by using a set of almost orthogonal up-down chirped waveforms as in [82], [104], [105]; obviously their cross-correlation degrades image quality (sidebe level and its integrated ratio) giving rise to a floor of not compressed residual signal. As discussed in [86] strategies based on separation in the slow time domain or in the Doppler domain could be applied to obtain fully orthogonal waveforms. However it is worth to notice that the proposed MIMO-2D coherently combines the images from the different equivalent sensors and thus provides a gain in peak power equal to the number of integrated sensors: this allows a further mitigation of the effects of the not compressed floor.

First of all an analysis of the achievable MIMO-2D, MIMO-ISAR and MIMO-SAR Point Spread Functions (PSFs) has been conducted. Figure 4-11.a and b show respectively the cross-range and cross-range PSFs compared to the SS conventional PSF, for the 1D rotation case; the MIMO-2D PSF achievable if the considered waveforms were perfectly orthogonal (labeled as MIMO-2D$_{ideal}$) is also

reported for comparison. Figure 4-11.c shows the corresponding -4 dB iso-level curves. As it is apparent from results in Figure 4-11 the MIMO-2D allows the achievement of a considerable improvement in both the range and cross-range resolutions independently on the motion characteristics of the target. In particular we obtain a range resolution of about 1.5 m in the SS (transmitted bandwidth B = 100 MHz) and MIMO-ISAR cases and of 58 cm in the MIMO-SAR and MIMO-2D cases. On the other hand a cross-range resolution of 1.2 m is achieved in the SS (synthetic aperture time 1.8 sec) and MIMO-SAR cases and of 46 cm in the MIMO-ISAR and MIMO-2D cases. Specifically we obtain the improvement factors γ_r = 2.60, γ_{cr} = 2.59 and γ = 6.74. We point out that in both frequency and view angle domains overlaps have been considered (η_f=Δf/B=0.8 and η_T=|ϕ_1|/(ωT)=0.79) reducing the resolution improvements factors with respect to the maximum theoretical values but allowing the phase junction steps to work properly. Finally we notice that results in Fig. 6 confirm our previous observations concerning the use of not perfectly orthogonal waveforms. In particular, slight asymmetries in the secondary lobe region of the range PSF, Figure 6b, can be observed which could be removed by using fully orthogonal waveforms. This can be easily proved by comparing the MIMO-2D to the ideal MIMO-2D.
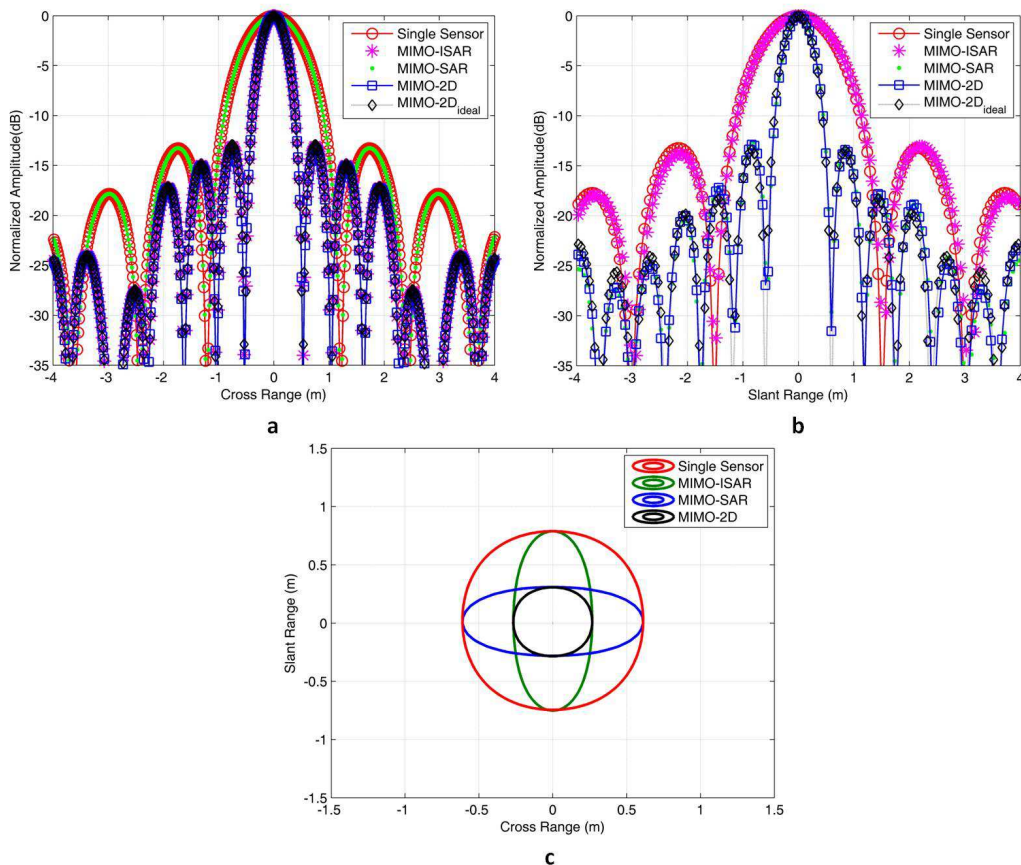

Figure 4-11. Point Spread Function – a) Cross-range, b) Slant-Range, c) -4 dB iso-level curves.

The case of an extended target is then considered. Figure 4-12 shows the image of a grid of point-like scatterers interested by 1D rotation, with the same parameters of the previous case. Two clusters of four scatterers are placed at distances such that they cannot be separated with the conventional SS

technique, Figure 4-12.a (with white "×" representing the true scatterers positions); moving to MIMO-ISAR case, Figure 4-12.b, we observe the improvement of the cross-range resolution which allows us to better resolve in cross-range but not in range, while the reverse situation is observed for MIMO-SAR, Figure 4-12.c. Finally, in the 2D-MIMO case, Figure 4-12.d, we can see the improvement of both range and cross-range resolutions which allows us to separate the four different scattering centers. These results are further confirmed by the inspection of Figure 4-12.e and f showing the range and cross range cuts of the scatterers around the scene center.
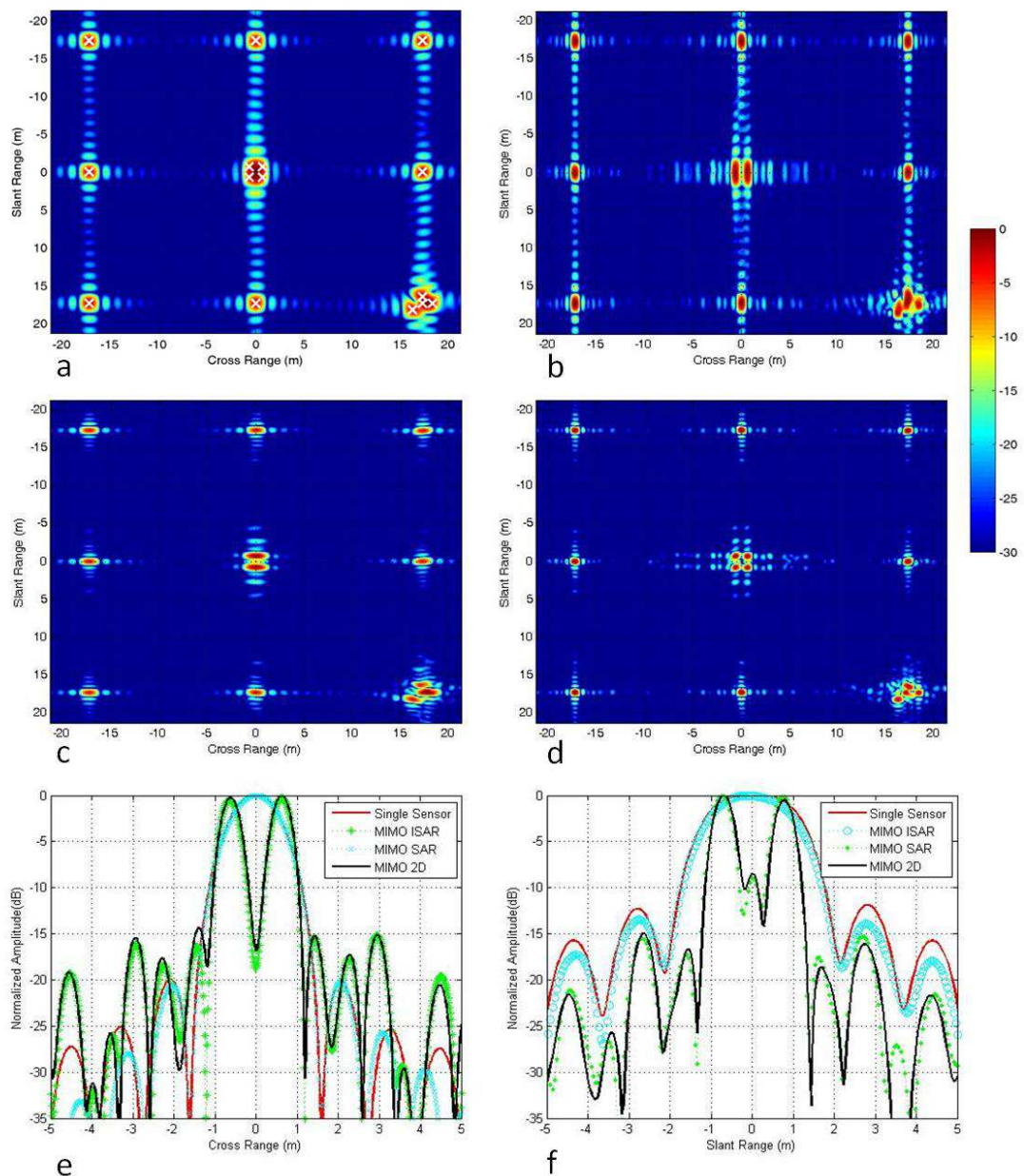
Figure 4-12. Grid of point-like scatterers – a) Single Sensor, b) MIMO-ISAR, c) MIMO-SAR, d) 2D-MIMO images; e) Cross-range and f) Slant range cuts comparison.

A more complex target is considered in Figure 4-13 showing a ship with length about 120 m and different levels of superstructure. In this case a transmitted bandwidth of 33.3 MHz and an aperture time equal to 0.6 s have been considered being the remaining parameters as above. For such case we have a slant range resolution of 4.5 m in the SS case and 1.78 m in the 2D-MIMO, while in the cross-range we move from 3.58 m to 1.38 m. We observe how the resolution increases so that scattering centers not resolvable with SS (Figure 4-13.a), MIMO ISAR (Figure 4-13.b) or MOMO SAR (Figure 4-13.c) can be resolved via MIMO-2D (Figure 4-13.d).
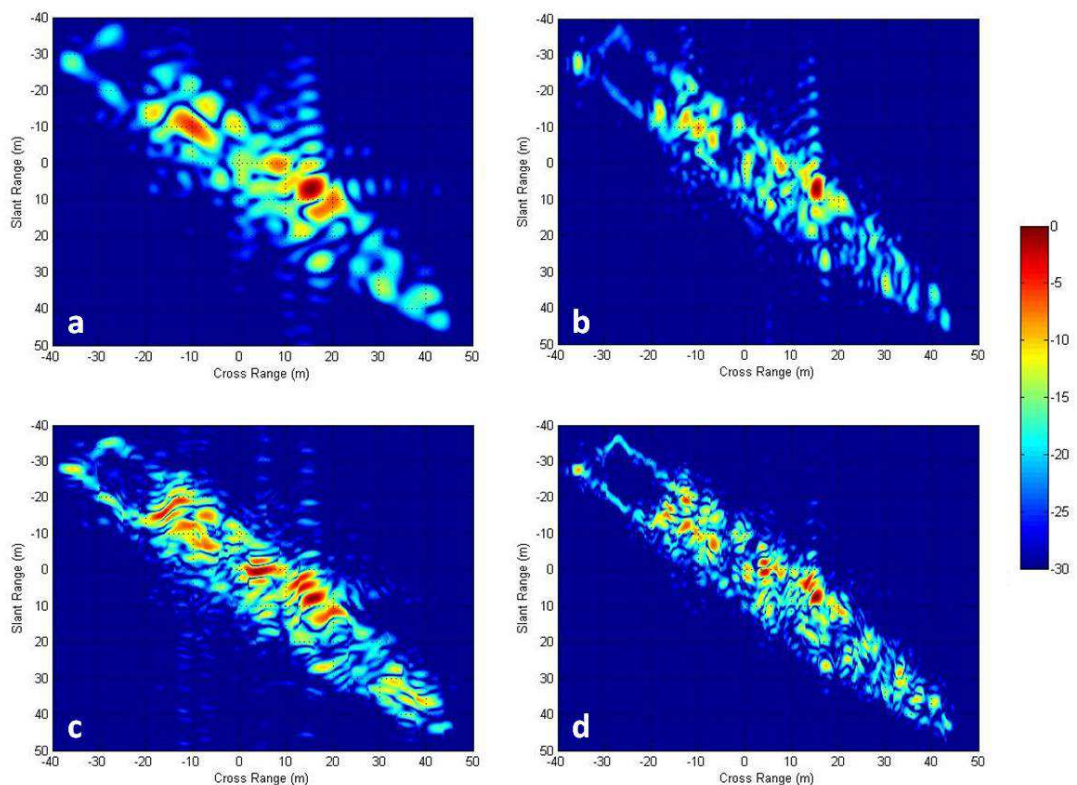
Figure 4-13. Ship target model – a) Single Sensor, b) MIMO ISAR, c) MIMO SAR, d) MIMO 2D.

The case of 3D rotation is then considered. Specifically, observing that 3D rotation motion impacts on the cross-range/Doppler domain and that scatterers belonging to the superstructure are the most sensitive to the presence of pitch and roll motions, [96], Figure 4-14 shows the Doppler PSF for the scatterer representing the apex of the mainmast of the above ship target. In this case MIMO-2D focusing technique has been applied matching the parameters to the vertical motion, [84], and to allow the comparison the PSFs have been centered on the same Doppler frequency value. The obtained results are also compared to the results achievable in the same conditions but setting to zero pitch and roll. We have to notice that similar results are achieved for the two cases of 3D and 1D rotation motions and the resolution gain is maintained also in the 3D case even if with a slightly different value since not only yaw, but also pitch and roll contribute to the vertical component of the motion.

It is worth notice that (in deriving the system and analyzing its performance) we have assumed all the imaged scatterers behaving as ideal point scatterers with same amplitude and phase for all the

exploited observations. Obviously this hypothesis is not always verified, especially when experiencing a wide change in the view angle. However our focus is on cases implying quite limited changes of the observation angle over the different acquisitions (i.e. medium resolution) so that we can assume the target to be in the pseudo-monostatic region. Obviously a moderate degradation of the image quality is expected if the operative conditions do not comply with the previous assumptions.
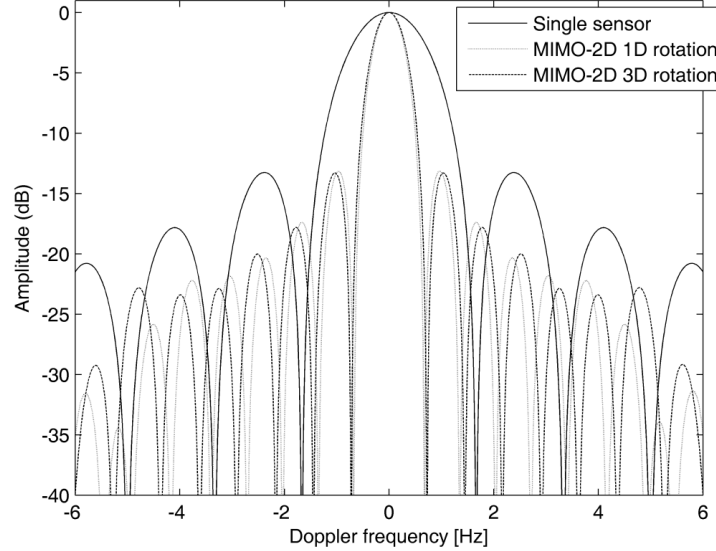

Figure 4-14. Comparison of Doppler PSF in presence of 1D and 3D rotation motion.

Finally to support the practical application of the proposed technique, we analyze the performance robustness in presence of disturbances causing deviations of the actual position of the platforms with respect to the nominal (desired) positions. Particularly we consider the position of each platform in the XYZ reference system as a random variable uniformly distributed in a sphere, with center on the nominal position and radius r. Different platforms are interested by independent perturbations. The performance robustness is investigated by analyzing the mean value (100 independent trials) of resolution and sidelobe level (in dB) of range and cross-range PSFs achieved by matching the focusing to the nominal geometry. Results are reported in TABLE 4-1. As evident the resolution improvement is basically maintained under non ideal conditions (theoretical $\Delta R = 0.58$ m and $\Delta CR = 0.46$ m), while a small degradation is observed for the Side Lobe Ratio (SLR). The considered robustness is obviously also a consequence of: (i) spaceborne geometry causing limited perturbations on the off-nadir and aspect angles even in presence of not negligible perturbations on the positions (more stringent requirements to be expected in the airborne case); (ii) overlap in the polar plane between the different acquisitions; (iii) presence of the phase junction step able to counteract the effect of disturbances inducing phase discontinuities.

r	ΔSR [m]	SLR SR [dB]	ΔCR [m]	SLR CR [dB]
5 Km	0.60	-12.94	0.47	-13.07

TABLE 4-1. MIMO 2D PERFORMANCE UNDER NON IDEAL CONDITIONS.

4.5. CONCLUSIONS

In this chapter a technique has been proposed to jointly increase the range and cross-range resolution of radar images of rotating targets. A 2D-MIMO SAR/ISAR system has been configured, consisting in a formation of platforms with proper cross-track and along-track displacements, each carrying an active radar system. A distributed focusing technique for the joint elaboration of the monostatic and bistatic acquired data has been developed and tested against simulated datasets. Obtained results show that the achievable images can have a 2D resolution cell improved of a factor up to 9 when a formation of four platforms is considered. The flexible use of such a constellation of platforms could allow the improvement of resolution in range or cross-range or in both directions on the basis of the specific needs and could be useful for example for non-cooperative ship target imaging.

5. ISAR WHILE-SCAN MODE FOR COASTAL SURVEILLANCE

The intense human activity affecting the coastal environment has made the coastal surveillance one of the main topic of the last years. The detection and identification of ships navigating in the coastal area is essential in order to prevent maritime accidents and to take countermeasures against piracy activities. Usually, coastal radars are used for the detection of vessels, while the ship classification is obtained by Automatic Target Recognition (ATR) procedures, that largely use ISAR images.

As well known the capability of obtaining an Inverse Synthetic Aperture Radar (ISAR) image of a ship is highly dependent on the ship motion conditions induced by the sea state [91]. Ship motion can be divided into rotation and translational motion, and usually ISAR images showing the ship on different image projection planes (such as top, side or mixed views of the ship) are obtained by properly exploiting the ship rotation around its centre of gravity [60].

In the case of low sea state the ship rotation motion can be not sufficient for the formation of an ISAR image with acceptable resolution. In chapter 2 we showed that the proper exploitation of the data acquired by multiple radar sensors allows to achieve a much wider observation angle than for a single aperture, and this corresponds to increase the overall Doppler bandwidth of the combined received signal, resulting in ISAR images with higher resolution (Distributed ISAR (D-ISAR)). In the case of a very low sea state the yaw, pitch and roll motions induced by the waves on the ship could be negligible for the formation of the ISAR image. In this case it is of interest to develop an ISAR mode relying on the target translation only. In particular, this paper aims at defining and studying an ISAR while-scan mode for coastal surveillance based on the exploitation of the signal transmitted by the coastal radar over successive scans.

The use of the translational motion of the ship as source of the needed Doppler gradient that makes the cross resolution possible imposes the need of a high synthetic aperture time in order to achieve an ISAR image with reasonable resolution. The usual values of scan rates of a coastal radar designed for detection purposes give rise to sampling frequencies considerably lower than the Doppler bandwidth, making the imaging impossible. The sampling frequency of the system can be increased locating multiple passive sensors properly spaced. Properly combining the signals received from the multiple passive devices we can obtain a sampling of the signal reflected from the target much more dense, such that a well focused image can be obtain. It is worth noticing that in the proposed system the diversity in the angles of the target observations has a different aim with respect to the D-ISAR technique. In the D-ISAR technique the angular diversity is exploited in order to increase the Doppler bandwidth, whereas here is used to synthesize a greater azimuth sampling frequency of the system allowing to respect the Nyquist rule.

As will be detailed in the chapter, it is expected that the number of the required passive devices depends on the ratio between the needed sampling frequency and the sampling done by the coastal surveillance radar according to the scan rate value, while their location is expected to depend on the desired cross range resolution.

5.1. ISAR WHILE-SCAN CONCEPT

The operative condition is given by a coastal surveillance radar equipped with a rotating antenna with a scan rate equal to ω_a deg/s and an azimuthal beamwidth Θ_a deg monitoring the coastal vessel traffic and used as illuminator of opportunity; N passive devices are located near the coast receiving the reflected signal. A pictorial view of this scenario is depicted in Figure 5-1.
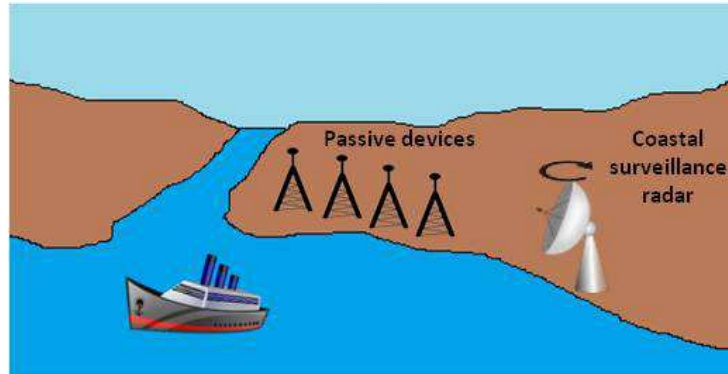

Figure 5-1. ISAR while-scan operative condition.

As well known [60], the cross range resolution that is achievable with a conventional ISAR processing is equal to:

$$\Delta_{cr} = \frac{\lambda}{2\Delta\theta} \tag{1}$$

with $\Delta\theta$ being the global variation of the view angle of observation of the individual point target and λ the wavelength. At a given distance R_0, $\Delta\theta$ depends on the tangential velocity V_t and the dwell time T_{obs} (see Figure 5-2):

$$\frac{L_s}{2} = R_0 tg\left(\frac{\Delta\theta}{2}\right) \Rightarrow \Delta\theta \cong \frac{T_{obs}V_t}{R_0} \tag{2}$$
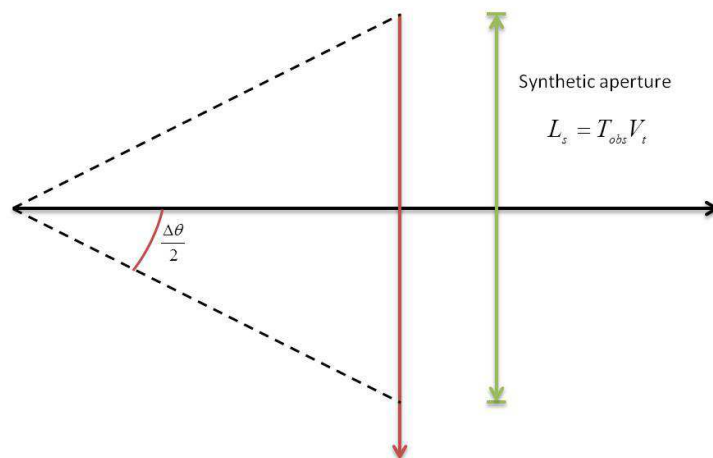
Figure 5-2. Evaluation of the global variation of the view angle during the dwell time.

Considering a single scan T_{obs} is equal to the Time on Target (ToT), given by the ratio between Θ_a and ω_a. Typical values of the ToT for a coastal radar for VTS (Vessel Traffic System) applications are in the order of ms [106], therefore not sufficient to obtain an image with reasonable cross range resolution when only the translational motion of the ship is considered (~10 m/s).

In order to increase the dwell time the target can be observed over M successive scans. Therefore, the overall duration of the acquisition is given by $T_{scan} \cdot M$. From (1) and (2), we have:

$$\Delta_{cr} = \frac{\lambda R_0}{2MT_{scan}V_t} \tag{3}$$

As follows from the Nyquist theorem, the possibility to realize a well focused image is subject to the constraint to have a sampling frequency at least equal to the Doppler bandwidth B_d observed by the radar. The Doppler bandwidth depends on the radial velocity of the target (see Figure 5-3), and it is given by:

$$B_d = \frac{4V_r}{\lambda} = \frac{4V_t}{\lambda}\sin\left(\frac{\Delta\theta}{2}\right) \approx \frac{2V_t}{\lambda}\Delta\theta = \frac{V_t}{\Delta_{cr}} \tag{4}$$
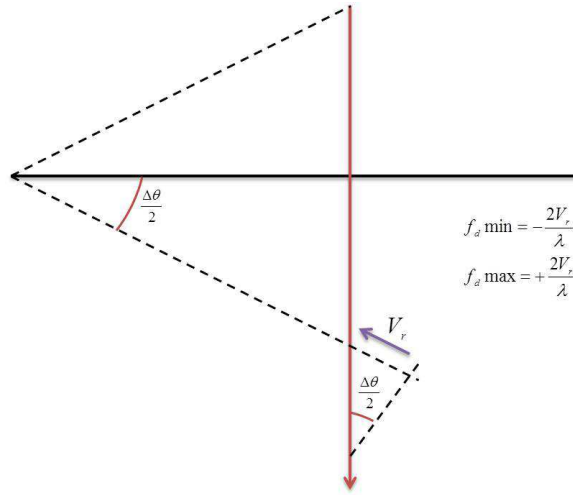
Figure 5-3. Evaluation of the Doppler bandwidth.

Assuming the receiver collecting a single sample during each ToT, the sampling time of the signal as viewed by the single passive device is equal to the duration of the single scan T_{scan} and the Nyquist condition can be written as:

$$B_d \leq \frac{1}{T_{scan}} \tag{5}$$

As example we consider a VTS radar operating in the X-band (λ = 3 cm) with a scan rate of 132°/s and an azimuthal beamwidth of 0.45° observing a ship at the distance of 10 Km moving with tangential speed 5 m/s. Exploiting the single scan observation (i.e. T_{obs} = ToT), the achievable Δ_{cr} is greater than 2 Km, not sufficient for imaging purposes. Exploiting the signal received during 6 scan (i.e. T_{obs} = M·T_{scan}), we are able to achieve a cross range resolution of about 1 m. However , the inequality in (5) cannot be satisfied, since $B_d \approx 5$Hz, while $1/T_{scan} \approx 0.37$Hz.

In order to increase the sampling frequency of the azimuth signal we use a multitude of passive devices. The number N of these receivers must be at least equal o the ratio between the needed sampling time T_c (=1/B_d) and the sampling time due to the scan rate value:

$$N_{min} = \left\lceil \frac{T_{scan}}{T_c} \right\rceil \tag{6}$$

Hypothesizing a constant velocity of the ship, in order to have a uniform sampling of the signal the several sensor have to be equally spaced. Let us consider the N passive devices aligned on the direction of the tangential velocity of the target and Δ be the distance between two sensors. The maximum value of Δ has to be such that two samples have a temporal distance equal to T_c. We recall that a bistatic couple transmitter (TX) – receiver (RX) corresponds to an equivalent monostatic configuration with a fictitious sensor at azimuth angle equal to the bisector of the TX and RX Line-of-Sight (LOS). Assuming the distance between TX and each RX negligible with respect to the radar – target distance we can set Δ_{max} equal to two times the minimum temporal distance between two samples:

$$\Delta_{max} = 2 \frac{T_{scan}}{N_{min}} V_r \tag{7}$$

Substituting (4) and (6) into (7) we found that the maximum value of Δ is equal to $2\Delta_{cr}$.

5.2. TARGET AND SIGNAL MODEL

We consider a ship target modeled as a rigid body in the far field characterized by K dominant scatterers with complex reflectivity constant during the time aperture; its motion can be decomposed as the translation of an arbitrary reference point and the rotation of the body around that point. We consider the case of a very low sea state, such that the rotational motion is negligible and the target is only translating with velocity $\vec{V}$.

For sake of simplicity we consider a planar geometry. The (X,Y) reference system is depicted in ; its origin is located in the target reference point at the instant t_0; the ship follows a straight trajectory with speed $\vec{V} = [V_x, V_y]$ and its kth scatterer is located in $[x_k(t), y_k(t)] = [x_k(t_0) + V_x t, y_k(t_0) + V_y t]$; the transmitter is located in $[x_{TX}, y_{TX}] = [0, -R0]$ and the ith receiver in $[x_{RX,i}, y_{RX,i}] = [x_{offset} + i\Delta, -R0]$, with i = 1,…,N and x_{offset} given by $x_{RX,1} - x_{TX} - \Delta$. We point out that in this geometry $V_x = V_t$.
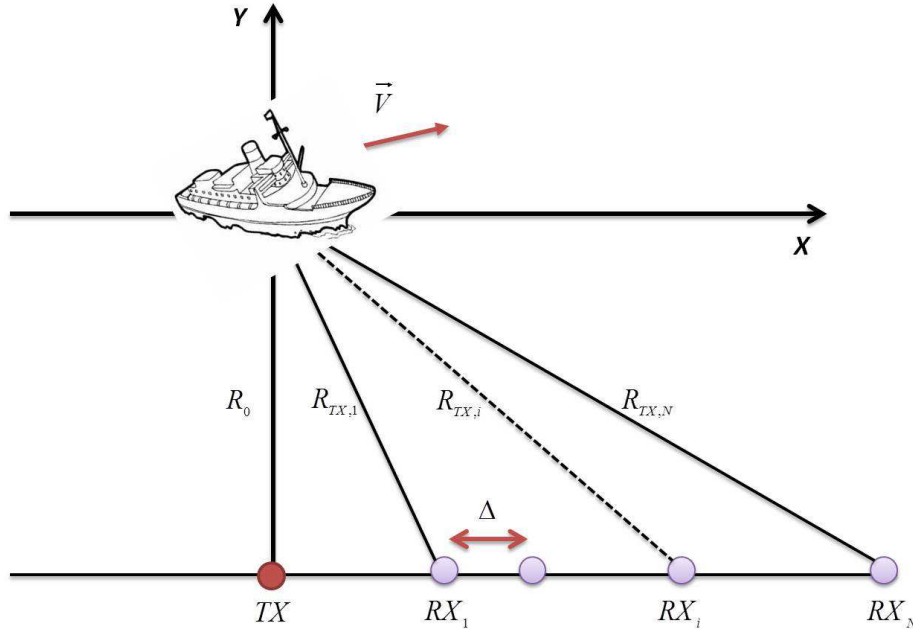
Figure 5-4. ISAR while scan system geometry.

Neglecting the constant complex reflectivity of the scatterer, the signal received from the ith sensor pertaining the kth scatterer in the mth instant of slow time (m = 1,…,M and $t_{m+1}-t_m = T_{scan}$) can be written as:

$$s_{i,k}(t_m) = e^{\left\{-j\frac{2\pi}{\lambda}r_{i,k}(t_m)\right\}} = e^{\left\{-j\frac{2\pi}{\lambda}[R_{TX,k}(t_m)+R_{RX,i,k}(t_m)]\right\}} \tag{8}$$

being $R_{TX,k}$ ($R_{RX,i,k}$) the distances between the kth scatterer and the transmitter (ith receiver):

$$R_{TX,k}(t_m) = \sqrt{\left(x_{TX} - x_k(t_m)\right)^2 + \left(y_{TX} - y_k(t_m)\right)^2} =$$
$$= \sqrt{(x_k(t_0) + V_x t)^2 + \left(R_0 - y_k(t_0) - V_y t\right)^2} \tag{9}$$

$$R_{RX,i,k}(t_m) = \sqrt{\left(x_{RX,i} - x_k(t_m)\right)^2 + \left(y_{RX,i} - y_k(t_m)\right)^2} =$$
$$= \sqrt{(x_{offset} + i\Delta - x_k(t_0) - V_x t)^2 + \left(R_0 - y_k(t_0) - V_y t\right)^2} \tag{10}$$

Assuming $x_{offset} = 0$, $r_{i,k}(t_m)$ for the reference point can be expanded in Taylor series at third order as:

$$r_{i,0}(t_m) \approx \sigma_{i,0} + \alpha_{i,0}t_m + \beta_{i,0}\frac{t_m^2}{2} + \gamma_{i,0}\frac{t_m^3}{6} \tag{11}$$

being

$$\sigma_{i,0} = R_0 + \sqrt{(i\Delta)^2 + R_0^2} \tag{12}$$

$$\alpha_{i,0} = V_y + \frac{V_y R_0 - V_x i\Delta}{\sqrt{(i\Delta)^2 + R_0^2}} \tag{13}$$

$$\beta_{i,0} = \frac{V_x^2}{R_0} + \frac{V_x^2 R_0^2 + V_y^2 i^2 \Delta^2 + 2 V_x V_y i\Delta R_0}{((i\Delta)^2 + R_0^2)^{\frac{3}{2}}} \tag{14}$$

$$\gamma_{i,0} = -\frac{3 V_x^2 V_y}{R_0^2} - \frac{3(V_x^2 R_0^2 + V_y^2 i^2 \Delta^2 + 2 V_x V_y i\Delta R_0)(-V_x i\Delta + V_y R_0)}{((i\Delta)^2 + R_0^2)^{\frac{5}{2}}} \tag{15}$$

5.3. FOCUSING TECHNIQUE

5.3.1. PSF ANALYSIS

In order to analyze the PSF and illustrate the azimuth processing let us consider the signal received by a point target located in (x_k, y_k) when $t = t_0$ assuming the range migration already compensated. The operative condition is given by the configuration in Figure 5-4 such that $N = N_{min}$ and $\Delta = \Delta_{max}$ according to the tangential velocity of the point target. Each device collects one sample each T_{scan} sec, but during the same scan the two samples collected by two consecutive devices have a temporal equivalent distance equal to $T_c^{eq} = T_c$. By means of an interleaving operation, as depicted in Figure 5-5, we are able to form a vector of the collected samples $s_k[i]$ ($i=1,…,M{\times}N$) taken at sampling period T_c^{eq}. At this point **s**[i] can be compressed by applying an azimuth matched filter with a reference signal given by the complex conjugate of (9) with (n,m) corresponding to the proper receiver and scan indexes, followed by a Fourier transform.

As a study case we consider a point target located on the target fulcrum at a distance of 10 Km when $t = t_0$ moving with velocity equal to 8 m/s with a squint angle $\alpha = 30°$ with respect to the x-axis, resulting in a tangential velocity of 6.93 m/s. T_{scan} is equal to 3 sec and the target is observed for 5 scans, therefore $T_{obs} = 15$ s, and λ is 3 cm. From (2), $\Delta\theta$ is about 0.6°, corresponding to an achievable cross range resolution of 1.43 m; $B_d \approx 4.7$ Hz and therefore $T_c \approx 0.21$ s. We consider $N = N_{min} = 14$ devices, spaced with distance $\Delta = \Delta_{max} = 3$ m allowing to have $T_c^{eq} = T_c$. The result of the compression on this interleaved (Figure 5-5) signal is shown in Figure 5-6: the achievable PSF confirms the capability of the overall system to provide proper cross range resolution.
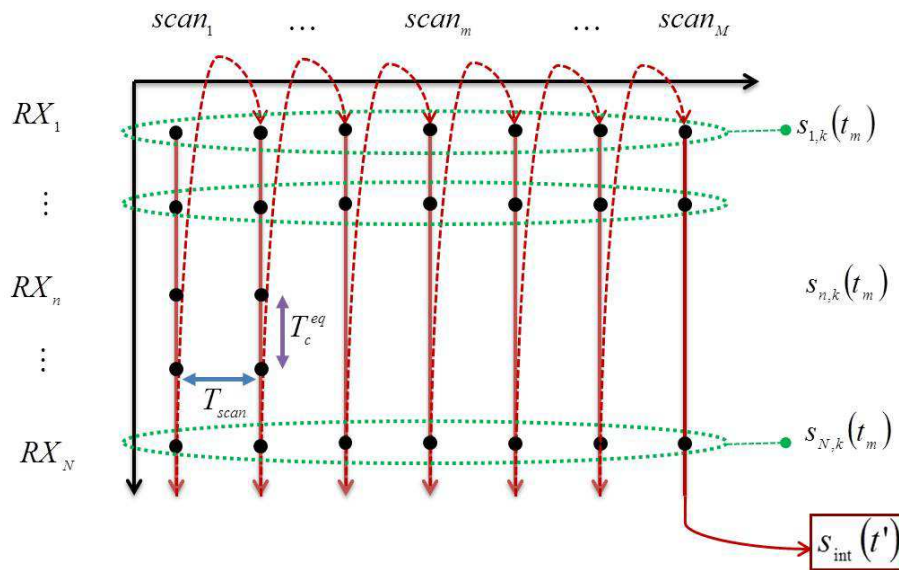
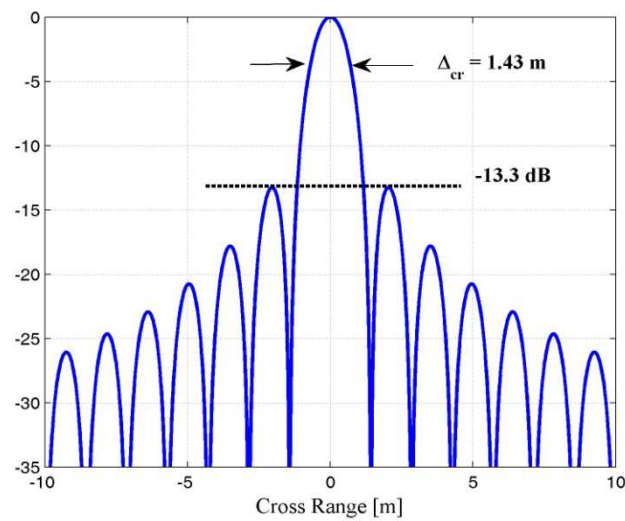Figure 5-5. Data interleaving for the special case of a single range bin.

Figure 5-6. Azimuth Point Spread Function.

Let us now consider the same configuration but a point target moving with a lower tangential velocity. As example, let us consider V_x = 5.6 m/s; therefore, $\Delta\theta \approx 0.48°$ and $\Delta_{cr} \approx 1.79$ m, $T_c \approx 0.32$ s and $T_c^{eq} \approx 0.27$ s. In these conditions, during the single scan, the overall samples collected by the N receivers cover a duration greater than T_{scan}. Therefore the samples collected by the first L receivers during each scan overlap in time with the samples collected by the last (N-L) receivers during the previous scan. To counteract this effect, a proper data selection must be performed: only the data collected by the first L receivers, covering a time slot equal to T_{scan}, have to be used to build the interleaved signal, while the data collected by the remaining sensors can be discarded, see Figure 5-7.

In the previous example L = 11; the result of the compression of the signal in $[x_T(t_0),y_T(t_0)] = [10,0]$ m is shown in Figure 5-8, both with and without applying the data selection (solid blue line and red dotted line, respectively). As we can observe, the proper selection of the data is required for the achievement of the cross-range PSF with the desired characteristics.
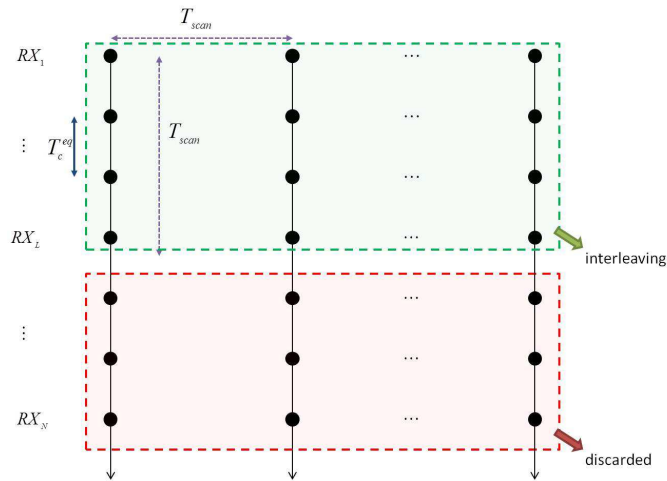

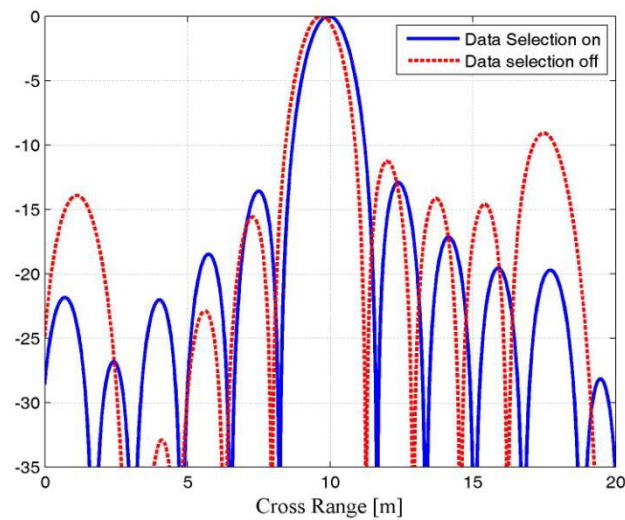Figure 5-7. Data selection for the special case of a single range bin.

Figure 5-8. Comparison of the cross-range PSF with and without applying the data selection.

5.3.2. ISAR WHILE-SCAN FOCUSING TECHNIQUE

The block diagram of the proposed focusing technique is sketched in Figure 5-9. Each branch of the scheme corresponds to the processing of the data received from the n-th sensor, collected in a matrix $\mathbf{S}_n$ of dimension H×M. $s_n[h,m]$ is the h-th fast time sample collected after the digitalization of the signal during the m-th scan. The processing is composed by the following steps:

1. Range Compression, which allows to go in the slant range domain. After the compression, the rows of the N matrices refer to the range domain.
2. Range Cell Migration Correction (RCMC), completely corrected for target fulcrum, achieved in the fast frequency/slow time domain by multiplying the transformed data by:

$$s_{rif}(f_r) = e^{j2\pi f_r \frac{\Delta R_n^0(t_m)}{c}} \tag{16}$$

being f_r the fast frequency and $\frac{\Delta R_n^0(t)}{c}$ the time delay due to the variation of the distance between the target fulcrum and the central sensor of the receiving array evaluated in $t = t_0$ and the distance between the target fulcrum and the n-th receiver evaluated in t_m. Finally, an Inverse FFT is applied.

3. Azimuth Dechirping, achieved as explained in sub-section 5.3.1 according to (11)-(15). We point out that the contribution of the term $\gamma_{n,0}$ may be negligible only if small enough synthetic aperture lengths are considered.

By following the above procedure, N matrices **A**$_n$ are achieved, whose columns contain the compressed range samples and the rows the phase history of a range bin after the compensation of the phase referring to the reference point.
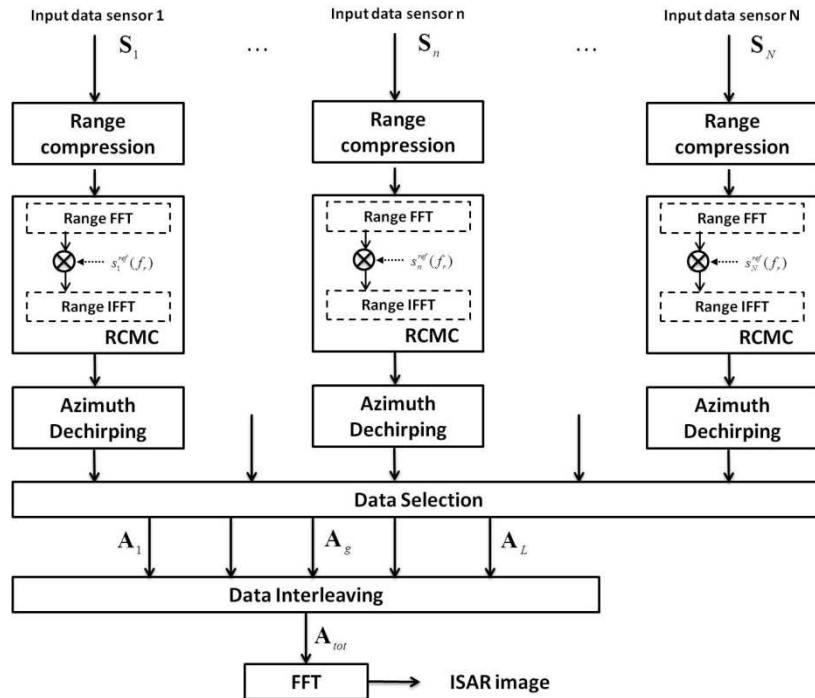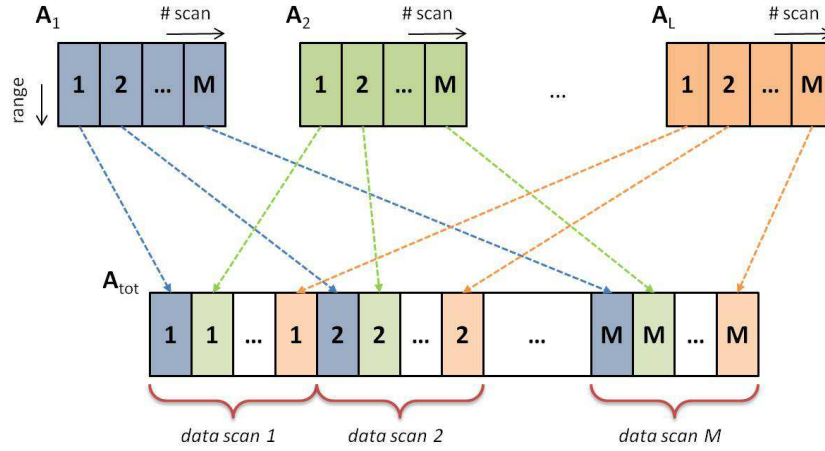

Figure 5-9. ISAR while-scan processing scheme.

Figure 5-10. Data interleaving.

At this point the data of the several sensors have to be properly combined. First of all, a Data Selection (DS) step is applied: as explained in the previous section, for each scan we have to use only the data of the first L devices such that a time slot equal to T_{scan} is covered, in order to avoid time overlapping of the data. Therefore, only the first L $\mathbf{A}_n$ matrices are used, while the remaining are discarded.

After the DS, the $\mathbf{A}_g$ (g=1,…, L≤N) output matrices have to be properly combined by the interleaving as depicted in Figure 5-10: the data are rearranged in a matrix $\mathbf{A}_{tot}$ with size H×ML, being the m-th H×L block composed by the columns of the $\mathbf{A}_g$ matrices corresponding to the m-th scan. By applying this procedure, each row of $\mathbf{A}_{tot}$ corresponds to a range bin observed in ML consecutive instants of slow time.

Finally, a Fourier Transform is applied to go in the final image domain.

5.4. SIMULATED RESULTS

We consider a VTS radar operating in the X-band (λ = 3 cm) with a scan rate equal to 132°/s and an azimuthal beamwidth of 0.45° and transmitting a chirp signal with bandwidth B = 22 MHz [107].

The system observes targets located at a distance of 10 Km from the transmitter when t = t_0, for a maximum dwell time equal to 6 scans. The maximum considered velocity for the target is 10 m/s. Therefore the maximum achievable Δ_{cr} is 0.91 m, (3), and the minimum number of passive device to place is 30, (6), that are located with x_{offset} = 0 and Δ = Δ_{max} = 1.82 m, (7). To be noticed that, for practical applicability, the number of required sensors can be considerably reduced by increasing Δ_{cr}. We chose here a demanding case with Δ_{cr} = 0.91 m to highlight the effectiveness of the proposed concept and processing.

As first study case we consider a distributed target given by a grid of 9 point scatterers (see Figure 5-11) interested by a translational motion $\vec{V}$ = [10,0] m/s. The N devices acquired the echoes during M scans of the antenna. Since the tangential velocity of the target is just equal to the maximum possible velocity for the considered scenario, the data received by the all of the passive devices are processed and the DS block of the processing scheme could be by-passed.
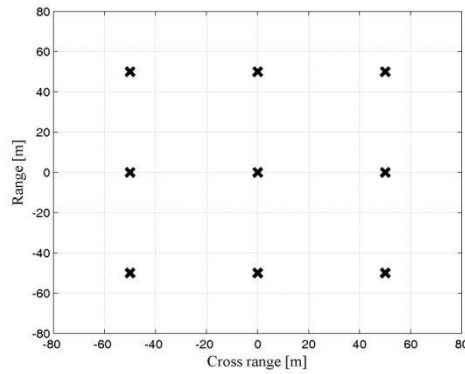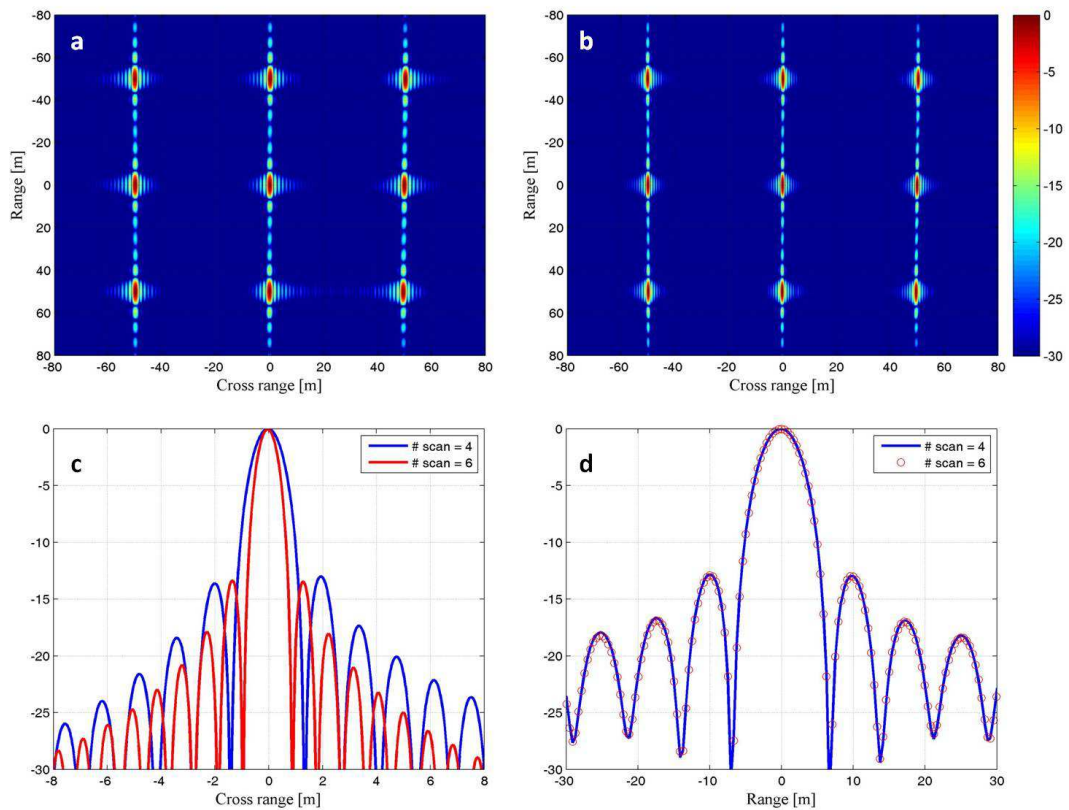
Figure 5-11. Grid of point scatterers.

Figure 5-12. ISAR images of the grid of point scatterers – a) 4 scans, b) 6 scans, c) Cross-range cuts, d) Range cuts.

Figure 5-12-a.b shows the ISAR images of the grid when 4 and 6 scans of the antenna are considered, respectively. As we can observe, increasing the number of scans we are able to improve the azimuth resolution of the images; this is confirmed by the cross range cuts around the central point in Figure 5-12.c: specifically, we found Δ_{cr} = 1.36 m and Δ_{cr} = 0.91 m in the two cases. As obvious, the slant range resolution, Figure 5-12.d, is fixed by the transmitted bandwidth.

The case of a simulated ship target composed by many point scatterers and with different superstructure levels is then considered. We considered the same geometry as in the previous study

case and 6 scans of the coastal radar. The ship moves in direction α = 20° with respect to the sensor alignment, but different velocities are considered, as reported in TABLE 5-1, resulting in different values of L.

Figure 5-13 shows the achieved ISAR images for the different target velocity cases. From these figures we can appreciate the effectiveness of the proposed technique in providing high-quality top-view images of vessels. We can also observe the improvement of the achieved cross range resolution with the increase of the processed synthetic aperture.

Case	V_t [m/s]	L	Δ_{cr} [m]
a	5	15	1.82
b	7.5	23	1.37
c	10	30	0.91

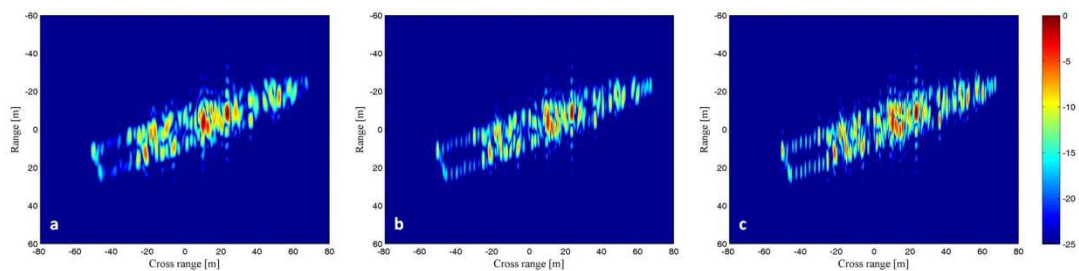TABLE 5-1. SHIP TARGET TANGENTIAL VELOCITY.

Figure 5-13. ISAR images of a ship target with tangential velocity 5 m/s (a), 7.5 m/s (b) and 10 m/s (c).

5.5. CONCLUSIONS

The aim of this chapter has been the assessing of a novel ISAR while-scan mode technique for coastal surveillance purposes. The technique exploits the signal transmitted by a coastal surveillance radar, having as main objective the detection of vessels navigating in the area under observation, and that is not otherwise involved in the imaging activity. A passive (receiving only) array located on the coast is exploited to form a physical aperture, that combined with the translational motion of a ship target produces a synthetic aperture allowing to achieve ISAR images. The relationships between the parameters of the VTS radar and the array configurations have been derived. An ad-hoc focusing technique has been proposed, able to combine the signal received by the several sensors of the array over successive scans of the coastal radar in order to form a final ISAR image.

The simulated performance analysis confirmed the effectiveness of the technique to provide radar images of ships with suitable resolution; the cross range resolution may be increased by integrating signal receptions over an increasing number of scans; also, because of the exploitation of the translational motion of the ships to produce the Doppler gradient, the achievable ISAR images are top-views of the ship, that can be properly exploited for vessels classification and identification purposes [93], thus helping ATR procedures for coastal surveillance.

6. MULTISTATIC GNSS-BASED SYNTHETIC APERTURE RADAR

Over the last years the Bistatic Synthetic Aperture Radars (BSARs) have been the focus of increasing research activity, [1][3]. A BSAR system operates with distinct spatially separated antennas for signal transmission and echo reception. Such a spatial separation has several operational advantages, which will increase the capability, reliability and flexibility of future SAR missions. Although the basic operation of all BSAR system is much the same, the differences are mainly as a consequence of the geometry employed. Several bistatic configurations have been proposed, involving different combinations of transmitters and receivers on moving (spaceborne, airborne): e.g. the transmitting and receiving platforms can be carried by two or more satellites (as the German TanDEM-X mission [51]), the transmitter can be mounted on an airborne platforms and the receiver on another one, [55], [56], or on the ground [108].

The examples of BSAR systems reported in [51], [55], [56] and [108] refer to cases of a cooperative transmitter. Another possibility is to configure a passive system using satellite illuminators as transmitters of opportunity. It is possible to use other radar transmitters [109], [110], transmissions from audio-video broadcasting [68], navigation or communication satellites [69]. The work presented in this chapter is dedicated to the case of such a system using Global Navigation Satellite System (GNSS) as transmitters, such as GPS, GLONASS or the forthcoming Galileo and Beidou. The feasibility of this system has been experimentally demonstrated for both moving and stationary receivers, [70], [71], however here we consider the stationary receiver case only.

As transmitters of opportunity, GNSS present some drawbacks compared with other satellite transmitters. The main one centers on their low-power budget. For example, Direct Satellite TV (DVB-T) broadcasting transmitters introduce about 20 dB stronger power flux density near the earth surface when compared with GNSS. On the other hand, long dwell times are possible. Another advantage is the relatively simple synchronization. This follows from the fact that navigation signals were designed to be optimal for remote synchronization, [69].

The main motivation for using GNSS as transmitters lies in the structure of the GNSS constellations. At any time of the day, there are 6-8 satellites in a single constellation (24-32 when all 4 GNSS systems are fully operational), illuminating any point on Earth from different angles. All of these signals can be received and processed separately or jointly using a single receiver, essentially forming a multi-static radar system. This feature has a number of advantages. First of all, it provides the potential for persistent area monitoring anywhere in the world. In addition, images obtained from the same scene, but different satellite illumination angles, may aid in terrain classification [111]. Furthermore, images obtained from different satellites may be fused to increase the amount of information in a given area.

Despite the low power budget, images with a suitable signal-to-noise ratio (SNR) and azimuth resolution (3-4m) can be obtained by considering long dwell times on target (typically 4-5 minutes). However, the range resolution is defined by the GNSS ranging signal bandwidth. For example, the Galileo E5bQ signal has a bandwidth of approximately 10 MHz (perhaps the broadest bandwidth GNSS signal), offering a resolution of 15m in the quasi-monostatic case. Furthermore, range resolution degrades rapidly as the bistatic angle increases [3]. In previous research , it was experimentally shown that using very long dwell times (10 mins or more) provides some improvement in range resolution as well as azimuth, however the improvement factor was not

sufficiently high. Therefore, as a bistatic system, GNSS-based SAR was found appropriate only for applications where a coarse resolution is acceptable.

This work considers the non-coherent combination of multiple BSAR images to provide multi-static imagery with improved resolution. In the first part we consider the study of the Multistatic Point Spread Function. Some initial considerations on this topic can be found in [112]. The idea is that different bistatic topologies yield Point Spread Functions (PSFs) with different orientations. Therefore, after their combination, a single multi-static PSF (MPSF) can be formed that is the intersection of all the individual PSFs. By appropriate selection of the bistatic topologies we may expect a dramatically improved resolution. The natural extension of this research is to consider the multi-static capability of this technology to explore its full potential on real radar images [111]. Some preliminary results on this topic is presented in section 6.4.

6.1. BISTATIC POINT SPREAD FUNCTION

One of the key parameter of any remote sensing system is the spatial resolution, i.e. the degree to which two scatterers of approximately equal amplitude can be separated in one or more directions, such as range or azimuth [1]. In a BSAR the range resolution ΔR depends on the signal bandwidth B and on the bistatic angle β (i.e. the angle between the transmitter and receiver line of sights), whereas the azimuth resolution ΔA depends on the dwell time on target T_d and the equivalent angular speed ω_E, as well as on the wavelength λ, [3]:

$$\Delta R = \alpha_r \frac{c}{2B \cos\left(\beta/2\right)} \tag{1}$$

$$\Delta A = \alpha_a \frac{\lambda}{2\omega_E T_d} \tag{2}$$

being α_r and α_a shape factors defining the -3dB resolution values.

However, in a BSAR range and azimuth resolutions are not generally orthogonal and therefore do not by themselves specify the two-dimensional bistatic resolution cell. It can be fully described by the Generalized Ambiguity Function (GAF) [3], [113]. It is given by the product of two functions, $p(\cdot)$ and $m_A(\cdot)$. The former is the matched filter output of the ranging signal and the latter is the inverse transform of the normalized received signal magnitude pattern:

$$|X(\mathbf{A},\mathbf{B})| \approx p\left(\frac{2\cos\left(\beta/2\right)\mathbf{\Theta}^T(\mathbf{B}-\mathbf{A})}{c}\right) \cdot m_A\left(\frac{2\omega_E\mathbf{\Xi}^T(\mathbf{B}-\mathbf{A})}{\lambda}\right) \tag{3}$$

where **A** is the vector position of the desired point reflection to be evaluated and vector **B** is an arbitrary position of another reflector in the vicinity of **A**; β is the bistatic angle and $\mathbf{\Theta}$ is a unit vector in the direction its bisector and defining the direction of the range resolution; ω_E and $\mathbf{\Xi}$ are referred to as the equivalent angular speed and the equivalent motion direction (since a monostatic SAR moving in the direction $\mathbf{\Xi}$ with angular speed ω_E would exhibit similar Doppler-based resolution characteristics); $\mathbf{\Xi}$ specifies the direction of the azimuth resolution. The several quantities are

depicted in Figure 6-1, showing the considered bistatic geometry. Since the transmitted signal from a GNSS satellite is a pseudo random code, the matched filter output can be approximated with a triangle function (and therefore $\alpha_r = 0.586$); because of the long dwell times, the received signal magnitude pattern can be accurately modeled as a rectangular function and, as a consequence, $m_A(.)$ is a sinc function (and therefore $\alpha_a = 0.886$).
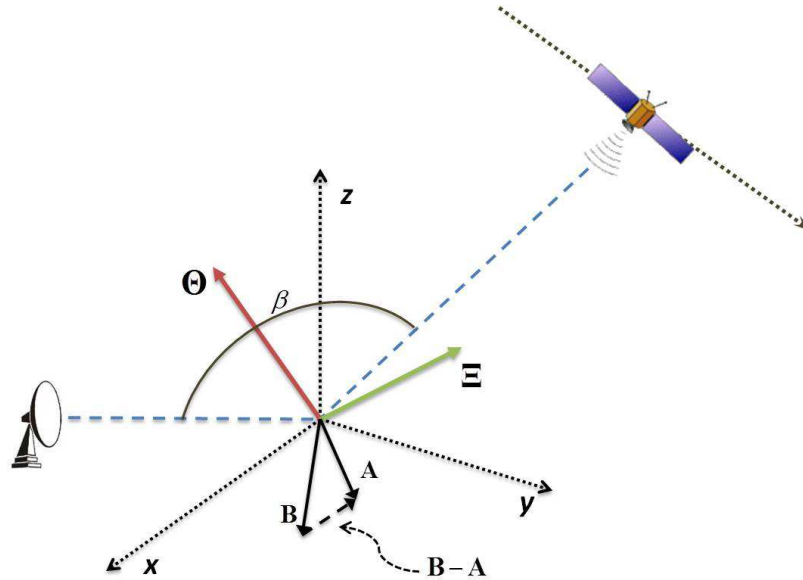

Figure 6-1. Bistatic SAR geometry.

The projection of onto the ground plane gives rise to a resolution cell that is approximately an ellipse (resolution ellipse), that can be evaluated using both numerical [112] and analytical methods. In subsection 6.1.1 we propose an analytical method to evaluate it. The resolution ellipse is characterized by its orientation ϕ, being function of the range and azimuth resolutions and the angle γ between their directions projected onto the ground plane, Θ_g and Ξ_g respectively. Since in a bistatic system range and azimuth are generally not orthogonal, γ is different from 90°. It should also be noted that according to their definition [3], the range and azimuth resolutions are indicators of a system's resolution capability, but their directions are not the ones where the spatial resolution is the worst. In the following, the range and azimuth resolution projected onto the ground plane will be indicated as ΔR_g and ΔA_g, respectively.

As example, Figure 6-2 shows a simulated PSF for a scatterer in the scene center and a GLONASS satellite; β is about 71° and ω_E is 0.005°/s; the dwell time is 200 s (therefore a linear trajectory of the satellite can be assumed [114]). The mutual positions of the receiver and the transmitter entail $\gamma \approx$ 34.2° and the orientation of the resulting resolution ellipse is $\phi \approx 122°$. The resolution in the range and azimuth directions is defined along Θ_g and Ξ_g. However, the worst spatial resolution, δ_{max}, is along the major axis (green line) of the PSF while the best one, δ_{min}, is along to minor axis of the PSF, being very close to Ξ_g. For this reason, the parameters δ_{min} and δ_{max} will be used to characterize the spatial resolution capability of this system hereafter, since they represent its bounds. In this example, the area of the resolution cell and the resolutions δ_{max} and δ_{min} (evaluated at the -3 dB contour hereafter) are about 163 m², 44.5 m (while ΔR_g is 25.80 m) and 4.7 m (slightly better than $\Delta A_g = 5.12$ m), respectively.
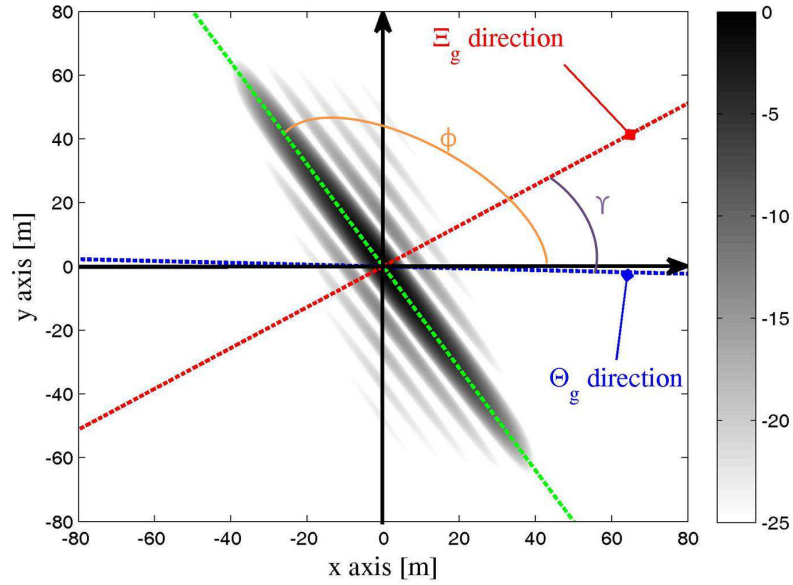
Figure 6-2. Bistatic Point Spread Function.

6.1.1. RESOLUTION ELLIPSE

The difference of vector $(\boldsymbol{B} - \boldsymbol{A})$ in (3) is the target separation vector. When it is normal to the line of Θ it lies along an iso-range contour, while if it is normal to the line of Ξ it lies on an iso-Doppler contour, [3]. Namely:

$$\boldsymbol{\Theta}^T(\boldsymbol{B} - \boldsymbol{A}) = \begin{bmatrix} \theta_x & \theta_y & \theta_z \end{bmatrix} \begin{bmatrix} x_B - x_A \\ y_B - y_A \\ z_B - z_A \end{bmatrix} = 0 \tag{4}$$

$$\boldsymbol{\Xi}^T(\boldsymbol{B} - \boldsymbol{A}) = \begin{bmatrix} \xi_x & \xi_y & \xi_z \end{bmatrix} \begin{bmatrix} x_B - x_A \\ y_B - y_A \\ z_B - z_A \end{bmatrix} = 0 \tag{5}$$

Assuming $\boldsymbol{A} = \boldsymbol{0}$ and the arbitrary vector $\boldsymbol{B}$ lying on the ground plane, from (4) and (5) we can obtained the equations of two straight lines defining the direction of the iso-range and iso-Doppler contours:

$$iso-range\ line{:}\ y = -\frac{\theta_x}{\theta_y}x \tag{6}$$

$$iso-Doppler\ line{:}\ y = -\frac{\xi_x}{\xi_y}x \tag{7}$$

The direction of decreasing of the sidelobes in the two domains is normal to these straight lines. Figure 6-3 highlights the iso-range and iso-Doppler lines for the same study case in Figure 6-2 along with the sidelobes direction.
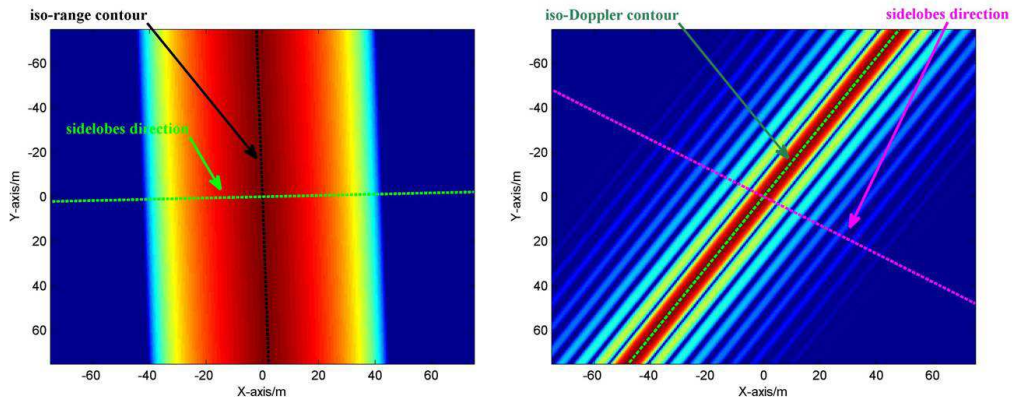
Figure 6-3. Bistatic PSF - a) iso-range contour, b) iso-Doppler contour.

Taking two points at $\pm \dfrac{\Delta R}{2}$ on the range sidelobes direction we can draw the straight lines parallel to the iso-range contour (the same for the azimuth case), as shown in Figure 6-4. Therefore, by multiplying the $p(\cdot)$ and $m_A(\cdot)$ functions we highlight a parallelogram, referred as resolution parallelogram. The resolution parallelogram is shown in Figure 6-7.
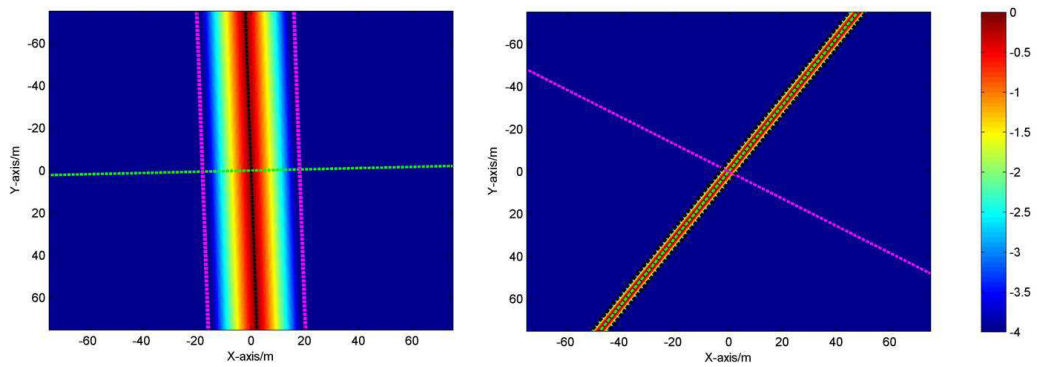

Figure 6-4. Building of the resolution parallelogram: straight lines – a) range, b) azimuth.
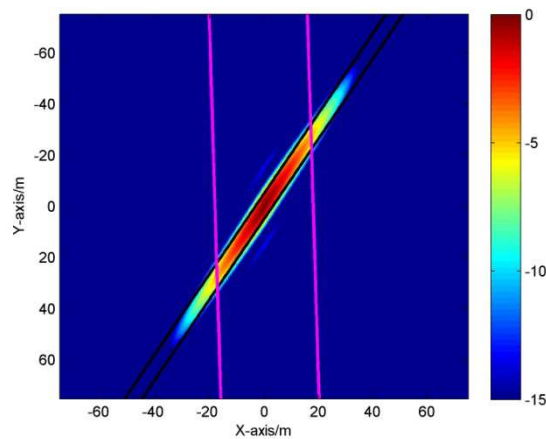
Figure 6-5. Resolution parallelogram.

The resolution ellipse can be derived as the circumscribed ellipse to the resolution parallelogram. The complete analytical derivation of the ellipse is reported in Appendix A. Figure 6-6 shows the comparisons of the theoretical ellipses (magenta plots) and simulated PSF achieved for the PSF in Figure 6-2.
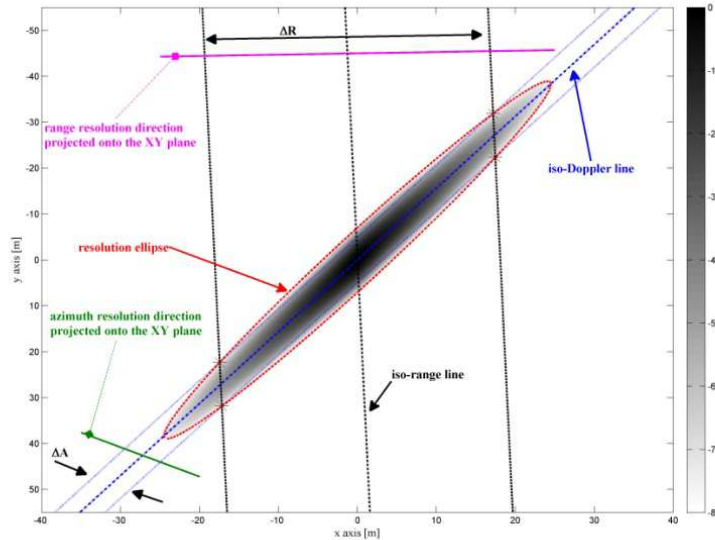
Figure 6-6. Comparison theoretical ellipse (magenta plot) – simulated PSF.

6.2. MULTISTATIC POINT SPREAD FUNCTION

6.2.1. MULTISTATIC PSF USING NON-COHERENT ADDITION

The use of GNSS transmitters entails a signal bandwidth much smaller than a conventional SAR. E.g. GLONASS signals have a bandwidth of 5.11 MHz and therefore the range resolution is 30 m at best (quasi-monostatic case); from (1), the resolution degrades even further as the bistatic angle increases. On the other hand, the use of GNSS makes possible long dwell times, in the order of 5 mins or higher, allowing azimuth resolutions considerably greater than the range ones (3-4 m). Therefore the most critical value of the resolution is in the range dimension, resulting in wide resolution cell areas.

In order to improve the resolution capability of the system we derive a multistatic scheme formed by several bistatic couples, where the same receiver fixed on the ground collects the signals from different GNSS satellites and combines all bistatic images obtained from them into a single, multi-static one. The considered geometry is depicted in Figure 6-7 for the case of two satellites. Different satellite positions and trajectories result in different bistatic PSF parameters: the n-th bistatic PSF (3) is characterized by specific directions of range and azimuth resolutions and different values of the bistatic angle (1) and the equivalent angular speed (2). Different Θ_n and Ξ_n result in a different angle γ_n, whereas different ω_{E_n} and β_n in different values of the range and azimuth resolutions ΔR_n and ΔA_n. Finally, different γ_n, ΔR_n and ΔA_n result in different PSF orientations ϕ_n.

Therefore, a non-coherent combination of the individual PSFs, with their different orientations, results in a multi-static PSF whose resolution cell area is the overlapping segment of the single bistatic PSFs, and therefore may be essentially reduced. As a first step, the non-coherent addition method is considered, as it is a linear operation. We define as Multistatic PSF (MPSF) the non-coherent addition of N ≥ 2 PSFs:

$$\text{MPSF:} \frac{1}{N} \sum_{n=1}^{N} \left| p\left(\frac{2 \cos\left({\beta_n}/{2} \right) \Theta_n^T (\mathbf{B} - \mathbf{A})}{c} \right) \cdot m_A \left(\frac{2\omega_{E_n} \Xi_n^T (\mathbf{B} - \mathbf{A})}{\lambda} \right) \right| \tag{8}$$
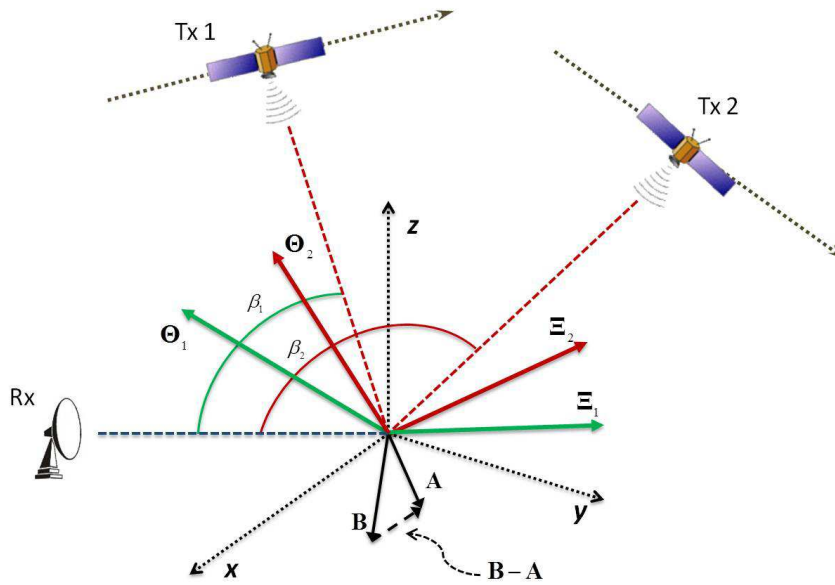
Figure 6-7. Multistatic SAR geometry (N = 2).

6.2.2. MAGNITUDES VS POWERS COMBINATION

We point out that the summation in (8) is performed on magnitudes rather than on powers. In order to explain the reason of this choice, let us consider the same simulated PSF in Figure 6-2 and the one obtained by a rotation of 90 deg. In Figure 6-8 we show the comparison between the resulting MPSF for the magnitudes and powers summations. It is evident that the summation on magnitudes has a better behavior than the one on powers, since the mainlobe is smaller and the sidelobes are lower.

The reason of this can be explained as follows. Let us consider the (i,j) pixel of the PSF projected onto the ground plane, being i the index of the x-axis and j the one of the y-axis; $a_{n_{i,j}}$ is the modulus of the (i,j) pixel of the nth PSF. Considering the combination of two PSF (the case of more than two can be easily extended) the pixel of the resulting MPSF in the power domain is given by A_{ij}^2 when the summation is performed on the magnitudes and by $I_{i,j}$ when it is performed on powers:
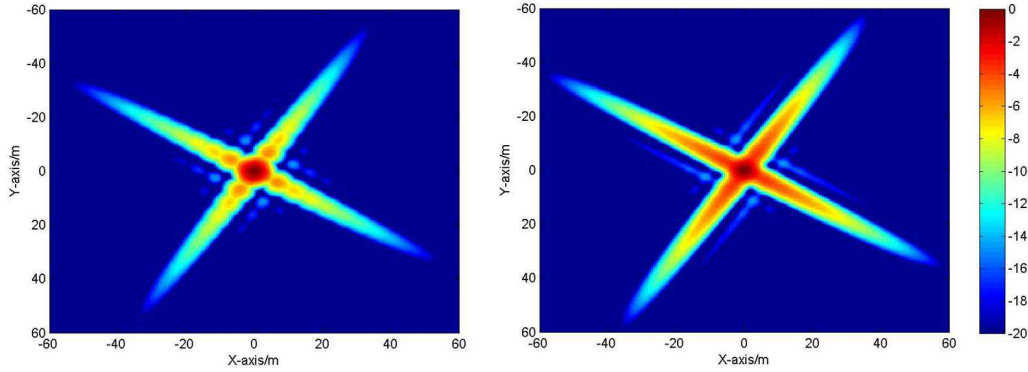
Figure 6-8. Magnitudes vs powers summation – a) summation on magnitudes, b) summation on powers.

$$\begin{cases} A_{ij}^2 = \left(a_{1_{i,j}} + a_{2_{i,j}}\right)^2 = \left(a_{1_{i,j}}^2 + a_{2_{i,j}}^2 + 2a_{1_{i,j}}a_{2_{i,j}}\right) \\ I_{i,j} = a_{1_{i,j}}^2 + a_{2_{i,j}}^2 \end{cases} \tag{9}$$

From (9), and considering that all the values are positive and lesser than 1 (achieved by normalization), follows that:

$$0 < I_{i,j} < A_{ij}^2 \le 1 \Rightarrow -\infty < 10 \log_{10} I_{i,j} < 10 \log_{10} A_{ij}^2 \le 0 \tag{10}$$

Finally, considering the absolute values we find:

$$\left|10 \log_{10} A_{ij}^2\right| \le \left|10 \log_{10} I_{i,j}\right| \tag{11}$$

6.2.3. APPROXIMATED VERSION OF THE MULTISTATIC PSF

One of the features of the single channel PSF represented by the GAF in (3) is that is given by the product of two functions dividing the range and Doppler domain: even if the range and Doppler directions are not orthogonal their domain are still separable. For the MPSF in (8) this cannot be done since the summation and the modulus operator. However, an approximated version of the MPSF is given by:

$$MPSF \approx \bar{p}\bar{m} \tag{12}$$

being:

$$\bar{p} = \frac{1}{N} \sum_{n=1}^{N} p_n = \frac{1}{N} \sum_{n=1}^{N} p\left(\frac{2\cos\left(\beta_n/2\right)\boldsymbol{\Theta}_n^T(\mathbf{B} - \mathbf{A})}{c}\right) \tag{13}$$

$$\overline{m} = \frac{1}{N} \sum_{n=1}^{N} m_{A_n} = \frac{1}{N} \sum_{n=1}^{N} m_A \left(\frac{2\omega_{E_n} \Xi_n^T (\mathbf{B} - \mathbf{A})}{\lambda} \right) \tag{14}$$

In this expression the range and Doppler domains are again separated. This approximation can be easily proven setting $p_n \approx p$. This assumption can be considered true in a wide zone around the mainlobe of the MPSF since the $p(\cdot)$ function has a very wide mainlobe. That is due to the bistatic geometry, the limited bandwidth and the elevation angle of the satellite [3].

6.2.4. INTERSECTING ELLIPSE

In this section we present a mathematical model for evaluating the resolution cell of the MPSF achieved from two single PSF, based again on an ellipse.

As described in section 6.1, the resolution cell of the single PSF can be described by the resolution ellipse. Considering the composition of two different PSF we have two different ellipses intersecting in four points, as depicted in Figure 6-9 for the PSF presented in Figure 6-2 and its rotated by 90° version. These four points describe a parallelogram; therefore it is possible building the ellipse following the procedure for the single PSF ellipse described in Appendix A.

Figure 6-10.a shows the intersecting ellipse superimposed to the MPSF; we can observe the capability of the intersecting ellipse to described the mainlobe of the MPSF; in Figure 6-10.b the -8 dB contour have been plotted, highlighting that the intersecting ellipse describe the mainlobe region at -8 dB.
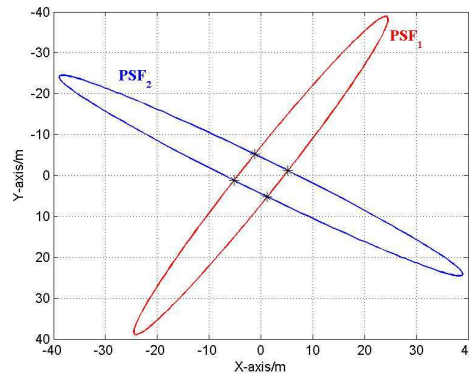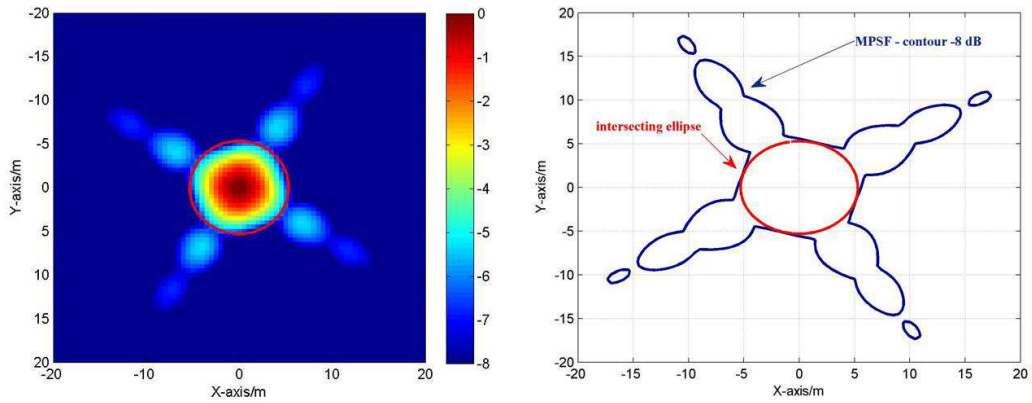

Figure 6-9. Intersecting points

Figure 6-10. MPSF, Intersecting ellipse - a) MPSF with dynamic range [-8 0] dB, b) -8 dB contour vs intersecting ellipse.

6.2.5. SIMULATED RESULTS

Potentially, the non-coherent addition method can be applied to images obtained from different satellites, belonging to different navigation satellite constellations. However, in this analysis satellites from the same GLONASS constellation are considered. Assume N = 3 bistatic geometries formed by GLONASS transmitters and a receiver fixed on the ground. The parameters of the acquisition are reported in TABLE 6-1 along with the parameters of the resulting PSF, shown in Figure 6-11. The worst resolution case has been found for Acquisition 1 (A1), namely the one having the minor angle γ, and the best one for A3, where γ ≈ 90°.

Acquisition	Satellite (Cosmos)	β [deg]	ω_E [deg/s]	T_d [s]	ΔR_g [m]	ΔA_g [m]	δ_{max} [m]	δ_{min} [m]	γ [deg]	φ [deg]	Area [m²]
A1	744	62.24	0.0045	300	22.74	3.98	67.23	3.62	19.46	79.91	189.21
A2	736	102.64	0.0048	250	43.09	4.14	49.10	3.85	59.33	37.64	144.37
A3	732	73.68	0.0048	200	26.74	4.97	26.88	4.83	80.64	-9.54	93.91

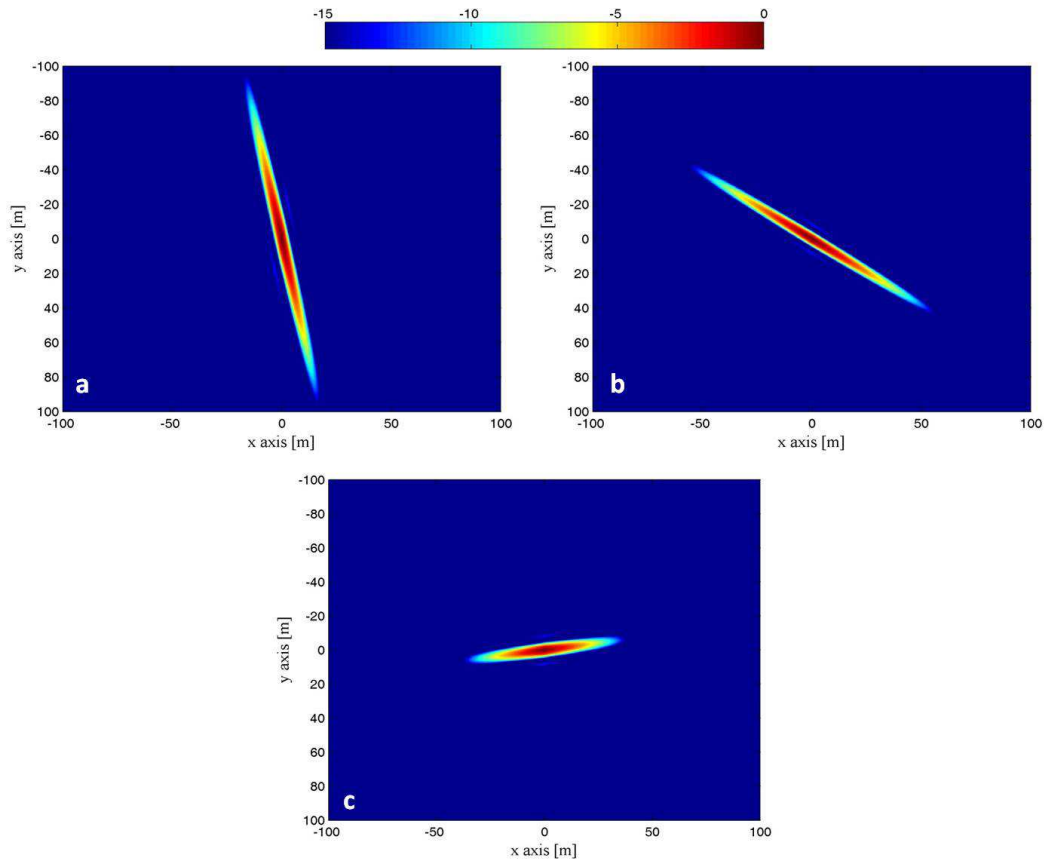TABLE 6-1. SIMULATED ANALYSIS PARAMETERS.

Figure 6-11. Simulated bistatic PSFs - a) A1, b) A2, c) A3.

The MPSFs are shown in Figure 6-12, both for the case of two bistatic channel (Figure 6-12.a,b,c) and the one achieved combining the all bistatic PSFs Figure 6-12.d). Comparing the bistatic PSFs in Figure 6-11 and the MPSFs in Figure 6-12, the reduction of the resolution cell area compared to the single PSFs is evident for $N = 2$. Increasing the number of combined channels, the main effect is the reduction of sidelobe levels around the peak, while the mainlobe region remains approximately the same as the one achieved by integrating two channels. The cell sizes of the MPSFs are reported in TABLE 6-2. Comparing the entries here to those of TABLE 6-1, an improvement of the worst spatial resolution is achieved, and as a consequence a reduction of the resolution cell area of about five times can be seen between the bistatic and multistatic cases.
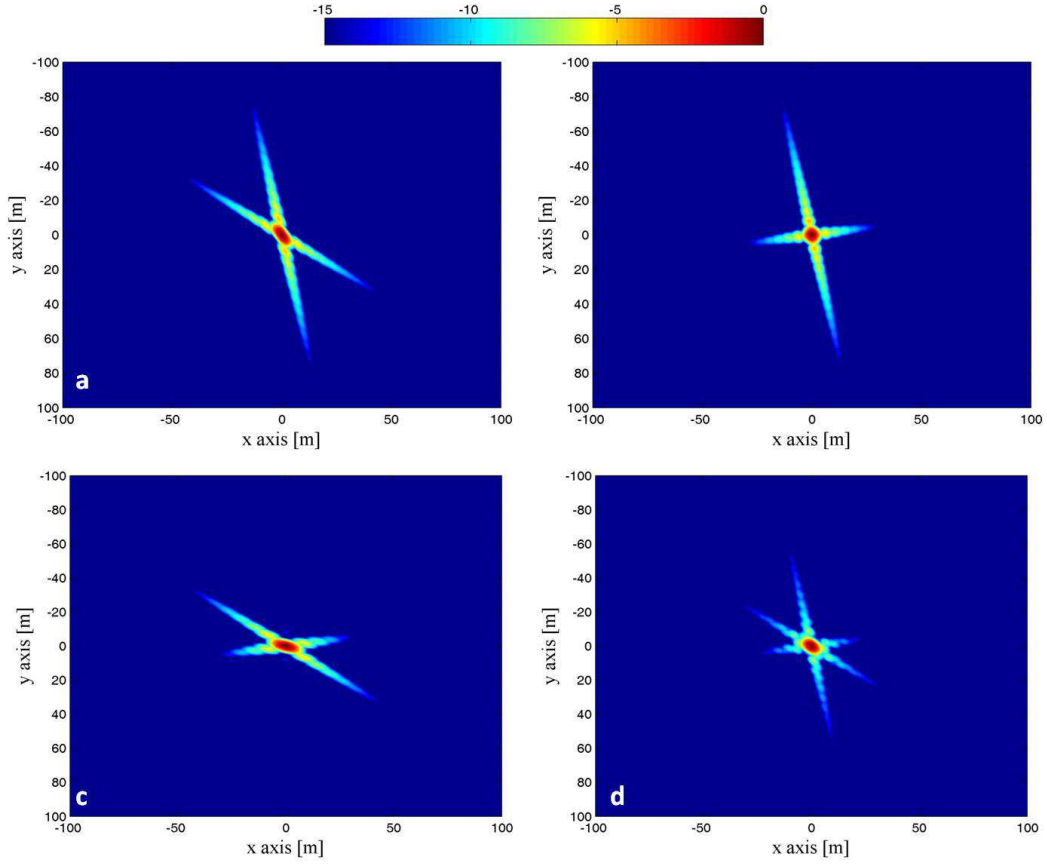
Figure 6-12. Simulated multistatic PSFs - a) A1 + A2, b) A1 + A3, c) A2 + A3, d) A1 + A2 + A3.

MPSF	A1+A2	A1+A3	A2+A3	A1+A2+A3
δ_{max} [m]	10.25	7.03	9.30	7.45
δ_{min} [m]	4.12	5.23	4.84	4.74
Area [m2]	36.33	28.79	38.77	29.61

TABLE 6-2. SIMULATED MPSF RESOLUTION CELL SIZE.

Figure 6-13 shows the approximated version of the MPSF achieved from (12) for the same cases in Figure 6-12.b (A1 + A3) and Figure 6-12.d (A1 + A2 + A3). A good agreement between the nominal and the approximated version of the MPSF can be observed, particularly around the mainlobe. The absolute error of the approximation is calculated as:

$$Err = \left| MPSF - MPSF_{app} \right| \times MPSF \tag{15}$$

where $MPSF_{app}$ is the approximated version of the MPSF in (12) and the $\times$ operator denotes a pixel-by-pixel multiplication.
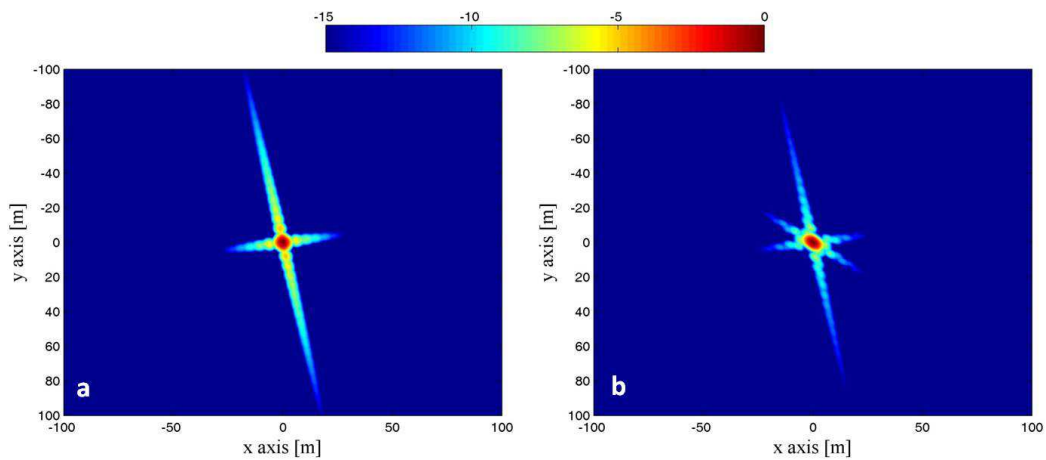
Figure 6-13. Approximated version of the simulated multistatic PSF – a) A1 + A3, b) A1 + A2 + A3.
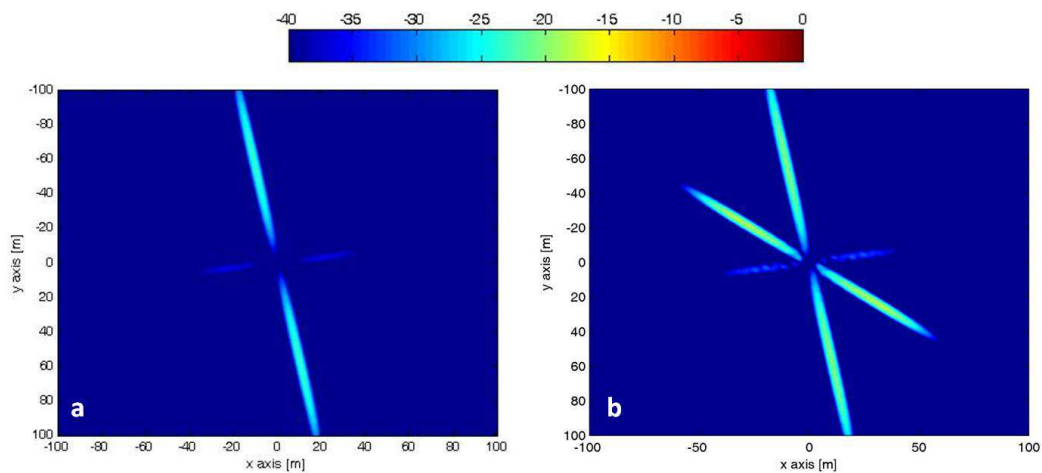

Figure 6-14. Absolute error of the MPSF approximation – a) A1+A3, b) A1+A2+A3.

Figure 6-14 shows the errors for the approximated MPSF in Figure 6-13, showing a negligible error in the mainlobe of the function and a limited error (below -20 dB) around it.

Figure 6-15 shows the comparison between the simulated PSFs and the theoretical resolution ellipses derived as in section 6.1.1. We can appreciate how the resolution ellipse describes very well the area at -8 dB of the mainlobe.

Figure 6-16 shows the comparison between the simulated MPSFs and the theoretical intersecting ellipses derived as in section 6.2.4. Also in this case we can appreciate the capability of the theoretical ellipse to describe the -8 dB region of the mainlobe of the resulting function when N = 2.

The integration of N > 2 single channel has the main goal of reducing the sidelobes around the peak, while the mainlobe region can be sufficiently well approximated by the smallest of the intersecting ellipses deriving from the combination of each couple of bistatic channel (Figure 6-16.d). A more accurate description could be achieved by means of numerical method.
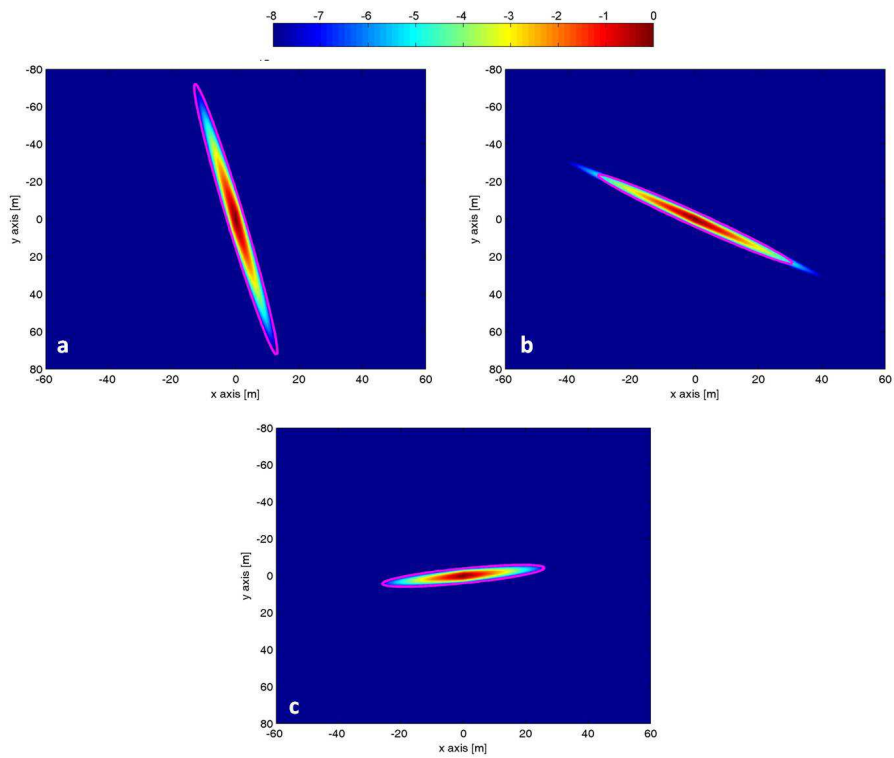
Figure 6-15. Comparison simulated PSF - theoretical resolution ellipses - a) A1, b) A2, c) A3.
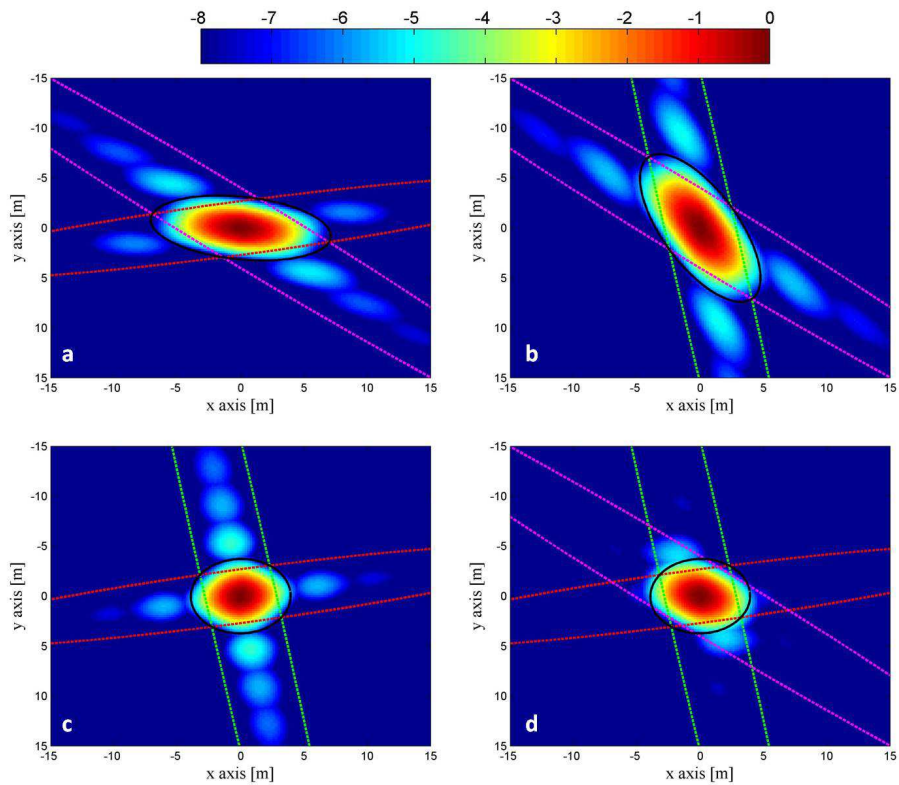

Figure 6-16. Comparison simulated MPSF - theoretical intersecting ellipses - a) A1 + A2, b) A1 + A3, c) A2 + A3, d) A1 + A2 + A3.

6.2.6. MULTISTATIC PSF WITH MINIMUM AREA

As in the bistatic case the minimum area is achieved when $\gamma \approx 90°$, in the multistatic case for N = 2 we expect the minimum value when $\Delta\phi = \phi_1 - \phi_2 \approx 90°$. For example, in the previous analysis the smallest area for the multistatic case was found combining A1 (with the poorest resolution) and A3, since the two PSFs are nearly orthogonal.

Considering two PSFs described by two resolution ellipses being one the rotated version of the other one around its centre, it is quite evident that the minimum intersecting area will be achieved for the case of the different in the orientation of 90 deg. An analytical proof is given in Appendix B. However, different orientations are achieved from different satellite trajectories, and in general the shape of the two PSFs will differ also for the length of the axes of the theoretical ellipses.

In order to show the resolution improvement as a function of the difference in PSF orientation, the following simulation scenario was carried out: a real GLONASS satellite trajectory 3h long was considered, with satellite elevation angles greater than 45° throughout. In real situation, this would allow a low-gain antenna pointed towards the sky to record the GLONASS direct signal for the whole acquisition time without the need to steer it in the satellite's direction. The whole trajectory was then divided in K frames, each one being T_d sec long. Each frame can yield a PSF whose orientation depends on the satellite position and direction during the frame interval. Therefore, frames have an angular separation $\Delta\phi$. The resulting PSF deriving from frame 1 is combined following (8) with the PSFs from all the other frames, so $\Delta\phi = \phi_h - \phi_1, h = 1, ..., K$.

Figure 6-17 shows the area of the MPSF as a function of $\Delta\phi$. We can observe how for all the considered frame time the area greatly decreases with the increase of $\Delta\phi$, moving from values around 500-1000 m^2 for $\Delta\phi \approx 0°$ (where $\Delta\phi = 0°$ is the single PSF case) up to 50-100 m^2 when $\Delta\phi \approx 90°$.
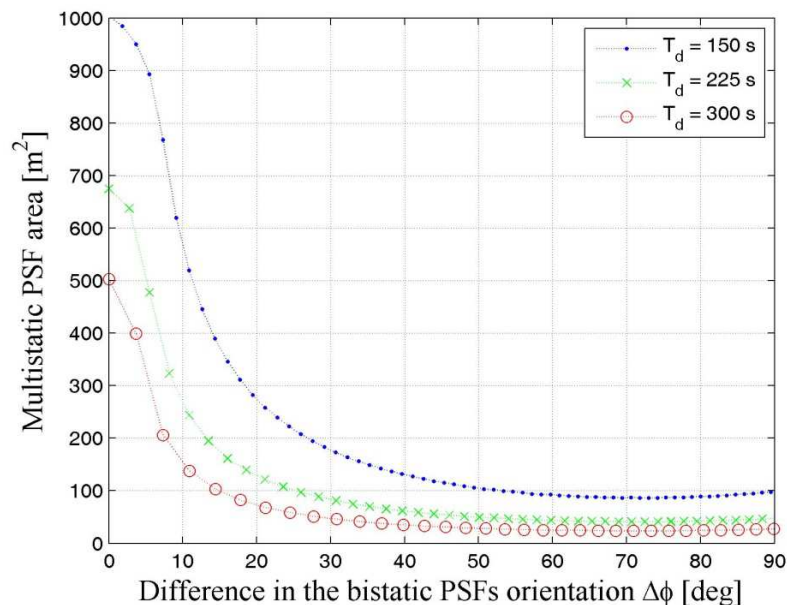

Figure 6-17. MPSF area as a function of the difference in bistatic PSF orientation

6.2.7. EXPERIMENTAL RESULTS

Data acquisitions using GLONASS satellites were conducted to confirm the proposed techniques. The experimental hardware, developed at the University of Birmingham, comprises a superheterodyne receiver with two channels. The first uses a low gain antenna to collect the direct signal from the satellite which is used for the synchronization providing the propagation delay and phase reference for image formation (heterodyne channel HC) [115]; the second uses a high-gain antenna receiving the signal reflections from the target area (radar channel RC). In this context we are interested in experimentally obtain the MPSF and compare it with theoretical results. Since in BSAR the use of passive point-target like corner reflector is not recommended, in order to emulate a point-like target both RC and HC antennas were pointed towards the satellite using low-gain antennas and we use the direct signals to generate the bistatic PSFs. The experimental setup is shown in Figure 6-18.
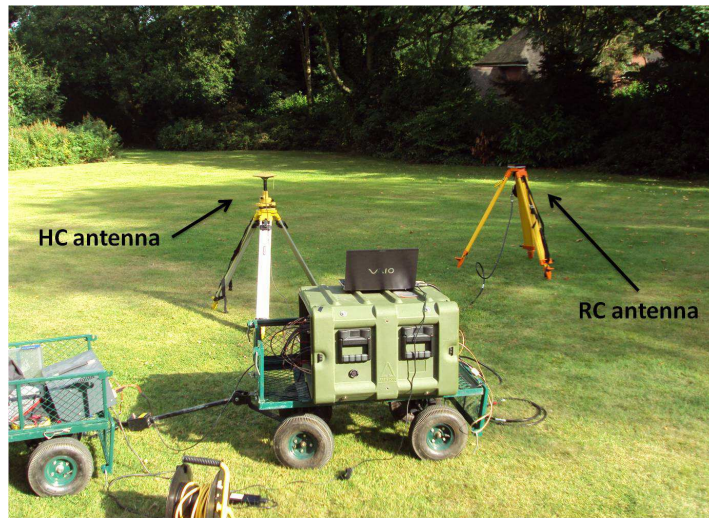

Figure 6-18. Experimental setup.

The parameters of the acquisitions are reported in TABLE 6-3 and the experimental bistatic PSFs are shown in Figure 6-19.a,c, along with the corresponding simulated ones, so that we can appreciate the very good accordance between simulated and experimental single channel results (Figure 6-19.b,d). We observe that the two satellite trajectories result in two nearly orthogonal PSFs and therefore, according with the results in Figure 6-17, we expect a considerably great improvement factor in the resolution cell area. The resulting MPSF is shown in Figure 6-19.e, with a good coincidence with the theoretical expectations, Figure 6-19.f. In addition, TABLE 6-4 reports the cell sizes of the bi/multi-static PSFs both for simulated and experimental results. It can be seen that the MPSF presents the worst spatial resolution that is improved of about five times with respect to worst resolution in the bistatic case, and the multistatic resolution cell area is approximately 2.5 and 4 times better than in data acquisitions A and B, respectively. Finally, Figure 6-20 shows the approximated MPSF achieved applying (12).

Acquisition	Satellite (Cosmos)	β [deg]	ω_E [deg/s]	T_d [s]	ΔR_g [m]	ΔA_g [m]	γ [deg]	ϕ [deg]
A	717	85.45	0.0049	300	31.28	3.25	62.78	43.77
B	716	100.14	0.0050	210	39.39	4.80	69.08	122.62

TABLE 6-3. EXPERIMENTAL ANALYSIS - ACQUISITION AND BISTATIC PSFS PARAMETERS.

	PSF A	PSF B	MPSF
δ_{max} [m]	32.38	40.49	7.26
δ_{min} [m]	3.00	4.67	4.38
Area [m2]	62.30	107.92	25.54

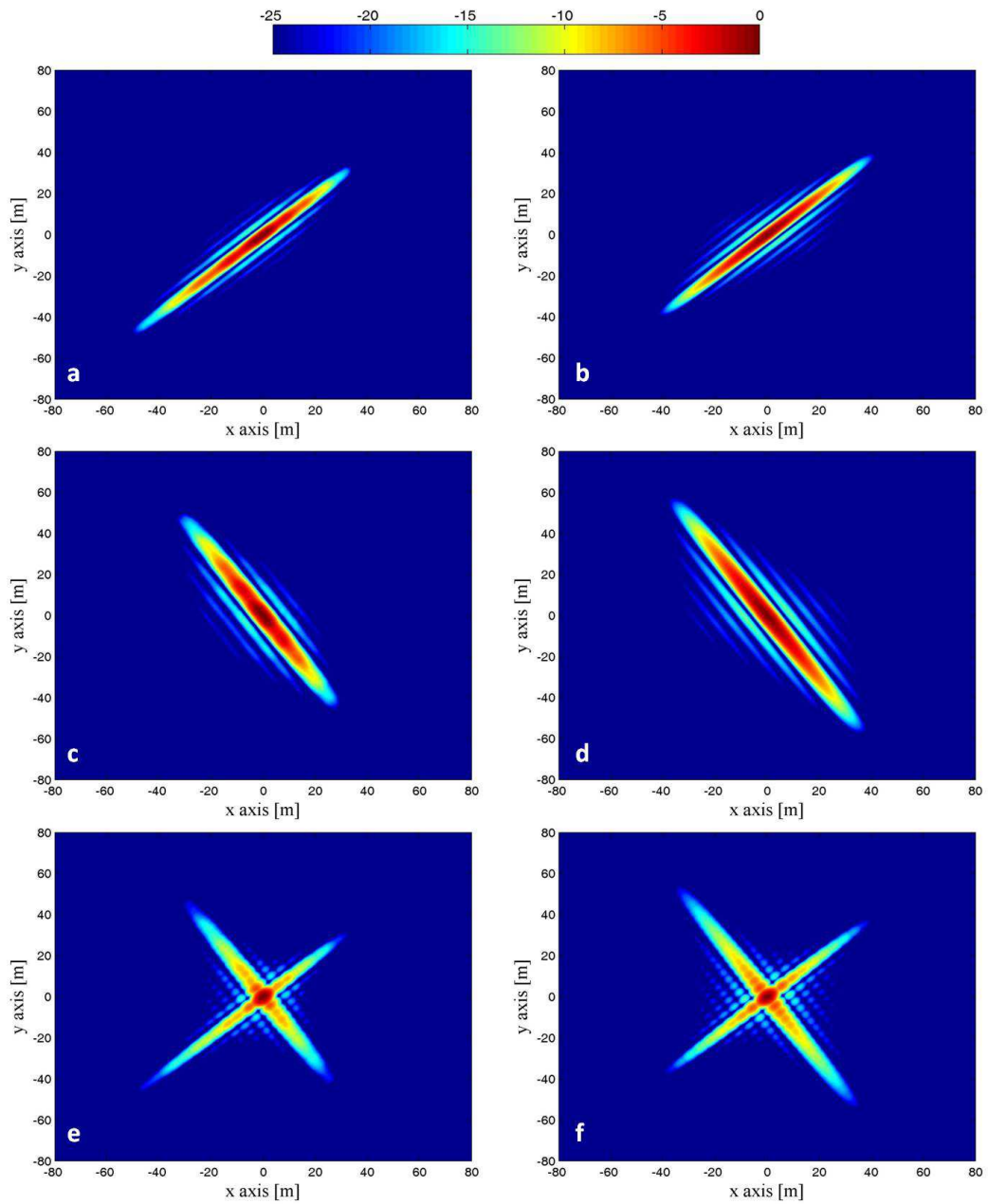TABLE 6-4. EXPERIMENTAL BI/MULTI-STATIC PSF PARAMETERS

Figure 6-19. Bistatic PSFs; a) Acq. A (simulated), b) Acq. A (experimental), c) Acq. B (simulated), d) Acq. B (experimental).
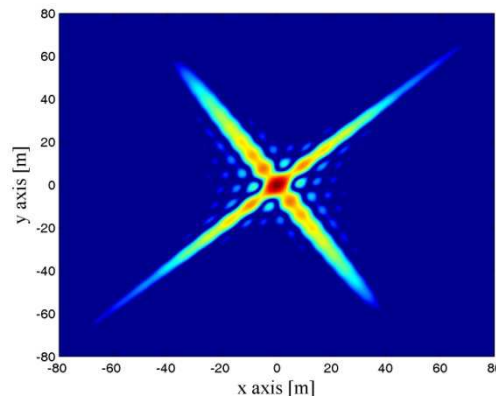
Figure 6-20. Approximated version of the experimental MPSF.

6.3. MULTIPLE SCATTERERS COMBINATION

In the previous sections we studied the proposed multistatic scheme for the combination of BSAR images and we studied it in the case of single point scatterers, resulting in the Multistatic PSF. The next step is to move from the point target analysis to the distributed targets. In this section we show some preliminary theoretical and results achieved by applying the proposed scheme to images composed by several point scatters, showing one of the main issue related to this kind of combination.

Let us consider a very simple distributed target composed by two scatterer of equal amplitude. Each one will result in a ellipsoidal shape which orientation is a function of the mutual position transmitter – receiver and the trajectory of the receiver. Since the satellite – target distance is much greater than the size of the scene we observe, we can consider this shape invariant with the target position. If proper satellites are chosen, two images with different PSF orientations can be formed. Depending on the mutual positions of the two point targets, two possible cases are possible:

1. The two different scattering centres split in the composite image.
2. Artefacts (ghosts) arise in the composite image.

To illustrate these two possible situations let us consider the image characterized by the PSF as in Figure 6-2 (image A) and a second image which PSF is the same one but rotated by 90° (image B). The scene is composed by two point targets of equal amplitude at a distance d ≈ δ_{max}. We consider two study cases: a) the target separation vector lies on the direction of the orientation of the PSF A, ϕ_A; b) the target separation vector is orthogonal to ϕ_A. The resulting single channel images are shown in Figure 6-21 (case a) and Figure 6-22 (case b).

As we can observe two situations can be highlighted: in the case a the two point targets give rise to a unique shape such that we see them as a unique scatterer in image A and they appear as two PSFs in image B; in the case b they appear as two separated point targets in both the images.
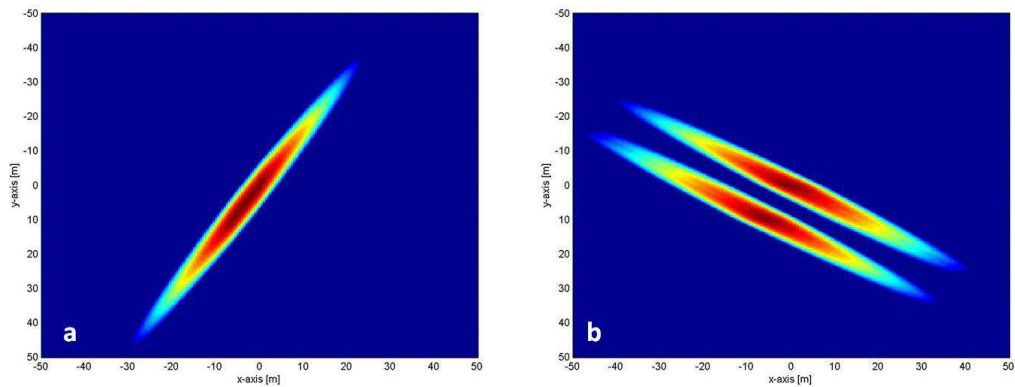
Figure 6-21. BSAR images of a distributed target composed by two point targets, case a – a) image A, b) image B.
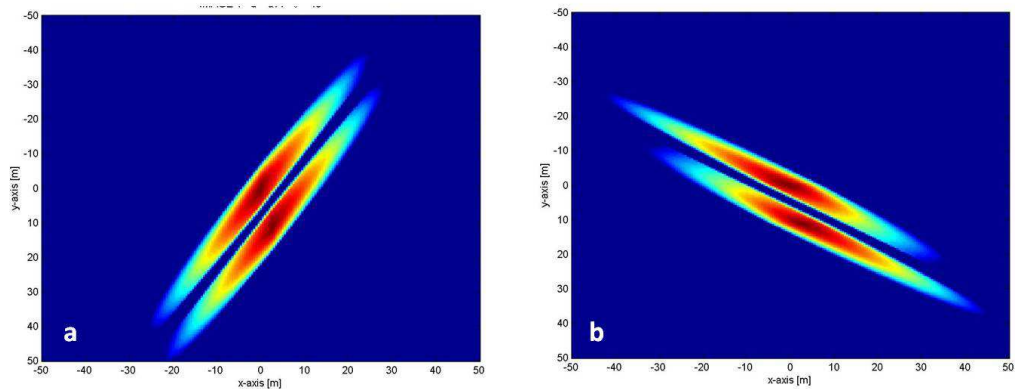

Figure 6-22. BSAR images of a distributed target composed by two point targets, case a – a) image A, b) image B.

The resulting multistatic images are shown in Figure 6-23. Figure 6-23.a is relative to the case a: we can observe the potential of the technique to separate the two different scattering centers, with an improvement in the image resolution as described in section 6.2; Figure 6-23.b is relative to case b: the issue of the technique is the possible presence of ghosts in the composite image.
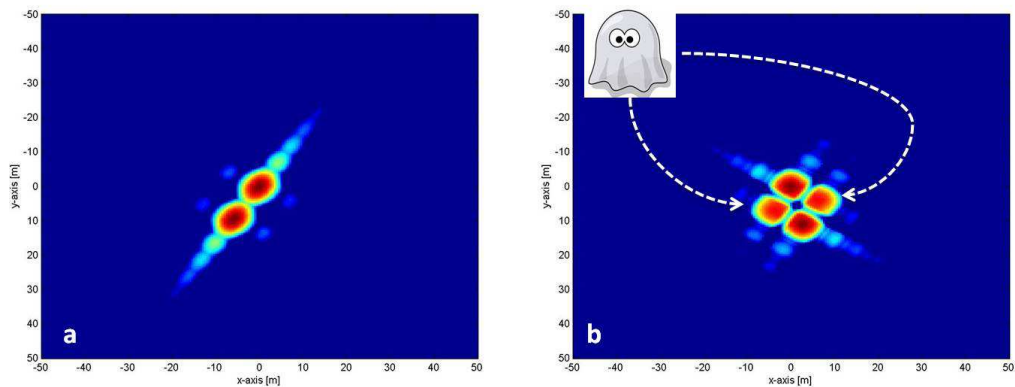

Figure 6-23. Combination of multiple scatterers, separation of different scattering centers (a) and ghost formation (b).

The situation become more and more complicated with the increase of number of the scattering centers. It should be pointed out that the problem of the ghost is one of the main challenge in the multistatic scenario [1] and in the past several solutions to reduce the number of artifacts in the final image have been proposed, e.g. [116], [117], [118].

A possible solution to counteract the effect is exploit a number of transmitters greater than two. Let us consider the three bistatic geometries in TABLE 6-1, and a scene composed by two point scatterers of equal amplitude located in [0,0]m and [10,10]m.

Figure 6-24 shows the three resulting BSAR images; as we can observe in images A1 and A3 we see as separated the two points, whereas in image A2 we see only one shape.

Figure 6-25 shows the three multistatic images obtained by the combination of the three couples of single images. As we can observe, ghosts appear in image b, resulting by the composition of image A1 and A3, whereas in images a and c the two scatterers appear as separated points.
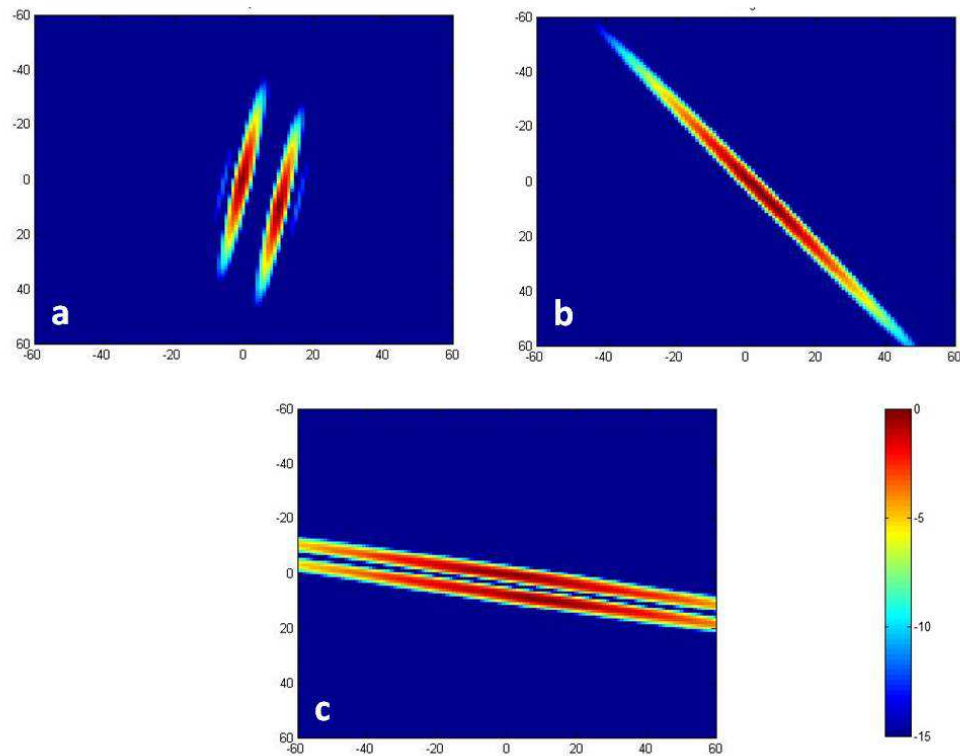

Figure 6-24. De-ghosting: BSAR images of a scene composed by two point targets – a) A1, b) A2, c) A3.
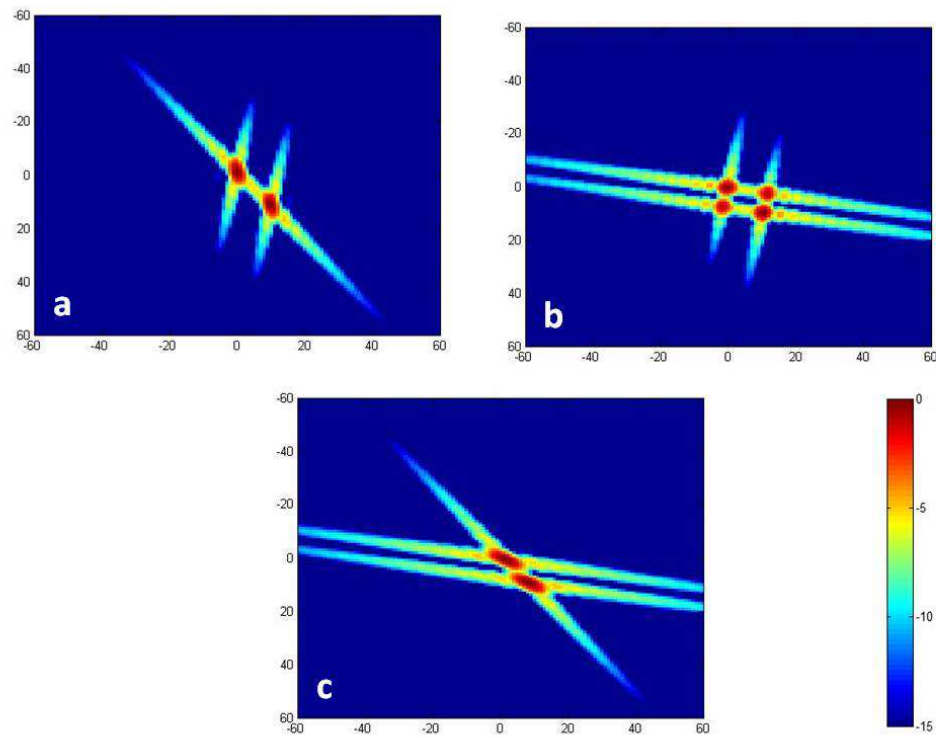
Figure 6-25. De-ghosting: Multistatic SAR images with N = 2 – a) A1 + A2, b) A1 + A3, c) A2 + A3.

The idea is that ghosts result in different positions if different couples of single channel images are used to form the multistatic ones, whereas the real scatterers appear in their true positions.

Figure 6-26.a shows the multistatic image resulting by the combination of the all the bistatic images. The real point scatterers have a bigger power than the ghosts, since the take advantage of a gain of non-coherent integration. If as example we apply the min operator to the three images in Figure 6-25 instead of the summation to form the final image (Figure 6-26) we can reduce much more the power of the ghosts in the final image.
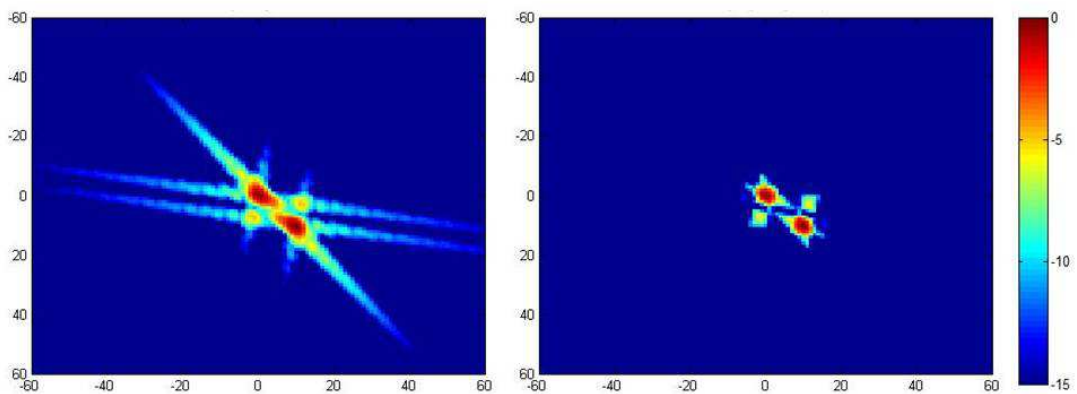

Figure 6-26. De-ghosting: Multistatic SAR images with N = 3 (a) and the result of the min operator (b).

6.4. ANALYSIS OF REAL BSAR IMAGES

In this section we present some preliminary experimental results of real BSAR images acquired at multiple bistatic geometries. The experimental campaign was conducted on the roof of the School of Electronic, Electrical and Computer Engineering of the University of Birmingham. The equipment used for experimentation was the same as presented in section 6.2.7, but in this case the RC uses a antenna pointed towards the imaging scene, collected satellite signal reflections for imaging. The experimental setup is shown in Figure 6-27.

The target area was Metchley Park, located to the West. A satellite photo of this area is shown in Figure 6-28. This area was selected for two reasons. First of all, there are four isolated towers approximately 1.2 Km away from the receiver (Figure 6-29.a), secondly, there are tree lines in the area facing towards the receiver, so they could yield strong echoes (Figure 6-29.b).

The results here presented refer to three experiments with four different satellite positions, reported in TABLE 6-5 (satellite azimuth angles are measured clockwise starting at the West direction, elevation angles are measured relative to the location of observation, bistatic angles are calculated according to bistatic geometries) [111].

The images obtained from the four experiments are shown in Figure 6-30, superimposed on the satellite photograph of the area in Figure 6-28.
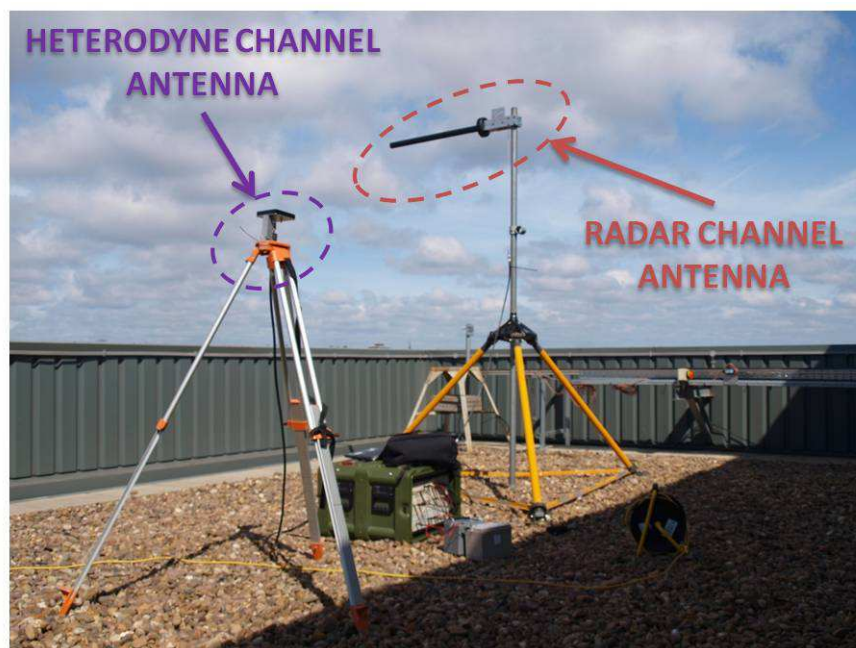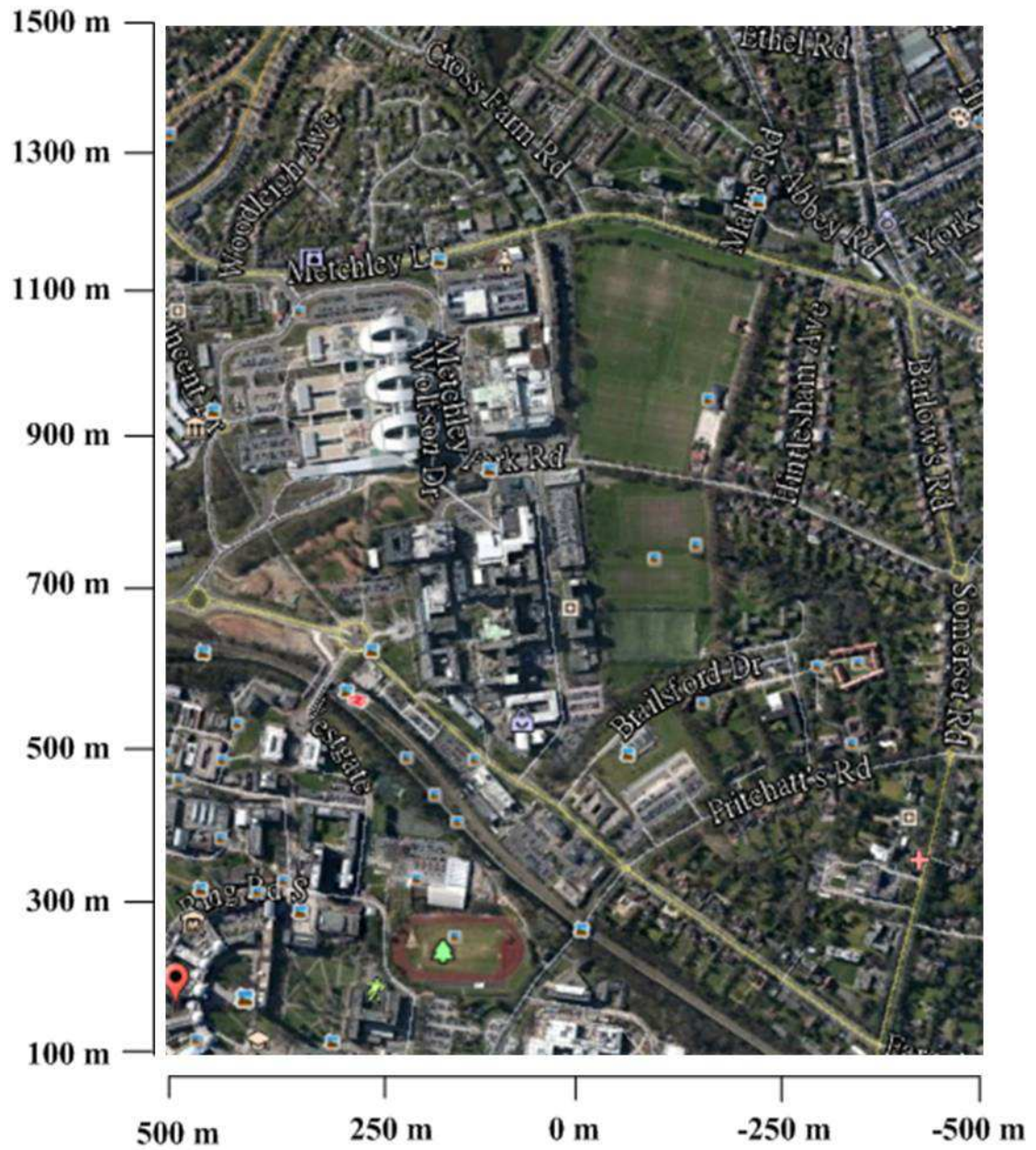

Figure 6-27.Real BSAR imaging - Experimental equipment.

Figure 6-28. Metchley Park area.

Figure 6-29. Metchley park – a) Building at far end, b) trees in the middle range.

Image	Satellite	Date of acquisition	Azimuth	Elevation	Bistatic angle
M	732	24 May 2012	170.6°-161.1°	75.8°-74.6°	74.4°
J	736	24 July 2012	187.7°-189.7°	54.3°-52.1°	63.5°
A	736	31 Aug 2012	42.1°-39.1°	70.6°-72.7°	90.8°
D	744	7 Dec 2012	148.2°-151.3°	52.4°-42.1°	54.2°

TABLE 6-5. POSITIONS OF SATELLITES IN DIFFERENT EXPERIMENTS.

Some preliminary considerations are in order:

- **Different time of acquisitions**: the images have been acquired in different times. This should not be a issue for the multistatic image combination we propose here, since we are investigating a non-coherent technique looking at stable scatterers.

- **Different elevation and azimuth views of the scene**: the differences in the point of view of the scene entail different reflectivity of the scatterers as a consequence of the different bistatic geometry. Different shadowing effects appear in the images and there is a strong decorrelation of the received signals. These could be very useful in areas such terrain classification, SAR image feature extraction or even SAR clutter cancellation, whereas in our

case these represent a problem and limitations on the differences of the azimuth and elevation angles of the observation have to be studied.

- **Very complex scene**: the scene is composed by natural and manmade objects, such as trees, grass and building, showing different scattering phenomenon, and it is a difficult situation for a starting analysis

The goal here is to show some very first real results showing the capability of the multistatic GNSS-based SAR to improve the quality of the images and to highlight some of the major challenges have to be faced in the future.
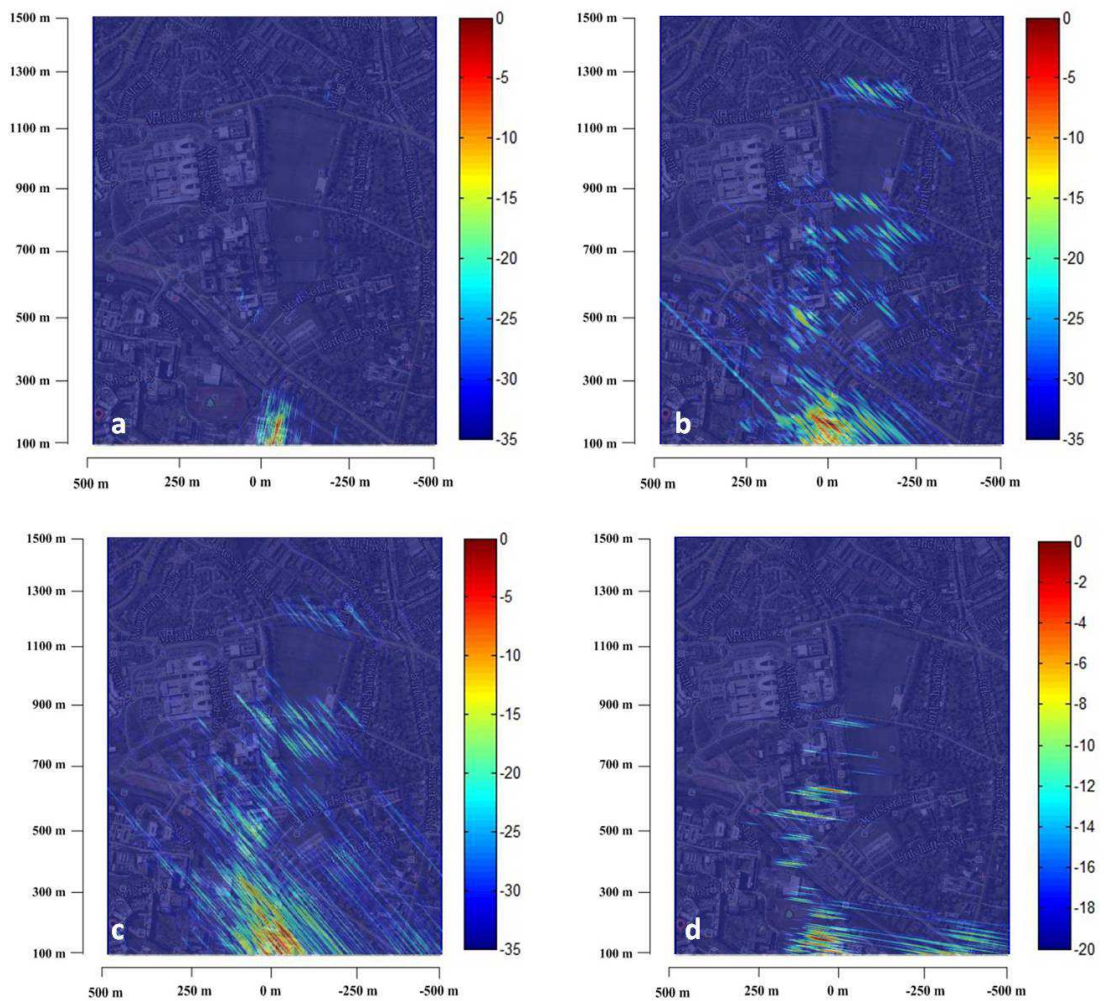

Figure 6-30. Metchley Park radar images – a) May (M), b) July (J), c) August (A), d) December (D).

6.4.1. RADAR CHANNEL BISTATIC PSF

Figure 6-19 showed the coincidence between the theoretical bistatic PSF and the one experimentally obtained from the RC when it collects the direct signal from the satellite. In this section we aim to show the coincidence between theory and experiment also for the PSF achieve by processing of the reflected signal.

Firstly, we extract an isolated scatterer from one of the images in Figure 6-30 and evaluate the theoretical PSF to make the comparison.
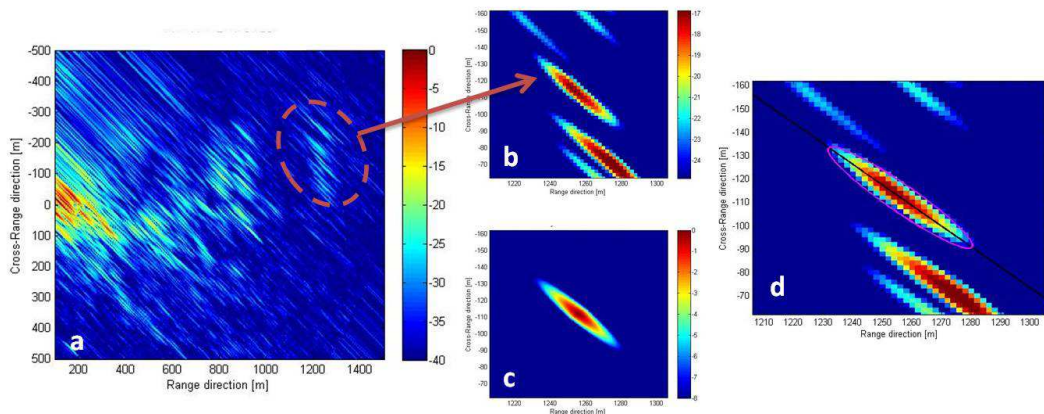

Figure 6-31. Radar channel PSF – a) BSAR image of Metchley Park (J), b) isolated scatterer, c) simulated PSF, d) comparison with the resolution ellipse.

Figure 6-31.a shows the image J. An isolated scatterer at the far end has been extracted (Figure 6-31.b) and observing the comparison with the simulated PSF (Figure 6-31.c) we can appreciate the very good agreement between theory and experiment; also, the comparison between the real scatterer image and the resolution ellipse has shown (Figure 6-31.d).

6.4.2. MULTISTATIC IMAGES

Here we show and discuss the multistatic images obtained by the combination of the images in Figure 6-30. The several images resulting by the combination of N = 2 channels are shown in Figure 6-32. In order to analyze some feature of the images, we focus on the two areas in Figure 6-29: the tree lines in the middle range and the buildings at the far end.

Tree lines

Figure 6-33 shows the multistatic image achieved as combination of the images M and D, while the multistatic image achieved by the combination of three channels is shown in Figure 6-34. We can observe the capability of the system to start to isolate the scattering centers probably due to the trunks of the trees. However, as previously discussed, several bright points are ghosts. We try to apply the rule described in section 6.3 and the image resulting from the min operator is shown in Figure 6-35. We can observe the great reduction of the number of scattering points, so that we can expect that the most of the remaining bright points are due to the reflections from the trees. The optical photo of the trees is shown in Figure 6-36. Counting the number of bright points and the

number of trunks we found a very good coincidence. We underline that this is only a very first result, highlighting the capability of the technique to improve the imaging capability of the passive system.

Buildings at the far end

Figure 6-37 shows the single channel images of the area at the far end of the image. We can observe how several scatterers visible in one image cannot be visible in the others. Moreover, in this area there are different kind of objects as well as the buildings, such as trees and bushes. Therefore, as well as the ghosts due to the near scatterers from the same object, in this area we have ghosts due to returns from different targets. The multistatic image as composition of M, A and D is shown in Figure 6-38, along with the image resulting by the application of the min operator. We start to identify the shape of the buildings, but many problems are still to be investigated.
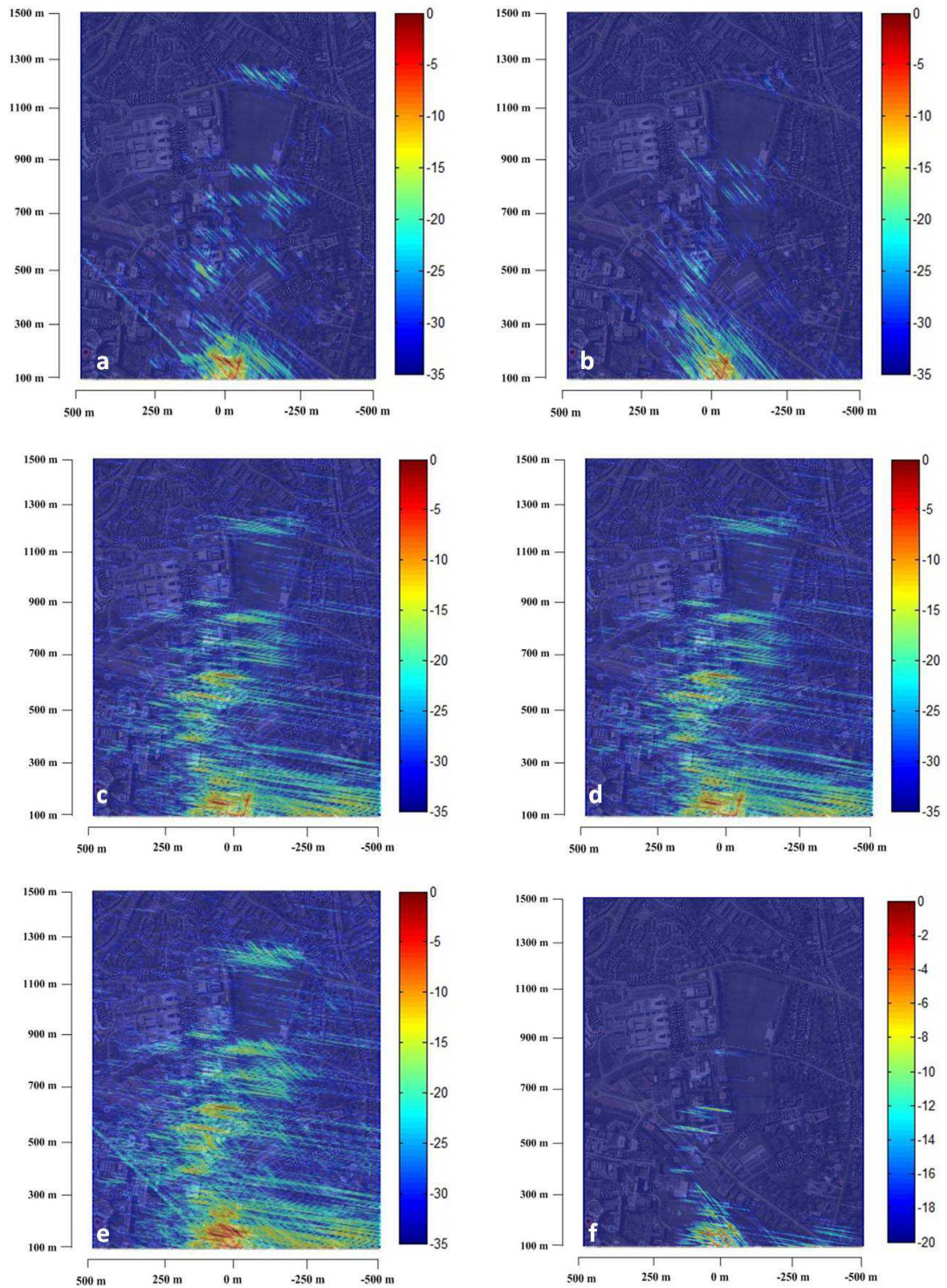
Figure 6-32. Metchley Park multistatic images – a) M + J, b) M + A, c) M + D, d) J + A, e) J + D, f) A + D.
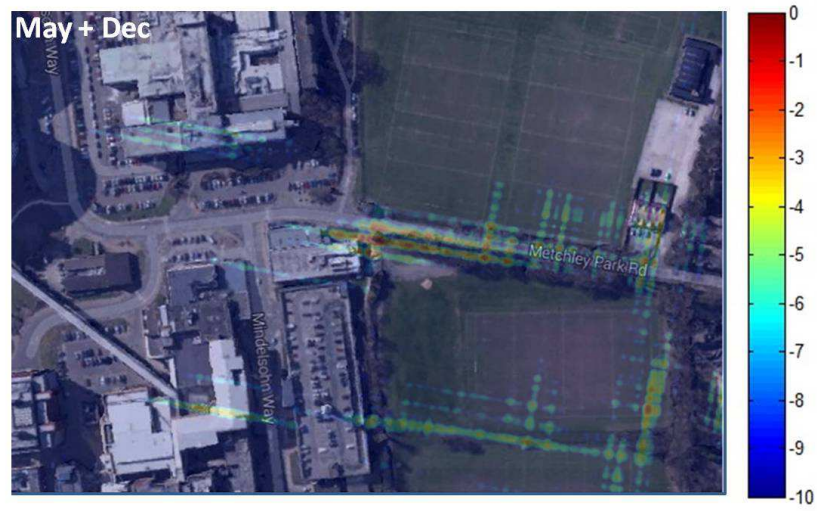
Figure 6-33. Tree lines area – multistatic image M+D.
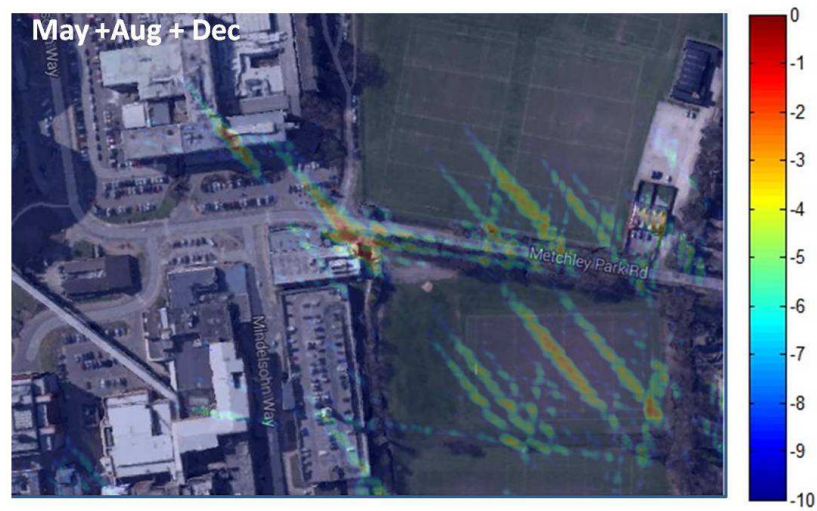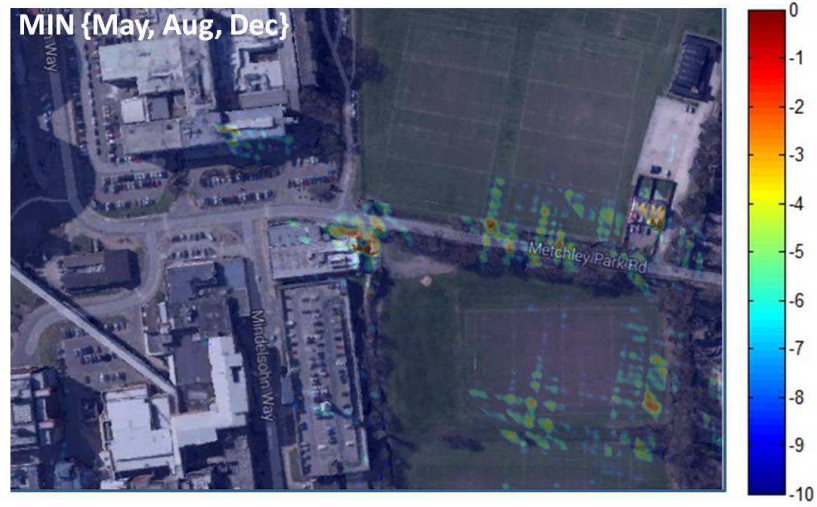

Figure 6-34. Tree lines area – multistatic image M+A+D.

Figure 6-35. Tree lines area – multistatic image min{M,A,D}.
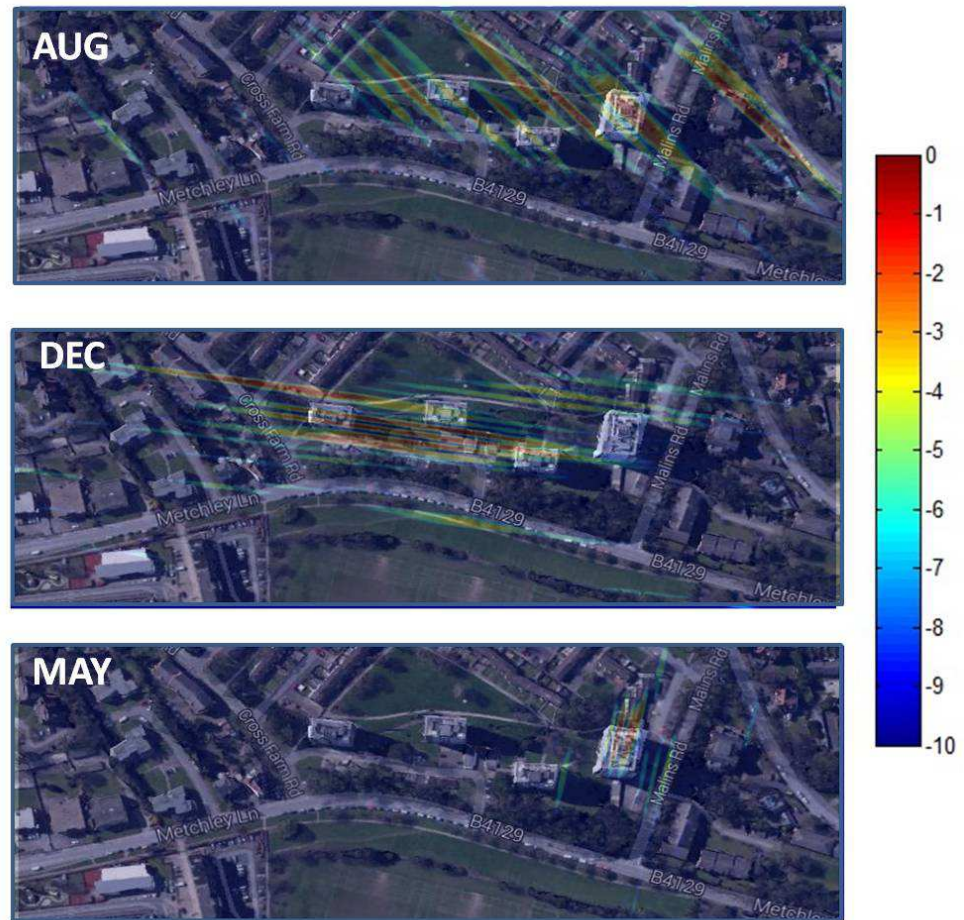

Figure 6-36. Optical photo of the tree lines.

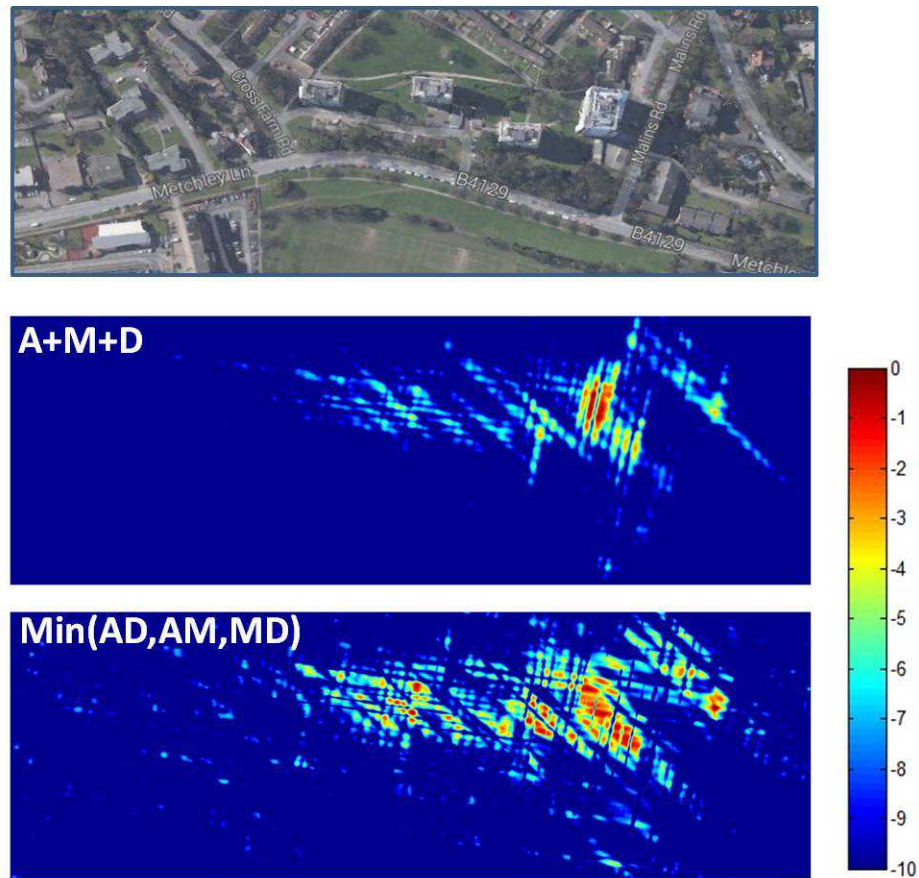Figure 6-37. Building at the far end, BSAR images – a) Aug, b) Dec, c) May.

Figure 6-38. Building at the far end – a) optical photo, b) Multistatic image M+A+D, c) multistatic image min{M,A,D}.

6.5. CONCLUSIONS

The work presented in this chapter puts forward a multistatic SAR system using GNSS satellites as transmitters of opportunity and a stationary receiver on the ground. The use of such a technology is cost-effective since only the development of the receiver is required and can be potentially used for persistent local area monitoring. The first part of the presented work shows the theoretical analysis of the multistatic PSF achieved combining the single images resulting from several GNSS satellites transmissions. Such a system has the potentiality to considerably improve the resolution cell with respect to the single bistatic channel case properly selecting satellites positions and trajectories. The theoretical analysis was verified by both simulations and experimental results. It is worth to notice that all the results are applicable for the configuration using a moving receiver, where a Doppler resolution less than 1 m is expected; therefore in such a configuration a resolution cell of about 1 m^2 could be achieved.

The second part of the chapter shows a preliminary experimental study on the application of such technology on real BSAR images, showing the potentialities of such of technique to extract an increased amount of information from the observed area by exploiting several GNSS satellites. Even if many issues are still to be faced, the technique has the potential to be a powerful and low cost remote sensing tool, due to the choice of GNSS as transmitters.

APPENDIX

A. RESOLUTION ELLIPSE

Let the vertices of the parallelogram be O, P, Q and R and d_1 and d_2 the two diagonals, i.e. $d_1: \overrightarrow{OQ}$ and $d_2: \overleftrightarrow{PR}$; the centre of the parallelogram is C: $(x_C, y_C) = \{d_1 \cap d_2\}$ (see Figure A 1).
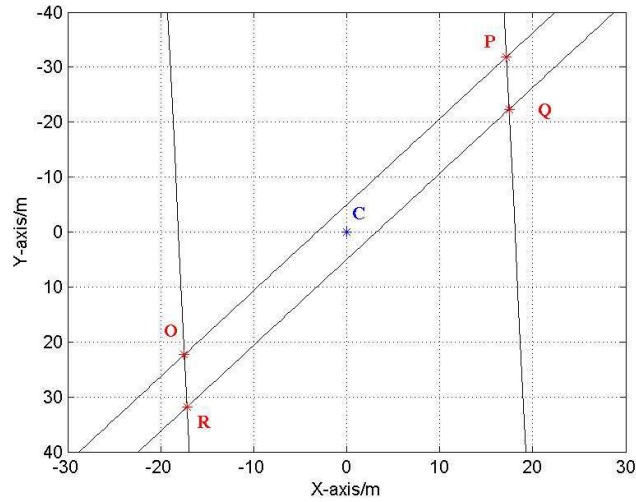
Figure A 1. Resolution parallelogram.

The general form of an ellipse is [119]:

$$E(x, y): ax^2 + 2bxy + cy^2 + 2dx + 2fy + g = 0 \tag{A1}$$

satisfying $\Delta \neq 0$, $J > 0$ and $\dfrac{\Delta}{I} < 0$, being:

$$\Delta = \begin{vmatrix} a & b & d \\ b & c & f \\ d & f & g \end{vmatrix} \quad , \quad J = \begin{vmatrix} a & b \\ b & c \end{vmatrix} \quad , \quad I = a + c \tag{A2}$$

The semi-major and the semi-minor axes are given by respectively:

$$a' = \sqrt{\frac{2(af^2 + cd^2 + gb^2 - 2bdf - acg)}{(b^2 - ac)\left(\sqrt{(a-c)^2 + 4b^2} - (a+c)\right)}} \tag{A3}$$

$$b' = \sqrt{\frac{2(af^2 + cd^2 + gb^2 - 2bdf - acg)}{(b^2 - ac)\left(-\sqrt{(a-c)^2 + 4b^2} - (a+c)\right)}} \tag{A4}$$

The counter clockwise angle of rotation from the x-axis to the semi-major axis of the ellipse is given by:

$$\phi = \begin{cases} 0 & , \quad \text{b} = 0, \text{a} < c \\ \dfrac{\pi}{2} & , \quad \text{b} = 0, \text{a} > c \\ \dfrac{1}{2}\cot^{-1}\left(\dfrac{a-c}{2b}\right) & , \quad \text{b} \neq 0, \text{a} < c \\ \dfrac{\pi}{2} + \dfrac{1}{2}\cot^{-1}\left(\dfrac{a-c}{2b}\right) & ' \quad \text{b} \neq 0, \text{a} > c \end{cases} \tag{A5}$$

It is known that the diagonals of the parallelogram are two conjugate diameter of the circumscribed ellipse, so that we can exploit this information to extract the equation of the searched ellipse. For starters, C is the centre of the ellipse, being the intersection point of a couple of conjugate diameters. By means of the translation of the plane T_C we can shift the centre of the ellipse in (0,0):

$$(x', y') = T_C\{x, y\}: \begin{cases} x' = x - x_C \\ y' = y - y_C \end{cases} \tag{A6}$$

We point out that in the case presented in Figure A 1 the ellipse is centered in (0,0) and the translation T_C is unnecessary; however it is necessary if the center is located in different position.

The equation of an ellipse having its centre in (0,0) is given by:

$$E(x, y): ax^2 + 2bxy + cy^2 = 1 \tag{A7}$$

i.e., referring to (A1), $d = f = 0$ and $g = -1$ (for sake of simplicity the apex ' accounting for the isometry in (A6) will be omitted).

In order to define the ellipse now we need three information. We can substitute two endpoints of the segments OQ and PR, obtaining two linear equations with variables a, b, c (we cannot use the other endpoints, because the equations are not independent).

The third equation can be obtained implicitly differentiating the equation of the ellipse

$$2ax + 2b\left(y + x\frac{dy}{dx}\right) + 2cx\frac{dy}{dx} = 0 \tag{A8}$$

Then, substituting one endpoint from a chord and the slope of its tangent line (= dy/dx) into this equation we get a third linear equation with variables a, b, and c. The value of dy/dx is known because in the point which a diameter across the ellipse, the tangent line is parallel to the conjugate diameter (see Figure A 2).
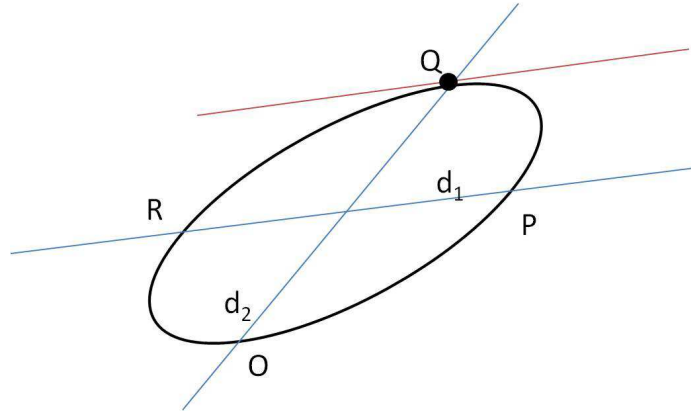
Figure A 2. Conjugate diameters of the ellipse

In order to find the parameters a, b and c we can resolve the following linear system:

$$\begin{cases} ax_O^2 + 2bx_Oy_O + cy_O^2 = 1 \\ ax_P^2 + 2bx_Py_P + cy_P^2 = 1 \\ 2ax_R + 2b(y_R + x_Rm_{d_1}) + 2cx_Rm_{d_1} = 0 \end{cases} \quad \text{(A9)}$$

or, in matrix form:

$$\begin{bmatrix} a \\ b \\ c \end{bmatrix} \begin{bmatrix} x_O^2 & 2x_Oy_O & y_O^2 \\ x_p^2 & 2x_Py_P & y_p^2 \\ 2x_R & 2(y_R + x_Rm_{d_1}) & 2x_Rm_{d_1} \end{bmatrix} = \begin{bmatrix} 1 \\ 1 \\ 0 \end{bmatrix} \rightarrow \boldsymbol{uD} = \boldsymbol{k} \quad \text{(A10)}$$

being (x_i, y_i) the coordinates of the point i = O, P, Q, R after the transformation in (A6) and m_{d_1} the angular coefficient of the straight line passing through R and P. Applying the Cramer's rule we find:

$$D_a = \begin{vmatrix} & 2x_Oy_O & y_O^2 \\ \boldsymbol{k} & 2x_Py_P & y_p^2 \\ & 2(y_R + x_Rm_{d_1}) & 2x_Rm_{d_1} \end{vmatrix}$$

$$D_b = \begin{vmatrix} x_O^2 & & y_O^2 \\ x_p^2 & \boldsymbol{k} & y_p^2 \\ 2x_R & & 2x_Rm_{d_1} \end{vmatrix} \quad \text{(A11)}$$

$$D_c = \begin{vmatrix} x_O^2 & 2x_Oy_O & \\ x_p^2 & 2x_Py_P & \boldsymbol{k} \\ 2x_R & 2(y_R + x_Rm_{d_1}) & \end{vmatrix}$$

Finally, the five parameters defining the ellipse in (A1) are:

$$a = \frac{|D_a|}{|D|} \ ; \ b = \frac{|D_b|}{|D|} \ ; \ c = \frac{|D_c|}{|D|}$$

$$d = f = 0 \ ; \ g = -1 \tag{A12}$$

Substituting (A12) in (A3), (A4) and (A5) we have the axes of the ellipse and its orientation.

Figure A 3 shows the circumscribed ellipse to the parallelogram in Figure A 1.
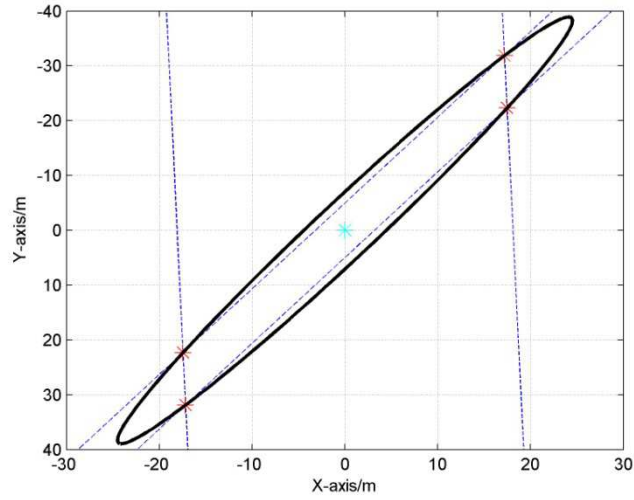

Figure A 3. Circumscribed ellipse.

B. MINIMUM INTERSECTING AREA

Without loss of generality we consider the centre of the ellipse describing the PSF of the first channel (reference) in (0,0) and its major axis lying on the x-axis; any different situation can be achieved by means of isometries of the plane. We assume the ellipse describing the PSF of the second channel having the same centre and the same axes length but rotated of ϕ deg.

The ellipse in (A1) having its major axis lying on the x-axis is given by the following parametric form:

$$E_0 = \begin{cases} x = a' \cos(t) \\ y = b' \cos(t) \\ t = [0,2\pi) \end{cases} \tag{A13}$$

The rotated ellipse can be obtained applying a rotation matrix:

$$\begin{bmatrix} x_\phi \\ y_\phi \end{bmatrix} = \begin{bmatrix} cos\phi & -sin\phi \\ sin\phi & cos\phi \end{bmatrix} \begin{bmatrix} x \\ y \end{bmatrix} \rightarrow E_\phi = \begin{cases} x_\phi = xcos\phi - ysin\phi \\ y_\phi = xsin\phi + ycos\phi \end{cases} \tag{A14}$$

We consider $\phi \in \left[0, \frac{\pi}{2}\right]$, since the other cases can be achieved by symmetry. The two ellipses are shown in Figure A 4.
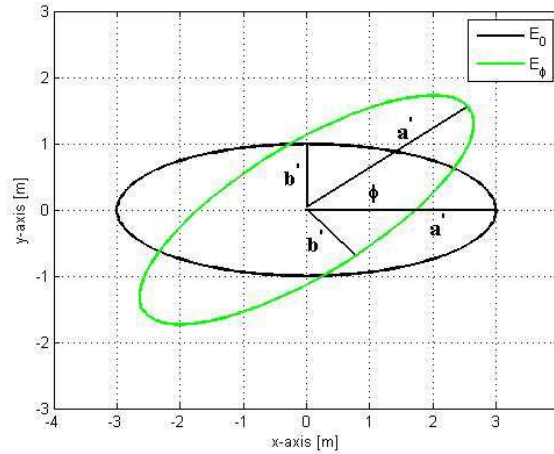
Figure A 4. Ellipses E_0 and E_ϕ for a' = 3 m, b' = 1 m, φ = 30°.

The area of an elliptical sector defined by the angle θ_0 and θ_1 (see Figure A 5) is given by:

$$A(\theta_0, \theta_1) = F(\theta_1) - F(\theta_0) \tag{A15}$$

being

$$F(\theta) = \frac{a'b'}{2}\left[\theta - tg^{-1}\left(\frac{(b-a)\sin(2\theta)}{(b+a)+(b-a)\cos(2\theta)}\right)\right] \tag{A16}$$
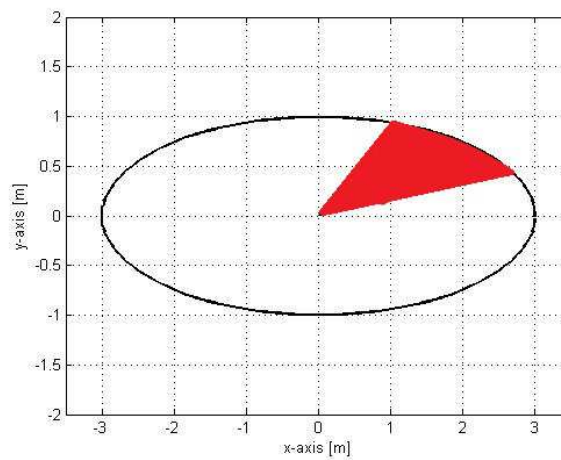

Figure A 5. Elliptical sector.

Intersecting the two ellipses four elliptical sectors can be highlighted. The intersecting area is given by the summation of these four areas. Referring to Figure A 6:

$$A_{intersection} = \sum_{i=1}^{4} A_i \tag{A17}$$

where A_i is given by (A15) using the proper angles measured in anticlockwise direction from the x-axis. However, it easy to verify that $A_i = \frac{A_{intersezione}}{4}, \forall i$. Therefore we can write (A17) as:

$$A_{intersection} = 4A_1 = 4\left\{F(\theta_R) - F(\theta_Q)\right\} \tag{A18}$$
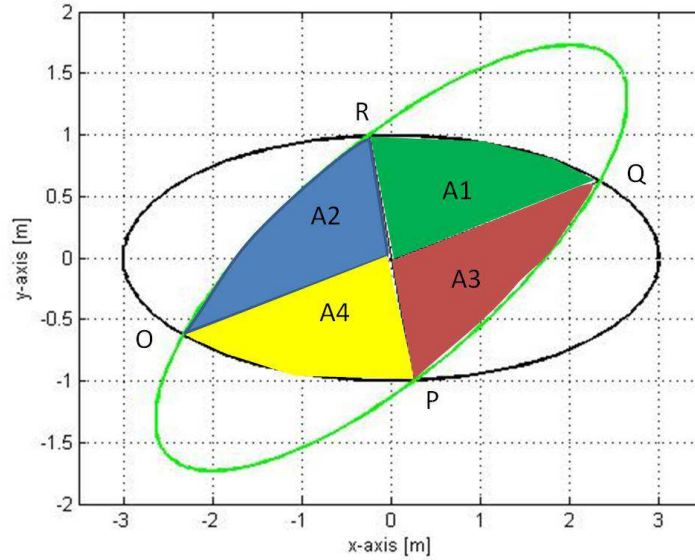
Figure A 6. Area of the intersecting ellipses

The two angles θ_R and θ_Q do not depend on the shape of the ellipse (i.e. the major and minor axes), but only on the rotation angle. As an example, in Figure A 7 two cases of ellipses are shown. Both the ellipses are rotated of 30 deg (dotted lines). As we can observe, the chords connecting the intersection points for the case E_1, E_1^{ϕ} (pink points) and E_2, E_2^{ϕ} (green points) lie on the same straight lines, therefore describing the same angles.

Also, for symmetry, θ_Q is an half of ϕ and the separation between the straight lines with angular coefficient θ_R and θ_Q is right 90 deg, being the direction of the ellipses achieved by means a rotation of $\frac{\phi}{2}$ (see Figure A 8).
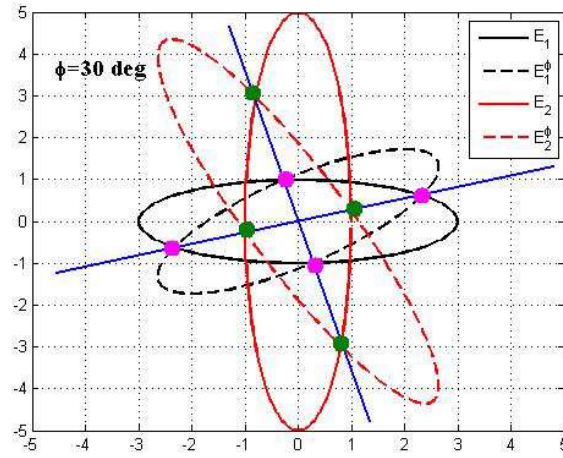
Figure A 7. The angles defining the intersection points do not depend on the specific form of the ellipse, but only on the rotation angle. E1: a' = 3, b' = 1 ; E2: a' =1, b' = 5.
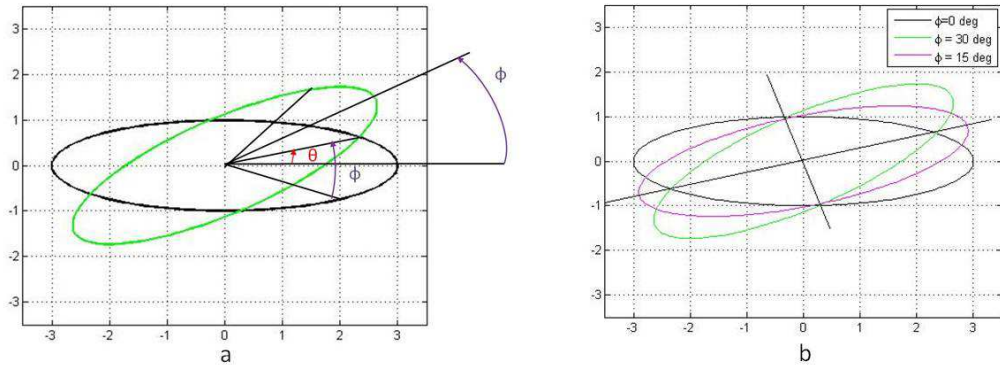
Figure A 8 Relationship between the rotation angle and the angle describing the first intersection point – a) this angle is an half of the rotation, b) the directions of the intersecting lines of the two ellipses are orthogonal.

Therefore we have:

$$A_{intersection} = 4A_1 \begin{cases} \theta_Q = \dfrac{\phi}{2} \\ \theta_R = \dfrac{\pi}{2} + \theta_Q = \dfrac{\pi}{2} + \dfrac{\phi}{2} \end{cases} 4\left\{F(\theta_R) - F(\theta_Q)\right\} \tag{A19}$$

Using (A19) we can write (A18) as a function of ϕ:

$$A = 2ab\left\{\theta_Q - tg^{-1}\left(\frac{(b-a)\sin(2\theta_Q)}{(b+a) + (b-a)\cos(2\theta_Q)}\right) - \theta_R + tg^{-1}\left(\frac{(b-a)\sin(2\theta_R)}{(b+a) + (b-a)\cos(2\theta_R)}\right)\right\} =$$

$$= 2ab\left\{\frac{\pi}{2} + \frac{\phi}{2} - tg^{-1}\left(\frac{(b-a)\sin(\pi+\phi)}{(b+a) + (b-a)\cos(\pi+\phi)}\right) - \frac{\phi}{2} + tg^{-1}\left(\frac{(b-a)\sin(\phi)}{(b+a) + (b-a)\cos(\phi)}\right)\right\} =$$

$$= 2ab \left\{ \frac{\pi}{2} + tg^{-1} \left(\frac{(b-a)\sin(\varphi)}{(b+a) - (b-a)\cos(\varphi)} \right) + tg^{-1} \left(\frac{(b-a)\sin(\varphi)}{(b+a) + (b-a)\cos(\varphi)} \right) \right\} =$$

$$^* = 2ab \left\{ \frac{\pi}{2} + tg^{-1} \left(\frac{\dfrac{(b-a)\sin(\varphi)}{(b+a)+(b-a)} + \dfrac{(b-a)\sin(\varphi)}{(b+a)+(b-a)}}{1 - \dfrac{(b-a)^2\sin^2(\varphi)}{(b+a)^2 - (b-a)^2\cos^2(\varphi)}} \right) \right\}$$

After simple manipulations we have:

$$A_{int} = 2ab \left\{ \frac{\pi}{2} + tg^{-1} \left(\frac{(b^2 - a^2)}{2ab} \sin(\phi) \right) \right\} \tag{A20}$$

Since the inverse tangent is a monotonic increasing function, the minimum value of the area is achieved for the minimum argument. Since $(b^2 - a^2) < 0$, the minimum value is obtained for the maximum value of $\sin(\phi)$, i.e. for $\phi = \frac{\pi}{2}$:

$$A_{min} = 2ab \left\{ \frac{\pi}{2} + tg^{-1} \left(\frac{(b^2 - a^2)}{2ab} \right) \right\} \tag{A21}$$

We point out that the case of $\phi = 0°$ corresponds to have two completely overlapped ellipses, and in such case $A_{int} = \pi ab$, namely the overall area of the ellipse.

---

* $tg^{-1}(x) \pm tg^{-1}(y) = tg^{-1}\left(\frac{x \pm y}{1 \mp xy} \right)$

PUBLICATIONS

JOURNALS

J1. F. Santi, M. Antoniou, D. Pastina, "**Point Spread Function analysis for GNSS-based multistatic SAR**", in press on IEEE Geoscience Remote Sensing Letters.

J2. D. Pastina, F. Santi, M. Bucciarelli, "**MIMO Distributed Imaging of Rotating Targets for Improved 2D Resolution**", in press on IEEE Geoscience Remote Sensing Letters.

CONFERENCE PROCEEDINGS

C1. F. Santi, M. Antoniou, D. Pastina, D. Tzagkas, M. Bucciarelli, M. Cherniakov, "**Passive multi-static SAR with GNSS transmitters: first theoretical and experimental results with point targets**", EUSAR 2014, June 2014.

C2. F. Santi, D. Pastina, P. Lombardo, "**ISAR while-scan mode for coastal surveillance**", IEEE 2014 Radar Conference, May 2014.

C3. F. Santi, D. Pastina, M. Bucciarelli, "**Multi-sensor ISAR techniques for motion estimation of pitching, rolling and yawing targets**", IEEE 2013 Radar Conference, May 2013.

C4. F. Santi, M. Bucciarelli, D. Pastina, "**2D-MIMO distributed ISAR imaging of rotating targets with improved range and cross-range resolution**", IEEE 2012 GOLD Remote Sensing Conference, June 2012.

C5. F. Santi, M. Bucciarelli, D. Pastina, "**Target rotation motion estimation from distributed ISAR data**", IEEE 2012 Radar Conference, May 2012.

C6. D. Pastina, F. Santi, M. Bucciarelli, P. Lombardo, "**2D-MIMO SAR/ISAR imaging of moving targets with reconfigurable formation of platforms**", EUSAR 2012, April 2012.

C7. D. Pastina, F. Santi, M. Bucciarelli, "**Multi-angle distributed ISAR with stepped-frequency waveforms for surveillance and recognition**", CIE International Conference on Radar, October 2011.

C8. F. Santi, P. Lombardo, D. Pastina, "**Oil spill detection using a coastal high-resolution radar**", IEEE 2011 Radar Conference, May 2011.

TECHNICAL REPORTS

T1. M. Bucciarelli, F. Santi, D. Pastina, "**Study on Distributed ISAR techniques**" - final technical report, July 2012 .

ACCEPTED FOR PUBLICATION

A1. F. Santi, M. Antoniou, D. Pastina, D. Tzagkas, M. Bucciarelli, M. Cherniakov, "**Passive multistatic SAR with GNSS transmitters: preliminary experimental study**", EuRAD 2014, October 2014.

A2. F. Santi, M. Bucciarelli, D. Pastina, "**Multi-sensor ISAR techniques for feature-based motion estimation of ship targets**", International Radar Conference, October 2014.

REFERENCES

[1] N. J. Willis, Bistatic Radar, Boston, MA: Artech House, 1991.

[2] H. Griffith, "Bistatic: introduction and historical background", NATO SET-136 Lecture Series, 2009.

[3] M. Cherniakov (ed.), Bistatic Radar: Emerging Technology, New York: Wiley, 2008.

[4] C.J. Baker, "An introduction to multistatic radar", NATO SET-136 Lecture Series "Multistatic Surveillance and Reconnaissance: Sensor, Signals and Data Fusion", April 2009.

[5] R.L. Easton, J.J. Fleming, "The Navy Space Surveillance System," Proceedings of the IRE , Vol. 48, No. 4, pp. 663-669, April 1960.

[6] Peterson Air Force Base website – http://www.peterson.af.mil

[7] J.I. Glaser, "Fifty years of bistatic and multistatic radar", IEE Proceedings on Communications, Radar and Signal Processing, Vol. 133, No. 7, pp. 596-603, December 1986.

[8] K. Milne, "Principles and concepts of multistatic surveillance radar", Radar-77; Proceedings of the International Conference, London, England, October 25-28, 1977.

[9] D. Baumgarten, "Optimum detection and receiver performance for multistatic radar configurations," ICASSP 1982, IEEE International Conference on Acoustics, Speech, and Signal Processing, Vol. 7, pp. 359,362, May 1982.

[10] V.S. Cherniyak, "Fundamentals of Multisite Radar Systems", Gordon and Breach Science Publisher, 1998.

[11] M.I. Skolnik, Introduction to Radar Systems, Third edition, McGraw-Hill, New York, 2001.

[12] L.V. Blake, Radar range-performance analysis, MA: Lexington Books, 1986.

[13] G. Krieger, A. Moreira, "Spaceborne bi- and multistatic SAR: potential and challenges", IEE Proc. Radar, Sonar and Navig., Vol. 153, No. 3, June 2006, pp. 184-198.

[14] S. Barbarossa, "Multiantenna Wireless Communication System", Artech House, 2005.

[15] E. Fishler, A. Haimovich, R. Blum, D. Chizhik, L. Cimini, R. Valenzuela, "MIMO radar: an idea whose time has come," Proceedings of the 2004 IEEE Radar Conference, pp. 71-78, 26-29 April 2004.

[16] L. Jiani, P. Stoica, "MIMO Radar with Colocated Antennas", IEEE Signal Processing Magazine, Vol. 24, No. 5, pp.106-114, Sept. 2007.

[17] A.M. Haimovich, R.S. Blum, L.J. Cimini, "MIMO Radar with Widely Separated Antennas", IEEE Signal Processing Magazine, Vol 25, No 1, pp.116-129, 2008.

[18] C.Y. Chen, P.P. Vaidyanathan, "MIMO radar waveform optimization with prior information of the extended targets and clutter", IEEE Trans. on Signal Processing, Vol. 57, pp. 3533-3544, Sept. 2009.

[19] D.R. Fuhrmann, G.S. Antonio, "Transmit beamforming for MIMO radar systems using partial signal correlation," in Proc. 38th IEEE Asilomar Conf. Signals, Syst., Comput., Nov. 2004, pp. 295–299.

[20] D.R. Fuhrmann, G.S. Antonio, "Transmit beamforming for MIMO radar systems using signal cross-correlation", IEEE Trans. Aerosp. Electron. Syst., Vol. 44, pp. 171–186, Jan. 2008.

[21] P. Stoica, J. Li, Y. Xie, "On probing signal design for MIMO radar", IEEE Trans. Signal Process., Vol. 55, No. 8, pp. 4151–4161, Aug. 2007.

References

[22] P. Stoica, J. Li, X. Zhu, "Waveform synthesis for diversity-based transmit beampattern design", IEEE Trans. Signal Process., Jun. 2008.

[23] C.Y. Chen, P.P. Vaidyanathan, "MIMO radar ambiguity properties and optimization using frequency-hopping waveforms", IEEE Trans. Signal Process., Dec. 2008.

[24] B. Liu, Z. He, J. Zeng, and B. Y. Liu, "Polyphase orthogonal code design for MIMO radar systems," in Proc. Int. Conf. Radar, Oct. 2006.

[25] B. Liu, Z. He, Q. He, "Optimization of orthogonal discrete frequency-coding waveform based on modified genetic algorithm for MIMO radar", in Proc. Int. Conf. Commun., Circuits, Syst., pp. 966–970, Jul. 2007.

[26] B. Friedlander, "Waveform design for MIMO radars", IEEE Trans. Aerosp. Electron. Syst., Vol. 43, pp. 1227–1238, Jul. 2007.

[27] Y. Yang, R.S. Blum, "Minimax robust MIMO radar waveform design", IEEE Journal of Selected Topics on Signal Processing, Vol. 1, No. 1, pp. 147-155, Jun. 2007.

[28] H. Griffiths, "Multistatic, MIMO and networked radar: the future of radar sensors?", Proc. of 7th European Radar Conference, EuRAD 2010, pp. 81-84, Sept. 30 2010-Oct. 1 2010.

[29] F. Daum, J. Huang, "MIMO radar: Snake oil or good idea?", IEEE Aerospace and Electronic Systems Magazine, Vol. 24, No. 5, pp. 8-12, May 2009.

[30] H. Griffith, "Passive bistatic radar", NATO SET-133-06 Lecture Series, April 2009.

[31] Special Issue on Passive Radar Systems – IEE Proc. on Radar, Sonar and Navigation, Vol. 152, Issue 3, pp.106-223, June 2005.

[32] R. Eigel, P. Collins, A. Terzuoli, G. Nesti, J. Fortuny, "Bistatic characterization of complex objects", IEEE Trans. on GRS, Vol. 38, No. 5, pp. 2078-292, 2000.

[33] R.J. Burkholder, I.J. Gupta, J.T. Johnson, "Comparison of monostatic and bistatic radar images", IEEE Antennas Propoag. Mag., Vol. 45, No. 3, pp.41-50, 2003.

[34] D.A.R. Beale, A.L. Hume, "Bistatic RCS tools for the assessment of multi-static radar," RADAR 2002 , Edinburgh (UK), pp. 31-35, 15-17 Oct. 2002.

[35] A.K. Mishra, B. Mulgrew, "Ground target classification for airborne bistatic radar", 1st EMRS DTC Technical Conf. Edinburgh, 2004.

[36] S.R. Doughty, K. Woodbridge, C.J. Baker, "Improving resolution using multistatic SAR", Proc. IET Int. Conf. Radar Systems, 2007.

[37] L.M.H. Ulander, T. Martin, "Bistatic ultrawideband SAR for imaging of ground targets under foliage", Proc. IEEE Radar Conf., pp. 419-423, May 2005.

[38] W. Goj, "Synthetic Aperture Radar and Electronic Warfare", MA: Artech House, Boston, 1993.

[39] G. Krieger, H. Fiedler, J. Mittermayer, K. Papathanassiou, A. Moreira, "Analisys of multi-static configurations for spaceborne SAR interferometry", IEE Proc. Radar Sonar Navig., 2003, 150 (3), pp.87-96.

[40] G. Ferraiuolo, F. Meglio, V. Pascazio, G. Schirinzi, "DEM Reconstruction Accuracy in Multichannel SAR Interferometry", IEEE Trans. on GRS, Vol.47, No.1, pp.191-201, Jan. 2009.

[41] G. Krieger, M. Younis, N. Gebert, S. Huber, F. Bordoni, A. Patyuchenko, A. Moreira , "Advanced Concepts for High-Resolution Wide-Swath SAR Imaging", 8th European Conference on Synthetic Aperture Radar (EUSAR 2010), pp. 524-527, 7-10 June 2010.

[42] N.H. Lehmann, A.M. Haimovich, R.S. Blum, L. Cimini, L., "High Resolution Capabilities of MIMO Radar", Fortieth Asilomar Conference on Signals, Systems and Computers, 2006. ACSSC '06, pp.25,30, Oct. 29 2006-Nov. 1 2006.

[43] S.D. Blunt, W. Dower, K. Gerlach, "Hybrid interference suppression for multistatic radar", IET Radar, Sonar & Navigation, Vol.2, No.5, pp.323-333, Oct. 2008.

References

[44] G. Bin V. Duc, X. Luzhou, X. Ming, L. Jian, "Ground Moving Target Indication via Multichannel Airborne SAR", IEEE Trans. on GRS, Vol.49, No.10, pp.3753-3764, Oct. 2011.

[45] F. Baselice, A. Budillon, G. Ferraioli, V. Pascazio, G. Schirinzi, A. Evangelista, "New trends in SAR tomography", 2010 IEEE International Geoscience and Remote Sensing Symposium (IGARSS), pp.25-28, 25-30 July 2010.

[46] W. Yong , D.C. Jr. Munson, "Multistatic passive radar imaging using the smoothed pseudo Wigner-Ville distribution", Proc. of 2001 International Conference on Image Processing, Vol. 3, pp. 604-607, 2001.

[47] V. Krishnan, J. Swoboda, C.E. Yarman, B. Yazici, "Multistatic Synthetic Aperture Radar Image Formation", IEEE Transactions on Image Processing, Vol.19, No.5, pp.1290-1306, May 2010.

[48] D. Massonett, "Capabilities and limitations of the interferometric cartwheel", IEEE Trans. on GRS, 39 (3), pp. 87-96, 2001.

[49] M. D'Errico, A. Moccia, "The BISSAT mission: A bistatic SAR operating in formation with COSMO/SkyMed X-band radar," 2002 IEEE Aerospace Conference Proceedings, Vol. 2, pp. 809-818, 2002.

[50] M. Martin, P. Kulpar, S. Kilberg, J. Winter, "Techsat 21 and revolutionizing space missions using microsatellites", Proc. of 15th American Institute of Aeronautics and Astronautics Conference on Small Satellites, Utah (USA), 2001.

[51] G. Krieger, A. Moreira, H. Fiedler, I. Hanjnsek, M. Werner, M. Younis, M. Zink, "TanDEM-X: A satellite formation for high-resolution SAR interferometry", IEEE Trans. Geosci. Remote Sens., vol. 45, no. 11, pp. 3317-3341, Nov. 2007.

[52] http://en.wikipedia.org/wiki/TanDEM-X

[53] J.L. Auterman, "Phase stability requirements for a bistatic SAR", IEEE National Radar Conference 1984, Atlanta, 13.-14. March, pp. 48-52.

[54] G. Yates, M. Horne, A. Blake, R. Middleton, D.B. Andre, "Bistatic image formation", Proc. of EUSAR 2004, Ulm, Germany, 25-27 May 2004.

[55] I. Walterscheid, A.R. Brenner, J.H.G. Ender, "Results on bistatic synthetic aperture radar", Electronics Letters 2004, 40(19), pp. 1224-1225.

[56] P. Dubois-Fernandez, H. Cantalloube, B. Vaizan, G. Krieger, R. Horn, M. Wendler, V. Giroux, "ONERA-DLR bistatic SAR campaign: Planning, data acquisition, and first analysis of bistatic scattering behaviour of natural and urban targets", Proc. IET Radar Sonar Navig., vol. 153, no. 3, pp. 214-223, Jun. 2006

[57] C.C. Chen, H.C. Andrews, "Target-motion-induced radar imaging," IEEE Trans. Aerosp. Electron. Syst., Vol. AES 16, No. 1, pp. 2–14, 1980.

[58] J.L. Walker, "Range-Doppler imaging of rotating objects," IEEE Trans. Aerosp. Electron. Syst., Vol. AES-16, No. 1, pp. 23–52, Jan. 1980.

[59] T. Hagfors, D. Campbell, "Mapping of planetary surfaces by radar," Proc. IEEE, Vol. 61, p. 1219, Sept. 1973.

[60] D.R. Wehner, "High-Resolution Radar", Artech House, Boston, 1995.

[61] S. Musman, D. Kerr, C. Bachmann, "Automatic recognition of ISAR ship images", IEEE Transactions on Aerospace and Electronic Systems, Vol. 32, No. 4, pp. 1392-1404, Oct. 1996.

[62] J. Palmer, J. Homer, I.D. Longstaff, M. Martorella, B. Littleton, "ISAR imaging using an emulated multistatic radar system", IEEE Trans. Aerosp. Electron. Syst., Vol. 41, No. 4, pp. 1464–1472, Oct. 2005.

[63] M. Martorella, J. Palmer, J. Homer, B. Littleton, and I. D. Longstaff, "On bistatic inverse synthetic aperture radar", IEEE Trans. Aerosp. Electron. Syst., Vol. 43, No. 3, pp. 1125–1134, Jul. 2007.

[64] G. Wang, X.G. Xia, V.C. Chen, "Three dimensional ISAR imaging of manoeuvring targets using three receivers", IEEE Trans. on Image Processing, Vol. 10, No. 3, Mar. 2001, pp. 436-447.

[65] Q. Zhang, T.S. Yeo, G. Du, S. Zhang, "Estimation of three dimensional motion parameters in interferometric ISAR imaging", IEEE Trans. on GRS, Vol. 42, No. 2, Feb. 2004, pp. 292-300.

[66] C. Ma, T.S. Yeo, Q. Zhang, H.S. Tan, J. Wang, "Three-dimensional ISAR imaging based on antenna array", IEEE Trans. on GRS, Vol. 46, No. 2, Feb. 2008, pp.504-515.

[67] C. Prati, F. Rocca, D. Giancola, A. Monti Guarnieri, "Passive geosynchronous system reusing backscattered digital audio broadcasting signals", IEEE Trans. On GRS, Vol. 36, No 6, 1998, pp. 1973-1976.

[68] L. Cazzani, C. Colesanti, D. Leva, G. Nesti, C. Prati, F. Rocca, D. Tarchi, "A ground-based parasitic SAR experiment", IEEE Trans. On GRS, Vol. 38, Issue 5, Part: 1, 2000, pp.2132-2141.

[69] M. Cherniakov, R. Saini, R. Zuo, M. Antoniou, "Space-surface bistatic synthetic aperture radar with global navigation satellite system transmitter of opportunity – experimental results", IET Radar Sonar Navig.,1, (6), pp. 447 – 458, 2007.

[70] M. Antoniou, M. Cherniakov, "GNSS-based SAR: A signal processing view", EURASIP Journal on Advances in Signal Processing, 2013:98, May 2013.

[71] M. Antoniou, Z. Zeng, L. Feifeng, M. Cherniakov, "Experimental demonstration of passive BSAR imaging using navigation satellites and a fixed receiver", IEEE GRLS, Vol. 9, No. 3, pp. 477-481, May 2012.

[72] G. Ginolhac, F. Schmitt, F. Daout, P. Forster, "Multifrequency and multistatic inverse synthetic aperture radar, with application to FM passive radar", EURASIP Journal on Advances in Signal Processing, 2010:497074.

[73] D. Olivadese, E. Giusti, D. Perti, M. Martorella, A. Capria, F. Berizzi, "Passive ISAR with DVB-T signals", IEEE Trans. On GRS, Vol. 51, No. 8, 2013, pp. 4508-4517.

[74] F. Maussang, F. Daout, G. Ginolhac, F. Schmitt, "GPS ISAR passive system characterization using Point Spread Function", Conference on New Trends for Environmental Monitoring Using passive Systems, Hyères (France), Oct. 2008.

[75] D. Pastina, M. Sedhei, D. Cristallini, "Geostationary satellite based passive bistatic ISAR for coastal surveillance", 2010 IEEE Radar Conference, Washington (USA), May 2010.

[76] F. Turin, D. Pastina, "Multistatic passive ISAR based on geostationary satellites for coastal surveillance", 2013 IEEE Radar Conference, Ottawa (Canada), May 2013.

[77] G. Krieger, M. Younis, "Impact of oscillator noise in bistatic and multistatic SAR", IEEE Geosci. Remote Sens. Lett., Vol. 3, No. 3, pp. 424-428, July 2006.

[78] M. Weib, "Synchronization of bistatic radar systems", IGARSS 2004, Anchorage (USA), 2004.

[79] R. Kroes, O. Montenbruck, "Spacecraft formation flight: relative positioning using dual-frequency carrier phase", GPS World, pp. 37-42, July 2003.

[80] Wen-Qin Wang, "MIMO SAR imaging: Potential and challenges", IEEE Aerospace and Electronic Systems Magazine, Vol. 28, No. 8, pp. 18-23, Aug. 2013.

[81] J.H.G. Ender, I. Walterscheid, A.R. Brenner, "New aspects of bistatic SAR: processing and experiments", Proceedings. 2004 IEEE International Geoscience and Remote Sensing Symposium IGARSS '04, Vol.3, pp.1758-1762, 20-24 Sept. 2004.

[82] D. Pastina, M. Bucciarelli, P. Lombardo, "Multistatic and MIMO distributed ISAR for enhanced cross-range resolution of rotating targets", IEEE Trans. On GRS, Vol. 48, Issue: 8, 2010.

[83]   M. Bucciarelli, D. Pastina, "Multi-grazing ISAR for side-view imaging with improved cross-range resolution", Proc. of 2011 IEEE Radar Conference, Kansas City (USA), May 2011.

[84]   M. Bucciarelli, D. Pastina, "Distributed ISAR focusing for targets undergoing 3D motion", Proc. of IET International Conference on radar Systems, Glasgow (UK), Oct. 2012.

[85]   C. Prati, R. Rocca, "Improving slant-range resolution with multiple SAR surveys", IEEE Trans. on AES, Vol. 29, Issue 1, 1993, pp. 135-144.

[86]   D. Cristallini, D. Pastina, P. Lombardo, "Exploiting MIMO SAR potentialities with efficient cross-track constellation configurations for improved range resolution", IEEE Trans. on GRS, Vol. 49, Issue 1, Jan. 2011, pp.38-52.

[87]   H. Jeong, H. Kim, K. Kim, "Application of Subarray Averaging and Entropy Minimization Algorithm to Stepped-Frequency ISAR Autofocus", IEEE Trans. On Antennas and Propagation, Vol.56, No. 4, April 2008.

[88]   P. Cao, M. Xing, G. Sun, Y. Li, Z. Bao, "Minimum entropy via subspace for ISAR autofocus", IEEE Geoscience Remote Sensing Letters, Vol. 7, No. 1, Jan. 2010, pp.205-209.

[89]   F. Berizzi and G. Corsini, "Autofocusing of inverse synthetic aperture radar images using contrast optimization," IEEE Trans. Aerosp. Electron. Syst., Vol. 32, No. 3, pp. 1185–1191, Jul. 1996.

[90]   X. Li, G. S. Liu, and J. L. Ni, "Autofocusing of ISAR images based on entropy minimization", IEEE Trans. Aerosp. Electron. Syst., Vol. 35, No. 4, pp. 1240–1251, Oct. 1999.

[91]   AW Doerry, "Ship dynamics for maritime ISAR imaging", SANDIA Report: SAND2008-1020, Feb. 2008.

[92]   V.C. Chen, R. Lipps, "ISAR imaging of small craft with roll, pitch and yaw analysis", Proc. Of 2000 International Radar Conference, May 2000.

[93]   A.W. Rihaczek, S.J. Hershkowitz, "Theory and practice of radar target identification", Artech House, Boston, 2000, Chapter 5.

[94]   D. Pastina, "Rotation motion estimation for high-resolution ISAR and hybrid SAR/ISAR imaging", Proc. of 2008 IEEE Radar Conference, Rome (Italy), May 2008.

[95]   M. Martorella, "Novel approach for ISAR image cross-range scaling", IEEE Trans. on AES, Vol. 44, Issue 1, Jan. 2008, pp. 281-294.

[96]   D. Pastina, C. Spina, "Slope-based frame selection and scaling technique for ship ISAR imaging", IET Proc. on SP, Vol. 2, Issue 3, Sep. 2008, pp. 265-276.

[97]   K. Suwa, T. Wakayama, M. Iwamoto, "Three-dimensional target geometry and target motion estimation method using multistatic ISAR movies and its performance", IEEE Trans. on GRS, Vol. 49, No. 6, June 2011, pp. 2361-2373.

[98]   M. Younis, R. Metzig, G. Krieger, "Performance prediction of a phase synchronization link for bistatic SAR", IEEE Geoscience Remote Sensing Letters, Vol. 3, No. 3, July 2006, pp. 429-433.

[99]   G. Fornaro, V. Pascazio, G. Schirinzi, "Resolution improvement via multipass SAR imaging", Proc. of IGARSS, Sydney (AUS), July 2001.

[100]   S. Guillaso, A. Reigber, L. Ferro-Famil, E. Pottier, "Range resolution improvement of airborne SAR images", IEEE Geoscience Remote Sensing Letters, Vol. 3, No. 1, "006, pp.135-139.

[101]   B. Correll, "Efficient spotlight SAR MIMO linear collection geometries", Proc. EuRAD, Amsterdam (NL), Oct. 2008.

[102]   F. Gatteli, A.M. Guarnieri, F. Parizzi, P.Pasquali, C. Prati, F. Rocca, "The wavenumber shift in SAR interferometry", IEEE Trans. on GRS, Vol. 29, No. 5, pp. 855-864, Sep. 1993.

[103]   M. Martorella, F. Berizzi, "Time Windowing for Higly Focused ISAR image Reconstruction", IEEE Trans. on AES, Vol. 41, Issue 3, July 2005, pp. 992-1007.

References

[104] S.U. pillai, B. himed, K.Y. Li, "Orthogonal pulsing Schemes for Improved Target Detection in Space Based Radar", 2005 IEEE Aerospace Conference, Big Sky, MT, March 5-12, 2005.

[105] S.U. Pillai, B. Himed, K.Y. Li, "Effect of Earth's rotation and range foldover on space-based radar performance", IEEE Trans. on AES, 2006, (42), (3), pp. 917-932.

[106] "Technical characteristics of maritime radio-navigations radars", ITU-R Recommendation M.1313, International Telecommunication Union, Geneva.

[107] RADAR LYRA 50 SERIES- VTS APPLICATION, http://selex-systemintegration.de/fileadmin/media/pdf/LYRA.pdf.

[108] F. Balke, "Field test of bistatic forward-looking synthetic aperture radar", in Proc. IEEE Radar Conf., 2005, pp. 423-429.

[109] M. Rodriguez-Cassola, S.V. Baumgartner, G. Krieger, A. Moreira, "Bistatic TerraSAR-X/F-SAR spaceborne-airborne SAR experiment: description, data processing and results", IEEE Trans. On GRS, Vol. 48, NO. 2, pp. 781 − 794, 2010.

[110] J. Sanz-Marcos, P. Lopez-Dekker, J.J. Mallorqui, A. Aguasca, P. Prats,"SABRINA − A SAR bistatic receiver for interferometric applications", IEEE GRSL, Vol. 4, NO. 2, pp. 307 − 311, Apr. 2007.

[111] Z. Zeng, M. Antoniou, Q. Zhang, M. Hui, M. Cherniakov, "Multi-perspective GNSS-based passive BSAR: Preliminary experimental results", 14th International Radar Symposium 2013, pp. 467-472, June 2013.

[112] F. Daout, F. Schmitt, G. Ginolhac, P. Fargette, "Multistatic and multiple frequency imaging resolution analysis − Application to GPS-based multistatic radar", IEEE trans. AES, vol. 48, no. 4, pp. 3042-3057, Oct. 2012.

[113] T. Zeng, M. Cherniakov, T. Long, "Generalized Approach to Resolution Analysis in BSAR", IEEE Trans. Aereosp. Electron. Syst., vol. 41, no. 2, pp. 461-474, Apr. 2005.

[114] F. Liu, M. Antoniou, Z. Zeng, M. Cherniakov, "Point spread function analysis for BSAR with GNSS transmitters and long dwell times: Theory and experimental confirmation", IEEE Trans. Geosci. Remote Sens. Letters, vol. 10, no. 4, pp. 781-785, July 2013.

[115] R. Saini, R. Zuo, M. Cherniakov, "Problem of syncronisation in Space-Surface Bistatic SAR based on GNSS emissions − Experimental results", IET Radar, Sonar Navig., vol. 4, no 1, pp. 10-125, Feb. 2010.

[116] M. Daun, "Deghosting in passive air surveillance systems," 2010 11th International Radar Symposium (IRS), 16-18 June 2010.

[117] D.E. Hack, L.K. Patton, A.D. Kerrick, M.A. Saville, "Direct Cartesian detection, localization, and de-ghosting for passive multistatic radar", IEEE 7th Sensor Array and Multichannel Signal Processing Workshop (SAM), 2012, pp. 45-48.

[118] A. Fasoula, H. Driessen, P.V. Genderen, "De-ghosting of tomographic images in a radar network with sparse angular sampling", International Journal of Microwave and Wireless Technologies, 2010, 2(3-4), 359–367.

[119] E.W. Weisstein, Ellipse, From MathWorld − A Wolfram Web Resource, online http://mathworld.wolfram.com/Ellipse.html.